MODELING AND STABILITY OF FLOWS IN COMPLIANT MICROCHANNELS

by

Xiaojia Wang

A Dissertation

Submitted to the Faculty of Purdue University

In Partial Fulfillment of the Requirements for the degree of

Doctor of Philosophy

School of Mechanical Engineering

West Lafayette, Indiana

August 2022

THE PURDUE UNIVERSITY GRADUATE SCHOOL
STATEMENT OF COMMITTEE APPROVAL

Dr. Ivan C. Christov, Chair

School of Mechanical Engineering

Dr. Jun Chen

School of Mechanical Engineering

Dr. Hector Gomez

School of Mechanical Engineering

Dr. Guang Lin

Department of Mathematics

Approved by:

Dr. Nicole L. Key

To my parents

ACKNOWLEDGMENTS

I would like to express my deepest gratitude to my advisor, Prof. Ivan C. Christov. This thesis would not have been possible without his intellectual guidance and persistent support. He is the best mentor and also a reliable friend to me, always accessible, willing to listen, share and help. He teaches me what a resilient researcher should be like, through his own examples, with his scrupulous attitudes and incredible patience. He helps me build my confidence by celebrating every accomplishment that I have achieved, and encourages me whenever I become hesitant and timid. The past four years of being his student has been the most enjoyable period in my life.

I would also like to thank my committee members, Prof. Jun Chen, Prof. Hector Gomez and Prof. Guang Lin, for being always supportive. Their advice has been very helpful in improving this thesis.

I am also very grateful to my parents for their unconditional love to me. They had been very worried and anxious about my decision of studying abroad, but they still chose to respect my choice. As always, they are standing with me to support whatever I want to pursue.

I would also like to express my love and gratitude to my husband, Ke Zhou. We met when we were both undergraduate students, went to Shanghai together for the master's degree, and embarked on the Ph.D. studies at the same time. This long journey has never been lonely with his company. He is my best friend, who applauds for my success, comforts me when I am down, and supports me to get through all the hard times.

I also want to thank my roommate, Fei Qin, for her company over the past four years. Those trails that we explored together, those afternoons when we made ugly desserts, and those games that made us laugh have been composited into many many beautiful memories of mine.

I am also thankful for being a part of a welcoming and inclusive group at the TMNT-Lab, where I have many friendly and helpful colleagues: Dr. Daihui Lu, Dr. Evgeniy Boyko, Dr. Kimberly A. Stevens Boster, Zongxin Yu, Shrihari Pande, Tanmay C. Shidhore, Pranay P. Nagrani, and Jielin Yang.

My last acknowledgment is made to the U.S. National Science Foundation for partial support of this research under grants No. CBET-1705637 and No. CMMI-202954, as well as a Ross Fellowship from The Graduate School at Purdue University.

TABLE OF CONTENTS

LIST OF TABLES

LIST OF FIGURES

ABSTRACT

Fluids conveyed in deformable conduits are often encountered in microfluidic applications, which makes fluid–structure interactions (FSIs) an unavoidable phenomenon. In particular, experiments reported the existence of FSI instabilities in compliant microchannels at low Reynolds numbers, Re, well below the established values for rigid conduits. This observation has significant implications for new strategies for mixing at the microscale, which might harness FSI instabilities in the absence of turbulence. In this thesis, we conduct research on the modeling and stability of microscale FSIs. Understanding the steady response, the dynamics and the stability of these FSIs are the three major objectives. This thesis begins with the analysis of the steady-state scalings and the linear stability of a previously derived mathematical model, through which we emphasize the power of reduced modeling in making the FSI problems tractable. Next, we turn to a more realistic problem regarding FSIs in a common configuration of low-Re flows through long, shallow rectangular three-dimensional microchannels. Through a scaling analysis, which takes advantage of the geometric separation of scales, we find that the flow can be simplified under the lubrication approximation, while the wall deforms like a variable-stiffness Winkler foundation at the leading order. Coupling these dominant effects, we obtain a new fitting-parameter-free flow rate–pressure drop relation for a thick-walled microchannel, which rationalizes previous experiments. Then, we derive a one-dimensional (1D) steady model, at both vanishing and finite Re, by coupling the reduced flow and deformation models. To satisfy the displacement constraints along the channel edges, weak tension is introduced to regularize the underlying Winkler-foundation-like mechanism. This model is then made dynamic by introducing flow unsteadiness and the elastic wall's inertia. We conduct a global stability analysis of this system by perturbing the non-flat steady state with infinitesimal perturbations. We identify the existence of globally unstable modes, typically in the weakly inertial flow regime, whose features are consistent with experimental observations. The unstable eigenmodes oscillate at frequencies close to the natural frequency of the wall, suggesting that the instabilities are resonance phenomena. We also capture the transient energy amplification of perturbations through a linear non-normality analysis of the proposed reduced 1D FSI model.

1. INTRODUCTION

1.1 Literature survey on microscale fluid–structure interactions

Microfluidic devices have enabled the miniaturization of processes that involve the flow and manipulation of small volumes of fluids, down to the nanoliter [1]. In recent years, polymer-based materials have become popular for the fabrication of microfluidic devices because they promise cheaper and faster production cycles [2]. A widely-used material for microfabrication is the elastomer poly(dimethylsiloxane) (PDMS) [3]–[5]. The development of PDMS-based microfluidic devices is intimately related to the emergence of the cutting-edge technology known as *lab-on-a-chip* [6], [7]. Also, as PDMS is bio-compatible, microchannels made from PDMS have found many applications [8], such as platforms for organ-on-a-chip models [9] and various biological studies (*e.g.*, assays and combinatorial screening) [10]. PDMS, also known commercially as SYLGARD™ 184, typically has a low tensile modulus [11], and PDMS-based micro-conduits are prone to deformation ("bulging") under applied forces [12], [13]. Although early studies considered deformation to be a drawback, because it may restrict the structural viability of a device [14], [15], the compliance of PDMS microchannels has been exploited to design microfluidic devices with specific functions, such as pressure-actuated valves [16], passive fuses [17], pressure sensors [18], [19], strain sensors [20], impedance-based flow meters with improved sensitivity [21], micro-rheometers with increased sensitivity [22], and passive technique for profiling microchannels' shape [23].

The soft nature of microfluidic devices made from PDMS or similar materials requires the consideration of *fluid–structure interactions* (FSIs), even at the low Reynolds numbers encountered at these scales [24]. Given the broad range of applications of these microsystems, understanding the interplay between fluid and solid mechanics is important and necessary [25]. Conceptually speaking, the soft wall of the microchannel will deform due to the hydrodynamic pressure within the conduit, and this deformation will, in turn, modify the flow velocity and pressure gradient by changing the cross-sectional area of the conduit. This two-way coupling between the internal low-Reynolds-number flow and the soft boundary deformation/motion has led to new observations, which are not possible in rigid conduits, regarding both the steady and dynamic responses of the coupled system.

1.1.1 The steady response: nonlinear flow rate–pressure drop relation

On prominent feature of flow in deformable conduits is that the pressure drop required to maintain a steady flow varies nonlinearly with the volumetric flow rate, unlike the classic Hagen–Poiseuille law. Due to FSIs, the cross-sections of the soft conduit at different flowwise positions usually deform to a different extent, modifying the local velocity field and pressure gradient, and consequently, introducing a nonlinear coupling between the flow rate and the pressure drop. Quantifying this nonlinear flow rate–pressure drop relation, which is important for guiding the design of microfluidic devices, remains a challenging task.

Gervais *et al.* [12] were the first to put forward a model for the experimentally observed nonlinear flow rate–pressure drop relation in compliant micro-conduits. In their model, the strain in the elastic solid is taken to be linearly proportional to the hydrodynamic pressure, with the proportionality constant to be determined via calibration with experiments. In this way, they were able to quantify the flow rate–pressure drop relation in the inertialess flow regime and show that this relation deviates from the linear proportionality predicted by Poiseuille's law. Although the model in [12] was initially developed for microchannels with walls behaving like a semi-infinite elastic medium, the model has actually (with varying degrees of success) been also applied to FSIs in microchannels with elastic walls of various thicknesses [26]–[28].

The fitting parameter in the model from [12] is inconvenient in applications because it has to be recalibrated for each microchannel's geometric and material properties. This model also neglects many fluid–solid coupling details because a solution of the elasticity problem has not been obtained from its governing equations. It has been previously observed that the fitting parameter has to be related to the top wall thickness [26]. Seker *et al.* [29] argued that half-space-like thick walls and plate-like thin walls should be treated differently, and they used an empirical formula to determine the fitting parameter in these two regimes.

Tremendous efforts have been made to resolve the fitting parameter by constructing appropriate theories for the steady FSIs, one key step of which is to build a pressure–deformation relation that suits the specific configuration of the microconduit [30]. Christov *et al.* [31] used perturbation methods to derive such a relation between the flow pressure and the deformation of a microchannel with a clamped top wall modeled as bending-dominated thin plate. Then, they successfully obtained a fitting-parameter-free flow rate–pressure drop relation by coupling the Stokes flow in the channel to the wall deformation. This result was also confirmed by Boyko *et al.* [32], at the leading order, using the so-called reciprocal theorems for Stokes flow and linear elasticity. The results in [31] were then extended by Shidhore and Christov [33] to account for the deformation of microchannels whose top wall behaves like a thick plate. Also, Anand *et al.* [34] discussed different deformation regimes in a similar microchannel configuration when the plate-like top wall was pre-stressed, while Boyko *et al.* [35] further considered nonlinear tension effects for a membrane-like wall. The steady flow rate–pressure drop relation in deformable channels conveying non-Newtonian fluids with shear-dependent viscosity [36], as well as viscoelastic response [37], have also been derived, based on the approaches from [31], [33]. Apart from the steady FSIs in rectangular microchannels, the nonlinear flow rate–pressure drop relation is also derived for several configurations of microtubes, considering the flow of both Newtonian and non-Newtonian fluids (with shear-dependent viscosity) [38], [39]. This line of research has shown that fitting parameters are not necessary to quantify microscale FSIs, and they can be avoided entirely by seeking a solution to the associated elasticity problem.

However, the predictive theories constructed in previous studies are focused on thin structures in rectangular microchannels. For a microchannel embedded in a thick soft material with a configuration as [12], as the solution for the wall deformation was lacking, no successful fitting-parameter-free models was put forward to account for the nonlinear flow rate–pressure drop relation in this configuration. Also, all of the discussions mentioned above consider inertialess flow only. As current PDMS-based microchannel technologies can actually access the inertial regime of $Re \simeq 10^2$ [40], a theory of the steady microchannel FSI at finite Reynolds number remains an open question.

1.1.2 The dynamic response: instabilities at low Reynolds number

Even a Reynolds number up to $Re \simeq 10^2$ is low compared to the well-documented flow-instability Re for flow in rigid conduits. However, such low-Re flows in compliant micro-

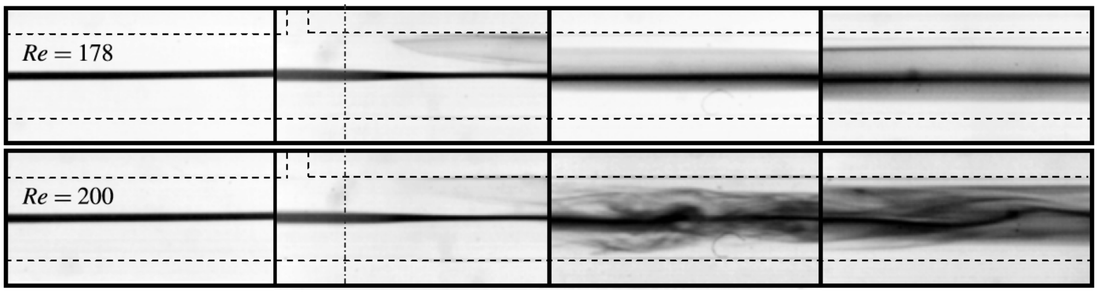

Figure 1.1. Dye breakup induced by flow instability visualized by a dye stream in clear water in a soft rectangular microchannel at low Reynolds number, reproduced from [41] © 2013 Cambridge University Press with permission.

conduits, surprisingly, have been observed to go unstable. A dye stream experiment by Verma and Kumaran [41] in a rectangular microchannel with a soft bottom wall, shown in figure 1.1, demonstrated that the stream begins to oscillates at $Re \approx 178$ and can break up at $Re \approx 200$. It was argued that the instabilities observed are induced by FSIs. Importantly, the resulting unstable flows increased the mixing efficiency by several orders of magnitude, compared to a stable steady flow. The observation has important implications for new strategies of harnessing FSI-induced instabilities to enhance mixing at the microscale, which is notoriously challenging [42], [43].

Further experimental studies bolster the hypothesis that FSIs lead to an instability of internal flows in compliant conduits at low Re. For example, it has been shown that Couette flows can be destabilized by soft boundaries at sufficiently low Re, even when fluid inertia is negligible [44], [45]. Interestingly, experiments by Shrivastava *et al.* [46] showed that the FSI-induced instability, in flows at $Re \approx 0.1$ to 60, could enhance mass transfer in a Couette flow by up to 25%. As for pressure-driven flows confined by soft boundaries, the earliest evidence of FSI-induced instability was provided by Krindel and Silberberg [47]. In a dye-stream visualization experiment, they observed that the lowest transition Re for water in a gel-walled tube was only 570, a strikingly low value in comparison to $Re \approx 2000$ for transition in a rigid tube, which is also valid at the microscale [48], [49]. Later experiments also showed unstable flows could be obtained for $Re < 1000$ in tubes with walls made from PDMS [50], [51]. Moreover, the transition Re is observed to be lower for more compliant tube walls.

Similar situations exist in channel flows. Apart from the experiment by Verma and Kumaran [41], Kumaran and Bandaru [52] also demonstrated that unstable flows can be triggered in a rectangular microchannel if one of the channel's walls is made sufficiently compliant. By taking advantage of this flow instability, almost complete mixing was achieved at $Re < 300$ between clear and dyed water. The terms "ultrafast mixing" and "soft-wall turbulence" have thus been coined to refer to such phenomena. However, it should be clarified that FSI-induced unstable flows are fundamentally different from the usual wall-bounded turbulent flows at high Re [53], [54].

Unlike shear flows, the initiation of instability by FSIs in pressure-driven flows in compliant conduits remains poorly understood. Early studies considered the classical unidirectional flows in rigid conduits (*e.g.*, Poiseuille or Hagen–Poiseuille flows) as the base state and derived Orr–Sommerfeld-type equations by perturbing the fluid–solid interface with infinitesimal disturbances. For example, Kumaran [55] analyzed the stability of a Newtonian fluid flow in a tube with walls made from a linearly viscoelastic material and predicted instabilities in the regime in which both fluid and solid inertia are negligible. The latter work was then extended by Gaurav and Shankar [56] by considering the tube wall as a neo-Hookean solid. However, one drawback of these analyses is that the effect of FSIs on the base state itself is not taken into account. As discussed in section 1.1.1, even at steady state, a compliant channel wall will deform due to the hydrodynamic pressure within, and this deformation will, in turn, influence the velocity and pressure fields in the flow [12], [30]. Since the pressure decreases along the flow-wise direction in a pressure-driven flow, the deformation is not uniform, with larger deformation near the inlet and smaller deformation near the outlet, typically. This non-flat shape of the deformed channel was indeed observed in the experiments by Verma and Kumaran [41]. Importantly, the coupling between the flow and the solid deformation gives rise to a *non-constant* pressure gradient in the streamwise direction, leading to a *nonlinear* relationship between the flow rate and the total pressure drop [12], [29], [31].

Subsequent studies sought to improve the linear stability analyses by incorporating the effect of nonuniform deformation of the conduit wall. The deformed shape of the channel was imaged experimentally and then reconstructed for use in computational fluid dynamics (CFD) simulations. By assuming steady flow, the simulated velocity profile and the pressure distribution were taken as the base state and "imported" into the linear stability analysis [41], [57]. Nevertheless, the stability analysis was still of Orr–Sommerfeld type, requiring the assumption that the variation of the channel deformation along the streamwise direction is so slow that the flow is nearly parallel. Therefore, this analysis is only applicable *locally*, and long-wave perturbations cannot be applied. Notably, the local unstable modes were predicted at $Re \simeq 100$ or below, both in channels [41], [58] and in tubes [57]. However, it is difficult to reach a unified understanding from the current state of the literature because a different explanation for the onset of the instabilities has been put forth for each of these various situations. For instance, replacing the linearly elastic model for the solid with a neo-Hookean model can change the linear stability of the flow in a compliant tube [56]. The different formulations of the linear stability analysis can also lead to completely different conclusions [59]. The most recent advances and perspectives following this line of research (which, in this thesis, we term as the "Kumaran family" of works) are thoroughly reviewed by Kumaran [60].

1.1.3 Reduced models for fluid–structure interactions

Understanding the FSI induced instabilities at low Re requires a methodology for quantifying the dynamics of FSIs, which is even more challenging than studying the steady FSIs. To reduce the mathematical complexity, reduced models are often derived. For example, using the same scaling approach as in [12], Dendukuri *et al.* [61], [62] proposed a one-dimensional (1D) model for studying unsteady stop-flow lithography in a thick-walled microfluidic device. Mukherjee *et al.* [63], following Skotheim and Mahadevan [64], [65] in their modeling, then considered actuation of the soft wall via electroosmotic flow. Notably, these studies started right away with two-dimensional (2D) configurations, and the solid inertia was not included. Moreover, the flow considered therein was creeping flow, with Reynolds number $Re \ll 1$, so that the final models could be reduced to a single (albeit nonlinear) partial differential equation (PDE) for the deformed channel height. Although Martínez-Calvo *et al.* [66] were able to extend the unsteady models, following [31] in their modeling, to capture the unsteady relaxation of 3D microchannels, the earlier approaches are generally not suitable for extensions to flows through 3D microchannels at *low but finite* Reynolds number, when instability occurs.

Reduced-order formulations (2D, or even 1D) have also been used to study the instabilities in the coupled flow–compliant wall problems, but typically in the high-Reynolds-number regime [67]–[69]. Specifically, there is a line of research, on the so-called collapsible tubes (such as arteries or other large blood vessels [70], [71]), also concerned with FSI-induced instabilities [72]–[74]. Over the past thirty years, tremendous efforts have been focused on understanding the various patterns of self-excited oscillations observed in collapsible tubes [71], [72], [75], [76]. Further, beyond theory and reduced models, CFD studies have provided accurate quantitative descriptions of the dynamics of collapsible tubes [73], [74], [77]–[80]. Nevertheless, reduced theoretical models are more flexible for exploring the (potentially large) parameter space of such systems. The relative simplicity of reduced models can also aid the mathematical analysis and thus promote the understanding of the instability mechanisms. Several reduced models have been put forward to give insights into the self-sustained oscillations in collapsible tubes. Although the early one-dimensional (1D) models [81] incorporated *ad hoc* assumptions, such as an empirical tube law for deformations and an energy loss term for flow separation, these models surprisingly provided good qualitative agreement with experimental observations [82] and predicted the expected complex oscillations [83], [84]. Later models used different strategies. For example, Pihler-Puzović and Pedley [85] constructed a 1D model based on the so-called interactive boundary layer theory and predicted oscillations induced by wall inertia. Stewart *et al.* [86] invoked the long-wave approximation and built another 1D model to study the global and local instabilities in collapsible tubes. This model was then used extensively to investigate the effect of the pretension of the soft wall [87], of the length of the downstream rigid segment [88], [89], and the model was also applied to understand retinal venous pulsation [90].

However, the reduced models derived for the collapsible tubes cannot be used for FSIs at the microscale. Even though it is reported that $Re \simeq 10^2$, instead of considering viscous flows as the Kumaran family of studies, the research on the collapsible tubes focuses on inertial flows at high Re. As we will show in chapter 3, in a slender conduit, the "reduced" $\hat{R}e = \epsilon Re$, is more suitable for quantifying the inertial effects in the flow. Here, ϵ is the aspect ratio of the conduit (radius to length for a tube, or height to length for a channel). Since collapsible tubes have much larger ϵ than microchannels, $\hat{R}\mathrm{e} \gg 1$ is typical, unlike $\hat{R}\mathrm{e}$ up to $\mathcal{O}(1)$ for flows in the Kumaran family.

Besides the regime of $\hat{R}\mathrm{e}$, the research on collapsible tubes is different from the microflows in soft conduits because collapsible tubes usually have an undeformed radius on the order of centimeters, thus they are not conveying flows at the microscale. Furthermore, many studies on collapsible tubes use the setup of the so-called Starling resistor [81], which is a device with an elastic thin-walled tube mounted between two rigid segments, placed in a pressurized chamber. Since the external pressure is larger than the internal pressure in the tube, the elastic tube undergoes large deformations, even buckling [81]. However, it is common in compliant microchannel/microtube experiments that the soft conduit is connected to a rigid segment upstream for the flow to be fully developed, while the downstream is open to air [41], [50]. Instead of collapse, the conduit will bulge with a mild increase of the cross-sectional area due to the internal hydrodynamic pressure of the flow. The thickness of the soft wall can be varied, though the standard approaches [3], [5] based on soft lithography often produce thick walls [12], [28].

Despite the above-mentioned differences, the methods used for analyzing FSIs in collapsible tubes might be useful for understanding the FSI-induced instabilities in compliant microchannels. As shown in table 1.1, the novelty of the work regarding the observed low-$R\mathrm{e}$ instabilities in this thesis comes from two aspects. First, we construct a new reduced model for microscale FSIs at low $R\mathrm{e}$. Second, we explain the FSI instabilities at low $R\mathrm{e}$ by investigating the global stability of the non-uniform steady state, which complements the local stability analysis in the Kumaran family of studies.

Beyond the linear global stability analysis (eigenvalue analysis) which concerns the evolution of infinitesimal perturbations around the base state in the long term ($t \to \infty$), we will also analyze the linear non-normality of the linearization around the base state to study the transient behaviors of the perturbations. The linear non-normality theory has been applied to explain the transient amplification of disturbances in shear flows [92]–[94], thin films [95], [96], as well as other fields such as meteorology [97], [98]. We refer to [99] for detailed discussions. As suggested by Thepfilis [100], the non-normal analysis "should complement

Table 1.1. Comparison of selected previous studies on instability of pressure-driven flows in complaint conduits. In the last column, 'OS' stands for Orr–Sommerfeld-type stability analysis; 'RM' stands for reduced modeling; 'Num.' specifically stands for 2D two-way coupled FSI simulations; 'Asym.' stands for asymptotic analysis; and 'MLEE' stands for matched local eigenfunction expansion method.

	Flat base?	$\hat{Re}$	Instability type	Method
Kumaran family				
Kumaran [55]	Yes	$\mathcal{O}(1)$	Local	OS
Gkanis and Kumar [58]	No	$\mathcal{O}(1)$	Local	OS
Gaurav and Shankar [56]	Yes	$\mathcal{O}(1)$	Local	OS
Verma and Kumaran [41]	No	$\mathcal{O}(1)$	Local	OS
Verma and Kumaran [57]	No	$\mathcal{O}(1)$	Local	OS
Collapsible tubes				
Jensen [83], [84]	No	$\gg 1$	Global	RM
Luo and Pedley [73], [74]	No	$\gg 1$	Global	Num.
Jensen and Heil [91]	No	$\gg 1$	Global	Asym. & Num.
Luo *et al.* [77]	No	$\gg 1$	Global	Num.
Stewart *et al.* [86]	Yes	$\gg 1$	Global & Local	RM
Stewart *et al.* [87]	Yes	$\gg 1$	Global & Local	OS & MLEE
Heil and Boyle [78]	Yes	$\gg 1$	Global	Num.
Liu *et al.* [79]	No	$\gg 1$	Global	Num.
Xu *et al.* [88], [89]	Yes	$\gg 1$	Global	RM
Pihler-Puzović and Pedley [85]	No	$\gg 1$	Global	RM
Wang *et al.* [80]	No	$\gg 1$	Global	Num.
This thesis, chapter 6	No	$\mathcal{O}(1)$	Global	RM

solutions of the [eigenvalue analysis]," which is useful especially in the case when "the latter disagrees with the physical reality."

1.2 Knowledge gap and organization of the thesis

The knowledge gaps identified by the literature survey in section 1.1, which will be addressed in different chapters of this thesis, are as follows:

- The dynamics and stability of FSIs at high Reynolds number have been typically analyzed by reduced models, in which it is explicitly assumed that fluid flow is 2D and the solid mechanics is 1D [72]. In principle, the same methodology can be applied to FSIs at the microscale, in the low-Reynolds-number regime. We adopt this point of view and discuss a 1D FSI model of viscous flow in a channel with a deformable in chapter 2, with emphasis on the steady scalings of pressure and deformation, as well as a linear stability analysis of the non-flat deformed channel shape. These two features, viscous flow at low Reynolds number and stability of the system with a non-flat base state, had not been analyzed previously in the literature.

- The reduced model introduced in chapter 2 was derived based on the explicit assumption of a 2D flow configuration. However, 3D configurations of flows through long, shallow complaint rectangular microchannels are more realistic [12]; indeed, channels in experiments have sidewalls a finite distance apart. Previous studies on this 3D FSI problem were focused on the inertialess flow regime and the microchannels often had plate-like thin walls [31], [33]. This thesis seeks to address the questions that arise from relaxing these previous assumptions. Specifically, *what dominant mechanisms can we identify, even at low but finite Reynolds number, by taking advantage of the channel being slender and shallow? If we expand the thickness range of the compliant wall, without requiring it to be thin, but still keeping its slenderness, what are the dominant effects for the wall deformation?* We answer these questions in chapter 3.

- As a specific example illustrating the dominant mechanisms discussed in chapter 3, slender and shallow rectangular microchannels with three walls surrounded by a thick elastic material are the common result of the soft lithography micromanufacturing technique [5]. However, a parameter-free theory accounting for the steady pressure and deformation characteristics (due to FSI) in this configuration was missing. Thus, a knowledge gap can be identified regarding this scenario: *How does a soft, three-dimensional thick wall respond to the imposed load from the hydrodynamic pressure due to flow underneath it, at steady state? What is the corresponding flow rate–pressure drop relationship? If a parameter-free flow rare–pressure drop relation can be derived from the basic equations, how does it compare to previously reported experimental mea-*

surements [12], [28] in microchannels with thick walls? We answer these questions in chapter 4.

- In previous studies [12], [31], [33], [101], the steady-state flow rate–pressure drop relation in the inertialess flow regime was derived, either by considering the full solution of the interface displacement at the leading order, or by introducing the width-averaged interface displacement as an "effective" displacement to simplify the expression for the pressure–deformation relation. Naturally, a knowledge gap thus exists, leaving unanswered the following questions: *How do the flow rate–pressure drop relations resulting from the "full solution" or the "effective" width-averaged relation compare with each other? If flow inertia is not negligible, then how does the flow rate relate to the pressure drop at steady state in the regime of the Reynolds number being low but nonzero?* We answer these questions in chapter 5 by deriving a reduced model for the FSI problem at steady state, capturing the various physical effects of interest.

- Although flow instabilities due to FSI have been observed experimentally in slender and shallow microchannels [41], no comprehensive global theory has been established to delineate the various physical effects present in such a multiphysics system. To understand the mechanisms that lead to the instability at low Reynolds number (such as flow inertia, wall inertia, wall elasticity, pressure gradients, wall tension, and so on), a knowledge gap must be filled pertaining to the unsteady dynamics of this microscale FSI problem. From the theoretical point of view, reduced modeling is a powerful tool that can be used to disentangle the various effects involved. Now, we would like to ask: *How can we extend the steady-state reduced model from chapter 5 to capture the flow's unsteadiness and the solid's inertia? How do the steady and dynamic responses of the resulting reduced model compare with experimental observations? What new perspectives based on global stability analysis can we provide, via our the proposed reduced model, for the observed instabilities?* We answer these questions in chapter 6.

- If the base state of a nonlinear system is perturbed by an infinitesimal disturbance, the long-term behavior of the perturbation can usually be determined by the linear stability analysis (*i.e.*, an eigenvalue, or "modal," analysis). The short-time evolution of disturbances, on the other hand, relates to the non-normality of the linearization about the base state. Since the linear evolution equations derived in chapter 6 are not normal, in part due to the novel non-flat base state introducing spatially-dependent coefficients into the evolution operator , we need to analyze the linear problem's non-normality to complement the eigenvalue analyses presented in chapter 6. Specifically, since the eigenspectrum of a non-normal problem can be sensitive to perturbations of the linearized operator, we must address the following open questions regarding our stability analysis: *how sensitive are the eigenvalues of the linearized system derived from the reduced model for unsteady microchannel FSIs? Will initially infinitesimal disturbances experience transient energy amplification, if so under what conditions? Do the system parameters affect the non-normality of the linearized operator and/or the transient energy growth of disturbances?* We answer these questions in chapter 7.

2. STEADY-STATE SCALINGS AND LINEAR STABILITY OF A MODEL OF TWO-DIMENSIONAL FLOW THROUGH A THIN-WALLED SOFT MICROCHANNEL

SUMMARY

We analyze the steady state and the linear stability of a one-dimensional (1D) fluid–structure interaction (FSI) model. The model targets microchannels with beam-like top walls. At steady state, an order-of-magnitude analysis (balancing argument) shows that the axially averaged pressure in the flow, $\langle P\rangle$, exhibits two different scaling regimes, while the maximum deformation of the top wall of the channel, $H_{\max}$, can fall into four different regimes. These regimes are physically explained as resulting from the competition between the inertial and viscous forces in the fluid flow as well as the bending resistance and tension in the elastic wall. All of the found scalings are validated by steady-state numerical simulations within a large range of parameters. To address the linear stability analysis with respect to the non-flat steady state, we conduct a modal analysis and the resulting generalized eigenvalue problem is solved by the Chebyshev pseudospectral method with modified Lagrange bases. Many highly oscillatory but stable modes are found, which highlights the computational challenge of simulating unsteady FSIs.

The material in this chapter was published as [T.C. Inamdar, X. Wang, I.C. Christov, "Unsteady fluid-structure interactions in a soft-walled microchannel: A one-dimensional lubrication model for finite Reynolds number," *Phys. Rev. Fluids*, vol. 5, art. 064101, 2020] [102] T.C.I. and I.C.C. derived the mathematical model and the formulation of the linear stability problem. T.C.I. wrote the Python scripts for the steady-state and the dynamic simulations of the model. Both T.C.I. and I.C.C. wrote the first draft of the manuscript. X.W. and I.C.C. updated the manuscript by rewriting the sections about the steady-state scaling analysis and the linear stability analysis. X.W. wrote the Python scripts and performed all the case studies in these two sections. Only this material is included in this chapter. X.W. and I.C.C. jointly discussed the results, drafted referee replies, and revised the manuscript for publication.

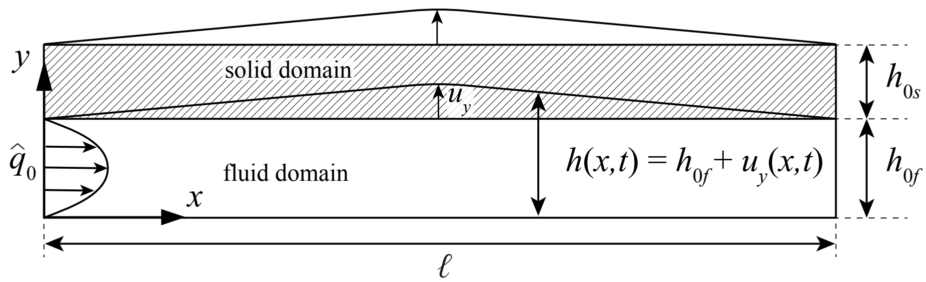

Figure 2.1. Schematic of the exemplar soft-walled microchannel geometry.

2.1 Problem statement and model equations

We start from a two-dimensional (2D) configuration in figure 2.1, which concerns 2D flows within a topologically rectangular fluid channel whose top wall is made from a soft, compliant solid. The length of the channel (in the flowwise direction) is ℓ, while h_{0f} and h_{0s} denote the undeformed heights (in the direction perpendicular to the flow) of the fluid channel and solid wall, respectively. The positive x-direction is taken as the flowwise direction, i.e., the fluid flows from left to right in figure 2.1. Meanwhile, the solid wall can deform in the perpendicular y-direction. The solid displacement is assumed to vary only with x, while the fluid flow is two-dimensional (2D) having both x and y velocity components each of which might depend on both x and y. The other key parameters for specifying system are listed in table 2.1. Note hats over quantities denote they are the 2D versions (e.g., per unit width) of the otherwise 3D quantities.

Next, we will introduce a 1D reduced model derived in [102]. Particularly, we will illustrate how enlightening the 1D FSI system can be by investigating its steady and unsteady responses.

Here we only provide a summary of the model while the detailed derivations are available in [102]. By assuming $\epsilon = h_{0f}/\ell \ll 1$, the lubrication approximation applies and suggests that the flow pressure, p, does not vary with y at the leading order in ϵ. Furthermore, it can be shown that the shear stresses, τ_{yx}, is negligible compared with p. Then, p is the only external load exerted on the top wall. The top wall is modeled as an Euler–Bounoulli beam with a nonlinear tension derived on the basis of von Kármán strains [103]. The nonlinear tension

Table 2.1. The definition of dimensional parameters used for specifying the system shown in figure 2.1.

Variable	Name	SI Unit
ℓ	channel's length	m
h_{0s}	solid's thickness	m
E	solid's Young's modulus	Pa
$\hat{\varrho}_s$	solid's mass per unit area	kg/m^2
ν	fluid's kinematic viscosity	m^2/s
ϱ_f	fluid's density	kg/m^3
$\hat{q}_0$	inlet area flow rate	m^2/s
h_{0f}	channel height	m

is non-uniform in x, which is a consequence of non-negligible rotations of the transverse normals due to the assumed large deformations. Next, assume the axial velocity, v_x, has a parabolic velocity profile by invoking the *von Kármán–Polhausen approximation* [104, p. 541], to introduce the flow rate, $\hat{q}$, into the formulation. The leading-order terms in 2D Navier–Stokes equations are then integrated along y with respect to the deformed fluid domain to get 1D equations. Finally, the dimensionless governing equations for the 1D model are written as

$$\frac{\partial Q}{\partial X} + St\frac{\partial H}{\partial T} = 0, \tag{2.1a}$$

$$ReSt\frac{\partial Q}{\partial T} + Re\frac{6}{5}\frac{\partial}{\partial X}\left(\frac{Q^2}{H}\right) = -H\frac{\partial P}{\partial X} - \frac{12Q}{H^2}, \tag{2.1b}$$

$$\frac{\partial^2 U_Y}{\partial T^2} + \frac{\partial^4 U_Y}{\partial X^4} - \alpha\left(\frac{\partial U_Y}{\partial X}\right)^2\frac{\partial^2 U_Y}{\partial X^2} = P, \tag{2.1c}$$

$$H = 1 + \beta U_Y. \tag{2.1d}$$

The independent variables in equation (2.1) are X and T while Q, H, U_Y, and P denote the dimensionless flow rate, deformed channel height, displacement of the top wall and flow pressure respectively.

The key dimensionless groups in equation (2.1) are defined as

$$\epsilon = \frac{h_{0f}}{\ell}, \quad \mathit{Re} = \frac{\epsilon \hat{q}_0}{\nu}, \quad St = \epsilon\sqrt{\frac{E\hat{I}}{\hat{\varrho}_s \hat{q}_0^2}}, \quad \Sigma = \frac{\epsilon^6 E\hat{I}}{\varrho_f \nu^2 h_{0f}}, \quad \alpha = 18\beta^2\left(\frac{h_{0f}}{h_{0s}}\right)^2, \quad \beta = \frac{\mathit{Re}}{\Sigma}. \tag{2.2}$$

We highlight Re, St and Σ here. First, $\mathit{Re} \equiv \epsilon \mathit{Re}^*$ quantifies the balance between inertial and viscous forces, which is introduced as the "reduced" Reynolds number, with the regular Reynolds number, $\mathit{Re}^* \equiv \hat{q}_0/\nu$ defined based on the inlet flow rate. Second, the Strouhal number (see, e.g., [104, p. 351]), St, is the ratio of a characteristic fluid time scale ($\tau_f \sim \ell h_{0f}/\hat{q}_0$) to a characteristic solid time scale ($\tau_s \sim \sqrt{\hat{\varrho}_s \ell^4/E\hat{I}}$). In the following discussions, we are interested in the regime where Re and St are $\mathcal{O}(1)$. Lastly, Σ is the reduced dimensionless bending rigidity $\Sigma \equiv \epsilon^6\Sigma^*$, where $\Sigma^* \equiv E\hat{I}/(\varrho_f \nu^2 h_{0f})$. Notably, β is not an independent variable but depends on the ratio of Re and Σ. Since Re and β represent the contributions to FSI from the fluid's and solid's side, respectively, β is thus termed FSI parameter, which is useful in gauging the "strength" of FSI in the system.

To fully specify the problem, we need initial and boundary conditions. The initial conditions are those of uniform flow under an undeformed wall:

$$Q|_{T=0} = 1, \qquad U_Y|_{T=0} = 0 \quad \Leftrightarrow \quad H|_{T=0} = 1. \tag{2.3}$$

The boundary conditions on the solid mechanics problem are those of clamping at $X = 0$ and $X = 1$, written as

$$U_Y|_{X=0} = \left.\frac{\partial U_Y}{\partial X}\right|_{X=0} = 0, \qquad U_Y|_{X=1} = \left.\frac{\partial U_Y}{\partial X}\right|_{X=1} = 0. \tag{2.4}$$

The boundary conditions on the fluid mechanics problem are the imposed inlet flow rate and the outlet pressure set to gauge:

$$Q|_{X=0} = 1, \qquad P|_{X=1} = 0. \tag{2.5}$$

2.2 Steady-state shape of the top wall of the inflated microchannel

In this section, we discuss the microchannel's steady-state characteristics. In the limit of $St \to 0$, equation (2.1a) simply states that Q is independent of X: $\partial Q/\partial X = 0$. The flow rate is, thus, simply given by the boundary condition imposed: $Q(X,T) \equiv 1\ \forall X \in [0,1]$, $T \geq 0$. Subsequently, equation (2.1c) can be reconstituted as a PDE for H using equation (2.1d). After taking an X derivative of the resulting PDE and dropping the remaining unsteady terms, we obtain a fifth-order PDE:

$$\frac{\partial^5 H}{\partial X^5} - \frac{\alpha}{\beta^2}\frac{\partial}{\partial X}\left[\left(\frac{\partial H}{\partial X}\right)^2 \frac{\partial^2 H}{\partial X^2}\right] = \beta\frac{\partial P}{\partial X}. \tag{2.6}$$

Observe that, due to pressure loading of the soft wall, $H \equiv 1$ is *not* a steady state, unless $\beta = 0$. This feature of the microchannel problems makes it distinct from the collapse vessel problems studied in the literature [86], [88], [105]. Next, equation (2.1b) can be used to solve for $\partial P/\partial X$, the expression for which can then be substituted into equation (2.6):

$$\frac{\partial^5 H}{\partial X^5} - 18\left(\frac{h_{0f}}{h_{0s}}\right)^2 \frac{\partial}{\partial X}\left[\left(\frac{\partial H}{\partial X}\right)^2 \frac{\partial^2 H}{\partial X^2}\right] = \frac{\mathit{Re}}{\Sigma}\left(\mathit{Re}\frac{6}{5}\frac{1}{H^3}\frac{\partial H}{\partial X} - \frac{12}{H^3}\right). \tag{2.7}$$

Here, we have made use of the relations $\alpha/\beta^2 \equiv 18(h_{0f}/h_{0s})^2$ and $\beta \equiv \mathit{Re}/\Sigma$ from equation (2.2), to make the parametric dependencies in equation (2.7) more explicit.

This final fifth-order nonlinear PDE (2.7) for H can be compared to Stewart et al. [86, equation (2.12a)], which was derived in the high-Re context. In the model in [86], stretching is the dominant solid mechanics response and bending is neglected by assuming small deformations. Thus, [86, equation (2.12a)] differs from equation (2.7) in two principal ways: (i) Re only modifies the fluid inertia term in equation (2.7), while it modifies *both* the fluid inertia and the nonlinear stretching terms in [86, equation (2.12a)]; (ii) the higher-order bending term on the left-hand side of equation (2.7) is not present in [86, equation (2.12a)] and, likewise, the nonlinear stretching term on the left-hand side of equation (2.7) is to be contrasted with the linearized tension term in [86, equation (2.12a)]. Consequently, we expect that the steady states governed by equation (2.7), and their linear stability, to differ significantly from those studied in the literature, paving the way to potentially rich new dynamic behaviors in the present viscous FSI model.

To compute the steady state channel shape, denoted $H_0(X)$, we re-interpret equation (2.7) as a two-point boundary-value problem, which can be solved numerically using SciPy's `solve_bvp` [106]. Specifically, equation (2.7) is subject to

$$H_0(X=0) = 1, \quad \left.\frac{\partial H_0}{\partial X}\right|_{X=0} = 0, \quad H_0(X=1) = 1, \quad \left.\frac{\partial H_0}{\partial X}\right|_{X=1} = 0, \quad \left.\frac{\partial^4 H_0}{\partial X^4}\right|_{X=1} = 0, \tag{2.8}$$

where the first four boundary conditions are simply the clamped conditions [see equation (2.4)], while the last one is the outlet pressure condition [see equation (2.5)] rewritten in terms of the steady-state channel height via equation (2.1c).

2.2.1 Example plots of steady-state shapes

Next, we show example plots of the steady-state shape, $H_0(X)$, and the corresponding pressure distribution, $P_0(X)$, along the microchannel. For these examples, we take $\Sigma = 9 \times 10^{-4}$, fix the height ratio at $h_{0f}/h_{0s} = 1$, and vary Re. Both $\alpha \neq 0$ and $\alpha = 0$ are considered. The solid curves represent the results with nonlinear tension included, while the dashed curves represent results without tension ($\alpha = 0$, i.e., pure bending).

First, in figure 2.2, we consider $Re = 0.5$. The remaining dimensionless parameters are $\beta = 5.56 \times 10^2$ and $\alpha = 5.56 \times 10^6$ for the case with tension. Whether tension is included or not, P_0 is a nonlinear function of X due to FSI, as can be seen in panel (b). However, note that for $\alpha \neq 0$, the microchannel displays much smaller deformation for a larger pressure drop, $P_0(0) - P_0(1)$. The reason for this observation is that tension in the beam restricts the deflection of the top wall, resulting in larger flow velocity at fixed flow rate ($Q = 1$) and, thus, causes larger pressure losses due to viscosity. Furthermore, P_0 is a decreasing function of X, because the inertial effects of the flow are negligible in this case (Re is small), thus viscous effects dominate and $\mathrm{d}P_0/\mathrm{d}X \sim -12/H_0(X)^3 < 0$, consistent with lubrication theory.

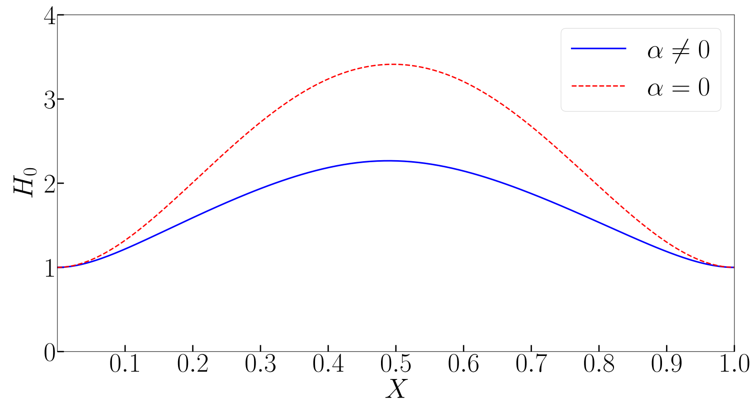

(a)

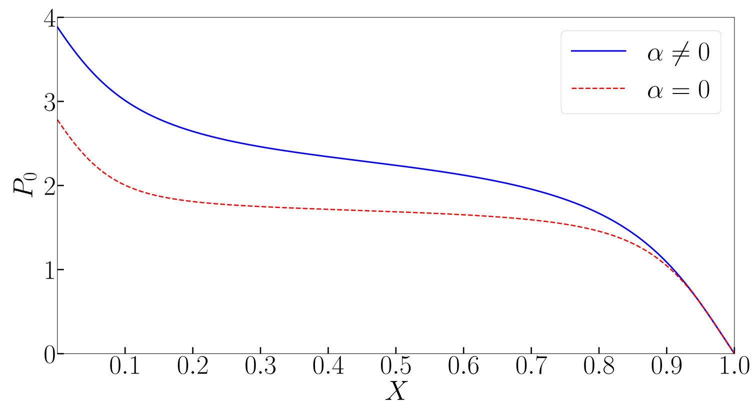

(b)

Figure 2.2. Typical steady-state shapes and pressure distributions inside the soft-walled microchannel. (a) Steady-state deflection, H_0, as a function of the flowwise position X. (b) Steady-state pressure distribution, P_0, as a function of the flowwise position X.

Next, we show a more "exotic" case at higher Re. The parameters for the case with tension are chosen as $\alpha = 2.22 \times 10^9$, $Re = 10$ and $\Sigma = 9 \times 10^{-4}$ while $Re = 1.8$ and $\Sigma = 9 \times 10^{-4}$ are set for the case without tension ($\alpha = 0$).

With the increase of Re, it is expected that inertial effects in the flow become prominent. While the top wall of the microchannel will still bulge under the pressure load from the flow, the pressure gradient does not have to remain negative, and P_0 will not necessarily be a decreasing function of X, as shown in figure 2.3(b) in contrast to figure 2.2(b). This observation can be justified by recognizing that $\mathrm{d}P_0/\mathrm{d}X$ is the consequence of the competition between the convective effects and viscous effects in the flow [see the right-hand side of equation (2.7)]. Since the top wall is clamped at both ends, its bulging leads to its slope, $\mathrm{d}H_0/\mathrm{d}X$, increasing near the inlet ($X = 0$) and decreasing near the outlet ($X = 1$). If inertia is dominant in the flow, a positive pressure gradient can be expected, for $R\mathrm{e}$ large enough. As shown in figure 2.3, this positive pressure gradient is observed upstream. Note that we have chosen a smaller $R\mathrm{e}$ value for the pure bending case (compared to the case with tension), in order to ensure that the deformation is within a reasonable range. Since $R\mathrm{e}$ is much larger in the case of $\alpha \neq 0$, it is not surprising that the positive pressure gradient is much more prominent. Interestingly, the pressure profiles are almost flat in the middle part of the channel, with or without tension, indicating a negligible pressure gradient in this region. Also observe that the deformations in both cases are large. Since the flow rate is fixed, the fluid's velocity has to decrease rapidly along the flowwise direction in the expanding section of the deformed microchannel, and the positive pressure gradient will help decelerate the flow.

2.3 Deformation and pressure scaling at steady state

In this subsection, we address the different scaling regimes of deformation and hydrodynamics with respect to key dimensionless groups of the problem. To frame the discussion, we define the maximum deformation $H_{\max} = \max_{0\le X\le 1} H_0(X)$ and the axially-average pressure $\langle P\rangle = \int_0^1 P_0(X)\,\mathrm{d}X$. We seek to establish how each of these scalar quantities scales with $R\mathrm{e}$ and Σ, as we encounter different regimes of physics: e.g., bending- or tension-dominated deformation, inertia- or viscosity-dominated pressure profile, and so on.

2.3.1 Scaling of $\langle P\rangle$

Before we start our analysis, it is worth mentioning the reason for choosing $\langle P\rangle$ as the quantity of interest instead of, say, the total pressure drop $P_0(0) - P_0(1)$, which is more commonly discussed in microchannel studies. First, $\langle P\rangle$ better captures the pressure variation, compared to $P_0(0)$, especially when the inertial forces in the flow are dominant, and a positive pressure gradient is observed upstream. In this case, the pressure in the

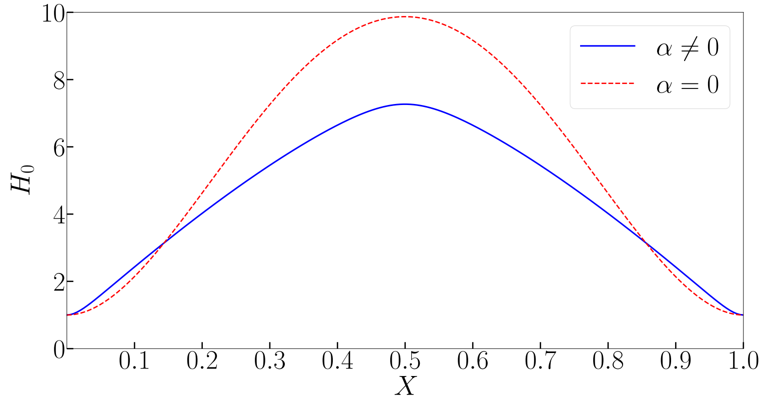

(a)

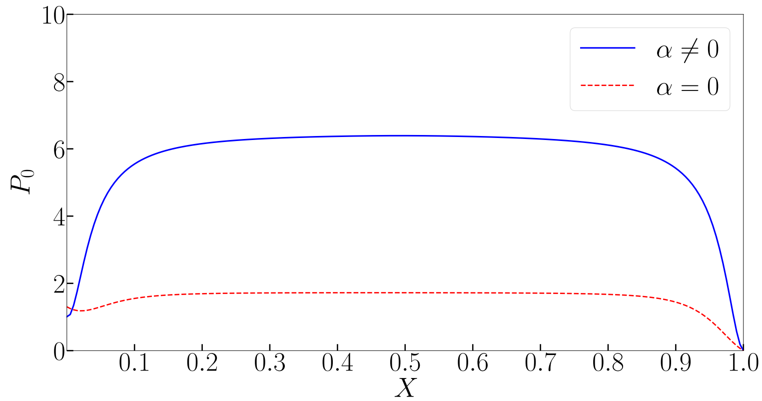

(b)

Figure 2.3. More "exotic" steady-state shapes, (a) $H_0(X)$, and pressure distributions, (b) $P_0(X)$, inside the soft-walled microchannel.

middle part of the channel is larger than the total pressure drop (see figure 2.3) and using $P_0(0)$ to infer the characteristic load on the structure will underestimate the deformation. Second, using $P_0(0)$ renders the inertial flow effects difficult to analyze. It is easy to show that $P_0(0) = \int_0^1 12/H_0(X)^3 \,\mathrm{d}X$ by integrating the right-hand side of equation (2.7) and applying the clamped boundary conditions. This expression does not necessarily mean that the inertia of the fluid is not important, rather it "hides" this effect in the shape of the channel, $H_0(X)$, which further serves to complicate the scaling analysis.

From section 2.2, we already know that the pressure gradient in the flow, $\mathrm{d}P_0/\mathrm{d}X$, is the outcome of the competition between the inertial and viscous forces in the flow. Then, it is natural to investigate the two limits, i.e., the viscosity-dominated and inertia-dominated regimes, respectively, and explore how $\langle P \rangle$ scales in each regimes.

Case 1: Viscous effects are dominant in the flow. In this case, $\mathrm{d}P_0/\mathrm{d}X \sim -12/H_0(X)^3 < 0$ and $P_0(X)$ is a decreasing function of X with a relatively flat middle part, as in figure 2.2(b). Observing that the deformation profile is almost symmetric in figure 2.2(a), we assume that the pressure in this flat region is a good estimate of $\langle P \rangle$.

To proceed, define a critical value of the deformed channel height as H_c such that $H_c = H_{\max}$ for small deformation and $H_c < H_{\max}$ with $1/H_c^3 \ll 1$ for large deformation. We want to find the flowwise position, X_c, at which $H_0(X_c) = H_c$ and also, $P_0(X_c) \sim \langle P \rangle$, per our assumption. Then, with a linear approximation of the deformation profile, we have $H_c/H_{\max} \sim 2(1 - X_c)$. Here, we have made use of the (almost) symmetry of the deformation profile. The deformation profile near the outlet is written as a linear function, $H_0(X) \approx -(H_c - 1)(X - 1)/(1 - X_c) + 1$, then

$$\begin{aligned}\langle P \rangle \sim P_0(X_c) \sim -\int_{X_c}^{1} \frac{\partial P_0}{\partial X}\,\mathrm{d}X \sim \int_{X_c}^{1} &\frac{12}{[-(H_c-1)(X-1)/(1-X_c)+1]^3}\,\mathrm{d}X \\ =&\frac{6(1-X_c)(1+H_c)}{H_c^2} \sim \frac{1}{H_{\max}}.\end{aligned} \tag{2.9}$$

Note that the actual value of H_c is not important in the scaling analysis.

Case 2: Convective (inertial) effects are dominant in the flow. In this case, as shown in figure 2.3, the deformation of the microchannel is usually large and, thus the profile $P_0(X)$ displays a flatter middle part. Again, assume that the pressure in this portion of the microchannel is still a good estimate of $\langle P \rangle$. Following a similar procedure to Case 1 above, but choosing H_c as $1/H_c^2 \ll 1$, further balancing the convective term and the pressure gradient in equation (2.1b), we can estimate

$$\langle P \rangle \sim -\int_{X_c}^{1} \frac{\partial P_0}{\partial X}\,\mathrm{d}X \sim \int_{X_c}^{1} \frac{3}{5} Re \frac{\partial}{\partial X}\left(\frac{1}{H_0^2}\right)\mathrm{d}X = \frac{3}{5}\mathrm{Re}\left(1 - \frac{1}{H_c^2}\right) \sim Re. \tag{2.10}$$

2.3.2 Scaling of H_{max}: Pure bending

Now, we are ready to analyze the solid mechanics problem to obtain the scaling of H_{max}. First, we consider pure bending ($\alpha = 0$). In this case, the governing equation of the solid mechanics is the classic Euler–Bernoulli beam equation, $\mathrm{d}^4 H_0/\mathrm{d}X^4 = \beta P_0 = Re P_0/\Sigma$, which implies that $H_{\text{max}} \sim Re\langle P\rangle/\Sigma$.

If viscous effects are dominant in the flow, using equation (2.9), we obtain the scalings

$$H_{\text{max}} \sim (Re/\Sigma)^{1/2}, \qquad \langle P\rangle \sim (Re/\Sigma)^{-1/2}. \tag{2.11}$$

However if the deformation is very small, i.e., $H_{\text{max}} \approx 1$, $P_0(X)$ is nearly linear with an almost constant gradient given by the lubrication approximation, $\mathrm{d}P_0/\mathrm{d}X \sim 1/H_{\text{max}}^3$. Then, a more appropriate scaling is obtained by considering $\mathrm{d}^5 H_0/\mathrm{d}X^5 = (Re/\Sigma)\mathrm{d}P_0/\mathrm{d}X$, indicating that $H_{\text{max}} \sim (Re/\Sigma)/H_{\text{max}}^3$ and thus yielding

$$H_{\text{max}} \sim (Re/\Sigma)^{1/4} \qquad \langle P\rangle \sim (Re/\Sigma)^{-1/4}. \tag{2.12}$$

Note that in this case, equation (2.9) is still valid. On the other hand, if the inertial effects are dominant in the flow, since $\langle P\rangle \sim Re$, we have

$$H_{\text{max}} \sim Re^2/\Sigma. \tag{2.13}$$

2.3.3 Scaling of H_{max}: Bending and tension

Now, we consider the beam equation (2.6) with bending and tension ($\alpha \neq 0$), which are expressed by the first and second term, respectively, and scale as H_{max} and $\alpha H_{\text{max}}^3/\beta^2$ (recall that $H_{\text{max}} \geq 1$), with $\alpha/\beta^2 = 18(h_{0f}/h_{0s})^2$. Varying the height ratio, h_{0f}/h_{0s}, will change the tension effects in the beam but it will not affect the classification of different regimes. Specifically, if $h_{0f}^2/h_{0s}^2 \ll 1$, then the tension is negligible and the previous discussions for the pure bending case will apply. In the following analysis, we are interested in the tension-dominated regime and thus we fix $h_{0f}/h_{0s} = 1$, yielding $\alpha/\beta^2 = 18$, which ensures that tension is the dominant effect in the elastic response of the top wall.

In the case of the viscosity-dominated flow regime, $H_{\max}^3 \sim Re\langle P\rangle/\Sigma \sim ReH_{\max}^{-1}/\Sigma$ leads to

$$H_{\max} \sim (Re/\Sigma)^{1/4}, \qquad \langle P\rangle \sim (Re/\Sigma)^{-1/4}, \tag{2.14}$$

according to equation (2.9). However, as discussed in section 2.3.2, if the deformation is small, it is more appropriate to consider $H_{\max}^3 \sim (Re/\Sigma)\mathrm{d}P/\mathrm{d}X \sim (Re/\Sigma)/H_{\max}^3$, indicating

$$H_{\max} \sim (Re/\Sigma)^{1/6}, \qquad \langle P\rangle \sim (Re/\Sigma)^{-1/6}. \tag{2.15}$$

On the other hand, for the regime with an inertia–tension force balance, $\langle P\rangle \sim Re$, as shown by equation (2.10), then $H_{\max}^3 \sim Re\langle P\rangle/\Sigma \sim Re^2/\Sigma$, yielding

$$H_{\max} \sim Re^{2/3}/\Sigma^{1/3}. \tag{2.16}$$

2.3.4 Validation and discussion

In this subsection, we validate the scalings discussed above by numerically calculating the steady state with variable combinations of parameters. In order for the beam theory to apply, we have strictly restricted the maximum deformation of the top wall to be no greater than 10% of the length of the channel, corresponding to $H_{\max} \leq 10$ with the aspect ratio $\epsilon = 0.01$. This restriction applies to all of the following discussion.

In figure 2.4 and figure 2.5, we show the results of pure bending cases ($\alpha = 0$). In the viscosity-dominated regime, as shown by figure 2.4, the scalings (2.11) and (2.12) are clearly observed. However, we also observe outliers for the last two cases with $\Sigma = 1.0 \times 10^{-3}$ and $\Sigma = 1.0 \times 10^{-2}$ at large β because, in these cases, Re can be large (even under the restrictions on the maximum deformation) so that the response of the system deviates from the viscosity–bending force balance/regime. Specifically, the outliers in the case of the most rigid microchannel actually belong to an inertia–bending force balance/regime, which is corresponding to figure 2.5. In figure 2.5, the scaling (2.13) for the inertia-dominated regime is observed. However, for the parameters chosen, which cover six orders of Σ (and thus we believe should cover a significant number of actual microchannel systems), only the last set

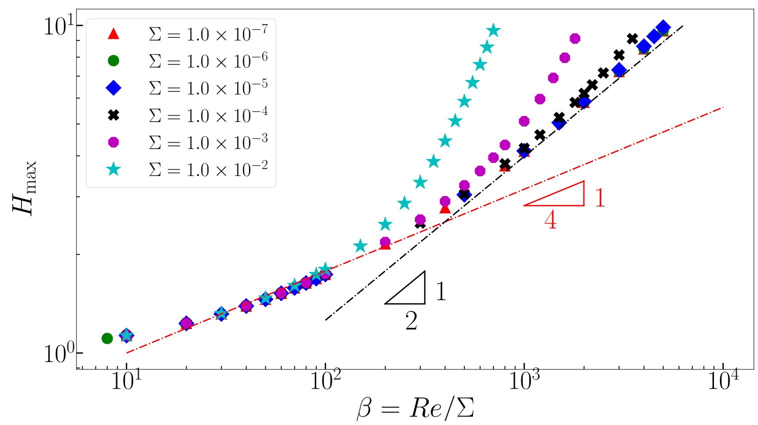

(a)

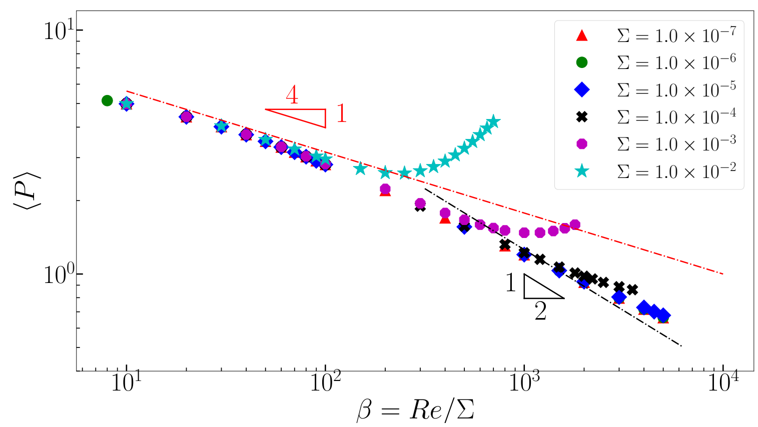

(b)

Figure 2.4. Scaling of (a) $H_{\max}$ and (b) $\langle P \rangle$ for the case of viscous–bending force balance. All regimes can be described in terms of the FSI parameter $\beta = Re/\Sigma$ in this case. The dash-dotted lines represent different slopes as shown.

of data with $\Sigma = 1.0 \times 10^{-2}$ reaches this regime, Meanwhile, the cases of $\Sigma = 1.0 \times 10^{-3}$ are more likely to be in the transitional stage at relatively high Re, as shown in figure 2.5.

The results of tension-dominated regime are shown in figure 2.6 and figure 2.5. In the viscosity-dominated flow regime, the two predicted scalings (2.14) and (2.15) are clearly observed in figure 2.6. Outliers exist in the cases with relatively large Re, for which the viscous effects are no longer dominant. On the other hand, the results for the regime with an inertia–tension force balance are shown in figure 2.7. Thanks to the tension effects

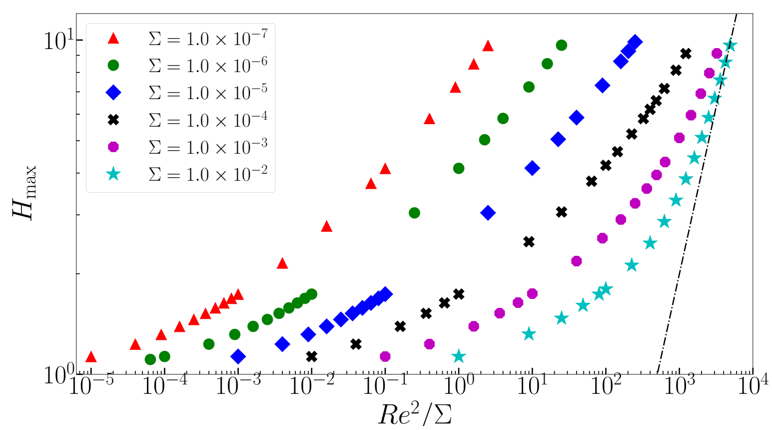

(a)

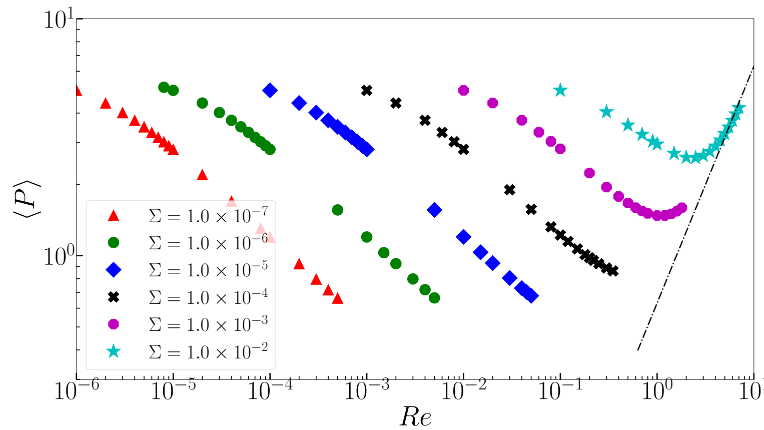

(b)

Figure 2.5. Scaling of (a) $H_{\max}$ and (b) $\langle P \rangle$ for the case of inertia–bending force balance. The dash-dotted lines represent a slope of 1.

suppressing the inflation of the microchannel, we are able to consider a larger range of Re than the bending-dominated cases so that more cases are observed to reach this regime. As shown in figure 2.7, the last three data sets all collapse along the line of slope 1, as predicted by the proposed $H_{\max}$ and $\langle P \rangle$ scalings.

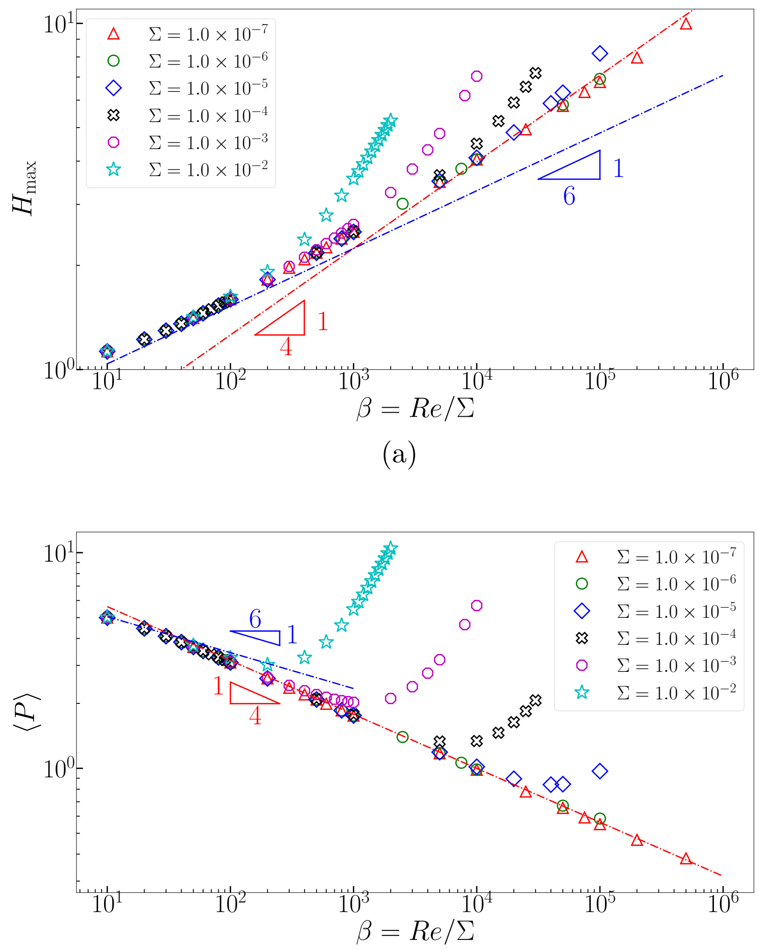

Figure 2.6. Scaling of (a) $H_{\max}$ and (b) $\langle P\rangle$ for the case of viscous–tension force balance. All regimes can be described in terms of the FSI parameter $\beta = Re/\Sigma$ in this case. The dash-dotted lines represent different slopes as shown.

2.4 Linear stability of the deformed microchannel

2.4.1 Perturbation about the non-flat steady shape

As noted in section 2.2, the flat state $Q, H = const.$, analyzed in a number of prior works on FSI, is *not* relevant to the microchannel problem under consideration because it is not a solution of the steady problem. Indeed, it is easy to show that equation (2.7) has *no* finite constant solutions that also satisfy the boundary conditions in equation (2.8). Thus, we

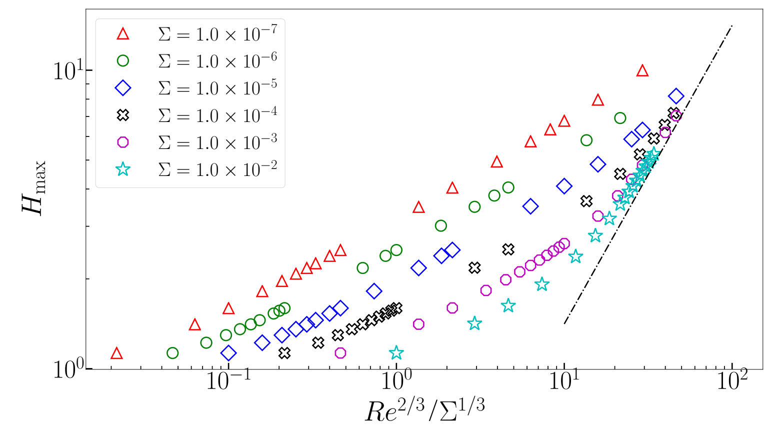

(a)

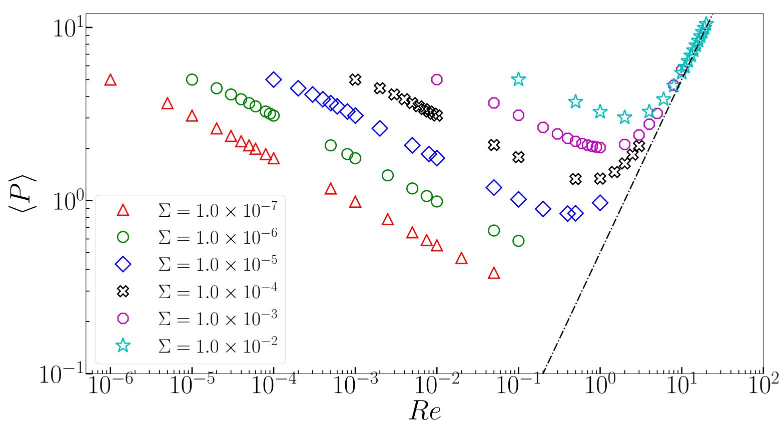

(b)

Figure 2.7. Scaling of (a) $H_{\max}$ and (b) $\langle P \rangle$ for the case of inertia–tension force balance. The dash-dotted lines in each panel indicate a slope of 1.

are interested in the stability of the *deformed* steady state in the presence of bending and tension of the top wall. To understand the stability of this non-flat steady state, we perturb about $Q = 1$ and $H = H_0(X)$ [i.e., the solution of equations (2.7) and (2.8)] as follows:

$$Q(X,T) = 1 + \delta Q_1(X)\mathrm{e}^{-\mathrm{i}\sigma T}, \tag{2.17a}$$

$$H(X,T) = H_0(X) + \delta H_1(X)\mathrm{e}^{-\mathrm{i}\sigma T}, \tag{2.17b}$$

where $\delta \ll 1$ is the (arbitrary, dimensionless) amplitude of a small perturbation and $\sigma \in \mathbb{C}$ denotes the growth/decay rate of the perturbations. The boundary conditions at both ends are already satisfied by the steady-state solution $(Q_0 = 1, H_0)^\top$, thus the perturbation $(Q_1, H_1)^\top$ must satisfy *homogeneous* boundary conditions. Specifically, the perturbation should satisfy the boundary conditions from equation (2.5), as well as the clamped boundary conditions from equation (2.4). In other words,

$$Q_1|_{X=0} = 0, \qquad \left.\frac{\mathrm{d}Q_1}{\mathrm{d}X}\right|_{X=0} = \left.\frac{\mathrm{d}Q_1}{\mathrm{d}X}\right|_{X=1} = 0, \tag{2.18a}$$

$$H_1|_{X=0} = \left.\frac{\mathrm{d}H_1}{\mathrm{d}X}\right|_{X=0} = \left.\frac{\mathrm{d}H_1}{\mathrm{d}X}\right|_{X=1} = H_1|_{X=1} = 0, \qquad \left.\frac{\mathrm{d}^4 H_1}{\mathrm{d}X^4}\right|_{X=1} = 0. \tag{2.18b}$$

Note the second relation in equation (2.18a) is the natural consequence of equation (2.1a), taking into account that the deformation is restricted at both ends of the microchannel by clamping. Meanwhile the last relation in equation (2.18b) is the boundary condition that enforces a gauge outlet pressure.

To determine the growth/decay of the perturbation, we must derive a set of linear evolution equations for Q_1 and H_1. To this end, we substitute equations (2.17) into the governing set of equations (2.1), using the fact that $H_0(X)$ satisfies equation (2.7) and dropping all terms of $\mathcal{O}(\delta^2)$ or higher. The result is two linear evolution equations in which the coefficients depend on the steady-state solution $H_0(X)$ and its derivatives:

$$\begin{aligned}
&\frac{\mathrm{d}^5 H_1}{\mathrm{d}X^5} - \frac{\alpha}{\beta^2}\frac{\mathrm{d}}{\mathrm{d}X}\left[\left(\frac{\mathrm{d}H_0}{\mathrm{d}X}\right)^2\frac{\mathrm{d}^2 H_1}{\mathrm{d}X^2} + 2\frac{\mathrm{d}^2 H_0}{\mathrm{d}X^2}\frac{\mathrm{d}H_0}{\mathrm{d}X}\frac{\mathrm{d}H_1}{\mathrm{d}X}\right] = \frac{\sigma}{\mathrm{i}St}\frac{\mathrm{d}^2 Q_1}{\mathrm{d}X^2} - \beta\Bigg\{-\frac{\mathrm{i}ReSt}{H_0}\sigma Q_1 \\
&+ Re\frac{6}{5}\left[\frac{3H_1}{H_0^4}\frac{\mathrm{d}H_0}{\mathrm{d}X} - \frac{1}{H_0^3}\frac{\mathrm{d}H_1}{\mathrm{d}X} - \frac{2Q_1}{H_0^3}\frac{\mathrm{d}H_0}{\mathrm{d}X} + \frac{2}{H_0^2}\frac{\mathrm{d}Q_1}{\mathrm{d}X}\right] + 12\left(-\frac{3H_1}{H_0^4} + \frac{Q_1}{H_0^3}\right)\Bigg\},
\end{aligned} \tag{2.19a}$$

$$\frac{\mathrm{d}Q_1}{\mathrm{d}X} - \mathrm{i}St\sigma H_1 = 0. \tag{2.19b}$$

Equations (2.19) can be written in the matrix form

$$\underbrace{\begin{pmatrix} \dfrac{\mathrm{d}}{\mathrm{d}X} & 0 \\ \mathcal{L}_Q & \mathcal{L}_H \end{pmatrix}}_{=\boldsymbol{A}} \underbrace{\begin{pmatrix} Q_1 \\ H_1 \end{pmatrix}}_{=\boldsymbol{\psi}} = \sigma \underbrace{\begin{pmatrix} 0 & \mathrm{i}St \\ \dfrac{1}{\mathrm{i}St}\dfrac{\mathrm{d}^2}{\mathrm{d}X^2} + \dfrac{\mathrm{i}\beta ReSt}{H_0} & 0 \end{pmatrix}}_{=\boldsymbol{B}} \begin{pmatrix} Q_1 \\ H_1 \end{pmatrix}, \tag{2.20}$$

where we have defined the operators

$$\mathcal{L}_H = \frac{\mathrm{d}^5}{\mathrm{d}X^5} - \frac{\alpha}{\beta^2}\left\{4\frac{\mathrm{d}H_0}{\mathrm{d}X}\frac{\mathrm{d}^2H_0}{\mathrm{d}X^2}\frac{\mathrm{d}^2}{\mathrm{d}X^2} + \left[2\left(\frac{\mathrm{d}^2H_0}{\mathrm{d}X^2}\right)^2 + 2\frac{\mathrm{d}H_0}{\mathrm{d}X}\frac{\mathrm{d}^3H_0}{\mathrm{d}X^3}\right]\frac{\mathrm{d}}{\mathrm{d}X} + \left(\frac{\mathrm{d}H_0}{\mathrm{d}X}\right)^2\frac{\mathrm{d}^3}{\mathrm{d}X^3}\right\}$$
$$- \frac{6\beta Re}{5H_0^3}\frac{\mathrm{d}}{\mathrm{d}X} - \beta\left(\frac{36}{H_0^4} - \frac{18Re}{5H_0^4}\frac{\mathrm{d}H_0}{\mathrm{d}X}\right), \tag{2.21a}$$

$$\mathcal{L}_Q = -\beta\left(-\frac{12}{H_0^3} + \frac{12Re}{5H_0^3}\frac{\mathrm{d}H_0}{\mathrm{d}X} - \frac{12Re}{5H_0^2}\frac{\mathrm{d}}{\mathrm{d}X}\right). \tag{2.21b}$$

Equation (2.20) and the boundary conditions in equations (2.18) constitute a generalized eigenvalue problem $\boldsymbol{A}\boldsymbol{\psi} = \sigma\boldsymbol{B}\boldsymbol{\psi}$, with σ as the eigenvalue and $\boldsymbol{\psi} = (Q_1, H_1)^\top$ as the eigenfunction. Note the system in equation (2.20) has non-constant coefficients due to the non-flat steady-state shape $H_0(X)$ of the microchannel. We say the system is linearly unstable if $\mathrm{Im}(\sigma) > 0$, and we proceed to investigate whether this condition holds (or does not hold).

2.4.2 Chebyshev pseudospectral method for the generalized eigenvalue problem

We use the Chebyshev pseudospectral method [107], [108] to compute the spectrum (eigenvalues and eigenfunctions) of the system defined by equation (2.20) and the boundary conditions in equations (2.18). The numerical method was implemented in Python using routines from SciPy [106]. Since the Chebyshev pseudospectral method is derived for the domain $[-1,+1]$, we use the change of variables $\widetilde{X} \equiv 2X - 1$ to transform the computational domain from $\{X|X \in [0,1]\}$ to $\{\widetilde{X}|\widetilde{X} \in [-1,1]\}$. Then, $\mathrm{d}^m/\mathrm{d}X^m = 2^m\mathrm{d}^m/\mathrm{d}\widetilde{X}^m$ and we denote $\widetilde{Q}(\widetilde{X}) = Q_1(X)$ and $\widetilde{H}(\widetilde{X}) = H_1(X)$, dropping the "1" subscript for simplicity. Note that the non-constant coefficients in equation (2.20), which involve the steady-state shape of the microchannel $H_0(X)$ and its derivatives, have been precomputed using SciPy's `solve_bvp` and are known at this stage.

We introduce the Gauss–Lobatto points:

$$\widetilde{X}_j = -\cos\left(\frac{j\pi}{N}\right), \qquad j = 0, 1, \ldots, N. \tag{2.22}$$

Generally speaking, the aim of the Chebyshev pseudospectral method is to find a high-order polynomial, valid on the whole domain, to approximate the exact solution of the problem. In order to determine the coefficients of the polynomial, it is required that the differential equations be satisfied at the interior points, i.e., at $\widetilde{X} = \widetilde{X}_j$ with $j = 1, \ldots, N-1$, while the boundary conditions are imposed at $\widetilde{X} = \widetilde{X}_0 \equiv -1$ and $\widetilde{X} = \widetilde{X}_N \equiv +1$. For our problem, recall that there are three boundary conditions for $\widetilde{Q}$ and five boundary conditions for $\widetilde{H}$ [see equations (2.18)]. Therefore, we need to (and, indeed, can) uniquely determine a polynomial of order $N+1$ for $\widetilde{Q}$ and a polynomial of order $N+3$ for $\widetilde{H}$.

To this end, we follow Huang and Sloan [109], but we use different modified bases to construct polynomials for the eigenfunctions $\widetilde{Q}$ and $\widetilde{H}$. Actually, the modified bases in [109] [see equation (3.3) therein] do not apply to our problem because, here, the boundary conditions in equations (2.18) involve higher derivatives at $\widetilde{X}_N = +1$ and do not meet the requirements for boundary conditions in [109, equation (3.1)]. Instead, we construct the polynomials for eigenfunctions as follows:

$$\widetilde{Q}(\widetilde{X}) \approx (1+\widetilde{X}) \sum_{j=1}^{N} \frac{Q_j}{1+\widetilde{X}_j} l_j(\widetilde{X}), \tag{2.23a}$$

$$\widetilde{H}(\widetilde{X}) \approx (1+\widetilde{X})(1-\widetilde{X}) \sum_{j=1}^{N-1} \frac{H_j}{(1+\widetilde{X}_j)(1-\widetilde{X}_j)} l_j(\widetilde{X}) + (1+\widetilde{X})(1-\widetilde{X})^2 H_N l_N(\widetilde{X}), \tag{2.23b}$$

where Q_j and H_j are the function values at the collocation points. Here, $l_k(\widetilde{X})$ denotes the k-th basis Lagrange interpolating polynomial, defined as

$$l_k(\widetilde{X}) = \prod_{i=0, i\neq k}^{N} \frac{\widetilde{X} - \widetilde{X}_i}{\widetilde{X}_k - \widetilde{X}_i}, \qquad l_k(\widetilde{X}_j) = \delta_{kj}, \tag{2.24}$$

where δ_{kj} is the Kronecker delta symbol. With this property of the Lagrange interpolating polynomial, it follows that $\widetilde{Q}(\widetilde{X}_j) = Q_j$ $j = 1, 2, \ldots, N$, while $\widetilde{H}(\widetilde{X}_j) = H_j$ for $j = 1, 2, \ldots, N-1$. Note $H_N \neq H(\widetilde{X}_N)$. In fact, we already know from equation (2.18b) that $H(\widetilde{X}_N) = 0$ because of the clamped boundary condition. However, H_N is still needed, simply functioned as a coefficient, to satisfy the very last condition in equation (2.18b). More importantly, it is easily verified that equations (2.23) satisfy all the boundary conditions for

$\widetilde{Q}$ and $\widetilde{H}$ except $\mathrm{d}\widetilde{Q}/\mathrm{d}\widetilde{X} = 0$ and $\mathrm{d}^4\widetilde{H}/\mathrm{d}\widetilde{X}^4 = 0$. These two boundary conditions need to be imposed explicitly as extra two rows in the discretized matrix corresponding to the system in equation (2.20).

Next, we substitute equations (2.23) into equation (2.20) and discretize by requiring that equation (2.20) be satisfied at the interior collocation points, i.e., $\widetilde{X} = \widetilde{X}_j$ with $j = 1, 2, \ldots, N-1$. At the same time, we impose the two unsatisfied boundary conditions at $\widetilde{X}_N = +1$ and add them into the discretized system: $\widehat{\boldsymbol{A}}\widehat{\boldsymbol{\psi}} = \sigma\widehat{\boldsymbol{B}}\widehat{\boldsymbol{\psi}}$, where $\widehat{\boldsymbol{\psi}} = [Q_1, \ldots, Q_N, H_1, \ldots, H_N]^\top$. Both $\widehat{\boldsymbol{A}}$ and $\widehat{\boldsymbol{B}}$ are $2N \times 2N$ block matrices. Specifically, the matrix $\widehat{\boldsymbol{B}}$ is singular because the two homogeneous boundary conditions, imposed as its N-th and $2N$-th rows, respectively. These BCs do not involve the eigenvalue σ, which makes these two rows of $\widehat{\boldsymbol{B}}$ each equal to the zero vector.

One of the most important details that must be taken care of to obtain the discretized eigenvalue problem is dealing with the differentiation of equations (2.23) at the collocation points. Fortunately, derivatives of the Lagrange interpolating polynomials at the Gauss–Lobatto points have explicit representations [110]. Let $\boldsymbol{D}$ denote the first-order differentiation matrix of the Lagrange interpolating polynomial basis at the Gauss–Lobatto points, then

$$D_{kj} = \frac{\mathrm{d}l_j}{\mathrm{d}\widetilde{X}}\bigg|_{\widetilde{X}=\widetilde{X}_k} = \begin{cases} -\dfrac{2N^2+1}{6}, & k = j = 0, \\[2mm] \dfrac{\widetilde{c}_k}{\widetilde{c}_j}\dfrac{(-1)^{k+j}}{\widetilde{X}_k - \widetilde{X}_j}, & k \neq j, \ \ 0 \leq k, j \leq N, \\[2mm] -\dfrac{\widetilde{X}_k}{2(1-\widetilde{X}_k^2)}, & k = j, \ \ 1 \leq k, j \leq N-1, \\[2mm] \dfrac{2N^2+1}{6}, & k = j = N, \end{cases} \tag{2.25}$$

where $\widetilde{c}_0 = \widetilde{c}_N = 2$ and $\widetilde{c}_j = 1$ for $1 \leq j \leq N-1$. Furthermore, if we denote the m-th order differentiation matrix for the Lagrange interpolating polynomial basis as $\boldsymbol{D}^m$, the higher-order differentiation matrices can be obtained through matrix multiplication of the lower-order ones. For example, $\boldsymbol{D}^2 = \boldsymbol{D} \times \boldsymbol{D}$ and $\boldsymbol{D}^3 = \boldsymbol{D} \times \boldsymbol{D}^2 = \boldsymbol{D} \times \boldsymbol{D} \times \boldsymbol{D}$. However, what we really need is the differentiation matrix with respect to the modified polynomials in equations (2.23a) and (2.23b). Similarly, we denote the first-order differentiation matrix with respect to $\widetilde{Q}$ and $\widetilde{H}$ as $\widetilde{\boldsymbol{D}}_Q$ and $\widetilde{\boldsymbol{D}}_H$, respectively, and the m-th higher order differentiation matrices as $\widetilde{\boldsymbol{D}}_Q^m$ and $\widetilde{\boldsymbol{D}}_H^m$. Clearly, $\widetilde{\boldsymbol{D}}_Q$, $\widetilde{\boldsymbol{D}}_Q$, $\widetilde{\boldsymbol{D}}_Q^m$, and $\widetilde{\boldsymbol{D}}_H^m$ should be modified from equation (2.25). The complete expressions are quite lengthy, thus we do not include them here. Instead, we just write down $\widetilde{\boldsymbol{D}}_Q$ as an example:

$$\widetilde{\boldsymbol{D}}_Q = \Big[\boldsymbol{I} + \operatorname{diag}\Big((1+\widetilde{X}_k), 1 \le k \le N\Big) \times \boldsymbol{D}\Big] \times \operatorname{diag}\Big(1/(1+\widetilde{X}_k), 1 \le k \le N\Big), \tag{2.26}$$

where $\boldsymbol{I}$ is the identity matrix and $\operatorname{diag}(\cdot, 1 \le k \le N)$ denotes an $N \times N$ diagonal matrix with entries given by the first input. Furthermore, it is important to note that the modification of the Lagrange interpolating polynomial no longer allows us to build the higher-order differentiation matrix via multiplication of the lower-order differentiation matrices.

Before solving the discretized eigenvalue problem $\widehat{\boldsymbol{A}}\widehat{\boldsymbol{\psi}} = \sigma\widehat{\boldsymbol{B}}\widehat{\boldsymbol{\psi}}$, a preconditioner is needed to reduce the condition number of $\widehat{\boldsymbol{A}}$. By analogy to [109], we find that the following preconditioner successfully reduces the condition number of $\widehat{\boldsymbol{A}}$ by four orders of magnitude:

$$\widehat{\boldsymbol{S}} = \operatorname{diag}\left(\frac{1}{1+\widetilde{X}_k}, 1 \le k \le N; (1+\widetilde{X}_k)^2(1-\widetilde{X}_k)^2, 1 \le k \le N-1; 0.1\right). \tag{2.27}$$

Here, the semicolons denote concatenation of elements along the diagonals of the $2N \times 2N$ matrix $\widehat{\boldsymbol{S}}$. Therefore, the eigenvalue problem that we need to solve numerically is actually $\widehat{\boldsymbol{S}}\widehat{\boldsymbol{A}}\widehat{\boldsymbol{\psi}} = \sigma\widehat{\boldsymbol{S}}\widehat{\boldsymbol{B}}\widehat{\boldsymbol{\psi}}$.

Finally, for the computational results reported in the main text above, we invert the matrix $\widehat{\boldsymbol{S}}\widehat{\boldsymbol{A}}$ and solve the regular eigenvalue problem, $\widehat{\boldsymbol{A}}^{-1}\widehat{\boldsymbol{S}}^{-1}\widehat{\boldsymbol{S}}\widehat{\boldsymbol{B}}\widehat{\boldsymbol{\psi}} = \sigma^{-1}\widehat{\boldsymbol{\psi}}$, numerically. Note that $\widehat{\boldsymbol{S}}\widehat{\boldsymbol{B}}$ is not invertible because $\widehat{\boldsymbol{B}}$ is singular. SciPy's routine `eig` is used to obtain the spectrum (eigenvalues and eigenfunctions) of this system.

2.4.3 Validation of the Chebyshev pseudospectral method

In this subsection, we validate the Chebyshev pseudospectral method in section 2.4.2. The parameters used for simulation in this and next subsection are listed in table2.2. Furthermore, we order the calculated eigenvalues with magnitude in the following discussions.

Table 2.2. Summary of parameters used for simulation.

No. \ Parameter	Re	St	Σ	α
1	0.5	6.0	9.0×10^{-4}	0.0
2	0.5	6.0	9.0×10^{-4}	5.56×10^{6}
3	1.8	1.67	9.0×10^{-4}	0.0
4	10	0.3	9.0×10^{-4}	2.22×10^{9}

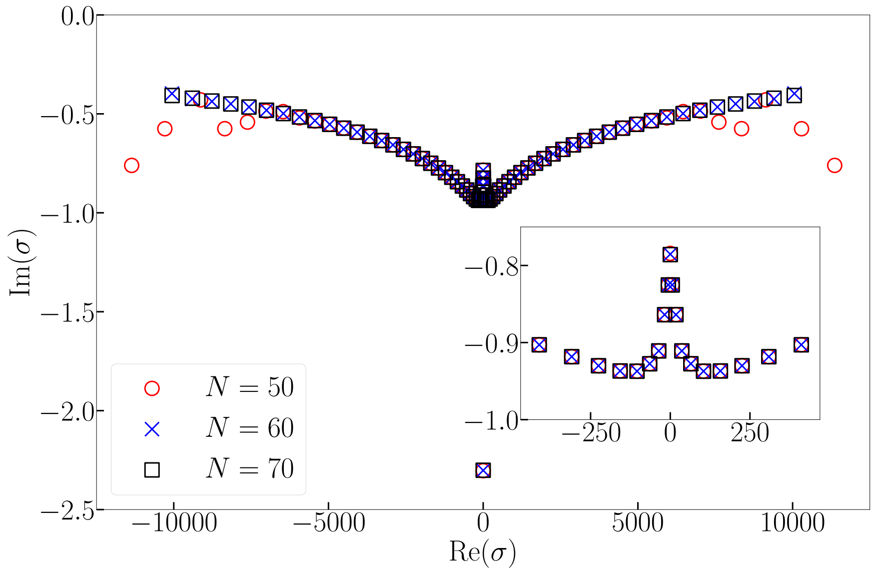

Figure 2.8. Convergence test: the computed eigenspectrum using the Chebyshev pseudospectral method with different number of Gauss–Lobatto points.

First, we show the convergence of the method by calculating the eigenspectrum using different sets of Gauss–Lobatto grids. In figure 2.8, we show the first 70 eigenvalues of No.1 case in table2.2 using grid number of $N = 50$, 60 and 70, respectively. As shown, the eigenvalues agree well when their magnitudes are relatively small. The results of $N = 50$ deviate from the other two as we enter into higher modes (with larger magnitudes). This is because as the magnitude of eigenvalue increases, the corresponding eigenfunction becomes more and more oscillatory, in which case the grid number of $N = 50$ is unable to provide adequate resolution.

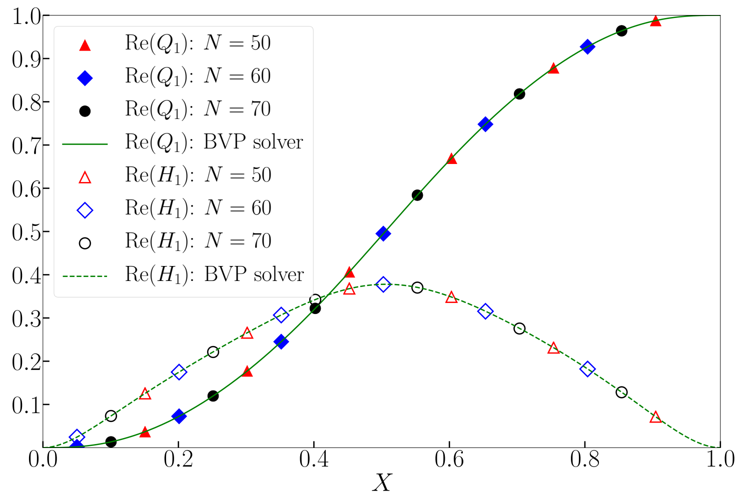

(a) First eigenmode: $\mathrm{Im}(\sigma) = -0.7859$.

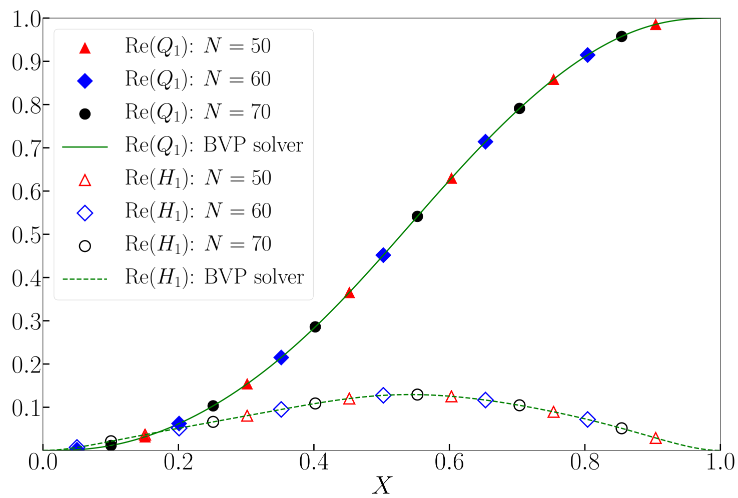

(b) Second eigenmode: $\mathrm{Im}(\sigma) = -2.3013$.

Figure 2.9. Comparisons of eigenfunctions, $Q_1(X)$ (filled symbols and solid curve) and $H_1(X)$ (empty symbols and dashed curve), of the first two modes (a,b) using different numbers of Gauss–Lobatto points, as well as a formulation that uses SciPy's `solve_bvp`.

Second, we can validate the Chebyshev pseudospectral method by comparing the results calculated with SciPy's `solve_bvp`. One interesting observation regarding the eigenspectra is that there are always two purely imaginary eigenvalues, for example, the first two modes in figure 2.8. It can be shown that the corresponding eigenfunctions are purely real. In relation to this observation, note that Butler et al. [111] used an alternative way to calculate the eigenvalue and eigenfunctions. Translated to our setting, we can introduce $\widetilde{\sigma} = -\mathrm{i}\sigma$ and substitute it into equations (2.19) to exclude any complex-valued solutions. Then, the system is linearly unstable if $\widetilde{\sigma} > 0$. The new set of equations can be viewed as a boundary value problem for $Q_1(X)$ and $H_1(X)$ with $\widetilde{\sigma}$ as an unknown parameter. The idea from [111] is to then use, e.g., SciPy's `solve_bvp` to solve the reformulated problem, provided that a proper initial guess for $\widetilde{\sigma}$ is given. However, this method can only provide a *single*, real eigenpair at a time (which corresponds to the case of purely imaginary σ in our model). The eigenvalue calculated in this way is sensitive to the initial guess. If a positive eigenvalue is returned by `solve_bvp`, then we would immediately conclude that the system is linearly unstable. However, it is important to note that the opposite is *not* true. If the eigenvalue returned is negative, then the result is inconclusive as we do not know whether this is the eigenvalue with smallest $|\operatorname{Im}(\sigma)|$, and we cannot make a definitive statement about the stability of the system.

Nevertheless, this approach can provide an independent validation of our stability calculation by the Chebyshev method. In figure 2.9, we compare the results from the Chebyshev pseudospectral method (using different N) with the results of the formulation based on [111] using `solve_bvp`, for the first two modes shown in figure 2.8. While the Chebyshev method reported the corresponding eigenvalues as $\operatorname{Im}(\sigma) = -0.7859$ and $\operatorname{Im}(\sigma) = -2.3013$ respectively, the eigenvalues calculated from `slove_bvp` were $\widetilde{\sigma} = -0.7849$ and $\widetilde{\sigma} = -2.3030$, respectively (recall, $\widetilde{\sigma} = -\mathrm{i}\sigma = \operatorname{Im}(\sigma)$). Furthermore, as shown in figure 2.9, the eigenfunctions from both methods agree completely. Thus, we can be confident in the accuracy of the eigenspectra computed by the Chebyshev method.

The final validation of this linear analysis is to compare the predicted growth of perturbations to the time-evolution of the nonlinear problem. To this end, we take the initial condition to be equations (2.17) (at $T = 0$), where Q_1 and H_1 given by the eigenfunctions of the linear problem computed above. Then, $Q(X,T)$ and $H(X,T)$ should evolve according to equations (2.17) with the corresponding eigenvalue setting the time dependence. For example, fixing $\delta = 0.1$ and taking $Q(X,0) = 1 + \delta Q_1(X)$ and $H(X,0) = H_0(X) + \delta H_1(X)$, where $\{Q_1, H_1\}$ is a linear eigenmode for $Re = 10$ (No. 4 case in table2.2), as the initial conditions

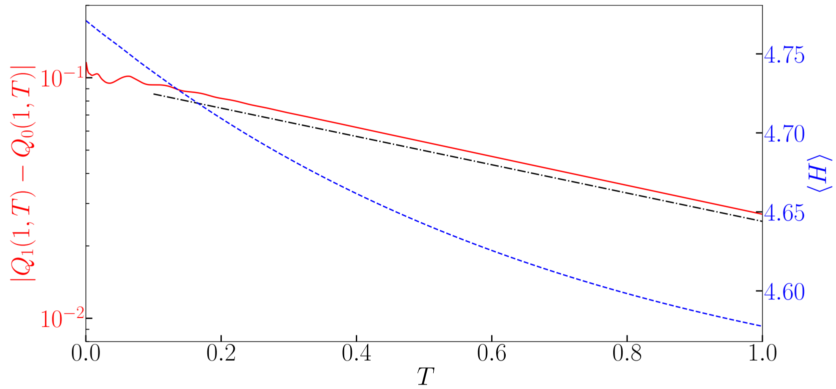

(a) First mode: $\sigma = -1.3547\mathrm{i}$.

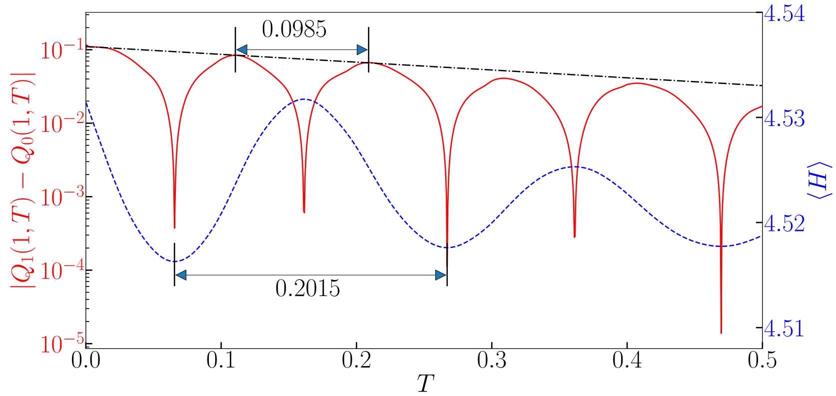

(b) Second mode: $\sigma = 31.2167 - 2.4504\mathrm{i}$.

Figure 2.10. The time histories of the difference of the instantaneous outlet flow rate from the base state, i.e., $|Q(1,T) - Q_0(1,T)|$, and the axially-average deformed channel height, $\langle H \rangle$, after substituting the eigenfunctions of the first and second mode for $Re = 10$ into the initial perturbations respectively (see equations (2.17) and taking $T = 0$). The slope of the dot-dashed lines represents the imaginary part of the corresponding eigenvalues from the linear stability calculation.

for the transient simulation of equation (2.1). The transient simulation was implemented using the algorithm in [102], which is a second-order accurate finite difference scheme. Figure 2.10 shows the time histories of the outlet flow rate and the deformed channel's height. Since the eigenvalue of the first mode is purely imaginary, figure 2.10a shows that the deviation of the outlet flow rate from the base state, $|Q(1,T) - Q_0(1,T)|$, as well as the average deformed channel height, $\langle H \rangle$, both decay without oscillations. Importantly, the decay rate of the fully-nonlinear simulation agrees with $\text{Im}(\sigma)$. As for the results of the second mode, shown in figure 2.10b, both Q and $\langle H \rangle$ oscillate in time because $\text{Re}(\sigma) \neq 0$. In this example, $\text{Re}(\sigma)$ represents the temporal period of the eigenmode, which is $\approx 2\pi/31.2167 = 0.2013$ based on the solution by the Chebyshev pseudospectral method. Clearly, the oscillation period observed in the transient simulation is very close to this predicted value. Furthermore, the decay rate of the amplitudes of $|Q(1,T) - Q_0(1,T)|$ agrees with $\text{Im}(\sigma)$.

2.4.4 Results and discussion

Before we present more numerical illustrations, we mention that for the present purposes, we are just interested in the *asymptotic* stability of the inflated steady-states, so it suffices to consider the eigenspectrum of $\boldsymbol{A}$ for different parameters, and determine the possibility of eigenvalues with positive imaginary part. However, since equations (2.19) do *not* give rise to an autonomous system with a self-adjoint matrix operator $\boldsymbol{A}$ due to the non-uniform base state (see, e.g., the discussion in [112] in the context of thin-film lubrication), issues of transient growth and non-modal analysis arise [112], [113], which can be addressed in future work.

Secondly, even without solving the generalized eigenvalue problem numerically, we can deduce some salient features. Specifically, note that in equation (2.20), the operator $\boldsymbol{A}$ is real, while the operator $\boldsymbol{B}$ is purely imaginary. This observation indicates that eigenvalues with non-zero real part should come in pairs. In other words, if there exists an eigenvalue σ with $\text{Re}(\sigma) \neq 0$ and $\boldsymbol{\psi} \neq \boldsymbol{0}$ such that $\boldsymbol{A}\boldsymbol{\psi} = \sigma\boldsymbol{B}\boldsymbol{\psi}$, then $\boldsymbol{A}\bar{\boldsymbol{\psi}} = -\bar{\sigma}\boldsymbol{B}\bar{\boldsymbol{\psi}}$ is automatically satisfied, meaning $-\bar{\sigma}$ and $\bar{\boldsymbol{\psi}}$ are another eigenpair of the problem. Here, $(\bar{\cdot})$ denotes the complex conjugate.

Next, we focus on the linear stability results of the four cases in table 2.2. The four cases include the cases with and without tension, and consider Re ranging from low to high, thus can provide a rather complete picture of the linear stability of the system.

Figure 2.11 and figure 2.12 show the first 70 eigenvalues (ordered by magnitudes) for the four cases in table 2.2. Two sets of numerical calculations are performed for each set of parameters (i.e., each panel), with $N = 60$ (regular grid) and $N = 70$ (fine grid), to ensure

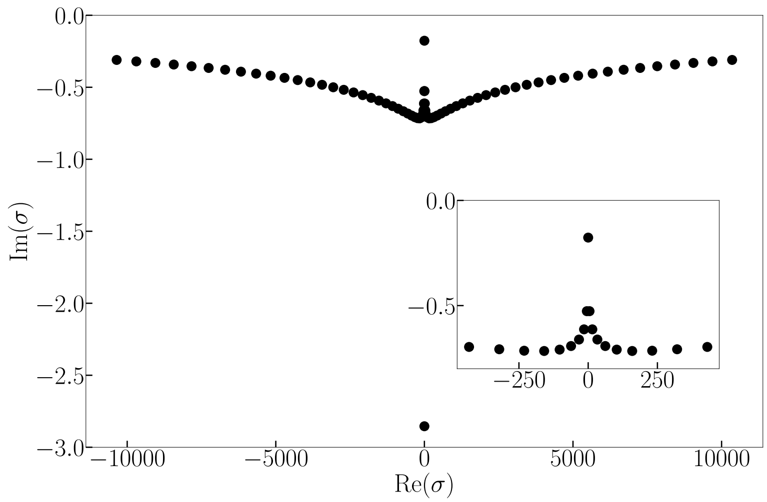

(a) $Re = 0.5$

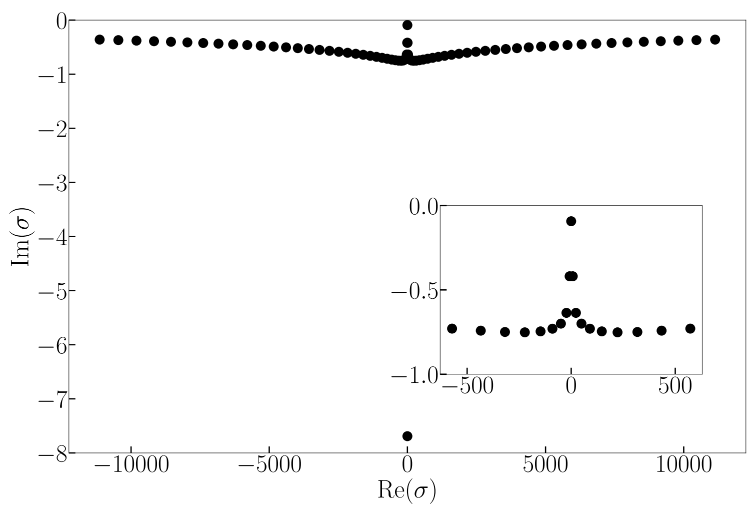

(b) $Re = 1.8$

Figure 2.11. Pure bending: Eigenspectra, in the complex plane $\mathbb{C}$, of the discretized linear eigenvalue problem, equations (2.20) and (2.18), governing the linear stability of the deformed microchannel shape.

the accuracy of eigenvalues reported. To accurately resolve even higher modes (> 70), we would have to further increase the number of Gauss–Lobatto grid points, denoted as $N+1$ in section 2.4.2, in the Chebyshev pseudospectral method. This increase is impractical because the condition number of the discretized operator matrix $\boldsymbol{A}$ grows rapidly with N, and finally, round-off error will dominate the calculation [108]. Therefore, admittedly, our

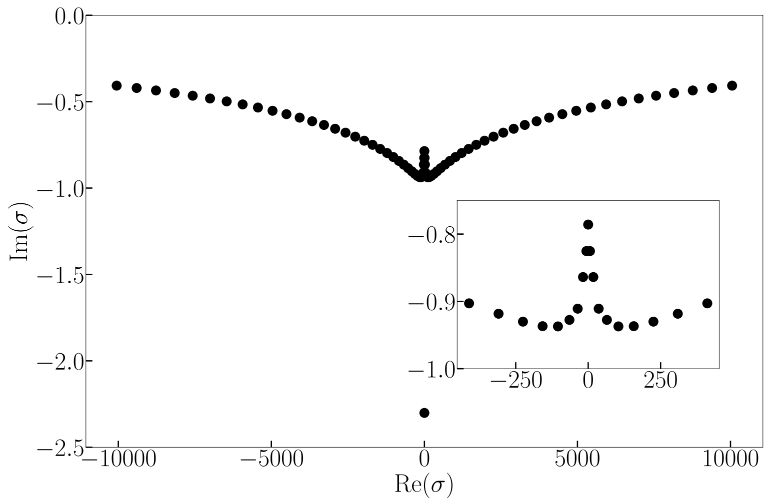

(a) $Re = 0.5$

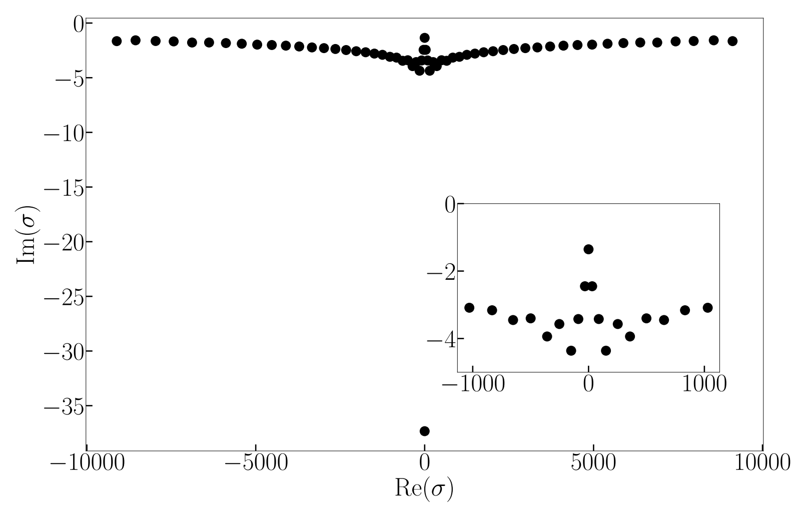

(b) $Re = 10$

Figure 2.12. Bening and tension: Eigenspectra, in the complex plane $\mathbb{C}$, of the discretized linear eigenvalue problem, equations (2.20) and (2.18), governing the linear stability of the deformed microchannel shape.

calculation does not lead to any conclusions about the higher-order modes that appear to have an increasing imaginary part. However, we shall report here, that for all the eigenvalues obtained (including those not shown in figure 2.11 and figure 2.12), only negative imaginary parts are found, except for two. The latter two are the usual "spurious" eigenmodes with magnitudes increasing as $\mathcal{O}(N^5)$; recall that the operator $\boldsymbol{A}$ is fifth order, and it has been

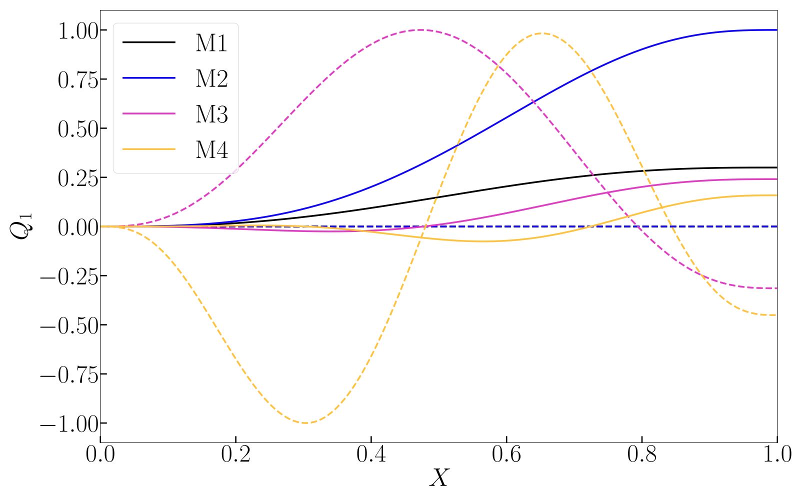

(a) $Re = 0.5$: $Q_1(X)$.

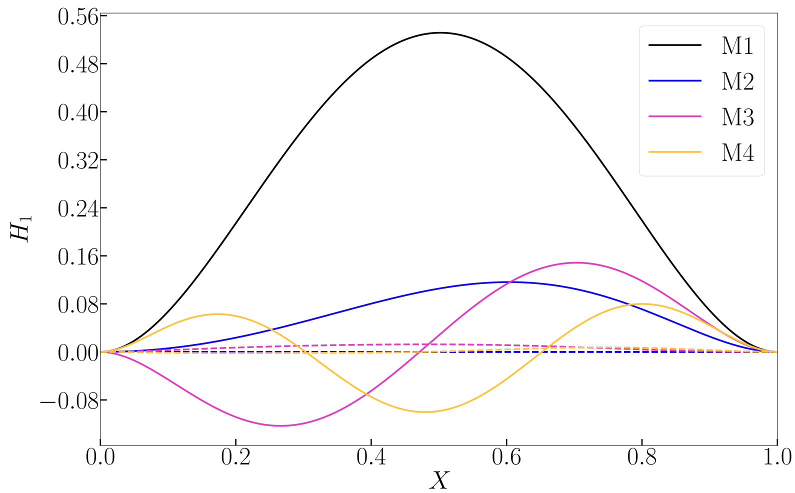

(b) $Re = 0.5$: $H_1(X)$.

Figure 2.13. Eigenfunctions $Q_1(X)$ and $H_1(X)$ for pure bending case No.1 in table 2.2. 'M1' to 'M4' denote mode 1 through 4, i.e., the first four eigenmodes with distinct $\mathrm{Im}(\sigma)$. Solid curves represent the real parts of the eigenfunctions, while dashed curves represent the imaginary parts.

found that the magnitude of the spurious eigenvalues should grow as $\mathcal{O}(N^m)$, where m is the highest order of the operator [108].

As shown in figure 2.11 and figure 2.12, the eigenspectra are discrete and symmetric about the imaginary axis. They resemble a "seagull" shape. As we zoom into the first 20

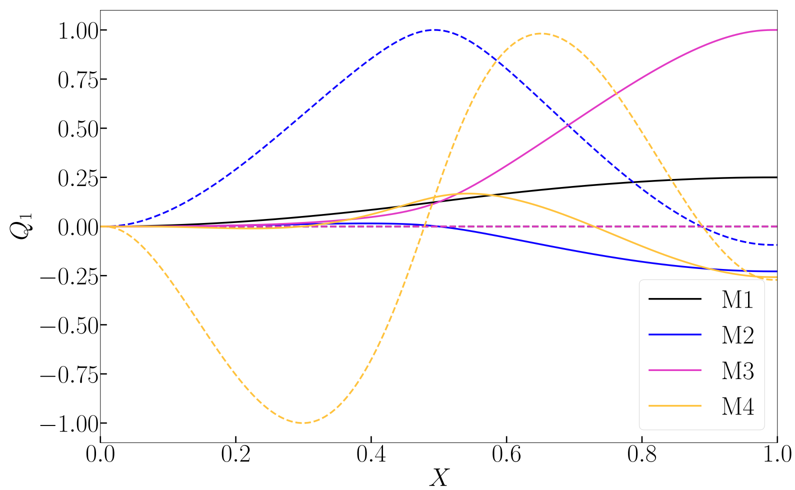

(a) $Re = 10$: $Q_1(X)$.

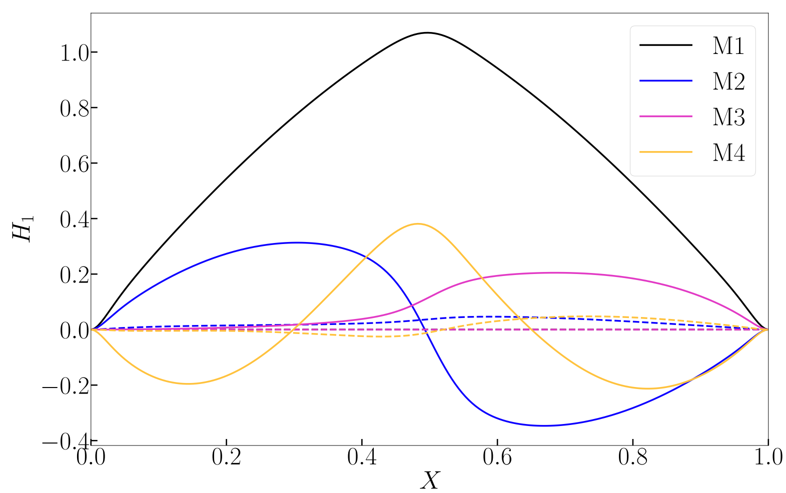

(b) $Re = 10$: $H_1(X)$.

Figure 2.14. Eigenfunctions $Q_1(X)$ and $H_1(X)$ for case No. 4 in table 2.2 with bending and tension. Again, 'M1' to 'M4' denote mode 1 through 4, i.e., the first four eigenmodes with distinct $\mathrm{Im}(\sigma)$. Solid curves represent the real parts of the eigenfunction, while dashed curves represent the imaginary parts.

eigenvalues, the shapes are "seagull"-like again but upside down. The case of $Re = 10$ in figure 2.12(b) is an exception in that the eigenvalues form a small hole in the middle of the complex plane. We believe that this change can be attributed to the strong inertial effects in the flow in this case.

Furthermore, for higher-order eigenvalues (i.e., larger $|\sigma|$), their real part grows much more rapidly than their imaginary part. Nevertheless, as shown in figure 2.11 and figure 2.12, $\mathrm{Im}(\sigma)$ appears to be plateauing for large $|\,\mathrm{Re}(\sigma)|$. The presence of a large number of eigenvalues with large $|\,\mathrm{Re}(\sigma)|$ suggests that there are corresponding eigenmodes that are highly oscillatory. This observation highlights the *stiffness* of the unsteady FSI problem. Since our transient simulation always reach a steady state, and no eigenvalues with $\mathrm{Im}(\sigma) > 0$ have been identified via the Chebyshev method, we are led to conclude that the steady-state deformation is linearly stable to small perturbations, or at least to relatively low-frequency perturbations. A detailed analysis could be performed in future work to understand the asymptotic behavior of the eigenspectra, and to completely address the stability of the system to high-frequency disturbances.

Finally, we show two example plots for eigenfunctions in figure 2.13 and figure 2.14, corresponding to the first four eigenvalues with distinct imaginary parts for No. 1 and No. 4 cases in table 2.2 respectively. For the plots shown, note the normalization of the eigenfunctions is arbitrary and only their qualitative features are being highlighted here. As discussed above, the eigenfunctions corresponding to the eigenvalues with the same imaginary part but opposite real part are conjugate pairs and thus not interesting to show here. One common feature of all the cases in table 2.2 is that, for the two modes with purely imaginary eigenvalues, $\mathrm{Re}(H_1)$ has only one maximum (hump), while the other two modes display two and three humps, respectively. Wavelike shapes are also observed in $\mathrm{Im}(Q_1)$ for the fourth mode. Of course, it is expected that there will be more humps in the eigenfunctions of higher-order modes. This observation is the reason for increasing the number of Gauss–Lobatto points to properly resolve the oscillatory nature of the higher-order eigenfunctions.

3. DOMINANT PHYSICAL EFFECTS IN LOW-REYNOLDS-NUMBER FLOWS THROUGH COMPLIANT RECTANGULAR MICROCHANNELS

SUMMARY

In this chapter, we investigate the dominant effects of flows through a common three-dimensional (3D) rectangular microchannel with a compliant wall. Assuming the channel is long and shallow even at the deformed state, we find that at the leading order in channel's small height to length ratio ϵ, the flow can be regarded unidirectional with a reduced Reynolds number $\hat{R}\mathrm{e} = \epsilon Re$ up to $\mathcal{O}(1)$. Specifically, the flow pressure varies along the streamwise direction mainly. At $\hat{R}\mathrm{e} = \mathcal{O}(1)$, there exists a balance between the finite fluid inertia, the dominant pressure gradient and the dominant shear stresses. We also assume that the compliant wall is made slender, with its width w and thickness d much smaller than its length ℓ. Further assuming weak solid inertia and linear elasticity, we find that owing to the wall slenderness, the dominant balance of the Cauchy stresses occurs at the cross-sectional plane of the wall, indicating that the deformation of the cross-sections at different streamwise locations is fully determined by the local pressure, like a Winkler foundation. Consequently, the displacement at the fluid–solid interface admits a separation-of-variable solution at the leading order. The dominant effects discussed in this chapter are generic for the fluid–structure interaction (FSI) systems with similar geometrical properties.

3.1 Problem statement, geometry and notation

From this chapter, we start to investigate the more realistic three-dimensional (3D) configuration. Consider a commonly seen rectangular microchannel, as shown in figure 3.1, with undeformed height of h_0, width of w, and length of ℓ. The microchannel is assumed to be long and shallow so that $h_0 \ll w \ll \ell$. Introducing the dimensionless parameters $\epsilon = h_0/\ell$ and $\delta = h_0/w$, then we have $\epsilon \ll \delta \ll 1$. In reality, the three walls of the channel can be made rigid with a soft wall bonded on top, as the geometry considered in [31], [33]. Alternatively, the top and side walls are soft and bonded to rigid bottom wall, as was the case in chapter 4 [101]. In either case, the deformation of the top wall is dominant. Therefore, in our modeling, the deformation of the side walls is neglected. Further, we denote the thickness of the top wall by d. To make the model general, at this stage, we do not specify the magnitude d compared to the other dimensions, but we do require that $d \ll \ell$. As the fluid is pushed through the microchannel, from the inlet to the outlet, the hydrodynamic pressure will deform the fluid–solid interface at the top wall. The displacement of the interface is denoted by $u_y(x, z, t)$. Finally, since the microchannel is often restricted from moving at the inlet ($z = 0$) and the outlet ($z = \ell$) planes by external connections (or the outlet is open to ambient gauge pressure, thus has negligible deformation), we assume zero displacement of the fluid–solid interface at both ends ($z = 0, \ell$).

For convenience, we introduce two coordinate systems. As shown in figure 3.1, the o_{xyz} coordinate system is located at the bottom wall of the microchannel, with its origin set at the center of the inlet. The $\hat{o}_{\hat{x}\hat{y}\hat{z}}$ coordinate system is the o_{xyz} system translated along y by h_0, thus its origin is located at the undeformed fluid–solid interface. Specifically, we have $x = \hat{x}$, $y = \hat{y} + h_0$ and $z = \hat{z}$.

We will discuss the dominant mechanisms in the fluid and solid mechanics problems in the following two sections, respectively. The conclusions made in this chapter will lay the foundation for our work hereafter.

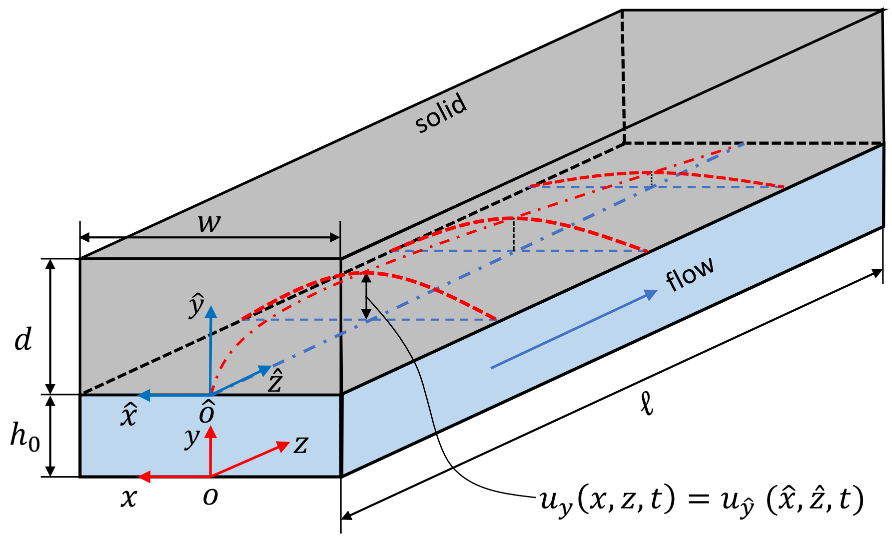

Figure 3.1. Schematic of the 3D geometry of the compliant microchannel with a deformable top wall [114], with key dimensional variables labeled. The red dash-dotted curve and the red dashed curves sketch the deformed fluid–solid interface at the mid-plane ($x = 0$), and the typical cross-sectional deformation profiles at the interface at different flow-wise locations, respectively.

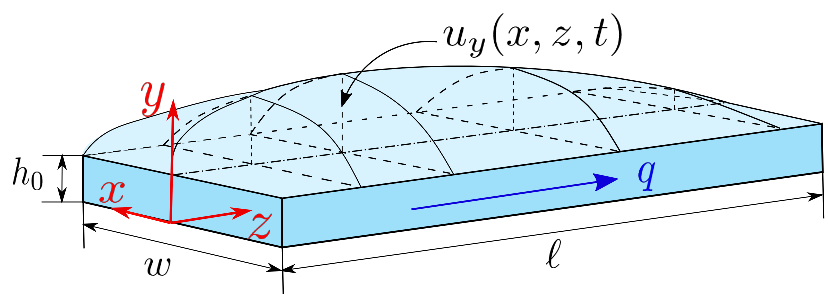

Figure 3.2. Schematic of flow through a deformed microchannel, with key dimensional variables labeled.

3.2 Dominant fluid mechanics effects

The fluid mechanics problem is about flows through a deformed microchannel, as shown in figure 3.2. Assume the working fluid is incompressible and Newtonian, with a density of ρ_f and dynamic viscosity of μ. With the displacement of the fluid–solid interface denoted as $u_y(x,z,t)$, the deformed channel height can be written as $h(x,z,t) = h_0 + u_y(x,z,t)$. Then, the deformed configuration of the fluid domain is $\{(x,y,z) \mid -w/2 \leq x \leq +w/2,\, 0 \leq y \leq$

Table 3.1. Scales for the variables in the incompressible Navier–Stokes equations (3.1).

Variable	t	x or $\hat{x}$	y	$\hat{y}$	z or $\hat{z}$	v_x	v_y	v_z	p
Scale	$\mathcal{T}_f$	w	h_0	d	ℓ	$\epsilon\mathcal{V}_c/\delta$	$\epsilon\mathcal{V}_c$	$\mathcal{V}_c$	$\mathcal{P}_c$

$h(x,z,t)$, $0 \le z \le \ell\}$. Further, we assume that $h(x,z,t) \ll w \ll \ell$, *i.e.*, the slenderness and shallowness assumptions on the conduit hold true even after its deformation. The former assumption is important because it allows us to use h_0 as the scale for y.

Under these assumptions, the governing unsteady incompressible Navier–Stokes equations take the form:

$$\underbrace{\frac{\partial v_x}{\partial x}}_{\mathcal{O}(1)} + \underbrace{\frac{\partial v_y}{\partial y}}_{\mathcal{O}(1)} + \underbrace{\frac{\partial v_z}{\partial z}}_{\mathcal{O}(1)} = 0, \tag{3.1a}$$

$$\underbrace{\frac{\partial v_x}{\partial t}}_{\mathcal{O}\left(\frac{\epsilon^2}{\delta^2}\hat{\mathrm{Re}}\right)} + \underbrace{v_x\frac{\partial v_x}{\partial x}}_{\mathcal{O}\left(\frac{\epsilon^2}{\delta^2}\hat{\mathrm{Re}}\right)} + \underbrace{v_y\frac{\partial v_x}{\partial y}}_{\mathcal{O}\left(\frac{\epsilon^2}{\delta^2}\hat{\mathrm{Re}}\right)} + \underbrace{v_z\frac{\partial v_x}{\partial z}}_{\mathcal{O}\left(\frac{\epsilon^2}{\delta^2}\hat{\mathrm{Re}}\right)} = -\underbrace{\frac{1}{\rho_f}\frac{\partial p}{\partial x}}_{\mathcal{O}(1)} + \underbrace{\frac{\mu}{\rho_f}\frac{\partial^2 v_x}{\partial x^2}}_{\mathcal{O}(\epsilon^2)} + \underbrace{\frac{\mu}{\rho_f}\frac{\partial^2 v_x}{\partial y^2}}_{\mathcal{O}\left(\frac{\epsilon^2}{\delta^2}\right)} + \underbrace{\frac{\mu}{\rho_f}\frac{\partial^2 v_x}{\partial z^2}}_{\mathcal{O}\left(\frac{\epsilon^4}{\delta^2}\right)}, \tag{3.1b}$$

$$\underbrace{\frac{\partial v_y}{\partial t}}_{\mathcal{O}(\epsilon^2\hat{\mathrm{Re}})} + \underbrace{v_x\frac{\partial v_y}{\partial x}}_{\mathcal{O}(\epsilon^2\hat{\mathrm{Re}})} + \underbrace{v_y\frac{\partial v_y}{\partial y}}_{\mathcal{O}(\epsilon^2\hat{\mathrm{Re}})} + \underbrace{v_z\frac{\partial v_y}{\partial z}}_{\mathcal{O}(\epsilon^2\hat{\mathrm{Re}})} = -\underbrace{\frac{1}{\rho_f}\frac{\partial p}{\partial y}}_{\mathcal{O}(1)} + \underbrace{\frac{\mu}{\rho_f}\frac{\partial^2 v_y}{\partial x^2}}_{\mathcal{O}(\epsilon^2\delta^2)} + \underbrace{\frac{\mu}{\rho_f}\frac{\partial^2 v_y}{\partial y^2}}_{\mathcal{O}(\epsilon^2)} + \underbrace{\frac{\mu}{\rho_f}\frac{\partial^2 v_y}{\partial z^2}}_{\mathcal{O}(\epsilon^4)}, \tag{3.1c}$$

$$\underbrace{\frac{\partial v_z}{\partial t}}_{\mathcal{O}(\hat{\mathrm{Re}})} + \underbrace{v_x\frac{\partial v_z}{\partial x}}_{\mathcal{O}(\hat{\mathrm{Re}})} + \underbrace{v_y\frac{\partial v_z}{\partial y}}_{\mathcal{O}(\hat{\mathrm{Re}})} + \underbrace{v_z\frac{\partial v_z}{\partial z}}_{\mathcal{O}(\hat{\mathrm{Re}})} = -\underbrace{\frac{1}{\rho_f}\frac{\partial p}{\partial z}}_{\mathcal{O}(1)} + \underbrace{\frac{\mu}{\rho_f}\frac{\partial^2 v_z}{\partial x^2}}_{\mathcal{O}(\delta^2)} + \underbrace{\frac{\mu}{\rho_f}\frac{\partial^2 v_z}{\partial y^2}}_{\mathcal{O}(1)} + \underbrace{\frac{\mu}{\rho_f}\frac{\partial^2 v_z}{\partial z^2}}_{\mathcal{O}(\epsilon^2)}, \tag{3.1d}$$

with the order-of-magnitude of each term listed underneath, based on the scales from table 3.1.

In table 3.1, $\mathcal{V}_c$ is the characteristic velocity scale. Specifically, to ensure the conservation of mass of equation (3.1a), $\epsilon\mathcal{V}_c/\delta$, $\epsilon\mathcal{V}_c$ and $\mathcal{V}_c$ are chosen to be the characteristic scales for the velocity components v_x, v_y and v_z, respectively. Also, as is standard for low-Reynolds-number flow, to achieve a balance between the pressure and the viscous stresses in equation (3.1d), the characteristic pressure scale, $\mathcal{P}_c$, and $\mathcal{V}_c$ are related by $\mathcal{P}_c = \mu\mathcal{V}_c\ell/h_0^2$. If the volumetric flow rate, q, at the inlet is fixed, we can choose $\mathcal{V}_c = q/(wh_0)$, then $\mathcal{P}_c = \mu q\ell/(wh_0^3)$. However, if the pressure drop, $\Delta p = p|_{z=0} - p|_{z=\ell}$, is prescribed, $\mathcal{P}_c = \Delta p$

Table 3.2. Scales for the variables in the linear elastodynamics equations (3.2).

Variable	t	$\hat{x}$	$\hat{y}$	$\hat{z}$	$u_{\hat{x}}$	$u_{\hat{y}}$ or u_y	$u_{\hat{z}}$	$\sigma_{\hat{x}\hat{x}}$	$\sigma_{\hat{x}\hat{y}}$	$\sigma_{\hat{x}\hat{z}}$	$\sigma_{\hat{y}\hat{y}}$	$\sigma_{\hat{y}\hat{z}}$	$\sigma_{\hat{z}\hat{z}}$
Scale	$\mathcal{T}_f$	w	d	ℓ	$\mathcal{U}_{c,x}$	$\mathcal{U}_c$	$\mathcal{U}_{c,z}$	$\mathcal{D}_{\hat{x}\hat{x}}$	$\mathcal{D}_{\hat{x}\hat{y}}$	$\mathcal{D}_{\hat{x}\hat{z}}$	$\mathcal{P}_c$	$\epsilon\mathcal{P}_c$	$\mathcal{D}_{\hat{z}\hat{z}}$

and, accordingly, $\mathcal{V}_c = \Delta p h_0^2/(\mu\ell)$. The Reynolds number is defined as $Re = \rho_f \mathcal{V}_c h_0/\mu$. However, the slenderness of the fluid domain makes the reduced Reynolds number, $\hat{R}e = \epsilon Re$ more suitable for quantifying the inertial effects of the flow. Finally, $\mathcal{T}_f$ is taken to be the characteristic time scale for axial advection (the dominant flow direction): $\mathcal{T}_f = \ell/\mathcal{V}_c$.

Recall that we are interested in the regime of $\epsilon \ll \delta \ll 1$. Based on the discussion above, it is clear that the dominant balance of terms occurs in the z-momentum equation (3.1d). Only the pressure terms are left in equations (3.1b) and (3.1c), indicating that, at the leading order in ϵ and δ, the hydrodynamic pressure p is *only* a function of the streamwise location z, as in the classic lubrication approximation [104], [115]. More importantly, this argument is true even at finite Reynolds number, *i.e.*, $\hat{R}e = \mathcal{O}(1)$, which is typical of the microfluidic experiments we compare to [41]. Specifically, with $\hat{R}e = \mathcal{O}(1)$, the dominant balance in the flow-wise momentum equation (3.1d) occurs between fluid inertia, the pressure gradient, and the viscous forces. The same balance was employed in Chapter 2 to derive a 1D FSI model from the 2D Navies–Stokes equations (but under different assumptions on the solid mechanics problem) [102].

Examining further the right-hand side of equation (3.1d), the balance of forces at the leading-order indicates that $\partial p/\partial z \sim \partial \tau_{yz}/\partial y$ because the shear stress is $\tau_{yz} \sim \mu \partial v_z/\partial y$. Introducing $\mathcal{S}_c$ as the characteristic scale for τ_{yz} and substituting the other scales from table 3.1, the balance suggests that $\mathcal{P}_c/\ell = \mathcal{S}_c/h_0$, leading to $\mathcal{S}_c = h_0/\ell\mathcal{P}_c = \epsilon\mathcal{P}_c$. For $\epsilon \ll 1$, we conclude that $\tau_{yz} \ll p$. Hence, at the leading order in ϵ and δ, $p(z)$ is the only flow-induced load exerted on the fluid–solid interface.

3.3 Dominant solid mechanics effects

The solid mechanics problem is described in figure 3.3, which concerns the deformation of the top compliant wall subject to the hydrodynamic pressure of the flow. It is more

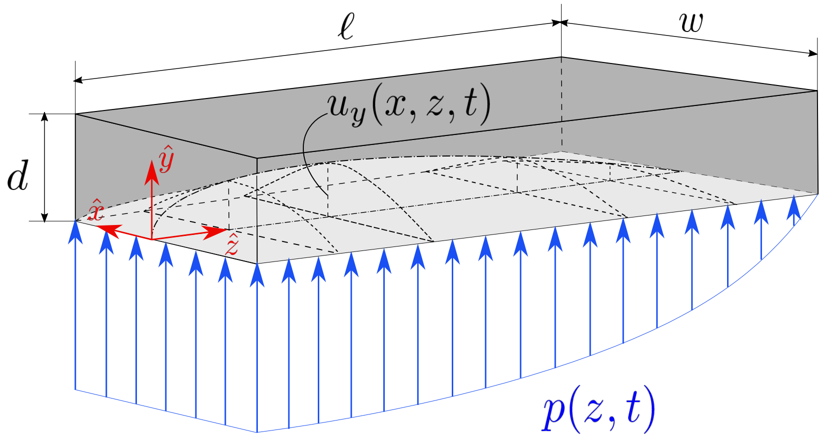

Figure 3.3. Schematic of the top compliant wall deformed by the distributed load due to the hydrodynamic pressure of the flow, with key dimensional variables labeled.

convenient to use the $\hat{o}_{\hat{x}\hat{y}\hat{z}}$ coordinate system, where we denote the displacement of the fluid–solid interface by $u_{\hat{y}}$, as shown in figure 3.3 as well as in figure 3.1. We consider the case in which the maximum of $\hat{u}_y$ is small compared with the smallest dimension of the solid, so that the small-strain theory of linear elasticity is applicable. Specifically, if the wall is "thick," meaning $w \lesssim d \ll \ell$, we require that $\hat{u}_y \ll w$. However, if the wall is "thin," meaning $d \lesssim w \ll \ell$, we require that $\hat{u}_y \ll d$ [114].

The following discussion follows that of [101]. However, here, we provide a more general derivation for the reader's convenience. First, using the scales from table 3.2, the balance between the Cauchy stresses and the solid inertia within the wall, neglecting any body forces,

$$\underbrace{\rho_s \frac{\partial^2 u_{\hat{x}}}{\partial t^2}}_{\mathcal{O}(\rho_s \mathcal{U}_{c,x}/\mathcal{T}_f^2)} + \underbrace{\frac{\partial \sigma_{\hat{x}\hat{x}}}{\partial \hat{x}}}_{\mathcal{O}(\mathcal{D}_{\hat{x}\hat{x}}/w)} + \underbrace{\frac{\partial \sigma_{\hat{x}\hat{y}}}{\partial \hat{y}}}_{\mathcal{O}(\mathcal{D}_{\hat{x}\hat{y}}/d)} + \underbrace{\frac{\partial \sigma_{\hat{x}\hat{z}}}{\partial \hat{z}}}_{\mathcal{O}(\mathcal{D}_{\hat{x}\hat{z}}/\ell)} = 0, \tag{3.2a}$$

$$\underbrace{\rho_s \frac{\partial^2 u_{\hat{y}}}{\partial t^2}}_{\mathcal{O}(\rho_s \mathcal{U}_{c}/\mathcal{T}_f^2)} + \underbrace{\frac{\partial \sigma_{\hat{x}\hat{y}}}{\partial \hat{x}}}_{\mathcal{O}(\mathcal{D}_{\hat{x}\hat{y}}/w)} + \underbrace{\frac{\partial \sigma_{\hat{y}\hat{y}}}{\partial \hat{y}}}_{\mathcal{O}(\mathcal{P}_c/d)} + \underbrace{\frac{\partial \sigma_{\hat{y}\hat{z}}}{\partial \hat{z}}}_{\mathcal{O}(\epsilon\mathcal{P}_c/\ell)} = 0, \tag{3.2b}$$

$$\underbrace{\rho_s \frac{\partial^2 u_{\hat{z}}}{\partial t^2}}_{\mathcal{O}(\rho_s \mathcal{U}_{c,z}/\mathcal{T}_f^2)} + \underbrace{\frac{\partial \sigma_{\hat{x}\hat{z}}}{\partial \hat{x}}}_{\mathcal{O}(\mathcal{D}_{\hat{x}\hat{z}}/w)} + \underbrace{\frac{\partial \sigma_{\hat{y}\hat{z}}}{\partial \hat{y}}}_{\mathcal{O}(\epsilon\mathcal{P}_c/d)} + \underbrace{\frac{\partial \sigma_{\hat{z}\hat{z}}}{\partial \hat{z}}}_{\mathcal{O}(\mathcal{D}_{\hat{z}\hat{z}}/\ell)} = 0. \tag{3.2c}$$

Here, $\sigma_{\hat{x}\hat{x}}$, $\sigma_{\hat{x}\hat{y}}$, $\sigma_{\hat{x}\hat{z}}$, $\sigma_{\hat{y}\hat{y}}$, $\sigma_{\hat{y}\hat{z}}$ and $\sigma_{\hat{z}\hat{z}}$ are the six independent components of the Cauchy stress in the solid. The order-of-magnitude of each term is listed underneath, based on the scales from table 3.2.

In table 3.2, $\mathcal{U}_{c,x}$, $\mathcal{U}_c$ and $\mathcal{U}_{c,z}$ are the characteristic scales for $u_{\hat{x}}$, $u_{\hat{y}}$ and $u_{\hat{z}}$, respectively. We immediately assume that $\mathcal{U}_{c,x} \ll \mathcal{U}_c$ and $\mathcal{U}_{c,z} \ll \mathcal{U}_c$, meaning that the wall is primarily bulging upwards, as in experiments. This assumption has previously been quantitatively validated against experiments [31], [33], [101]. Then the most prominent inertial term in the solid is in equation (3.2b). Note that the time scale for equation (3.2) is still the fluid's axial advection time scale, $\mathcal{T}_f$, in order to ensure the coupling between the solid and the fluid mechanics problems. (Note that this choice of time scale is different from the so-called "viscous–elastic" one used in related works [66], [116]. In the latter papers, the characteristic (common) time scale $\mathcal{T}_c$ was chosen based on the kinematic boundary condition at the fluid–solid interface, *i.e.*, $\partial \bar{u}_y/\partial t = v_y$, leading to a fluid time scale of $\mathcal{T}_c = \bar{\mathcal{U}}_c/(\epsilon\mathcal{V}_c) = (\bar{\mathcal{U}}_c/h_0)(\ell/\mathcal{V}_c) = \beta\mathcal{T}_f$. However, since β is typically at $\mathcal{O}(1)$ in our work, as discussed in chapter 5, these two different choices of the fluid time scale, $\mathcal{T}_c$ and $\mathcal{T}_f$, do not differ significantly.) To further elucidate the time scales involved, the scaling of the inertial term in equation (3.2b) can be written as $\rho_s\mathcal{U}_c/\mathcal{T}_s^2 \times (\mathcal{T}_s/\mathcal{T}_f)^2$, where we have explicitly introduced the solid time scale, $\mathcal{T}_s$. As we will show in chapter 6, in the microfluidic setting, $\mathcal{T}_s \ll \mathcal{T}_f$, leading to $\rho_s\mathcal{U}_c/\mathcal{T}_f^2 \ll 1$, thus the inertia of the solid is a weak effect.

Next, let us consider the balance of the Cauchy stresses. Due to the traction balance at the fluid–solid interface, it can be inferred that $\mathcal{D}_{\hat{y}\hat{y}} = \mathcal{P}_c$ and $\mathcal{D}_{\hat{y}\hat{z}} = \epsilon\mathcal{P}_c$, as tabulated in table 3.2. For convenience, we introduce $\gamma = d/w$. Then, a balance in equation (3.2b) can only occur between the second and the third terms, yielding $D_{\hat{x}\hat{y}} = \mathcal{P}_c/\gamma$. At the same time, the balance of the three terms in equation (3.2c) gives $\mathcal{D}_{\hat{x}\hat{z}} = \epsilon\mathcal{P}_c w/d = \epsilon\mathcal{P}_c/\gamma$ and $\mathcal{D}_{\hat{z}\hat{z}} = \epsilon\mathcal{P}_c\ell/d = \delta\mathcal{P}_c/\gamma$. Finally, from equation (3.2a), the only remaining possibility is that the second term balances the third term, indicating $\mathcal{D}_{\hat{x}\hat{x}} = w\mathcal{D}_{\hat{x}\hat{y}}/d = \mathcal{P}_c/\gamma^2$.

So far, we have only required that $d \ll \ell$, which is equivalent to $\gamma \ll \delta/\epsilon$, and covers a large range of wall thicknesses. However, it is also expected that $\gamma \gg \epsilon$, such that $\mathcal{D}_{\hat{x}\hat{z}}$ is a small quantity, excluding the case of an extremely thin wall. In fact, recalling that the application of linear elasticity requires that $\hat{u}_y \ll d$, any prominent deformation in a thin-walled microchannel is likely out of the scope the of the linear elastic theory.

Therefore, with $\epsilon \ll \gamma \ll \delta/\epsilon$ as well as $\epsilon \ll \delta \ll 1$, it is concluded that $\sigma_{\hat{x}\hat{z}}$ and $\sigma_{\hat{y}\hat{z}}$ are negligible compared to the other components. Depending on the wall thickness, the relative magnitude among the remaining four stress components can change. For example, if $\gamma^2 \gg 1$, we can further neglect $\sigma_{\hat{x}\hat{x}}$ as in [101]. Nevertheless, no matter how d varies, the dominant balances in equations (3.2a) and (3.2b) occur in the cross-sectional $(\hat{x}, \hat{y})$ plane, which reduces the original 3D elasticity problem to a 2D plane-strain problem. Since it has been shown in section 3.2 that p is a function of z only at the leading order (in ϵ), the deformation of the $(\hat{x}, \hat{y})$ cross-sections at different z-locations (recalling $z = \hat{z}$) decouple from each other. At each cross-section, the deformation is then determined by the local hydrodynamic pressure $p(z, t)$. Therefore, generally, we can express the displacement of the fluid–solid interface at the leading order (in ϵ) as

$$u_y(x, z, t) = u_{\hat{y}}(\hat{x}, \hat{z}, t) = \mathfrak{f}(x)p(z, t), \tag{3.3}$$

with $\mathfrak{f}(x)$ being the spanwise deformation profile. The separation-of-variables form of equation (3.3) suggests that the cross-sectional deformation profiles at different z-locations are, in a sense, self-similar. The displacement is fully determined by the local pressure, showing that the fluid–solid interface behaves like a Winkler foundation [117], [118], with a variable stiffness represented by $1/\mathfrak{f}(x)$. Importantly, this Winkler-foundation-like mechanism is *not* an assumption here, but rather it is a *consequence* of the slenderness of the top wall. Also, note that the assumption of $\mathcal{T}_s \ll \mathcal{T}_f$ has been applied here, meaning that the solid responds to pressure changes in the flow promptly.

It is also worth mentioning that if the top wall is thin with $\epsilon \ll \gamma \lesssim 1$, the elasticity problem is usually taken to be a plane stress problem, and a 1D engineering model is usually available for the displacement out of plane (*i.e.*, u_y here), such as the Kirchhoff–Love [119], [120] and Reissner–Mindlin [121], [122] plate theories. However, this fact does not fundamentally contradict with our plane-strain reduction because the decoupling of the cross-sections remains true [31], [33], [34] due to the separation of scales, $w \ll \ell$.

Moreover, the discussion above is only based on the balance of Cauchy stresses, and does not involve the boundary conditions either on the sides (*i.e.*, at $x = \pm w/2$) or at the upper surface of the wall (*i.e.*, at $\hat{y} = d$ or $y = h_0 + d$). The decoupling of the cross-sectional deformation is just a consequence of the wall slenderness. However, the boundary conditions do have an important influence on the displacement field in the solid, which will give rise to different forms of $\mathfrak{f}(x)$ in equation (3.3) [114].

4. THEORY OF FLOWS THROUGH THICK-WALLED RECTANGULAR MICROCHANNELS AT STEADY STATE

SUMMARY

In this chapter, we consider fluid–structure interactions (FSIs) in long, shallow microchannels embedded in thick soft materials. This configuration of microchannels is widely used in microfluidic devices for lab-on-a-chip applications. However, the bulging effect caused by fluid–structure interactions between the internal viscous flow and the soft walls has not been completely understood. Previous models either contain a fitting parameter or are specialized to channels with plate-like walls. This work is a theoretical study of the steady-state response of a compliant microchannel with a thick wall. Using lubrication theory for low-Reynolds-number flows and the theory for linearly elastic isotropic solids, we obtain perturbative solutions for the flow and deformation. Specifically, only the channel's top wall deformation is considered, and the ratio between its thickness d and width w is assumed to be $(d/w)^2 \gg 1$. We show that the deformation at each stream-wise cross-section can be considered independently, and that the top wall can be regarded as a simply supported rectangle subject to uniform pressure at its bottom. The stress and displacement fields are found using Fourier series, based on which the channel shape and the hydrodynamic resistance are calculated, yielding a new flow rate–pressure drop relation without fitting parameters. Our results agree favorably with, and thus rationalize, previous experiments.

The material in this chapter was published as [X. Wang and I.C. Christov, "Theory of the flow-induced deformation of shallow compliant microchannels with thick walls," *Proc. R. Soc. A*, vol. 475, art. 20190513, 2019] [101] (authors retain rights to reproduce article in a thesis or dissertation). Both authors contributed to the analysis of the problem and the derivation of the mathematical model. X.W. wrote the MATLAB scripts and conducted all the case studies and data analysis. X.W. and I.C.C. jointly discussed the results, drafted and revised the manuscript for publication.

4.1 Configuration of thick-walled microchannels

In this chapter, we focus on a specific case to illustrate how we can solve for $\mathfrak{f}(x)$ in equation (3.3) and realize the fluid–solid coupling in the case of negligible fluid inertia, *i.e.*, $\hat{R}\mathrm{e} \to 0$.

Consider the pressure-driven, steady flow of a Newtonian viscous fluid inside of a microchannel fabricated via soft lithographic techniques from an elastomer. A schematic configuration is shown in figure 4.1. The problem is symmetric about $x = 0$, with only half of it being shown in the figure. The other notations are the same as in figure 3.1 of chapter 3. It is also assumed that the microchannel is long and shallow, such that $h_0 \ll w \ll \ell$. Three sides (two lateral walls and the top wall) of the channel are composed of a soft elastic material, while the bottom wall is assumed to be rigid. Moreover, d denotes the thickness of the top solid slab, while the thickness of the lateral walls is assumed to be large enough to be considered as infinite. We also require that $d \ll \ell$. According to the scaling analysis of Gervais *et al.* [12], the strain of the displaced fluid–solid interface is proportional to the imposed stress, so $u_y(x, z) \propto wp(z)/E$, where $p(z)$ denotes the local pressure at flowwise position z, and E denotes the Young's modulus of the solid. Similarly, the side wall deformation is proportional to $h_0 p(z)/E$. In the regime $h_0 \ll w$, the deformation of the top wall is thus expected to be much larger than that of the lateral walls. Therefore, we only consider the deformation of the top wall, and the schematic diagram of figure 3.1 of chapter 3 still applies.

4.2 Formulation of the fluid mechanics problem

The lubrication approximation introduced in section 3.2 applies here. Since we only consider the steady-state response in this chapter, all the time-dependent terms in equation (3.1) vanish. We further assume that the fluid inertia is negligible, with $\hat{R}\mathrm{e} = \epsilon R\mathrm{e} \ll 1$. Then, based on the scaling analysis in section 3.2, the leading-order solution of equations (3.1), subject to no-slip condition at the top and bottom walls of the channel, is found as

$$v_z(x, y, z) = \frac{1}{2\mu}\frac{\mathrm{d}p}{\mathrm{d}z} y\,[y - h(x, z)] \qquad (0 \le y \le h)\,, \tag{4.1}$$

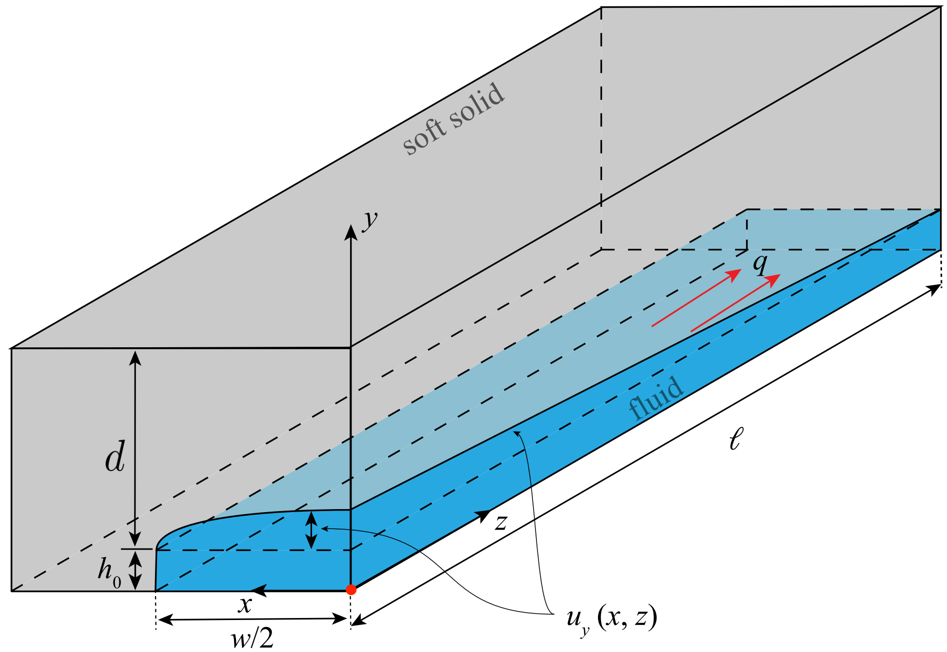

Figure 4.1. Schematic diagram of the thick-walled compliant microchannel with key variables labeled. The origin of the coordinate system o_{xyz} (labeled with a red a dot) is set at the centerline ($x = 0$) of the bottom of the channel. The fluid–solid interface is initially a distance h_0 above the rigid bottom channel wall. The microchannel is symmetric about $x = 0$ thus, for clarity, only half the channel (for $x \geq 0$) is shown. The deformed fluid–solid interface is denoted by the compliant top wall's y-displacement evaluated at $y = h_0$, i.e., $u_y(x, z)$. The fluid flow is in the $+z$-direction, as indicated by arrows, with an inlet at $z = 0$ and an outlet at $x = \ell$.

where $h(x, z) = h_0 + u_y(x, z)$. We can set $u_y = \mathcal{U}_c U_Y$ and $\lambda = \mathcal{U}_c/h_0$, where $\mathcal{U}_c$ has been introduced as the characteristic top wall deformation scale in section 3.3 (to be determined self-consistently by solving the corresponding elasticity problem in section 4.3). Then, $H(X, Z) = 1 + \lambda U_Y^0(X, Z)$ is the dimensionless deformed top wall profile, and λ can be interpreted as the *compliance parameter* that characterizes top wall's ability to deform due to the flow beneath it. Under the lubrication approximation, which requires $h \ll w$, it is expected that $\lambda \ll 1/\delta$ [31]. Using the scales in table3.1, the dimensionless form of equation (4.1) is written as

$$V_Z(X, Y, Z) = \frac{1}{2}\frac{\mathrm{d}P}{\mathrm{d}Z} Y[Y - H(X, Z)] \qquad (0 \leq Y \leq H). \tag{4.2}$$

At this stage, the (non-constant) pressure gradient $\mathrm{d}P/\mathrm{d}Z < 0$ remains unknown. Due to the chosen scaling (to balance conservation of mass), the velocity components V_X and V_Y come in at higher orders in the perturbation expansion. Systematic corrections in powers of ϵ can be obtained as regular perturbations [123], however the expansion in δ is singular [124]. For our purposes, it suffices to note that the flow is primarily unidirectional in the z-direction (as the familiar Reynolds lubrication approximation [125], [126]).

4.3 Formulation of the solid mechanics problem

4.3.1 Plane strain configuration and the thickness effect

As in section3.3, we work in $\hat{o}_{\hat{x}\hat{y}\hat{z}}$ fpr the solid mechanics problem. Since $x = \hat{x}$ and $z = \hat{z}$, we will drop the “hats” for x and z in the following analysis. It should be clarified beforehand that we “cut off” the solid from the sides and only consider the deformation of the top rectangular slab, with width w, thickness d and length ℓ with initial configuration occupying the domain $\Omega_{s0} = \{(x, \hat{y}, \hat{z}) \mid -w/2 \leq x \leq +w/2,\, h_0 \leq \hat{y} \leq d,\, 0 \leq \hat{z} \leq \ell\}$. At steady state, the linear elastic deformation of the solid results from the balance of Cauchy stresses. As we have discussed in section3.3, owing to $d \ll \ell$ and $w \ll \ell$, the dominant Cauchy stresses are $\sigma_{xx} \sim \mathcal{P}_c/\gamma^2$, $\sigma_{x\hat{y}} \sim \mathcal{P}_c/\gamma$, $\sigma_{\hat{y}\hat{y}} \sim \mathcal{P}_c$ and $\sigma_{\hat{z}\hat{z}} \sim \delta\mathcal{P}_c/\gamma$. Recall that $\gamma = d/w$. Then from equation (3.2), we conclude that the dominant balance of Cauchy stresses occurs in the x-$\hat{y}$ cross-sectional plane. It is important to note that γ (i.e., the solid thickness parameter) plays an essential role in the stress distribution. Accordingly, the boundary condition at the sidewalls $x = \pm w/2$, due to the reaction between the top wall and the remaining solid, will give rise to the thickness effect. Furthermore, based on the linear constitutive relation between the stress and the linear strain, as well as the fact that the microchannel is usually prevented from displacements in the flowwise direction by rigid inlet and outlet connectors, we are justified in reducing the problem to a plane strain configuration with dominant linear strains e_{xx}, $\mathrm{e}_{\hat{y}\hat{y}}$ and $\mathrm{e}_{x\hat{y}}$, in the cross-section.

For a plane strain problem, it is convenient to introduce the Airy stress function $\phi(x, \hat{y})$ that satisfies the homogeneous biharmonic equation (in dimensional form) [127]:

$$\frac{\partial^4 \phi}{\partial x^4} + 2\frac{\partial^4 \phi}{\partial x^2 \partial \hat{y}^2} + \frac{\partial^4 \phi}{\partial \hat{y}^4} = 0. \tag{4.3}$$

Then, the stresses are computed from the stress function as $\sigma_{xx} = \partial^2\phi/\partial\hat{y}^2$, $\sigma_{\hat{y}\hat{y}} = \partial^2\phi/\partial x^2$ and $\sigma_{x\hat{y}} = -\partial^2\phi/\partial x\partial\hat{y}$. Meanwhile, $\sigma_{zz} = \nu_s(\sigma_{xx} + \sigma_{\hat{y}\hat{y}})$ according to the constitutive equation of linear elasticity, where ν_s is the Poisson ratio. Note our analysis necessitates different characteristic scales for the y or $\hat{y}$ coordinate for the fluid and solid mechanics problems. Therefore, for consistency and convenience, we solve the solid mechanics problem in its dimensional form (4.3).

4.3.2 Large-thickness case

In the present study, we are interested in the case of thick top wall, which arises because microchannels are frequently embedded in half-space-like PDMS medium when manufactured by, e.g., replica molding [5]. From the scaling analysis of equation (3.2) in section3.3, we learned that, as the thickness increases, $\sigma_{x\hat{y}}$ decreases as $1/(\gamma)$, while σ_{xx} decreases even faster, as $1/\gamma^2$. Thus, consider the case when the thickness is large enough, specifically $(\gamma^2 \gg 1$. Then, σ_{xx} is much smaller than the other stresses in the solid, as well as at both sidewalls. Taking $\sigma_{xx}|_{x=\pm w/2} = 0$ and assuming that the displacement at the corner is negligible, the boundary condition at $x = \pm w/2$ is reduced to that of a simple support. This result is crucial to the analysis that follows because equation (4.3) can now be solved exactly using Fourier series in the simply supported rectangular configuration.

At $\hat{y} = 0$, the normal stress in the solid should match the local hydrodynamic pressure: $\sigma_{\hat{y}\hat{y}}|_{\hat{y}=0} = -p(\hat{z}) = -p(z)$ (due to $\hat{z} = z$). Since we seek a Fourier series solution for $\sigma_{\hat{y}\hat{y}}$, we must decompose this boundary condition into a (trivial) Fourier series:

$$\sigma_{\hat{y}\hat{y}}|_{\hat{y}=0} = -p(z)\sum_{m=1}^{\infty} A_m \sin\left[\kappa_m\left(x + \frac{w}{2}\right)\right], \tag{4.4}$$

where $\kappa_m = m\pi/w$ and $A_m = \frac{2}{m\pi}[1-(-1)^m]$, and it is easy to see that summation in (4.4) equals 1 for $x \in (-w/2, +w/2)$. Note, however, that the series converges to 0 at $x = \pm w/2$ because the odd extension has been used to construct the sine series, which causes the discontinuity at the two edges.

Next, the superposition principle comes into play. It is easily verified that

$$\phi_m(x,\hat{y}) = \sin\left[\kappa_m\left(x+\frac{w}{2}\right)\right]\left(C_1\mathrm{e}^{\kappa_m\hat{y}} + C_2\mathrm{e}^{-\kappa_m\hat{y}} + C_3\hat{y}\mathrm{e}^{\kappa_m\hat{y}} + C_4\hat{y}\mathrm{e}^{-\kappa_m\hat{y}}\right) \tag{4.5}$$

satisfies equation (4.3) for any integer $m = 1, 2, \ldots$. The corresponding stress state is

$$\begin{aligned}\sigma_{xx,m}(x,\hat{y}) = \sin\left[\kappa_m\left(x+\frac{w}{2}\right)\right]&\Big[C_1\kappa_m^2\mathrm{e}^{\kappa_m\hat{y}} + C_2\kappa_m^2\mathrm{e}^{-\kappa_m\hat{y}}\\ &+ C_3(2\kappa_m\mathrm{e}^{\kappa_m\hat{y}} + \mathrm{e}^{\kappa_m\hat{y}}) + C_4(-2\kappa_m\mathrm{e}^{-\kappa_m\hat{y}} + \kappa_m^2\hat{y}\mathrm{e}^{-\kappa_m\hat{y}})\Big],\end{aligned} \tag{4.6a}$$

$$\sigma_{\hat{y}\hat{y},m}(x,\hat{y}) = -\kappa_m^2\sin\left[\kappa_m\left(x+\frac{w}{2}\right)\right]\left(C_1\mathrm{e}^{\kappa_m\hat{y}} + C_2\mathrm{e}^{-\kappa_m\hat{y}} + C_3y\mathrm{e}^{\kappa_m\hat{y}} + C_4\hat{y}\mathrm{e}^{-\kappa_m\hat{y}}\right), \tag{4.6b}$$

$$\begin{aligned}\sigma_{x\hat{y},m}(x,\hat{y}) = -\kappa_m\cos\left[\kappa_m\left(x+\frac{w}{2}\right)\right]&\Big[C_1\kappa_m\mathrm{e}^{\kappa_m\hat{y}} - C_2\kappa_m\mathrm{e}^{-\kappa_m\hat{y}}\\ &+ C_3(\mathrm{e}^{\kappa_m\hat{y}} + \kappa_m\hat{y}\mathrm{e}^{\kappa_m\hat{y}}) + C_4(\mathrm{e}^{-\kappa_m\hat{y}} - \kappa_m\hat{y}\mathrm{e}^{-\kappa_m\hat{y}})\Big].\end{aligned} \tag{4.6c}$$

Four boundary conditions are needed to determine these coefficients. The stress continuity at the interface (equations $(4.7)_1$ and $(4.7)_2$) and the stress free conditions at the upper edge of the top wall (equations $(4.7)_3$ and $(4.7)_4$) require that

$$\sigma_{\hat{y}\hat{y},m}|_{\hat{y}=0} = A_m\sin\left[\kappa_m\left(x+\frac{w}{2}\right)\right], \quad \sigma_{x\hat{y},m}|_{\hat{y}=0} = 0, \quad \sigma_{\hat{y}\hat{y},m}|_{\hat{y}=d} = 0, \quad \sigma_{x\hat{y},m}|_{\hat{y}=d} = 0. \tag{4.7}$$

Imposing equations (4.7) on equations (4.6), we obtain

$$C_1 = -\frac{A_m(1+2\xi+2\xi^2-\mathrm{e}^{-2\xi})}{2\kappa_m^2(1+2\xi^2-\cosh 2\xi)}, \tag{4.8a}$$

$$C_2 = -\frac{A_m(1+2\xi\mathrm{e}^{-2\xi}-2\xi^2\mathrm{e}^{-2\xi}-\mathrm{e}^{-2\xi})}{\kappa_m^2[(\mathrm{e}^{-2\xi}-1)^2-4\xi^2\mathrm{e}^{-2\xi}]}, \tag{4.8b}$$

$$C_3 = \frac{A_m(1+2\xi-\mathrm{e}^{-2\xi})}{2\kappa_m(1+2\xi^2-\cosh 2\xi)}, \tag{4.8c}$$

$$C_4 = -\frac{A_m(1+2\xi\mathrm{e}^{-2\xi}-\mathrm{e}^{-2\xi})}{\kappa_m[(\mathrm{e}^{-2\xi}-1)^2-4\xi^2\mathrm{e}^{-2\xi}]}. \tag{4.8d}$$

Note the coefficients C_1, C_2, C_3 and C_4 are not fixed constants but vary with m and the thickness t via the definition $\xi = \kappa_m d = m\pi\gamma$. Finally, the solution to equation (4.3), as well as the three unique stress components, can be constructed by superposition:

$$\phi(x,\hat{y},z) = -p(z)\sum_{m=1}^{\infty}\phi_m(x,\hat{y}), \qquad \sigma_{xx}(x,\hat{y},z) = -p(z)\sum_{m=1}^{\infty}\sigma_{xx,m}(x,\hat{y}),$$
$$\sigma_{\hat{y}\hat{y}}(x,\hat{y},z) = -p(z)\sum_{m=1}^{\infty}\sigma_{\hat{y}\hat{y},m}(x,\hat{y}), \qquad \sigma_{x\hat{y}}(x,\hat{y},z) = -p(z)\sum_{m=1}^{\infty}\sigma_{x\hat{y},m}(x,\hat{y}). \tag{4.9}$$

4.3.3 Displacements at fluid–solid interface

Of course, the analysis above is only valid for small deformation gradients. In this regime, the stress–strain relations of linear elasticity [127] dictate that

$$\mathrm{e}_{xx,m} = \frac{\partial u^s_{x,m}}{\partial x} = \frac{1}{\bar{E}}\left(\sigma_{xx,m} - \bar{\nu}_s\sigma_{\hat{y}\hat{y},m}\right), \tag{4.10a}$$
$$\mathrm{e}_{\hat{y}\hat{y},m} = \frac{\partial u^s_{\hat{y},m}}{\partial \hat{y}} = \frac{1}{\bar{E}}\left(\sigma_{\hat{y}\hat{y},m} - \bar{\nu}_s\sigma_{xx,m}\right), \tag{4.10b}$$
$$\mathrm{e}_{x\hat{y},m} = \frac{1}{2}\left(\frac{\partial u^s_{\hat{y},m}}{\partial x} + \frac{\partial u^s_{x,m}}{\partial \hat{y}}\right) = \frac{1}{2G}\sigma_{x\hat{y},m}, \tag{4.10c}$$

where $G = E/[2(1+\nu_s)]$ is the shear modulus of elasticity, and $\bar{E}$ and $\bar{\nu}_s$ are related to the Young's modulus E and the Poisson's ratio ν_s by $\bar{E} = E/(1-\nu_s^2)$ and $\bar{\nu}_s = \nu_s/(1-\nu_s)$, respectively, because of the plane strain configuration considered herein [127].

Integrating equations (4.10a) and (4.10b), $u^s_{x,m}$ and $u^s_{\hat{y},m}$ are, respectively,

$$u_{x,m}(x,\hat{y}) = -\frac{1}{\bar{E}}\cos\left[\kappa_m\left(x+\frac{w}{2}\right)\right]\Big\{[-2C_4 + \kappa_m(1+\bar{\nu}_s)(C_2+C_4\hat{y})]\mathrm{e}^{-\kappa_m\hat{y}}$$
$$+ [2C_3 + \kappa_m(1+\bar{\nu}_s)(C_1+C_3\hat{y})]\mathrm{e}^{\kappa_m\hat{y}}\Big\} + f_2(\hat{y}), \tag{4.11a}$$
$$u_{\hat{y},m}(x,\hat{y}) = \frac{1}{\bar{E}}\sin\left[\kappa_m\left(x+\frac{w}{2}\right)\right]\Big\{[C_4(1-\bar{\nu}_s) + \kappa_m(1+\bar{\nu}_s)(C_2+C_4\hat{y})]\mathrm{e}^{-\kappa_m\hat{y}}$$
$$- [-C_3(1-\bar{\nu}_s) + \kappa_m(1+\bar{\nu}_s)(C_1+C_3\hat{y})]\mathrm{e}^{\kappa_m\hat{y}}\Big\} + f_1(x), \tag{4.11b}$$

where $f_1(x)$ and $f_2(\hat{y})$ are arbitrary functions of integration. Substituting equations (4.11a) and (4.11b) into equation (4.10c), we find

$$\frac{\partial f_1}{\partial x} + \frac{\partial f_2}{\partial \hat{y}} = 0. \tag{4.12}$$

From equation (4.12), it is easily concluded that both f_1 and f_2 should be constants. Since it is assumed that there are no vertical displacement at $x = \pm w/2$, $f_1 = 0$. According to the symmetry of the problem, i.e., $(\partial u_x^s/\partial x)|_{x=0} = 0$, $f_2 = 0$ as well.

Finally, the displacements are obtained by summing up all the $u_{x,m}$ and $u_{\hat{y},m}$ terms from equations (4.11):

$$u_x^s(x, \hat{y}, z) = -p(z) \sum_{m=1}^{\infty} u_{x,m}^s(x, \hat{y}), \qquad u_y^s(x, \hat{y}, z) = -p(z) \sum_{m=1}^{\infty} u_{\hat{y},m}^s(x, \hat{y}). \tag{4.13}$$

To obtain the fluid–solid interface deflection profile, $u_y(x, z)$, as well as the shape of the whole deformed cross-section, we simply take $\hat{y} = 0$ in equations (4.13). In order to evaluate the Fourier series numerically and generate the plots herein, we find that keeping 50 terms in the sum is sufficient.

However, in the large thickness case of interest herein, the above results can be further simplified because C_1 and C_3 are small compared to C_2 and C_4, respectively. As shown in figure 4.2, the dimensionless ratios C_1/C_2 and C_3/C_4 decrease very quickly with γ. Specifically, for $d/w \gtrsim 1$ (say, $d \simeq 1.5w$), C_1 and C_3 are negligible compared to C_2 and C_4. In this case, we can simply regard the stress-free boundary conditions in equations $(4.7)_3$ and $(4.7)_4$ as being satisfied at $\hat{y} = \infty$ instead of $\hat{y} = d$; hence, $C_1 = C_3 = 0$, $C_2 = -A_m/\kappa_m^2$ and $C_4 = -A_m/\kappa_m$. Then, the vertical displacement at the fluid–solid interface reduces to

$$u_y(x, z) = \frac{p(z)}{\bar{E}} \sum_{m=1}^{\infty} \frac{2A_m}{\kappa_m} \sin\left[\kappa_m \left(x + \frac{w}{2}\right)\right] \qquad (\gamma^2 = d^2/w^2 \to \infty). \tag{4.14}$$

The panel of figure 4.2 supports our observations. The interface profiles for the cases of $\gamma\delta = 1.5$ and $\gamma\delta = 2.0$ coincide with the curve predicted by equation (4.14). Also note that equation (4.14) is in the form of equation (3.3), with $(f)(x)$ solved as the right-hand side of equation (4.14) divided by $p(z)$.

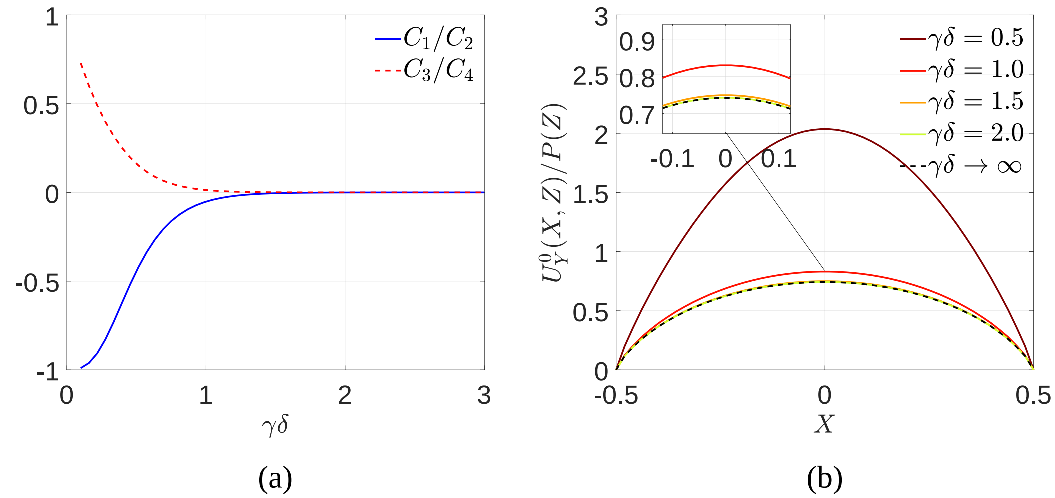

Figure 4.2. (a) Comparison of the coefficients from equations (4.8). (b) The fluid–solid interface deflection profile from equations $(4.13)_2$, (4.14) and (4.15) for different thickness-to-width ratios $\gamma\delta = t/w$. The magnified plot was generated using the script from [128].

It is easy to rewrite equation (4.14) in dimensionless form as

$$\frac{u_c \bar{E}}{w\mathcal{P}_c} U_Y(X,Z) = P(Z) \sum_{m=1}^{\infty} \frac{2A_m}{m\pi} \sin\left[m\pi\left(X+\frac{1}{2}\right)\right] = P(Z)F(X), \tag{4.15}$$

where, for convenience, we have denoted by F the function of X defined by the Fourier series. Now, the natural deformation scale is clearly $u_c = w\mathcal{P}_c/\bar{E}$, so that we can set the prefactor on the left-hand side of equation (4.15) to unity. This scale is similar to the one used in [12], where it was assumed $\langle u_y \rangle / w \sim p/E$. Note, however, that our analysis shows that $\bar{E} = E/(1-\nu_s^2)$ must be used in the deformation scale *instead* of E because the top wall in a long, shallow microchannel is in a plane strain configuration. Then, λ in equation (4.2) is finally determined to be $\lambda = u_c/h_0 = \mathcal{P}_c/(\bar{E}\delta)$.

We can see from equation (4.15) that the interface deflection profiles at different Z coordinates have the same shape, denoted by $F(X)$. It is easy to compute the maximum and average displacement at the interface from equation (4.15):

$$\max_X U_Y = F(0)P(Z) \approx 0.7426P(Z), \tag{4.16a}$$

$$\langle U_Y \rangle = P(Z) \int_{-1/2}^{+1/2} F(X)\mathrm{d}X \approx 0.5427P(Z) \approx 0.7311 \max_X U_Y. \tag{4.16b}$$

Note the prefactors here are different from previous studies, which either assumed a parabolic deformation profile of the fluid–solid interface, in which case $\langle U_Y \rangle = (2/3) \max_X U_Y$ [19], or obtained a quartic profile from plate theory with clamped boundary condition, in which case $\langle U_Y \rangle = (8/15) \max_X U_Y$ [31].

Observe that the simple support does not restrict the horizontal displacement (see equation $(4.13)_1$). Denoting the horizontal displacement at the fluid–solid interface by u_x, we can express this displacement in the large-thickness case as

$$u_x(x,z) = \frac{p(z)(1-\bar{\nu_s})}{\bar{E}} \sum_{m=1}^{\infty} \frac{A_m}{\kappa_m} \cos\left[\kappa_m \left(x + \frac{w}{2}\right)\right] \qquad (\gamma^2 = d^2/w^2 \to \infty). \tag{4.17}$$

Given that the typical Poisson ratio of PDMS is $\nu_s \approx 0.4$ to 0.5 [11], our theory predicts $u_x^0 \ll u_y^0$ since the ratio of the maximum value of these two displacements, from equations (4.15) and (4.17), is only $(1-\bar{\nu_s})/2 = (1-2\nu_s)/[2(1-\nu_s)]$. This result is consistent with experimental observations [12]. Interestingly, if we take the material of the top wall to be strictly incompressible with $\nu_s = 0.5$, the u_x is exactly zero, even though $u_x^s \neq 0$ for $\hat{y} > 0$. The latter is not important in the context of the present study because we focus on the fluid domain's shape inside the microchannel.

4.3.4 Summary and discussion of the solid mechanics results

To summarize, we have derived a mathematical expression for the fluid–solid interface deflection curve for the large thickness case. It should be clarified again that the thickness is considered "large" specifically when $1/\gamma^2 = (w/d)^2 \ll 1$. In this distinguished limit, we have shown that the top wall can be considered as a simply supported rectangle subject to uniform pressure at the bottom. Importantly, note the present thickness range includes but is wider than $w/d \ll 1$. For some cases with $w/d \simeq 1$, asymptotically, we can still satisfy $(w/d)^2 \ll 1$.

4.4 Hydrodynamic resistance of the compliant channel

Having solved for the leading-order velocity profile in section4.2 and the cross-sectional shape of the fluid–solid interface in section4.3.3, we are now in a position to solve the coupled fluid–structure interaction problem. Specifically, in the microfluidics context, of greatest interest is the *hydrodynamic resistance*, which characterizes the required pressure drop (i.e., force) to maintain steady flow at a given volumetric flow rate [2]. For fixed cross-sectional shapes, this quantity can be characterized for any number of shapes [129] using the ability to solve the Stokes equations for $Re = 0$ [130, section 2-5].

In a compliant channel, however, and the specific shape of the deformation profile in cross-section depends on the pressure itself. This results in a nonlinear relationship between the pressure drop and flow rate. We can determine this relation by directly calculating the flow rate under the deformed cross-section. On using equation (4.1) for $v_z(x, y, z)$, we obtain:

$$q = \int_{-w/2}^{+w/2} \int_{0}^{h(x,z)} v_z(x,y,z)\,\mathrm{d}y\,\mathrm{d}x = -\frac{1}{12\mu}\frac{\mathrm{d}p}{\mathrm{d}z}\int_{-w/2}^{+w/2} [h_0 + u_y(x,z)]^3\,\mathrm{d}x, \tag{4.18}$$

where $u_y(x, z)$ is given in equation (4.14) for the large-thickness case, and only the axial velocity component contributes to the flow rate at the leading order in the assumed small parameters. For a scenario with constant flow rate, equation (4.18) is a first-order differential equation for $p(z)$ given $q = const.$, which can be solved by assuming the outlet pressure sets the gauge, i.e., $p(\ell) = 0$.

In the large-thickness case, the self-similarity of the fluid–solid interface deflection profile makes it easy to solve equation (4.18) by separation of variables, yielding an implicit relation for the hydrodynamic pressure:

$$q = \frac{wh_0^3 p(z)}{12\mu(\ell - z)}\left[1 + \frac{3}{2}\mathcal{I}_1\left(\frac{wp(z)}{\bar{E}h_0}\right) + \mathcal{I}_2\left(\frac{wp(z)}{\bar{E}h_0}\right)^2 + \frac{1}{4}\mathcal{I}_3\left(\frac{wp(z)}{\bar{E}h_0}\right)^3\right], \tag{4.19}$$

where

$$\mathcal{I}_1 = \int_{-1/2}^{+1/2} F(X)\,\mathrm{d}X \ \approx 0.542742, \tag{4.20a}$$

$$\mathcal{I}_2 = \int_{-1/2}^{+1/2} F^2(X)\,\mathrm{d}X \approx 0.333333, \tag{4.20b}$$

$$\mathcal{I}_3 = \int_{-1/2}^{+1/2} F^3(X)\,\mathrm{d}X \approx 0.215834, \tag{4.20c}$$

and $F(X)$ is the self-similar deflection profile shared by every cross-section given in equation (4.15). The integrals in equations (4.20) are computed numerically using the trapezoidal with respect to 100 evenly-space integration points on $X \in [-1/2, +1/2]$. Observe that, while equation (4.19) has the same general structure (as already expected from [131]) as that arising from theories based on plate-like elastic top walls [31], the prefactors $\mathcal{I}_{1,2,3}$ related to the cross-sectional shape of the fluid–solid interface are *larger* by orders of magnitude.

Equation (4.19) can also be made dimensionless in the flow-rate-controlled regime as

$$Q = \frac{P(Z)}{12(1-Z)}\Big[1 + \frac{3}{2}\mathcal{I}_1\lambda P(Z) + \mathcal{I}_2\lambda^2 P^2(Z) + \frac{1}{4}\mathcal{I}_3\lambda^3 P^3(Z)\Big]. \tag{4.21}$$

Recall that we defined $\lambda = u_c/h_0 = \mathcal{P}_0/(\bar{E}\delta)$ so that $H(X,Z) = \lambda U_Y^0(X,Z)$. The dimensionless flow rate–total pressure drop relation is obtained by taking $Z = 0$ in equation (4.21). As the top wall deformation increases, i.e., for larger λ, the nonlinearity in the relation becomes more pronounced.

Finally, taking $z = 0$, the relation between the total pressure drop Δp and the volumetric flow rate q is obtained from (4.19):

$$q = \frac{wh_0^3\Delta p}{12\mu l}\left[1 + \frac{3}{2}\mathcal{I}_1\left(\frac{w\Delta p}{\bar{E}h_0}\right) + \mathcal{I}_2\left(\frac{w\Delta p}{\bar{E}h_0}\right)^2 + \frac{1}{4}\mathcal{I}_3\left(\frac{w\Delta p}{\bar{E}h_0}\right)^3\right]. \tag{4.22}$$

The important message is that with the consideration of the fluid–structure interaction in the microchannel, the flow rate and pressure drop relation deviates from the classic Poiseuille's law, which for a rectangular channel is $q = wh_0^3\Delta p/(12\mu l)$ (neglecting drag from the lateral sidewalls) [2], and displays nonlinearity. Although $\mathcal{I}_1 > \mathcal{I}_2 > \mathcal{I}_3$, it is important to emphasize that equation (4.22) is simply a polynomial, and *not* a perturbation series, in Δp.

4.5 Illustrated examples and validation

At the leading order in the small parameter ϵ, we have reduced the 3D deformation of the top wall to a 2D problem by considering each cross-section (in the (x, y) plane) as independent. Such decoupling is a natural consequence of the long and slender geometry and has also been shown asymptotically by Christov *et al.* [31] and numerically by Chakraborty *et al.* [13]. Based on this idea, various models, either with or without fitting parameters, have been put forward to account for the nonlinear flow rate–pressure drop relation. The very first one was from Gervais *et al.* [12] in the form of an implicit relation for the hydrodynamic pressure $p(z)$:

$$q = \frac{h_0^4 E}{48\alpha\mu(l-z)} \left\{ \left[1 + \alpha\frac{p(z)w}{Eh_0} \right]^4 - 1 \right\}, \tag{4.23}$$

where α came from the assumption $\langle u_y \rangle / h_0 = \alpha p(z)/(E\delta)$ for the thick top wall and has to be determined by fitting to experiments. Here $\langle u_y \rangle$ is the average interface deflection at each fixed-z cross-section. Even though this model has been employed in a lot of later works [26], [27], the unknown fitting parameter α is one of the biggest drawbacks. More recent work has focused on eliminating the fitting parameter, specifically for thinner top walls, plate theory [31], [33] or engineering pressure–displacement models [132] can be used [31], [33] to obtain the hydrodynamic resistance in the deformed microchannel.

Importantly, in the present study, our emphasis is on the thick top wall case, therefore our scaling is different from [28], [31], [33], wherein $\lambda = 12(w/d)^3\mathcal{P}_0/(\bar{E}\delta)$ was used. A prefactor $\propto (w/d)^3$ shows up in λ when the top wall is plate-like, i.e., $d \lesssim w$, which is a consequence of the assumed bending-dominated regime (and results in a very large value of λ for thick top walls). Nevertheless, these theories are self-consistent in that the coefficients in the flow rate–pressure drop relation (i.e., the counterpart of $\mathcal{I}_1$, $\mathcal{I}_2$ and $\mathcal{I}_3$ in equation (4.21) above) become much smaller to balance the large values of λ. However, in the large-thickness case, we have already shown that $\sigma_{xx} \sim 1/\gamma\delta^2$, meaning that the bending moment in the solid is actually

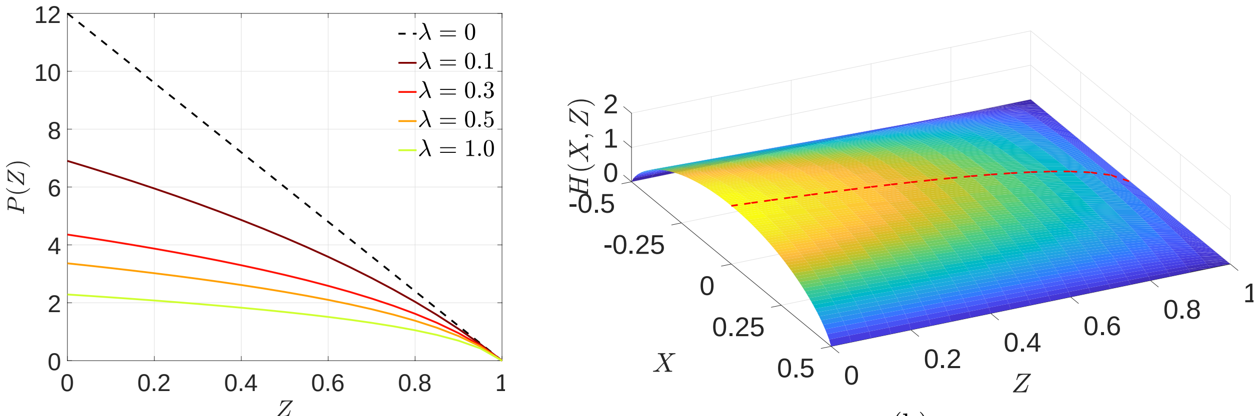

(a) (b)

Figure 4.3. (a) Pressure P as a function of the axial coordinate Z, computed by inverting equation (4.21), for different values of λ with $Q = 1$. (b) The deformed fluid–solid interface, $H(X, Z) = \lambda U_Y$, is computed from equation (4.15) with $P(Z)$ having been obtained from (4.21), for $Q = 1$ and $\lambda = 1$. The red dashed curve represents the maximum cross-sectional deflection of the interface.

negligible. This observation clearly shows that different solid deformation mechanisms are involved during FSI in microchannels with large versus small top wall thicknesses (compared to the width).

Next, we will give a systematic discussion of the predictions of our FSI theory for microchannels with thick top walls. At steady state, the flow rate $q = const.$, and each cross-section will inflate under the local pressure $p(z)$. The increase in area reduces the local fluid velocity, which introduces a non-constant pressure gradient along the flowwise z-direction. As shown in figure 4.3a for $\lambda = 0$ (i.e., when the channel is rigid), the pressure decreases linearly from the inlet to the outlet, and $\mathrm{d}P/\mathrm{d}Z$ is a constant in this case. However, as the top wall becomes softer, with the increase of λ, the $P(Z)$ profile deviates further from the linear profile, and $\mathrm{d}P/\mathrm{d}Z$ is a decreasing function of Z. Accordingly, based on equation (4.15), the maximum deflection at the fluid–solid interface, $H(0, Z)$, is expected to be concave, as illustrated in figures 4.3b and 4.4b.

Equation (4.21) is applicable in both the steady-state flow-rate-controlled and pressure-drop-controlled flows. As shown in figure 4.4a, with controlled flow rate, the total pressure drop is a linear function of flow rate for a rigid channel but a nonlinear function for a

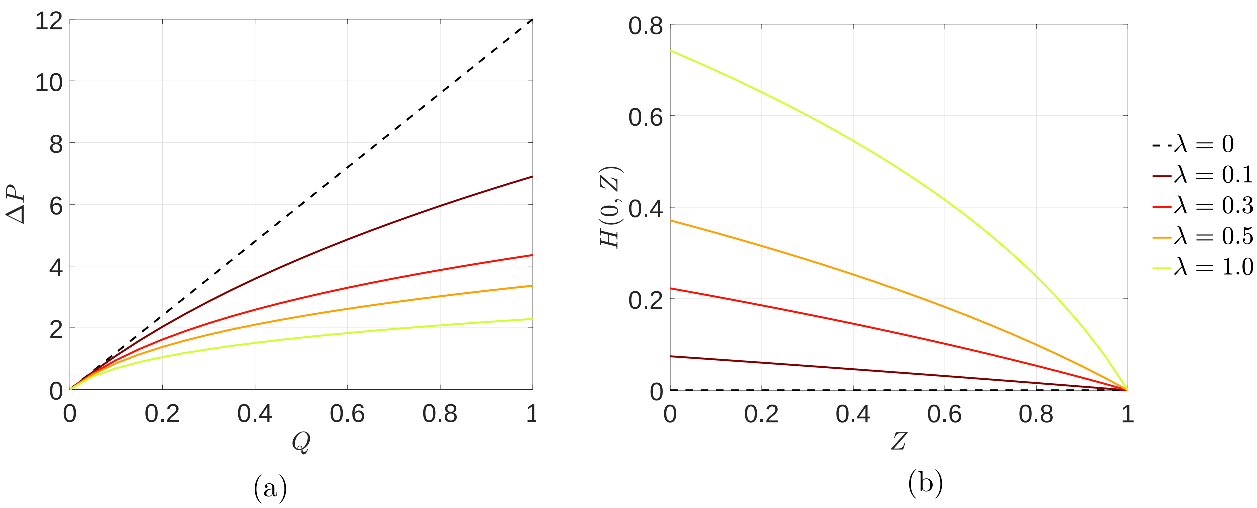

Figure 4.4. (a) Flow-rate-controlled regime: pressure drop across channel, computed using equation (4.21), as a function of Q, for different values of the compliance parameter λ. (b) Pressure-drop-controlled regime: The maximum (across the cross-section) interface deflection of the channel top wall as a function of the flowwise coordinate Z with $\Delta P = 1$; Q for different value of λ is computed via equation (4.21) evaluated at $Z = 1$, then $P(Z)$ is obtained by inverting the same equation. Substituting $P(Z)$ into equation (4.15), U_Y^0 is found, from which $H(X, Z) = \lambda U_Y$ and $\max_X H(X, Z) = H(0, Z)$ are calculated and plotted.

soft channel. Furthermore, the pressure drop decreases as the compliance of the channel increases because, under a fixed flow rate, the softer channel will deform more to reduce the flow velocity, and therefore, the pressure losses due to viscosity at each cross-section. In turn, for a pressure-drop controlled flow, the softer channel will allow a higher flow rate, as well as a larger deflection. As shown in figure 4.4b the maximum deflection at the fluid–solid interface also increases with λ, for a given pressure drop.

Next we compare our theory with previous experimental studies from the literature, namely [12], [28]. Apart from the model (4.23) proposed in [12], Gervais *et al.* performed experiment with microchannels with two different Young's moduli and two different widths. The important parameters are summarized in table 4.1. Note the thickness for experiment was reported to be larger than 6 mm, but it was numerically shown that 2 mm was thick enough for a sufficiently accurate comparison. Moreover, the undeformed height, h_0, for the case GEGJ 4 is corrected to 30 μm instead of the reported 26 μm based on the value of α.

We compute $1/\gamma^2$ in the last column of table 4.1 and show that our theory is applicable to all the four cases because $1/\gamma^2 \ll 1$ for all data sets. It is important to note that previous theory of microchannel FSI [31], [33] is not applicable, even as an approximation, to any of these cases.

Table 4.1. Values of physical parameters used in the experiments of Gervais *et al.* [12], where the Poisson ratio is $\nu_s = 0.5$, and the fluid's viscosity is $\mu = 0.001$ Pa·s for all the cases.

Case	h_0 [μm]	w [μm]	l [cm]	d [mm]	E [MPa]	δ [−]	ϵ [−]	γ [−]	$1/\gamma^2$ [−]
GEGJ 1 (▲)	26	250	1	2	2.2	0.1040	0.0026	8	0.0156
GEGJ 2 (■)	30	500	1	2	2.2	0.0600	0.0030	4	0.0625
GEGJ 3 (▲)	26	250	1	2	1.1	0.1040	8	76.92	0.0156
GEGJ 4 (■)	30	500	1	2	1.1	0.0600	4	66.67	0.0625

In figure 4.5, the flow rate–pressure drop relation curves predicted by equation (4.22) are shown to agree favorably with the experiments. The corresponding predicted maximum displacement at the interface is shown in figure 4.6. Although some deviations are observed, it is not easy for us to provide a definite reason as to why, due to the lack of information about experimental sources of error in [12]. In the cases GEGJ 2 and 4, there exists an almost constant shift from the experiment, which could be systematic error. For the cases GEGJ 1 and GEGJ 3, the pressure drops predicted by the theory at higher flow rates are larger than the experiments, which would indicate that the theory underestimates the channel deformation at higher flow rates. It is also relevant to note that the worst agreement in figure 4.5 is for case GEGJ 3, which exhibits the largest deformation in figure 4.6. Overall, the largest source of uncertainty, however, is the measurement of the undeformed channel height h_0. Indeed, one reason we have not included the maximum deformation data from [12] in figure 4.6 is that the error bars are too large to make a meaningful comparison. As we show in the next comparison with the experiments from [28], a small uncertainty in h_0 can lead to a large effect on the predicted pressure drop.

A further, quantitative, comparison between our theory and the fitting model (4.23) can be achieved by computing the values of the statistical coefficient of determination R^2 via

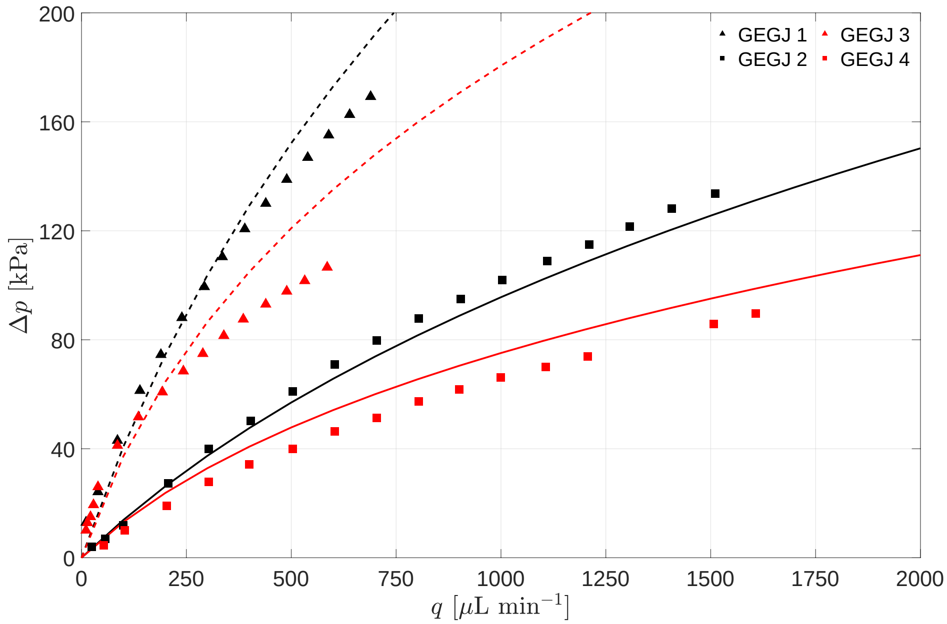

Figure 4.5. Comparison between our theory and the experimental data from [12] for the pressure drop Δp as a function of the flow rate q. The symbols represent the experimental data while the curves are the prediction from equation (4.22), without any fitting parameters. The black (dark) dashed and solid curves correspond to cases GEGJ 1 and GEGJ 2, respectively, while the red (light) curves correspond to GEGJ 3 and GEGJ 4, as described in table 4.1.

least squares [133] for each model, as shown in table 4.2. Unsurprisingly, the R^2 values of the model (4.23) are closer to 1 than those of the present theory because it is a one-parameter best-fit of the experimental data. Nevertheless, the present theory, without any fitting parameters, also give values of $R^2 \approx 1$, which means that the present fitting-parameter-free theory can capture the physics of the problem as accurately as a fitting model.

Table 4.2. The comparison of the values of R^2 between the present theory, equation (4.22), and the model in [12], denoted GEGJ fit (see equation (4.23)). The value of the fitting parameter α for each case is available in [12].

Case	GEGJ 1	GEGJ 2	GEGJ 3	GEGJ 4
Present theory	0.9633	0.9859	0.8904	0.9224
GEGJ fit	0.9904	0.9988	0.9792	0.9920

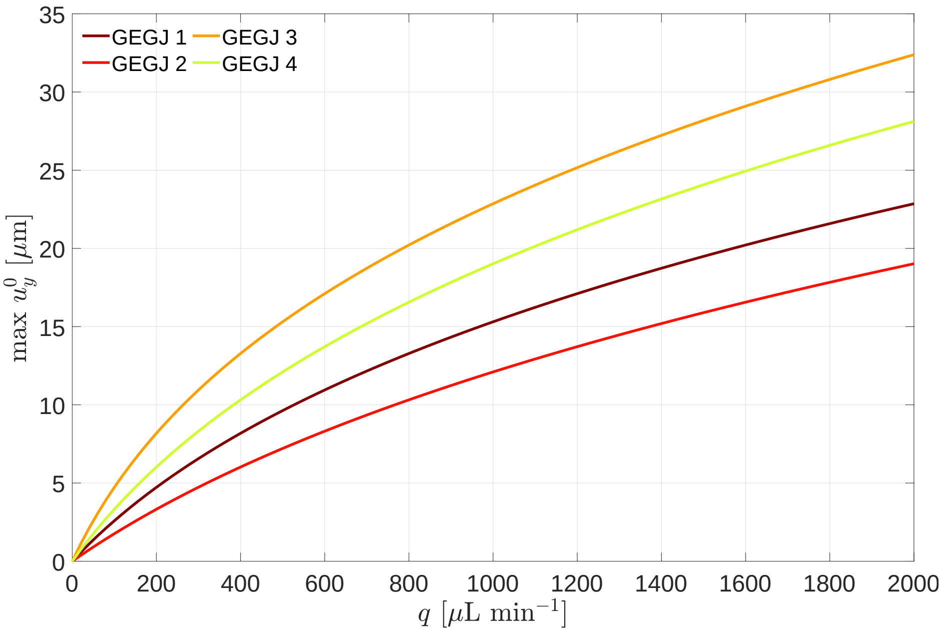

Figure 4.6. The maximum vertical displacement of the fluid–solid interface $\max u_y^0$ as a function of the flow rate q for the cases in table 4.1. The pressure drop is first computed by equation (4.22) and then substituted into equation (4.14) to obtain $\max u_y^0$ and plot it.

More recently, Raj *et al.* studied the hydrodynamic resistance in microchannels by varying the top wall thickness as well as the Young's modulus [28]. Six sets of experimental data were reported, with parameters summarized in table 4.3. A model based on the thick plate assumption was also proposed in [28]. Unfortunately, we have found that the model cannot explain the FSI because the top wall within the present thickness range cannot be regarded as the thick plate (recall section 4.3). In figure 4.7, we compare the flow rate–pressure drop relation from our theory to the experiments; once again, favorable agreement is observed. Note that equation (4.14) does not involve the thickness d, which is why only one prediction curve is obtained for all the three thicknesses used in these experiments. The shaded region represents the 5 μm uncertainty in the undeformed channel height reported in [28].

It is well known that microfluidic measurements are highly sensitive to the channel height because $\Delta p \sim \mu l q/(w h_0^3)$ in the lubrication limit [6]. Almost all the experimental data fall into the shaded region, showing that the present theory is able to give quantitative prediction of the hydrodynamic resistance, but perhaps the experiments in [28] were not accurate

Table 4.3. Values of the physical parameters used in the experiments of Raj *et al.* [28]. The microchannel is $w = 350$ μm wide, $l = 3$ cm long and $h_0 = 50 \pm 5$ μm in height. Based on the reported experimental conditions in [28], the fluid viscosity is taken to be $\mu = 9.110 \times 10^{-4}$ Pa·s, and the Poisson ratio is $\nu_s = 0.5$, for all the cases.

Case	t [mm]	E [MPa]	δ [$-$]	ϵ [$-$]	γ [$-$]	$1/\gamma^2$ [$-$]
RDC 1 (□)	2.0	2.801	0.1286–0.1571	0.0015–0.0018	5.7143	0.0306
RDC 2 (□)	1.0	2.801	0.1286–0.1571	0.0015–0.0018	2.8571	0.1225
RDC 3 (□)	0.5	2.801	0.1286–0.1571	0.0015–0.0018	1.4286	0.49
RDC 4 (○)	2.0	0.157	0.1286–0.1571	0.0015–0.0018	5.7143	0.0306
RDC 5 (○)	1.0	0.157	0.1286–0.1571	0.0015–0.0018	2.8571	0.1225
RDC 6 (○)	0.5	0.157	0.1286–0.1571	0.0015–0.0018	1.4286	0.49

enough to achieve their goal of addressing the effect of d/w. There are slight deviations in the cases RDC 3 and RDC 6 at large flow rates, which might be a consequence of the large elastic deformation in those cases. Also, these two cases have $1/\gamma^2 = 0.49$, thus they are already the least favorable ones from the point of view of the limits of applicability of the proposed theory, which requires $1/\gamma^2 \ll 1$. Overall, the agreement between the theoretical predictions and the experiments is quite satisfactory.

We also compare the maximum deflection of the fluid–solid interface at $z = 7.5$ mm, with $E = 0.157$ MPa, as a function of the flow rate. Figure 4.8 shows a comparison between the theoretical prediction and the experimental data from [28]. The agreement is best for the smaller flow rates. At larger flow rates, the experiment suggest that the deformation saturates, i.e., stops increasing, unlike the theoretical prediction. In this case, we believe that nonlinear elastic effects, which our linear elastic theory cannot capture, begin to dominate. Another two sets of experimental data for $z = 15$ mm and $z = 22.5$ mm were also provided in [28]. However, we believe that there are potentially some misprints in [28] because according to the previous discussions, the maximum displacement at the fluid–solid interface is expected to be a concave, instead of a convex, function of z (see figures 4.3b and 4.4b). Furthermore, in spite of the deviations of the interface deflection at large q, we find that the prediction of the hydrodynamic resistance is still good (see figure 4.7), which means that the flow rate–

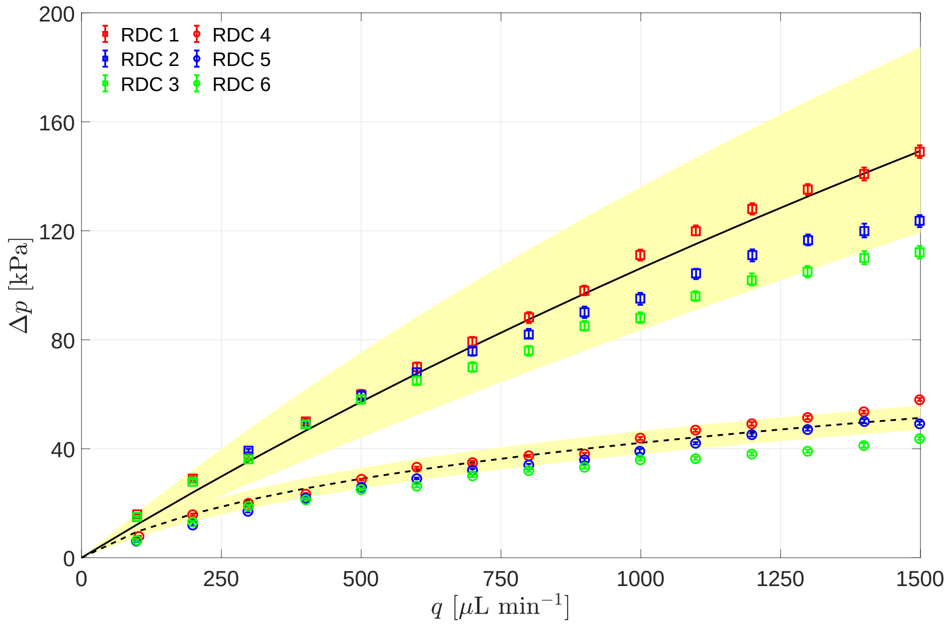

Figure 4.7. Comparison between our theory and the experimental data from [28] for the pressure drop Δp as a function of the flow rate q. The symbols represent the experimental data for the different cases described in table 4.3. The curves are the predictions from equation (4.22). The solid curve is for $E = 2.801$ MPa, while the dashed curve is for $E = 0.157$ MPa. The shaded region about each curve represents the uncertainty in Δp due to the reported uncertainty in the undeformed channel height (i.e., $h_0 = 50 \pm 5\mu$m).

pressure drop relation is not sensitive to discrepancies in the maximum deformation, and so it can be pushed to a larger range of flow rates than one might *a priori* expect.

4.6 Discussion

To this end, we have shown that our theory is able to capture the important physics of the steady-state fluid–structure interaction between a Newtonian fluid and a long and shallow microchannel with a thick compliant top wall. For the fluid mechanics, under the lubrication approximation, we appealed to the standard result that the axial velocity profile is parabolic in any cross-section, even if the cross-section varies (slowly) in the flowwise direction.

The more important discovery lies in the solid mechanics of the wall deformation. A scaling analysis of the elastostatics equations (3.2) for the solid showed that the stresses in the cross-sections perpendicular to the flowwise direction are dominant and, thus, the 3D

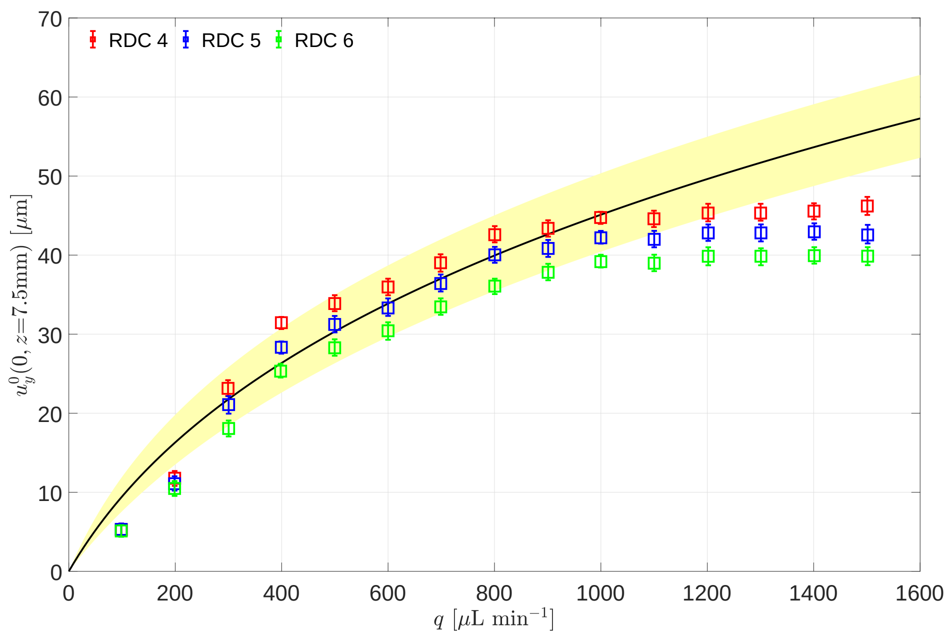

Figure 4.8. Comparisons of the maximum interface deflection $u_y(0, z)$ as a function of the flow rate q at the $z = 7.5$ mm cross-section with $E = 0.157$ MPa between our theory and the experimental data from [28]. The symbols represents the reported experimental data, as described in table 4.3, while the solid curve is the prediction from equation (4.14). The shaded region represents the uncertainty in Δp due to the reported uncertainty in undeformed channel height (i.e., $h_0 = 50 \pm 5$ μm).

solid mechanics problem is simplified to a 2D plane strain problem. Assuming small strains and using the linear theory of elasticity, we show that the top wall's thickness plays an important role in the stress distribution in solid and, accordingly, has a significant influence on the boundary conditions to be imposed at two lateral surfaces of the top wall. By requiring that width w and thickness t are such that $1/\gamma^2 = (w/d)^2 \ll 1$, also defined as the large-thickness case in the present study, the top wall deformation was decoupled in the flowwise direction, allowing us to treat it as a simply supported rectangle at each cross-section. This analysis yielded a self-similar deflection curve at the fluid–solid interface, when scaling the deformation by the pressure. Furthermore, the present analysis showed that the characteristic scale for the interface deformation for the thick-wall problem is independent of thickness as in [12] (but different from the plate-like problem [31], [33], [134]), specifically

$\mathcal{P}_0 w/\bar{E} = \mathcal{P}_c w(1-\nu_s^2)/E$, which is the expression from [12], $\mathcal{P}_c w/E$, corrected for a plane strain configuration.

Integrating the flow velocity at a cross-section, we obtained flow rate–pressure drop relation, which deviates from the Poiseuille's law because it nonlinearly depends on the compliance of the top wall. The results predicted by the present theory agree favorably with the previous experimental studies [12], [28]. While previous theoretical analyses [31], [33], [135], [136] have successfully addressed this type of fluid–structure interaction for thinner plate-like top walls with $d/w \lesssim 1$, the present theory is the first to quantify the hydrodynamic resistance in shallow compliant microchannels with *thick* top walls such that $(d/w)^2 \gg 1$.

The present theory is not only fitting-parameter-free but also directly solves for the fluid–solid interface deflection profile without assuming any specific shape. Our theory uncovers the physics hidden in the fitting parameter, α, of the widely used model (4.23), of which many *ad hoc* variations have been proposed [27], [28], [137]. The present analysis also provides a clear answer for why the previous plate-theory-based models [31], [33], [138] *cannot* be pushed to large-thickness regime (even qualitatively) by showing that the bending effects are trivial in the present model. The differences between these theories are also reflected by the different parameter dependencies of the dimensionless numbers quantifying compliance.

4.A Appendix: Moderate thicknesses and effect on the boundary conditions

Consider a configuration similar to that shown in figure 4.1 but the thickness of the top wall is not as large. (The side walls are still considered very thick, specifically infinite for the purposes of this discussion.) In this moderate-thickness case, the plane strain assumption is valid as long as the deformation is small enough, but the boundary conditions imposed at the sidewalls are not clear because σ_{xx} is not negligible. Specifically, it is not necessarily correct to impose the simply supported boundary conditions from section 4.3.2. At the same time, there is no good reason to impose clamped boundary conditions, as the previous studies on microchannels with thinner, plate-like walls [19], [31], [33], because for the geometry considered herein the side surfaces are allowed to deform, while they were assumed to be rigid in those previous studies.

To understand the type of support at the side walls in the moderate-thickness case, we start from the free body diagram in figure 4.9(b). Then, the reaction forces at the sidewalls are

$$T_s = p(z)h_0, \qquad N_s = \frac{1}{2}p(z)w, \qquad M_s = \frac{1}{2}p(z)(h_0^2 - wb), \tag{4.24}$$

where T_s, N_s, and M_s denote the tension, shear force and the moment respectively. Here b is introduced to represent the point of the reaction force at the bottom of the side solid. Since $h_0 \ll w$, we expect that $b \ll w$ due to stress concentration. Within the top wall, the resultant tension, T, shear force, N, and moment, M, are expected to scale as: $T \sim T_s$, $N \sim N_s$, $M \sim p(z)w^2/2 + M_s \sim p(z)w^2(1 + \delta^2 - b/w)/2 \sim p(z)w^2/2$. Hence, we neglect M_s in the following analysis.

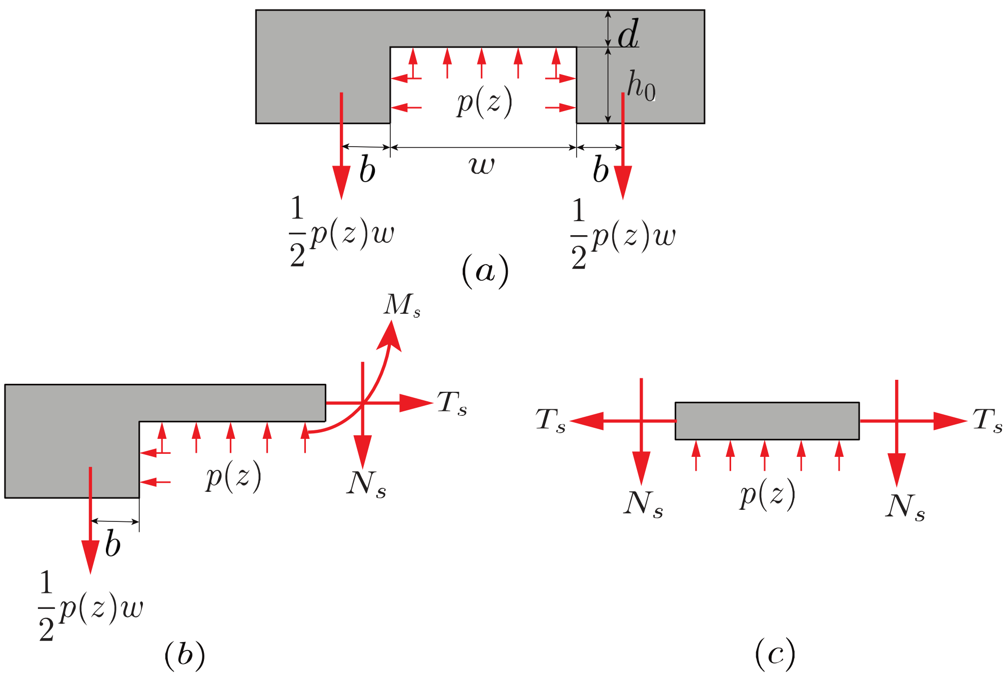

Figure 4.9. The force systems in the cross-section of the elastic solid's wall for moderate thickness.

Thus, we can consider the configuration from figure 4.9(c), a slender rectangle subject to pressure at the bottom, and shear and tension forces at the sidewalls. Note that the Airy stress function is still applicable in this case, but it is challenging to solve the corresponding biharmonic equation (4.3) with the inclusion of tension. Fortunately, the thinness of the structure makes Saint-Venant's principle applicable, which states that "a local force system has negligible effect on the stress distribution at distances that are large compared with the dimension of the surface where the forces are applied" [139]. Accordingly, the displacement field can be estimated based on a classic engineering model, without knowing the exact details of the stress distribution in solid. Thus, we regard the top wall as a simply supported beam with tension and solve for the displacement field by extending Timoshenko's beam theory.

Mechanical equilibrium requires that

$$\frac{\partial T}{\partial x} = 0, \tag{4.25a}$$

$$T\frac{\partial^2 u_y}{\partial x^2} + \frac{\partial N}{\partial x} + p(z) = 0, \tag{4.25b}$$

$$-\frac{\partial M}{\partial x} + N = 0, \tag{4.25c}$$

where u_y now represents the deflection of the mid-plane of the beam ($y = d/2$). The deformation at the fluid–solid interface is expected to be very close to that of the mid-plane due to the slenderness of the top wall. The corresponding constitutive relations are

$$M = -\bar{E}I\frac{\partial \varphi}{\partial x}, \tag{4.26a}$$

$$N = \kappa d G\left(-\varphi + \frac{\partial u_y}{\partial x}\right), \tag{4.26b}$$

where $I = d^3/12$ is the second area moment of the beam cross-section, φ represents the rotation of the normal of the cross-section, and κ is the shear correction factor [140]. Also recall that $\bar{E} = E/(1-\nu^2)$ is the modified Young's modulus and $G = E/[2(1+\nu)]$ is the shear modulus. As before, assuming zero displacement, as well as negligible moment at $x = \pm w/2$, the boundary conditions are

$$u_y|_{x=\pm w/2} = 0, \qquad M|_{x=\pm w/2} = 0. \tag{4.27}$$

Equation $(4.25)_1$ shows that the tension is constant in the cross-section, i.e., $T = T_s = p(z)h_0$. Then, equations (4.25) – (4.26) can be rewritten in terms of φ and made dimensionless:

$$\frac{\partial^4 \varphi}{\partial X^4} - \zeta P(Z)\left[\frac{\partial^2 \varphi}{\partial X^2} - \frac{(1+\bar{\nu})}{6\kappa}\left(\frac{d}{w}\right)^2 \frac{\partial^4 \varphi}{\partial X^4}\right] = 0. \tag{4.28}$$

Here the constant $\zeta = Tw^2/(\bar{E}I) = \mathcal{P}_c h_0 w^2/(\bar{E}I)$ has been introduced to quantify the tension effect. In equation (4.28), the first term represents the bending effect. The terms in the bracket represents the influence of tension, and the thickness effect is captured by the second term. Given the typical range of parameters for a microchannel, we conclude that the tension cannot be neglected here. Therefore, for the small thickness case, the top wall can no longer be regarded as a simply supported rectangle but, rather, it behaves like a beam with an immovable edge, i.e., simple support plus tension [120].

Soving equations (4.25) – (4.26), the vertical displacement of the mid-plane, which is also approximately the vertical displacement at the fluid–solid interface, is found to be

$$u_y(x,z) = \left[\frac{w^2}{4\mathfrak{u}^2(z)h_0} - \frac{(1+\bar{\nu})d^2}{6\kappa h_0}\right]\left\{\frac{\cosh\left[2\mathfrak{u}(z)x/w\right]}{\cosh \mathfrak{u}(z)} - 1\right\} - \frac{1}{2h_0}\left(x+\frac{w}{2}\right)\left(x-\frac{w}{2}\right), \tag{4.29}$$

where

$$\mathfrak{u}^2(z) = \frac{p(z)h_0 w^2}{4\bar{E}_Y I}\left[\frac{1}{p(z)h_0/(\kappa d G)+1}\right] = \frac{\zeta P(Z)}{4}\left[1 + \frac{(1+\bar{\nu})}{6\kappa}\left(\frac{d}{w}\right)^2 \zeta P(Z)\right]^{-1}. \tag{4.30}$$

If $(d/w)^2 \ll 1$, then $\mathfrak{u}^2(z) \approx \zeta P(Z)/4 = p(z)h_0 w^2/(4\bar{E}I)$ and the second term in the bracket in equation (4.29) also vanishes, then equation (4.29) is reduced to the Euler–Bernoulli beam with tension [120]. However, unlike equations $(4.13)_2$ and (4.14) of the large-thickness case, the deflection profile in equation (4.29) no longer displays self-similarity along the flow-wise direction because $p(z)$ cannot be factored out.

To get a sense of the tension effect, we compare this proposed moderate-thickness theory with other models in figure 4.10. Note that we compare $\delta H(X,Z)/P(Z)$, with $\delta H(X,Z) = h_0/w \times u_y(x,z)/h_0$, to show the magnitude of the deformation. For the applicability of linear elasticity, we expect that $\delta H(X,Z) \ll 1$. We can see that tension suppresses deformation,

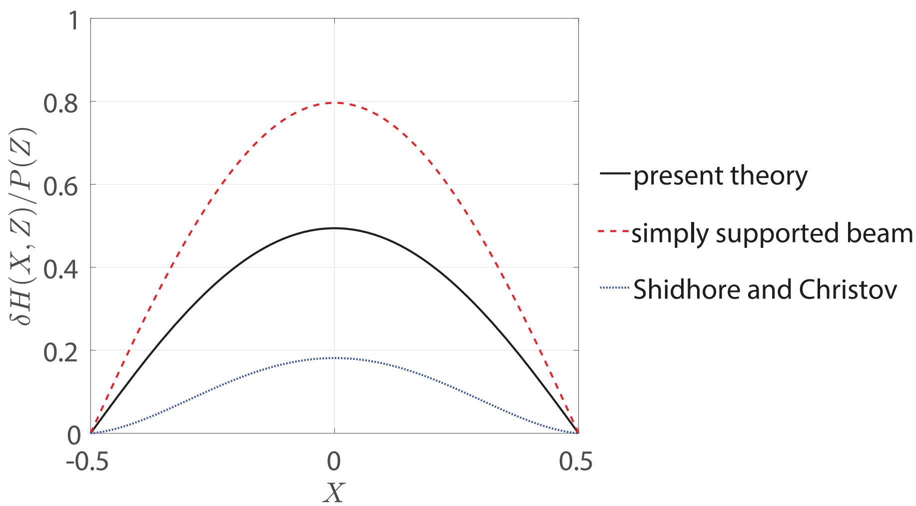

Figure 4.10. The cross-sectional deformation profile $\delta H(X,Z)/P(Z)$ versus X for a microchannel with $\delta = 0.1$ and $d/w = 0.1$ under a pressure drop such that $\zeta = 5$. The solid curve corresponds to equation (4.29). The dashed curve represents the deformation of a simply supported beam using equation $(4.13)_2$. For comparison, the dotted curve is the solution from Shidhore and Christov [33] for a clamped thick-plate-like wall.

compared to the case of simply supported beam. However, the tension is not as restrictive as the clamping considered in [33].

As before, the flow rate–pressure drop relation is obtained by integrating the axial fluid velocity across the cross-section. Then, we rewrite $p(z)$ as a function of $\mathfrak{u}(z)$, so that equation (4.18) can be written entirely in terms of $\mathfrak{u}$:

$$p(z) = \left[\frac{h_0 w^2}{4\bar{E}I\mathfrak{u}^2(z)} - \frac{\delta}{\kappa\gamma G}\right]^{-1} \quad \Rightarrow \quad q = -\frac{1}{12\mu}\frac{\mathrm{d}\mathfrak{u}}{\mathrm{d}z}\underbrace{\frac{\mathrm{d}p}{\mathrm{d}\mathfrak{u}}\int_{-w/2}^{+w/2}\left[h_0 + u_y(x,z)\right]^3 \mathrm{d}x}_{=\mathcal{R}(\mathfrak{u})}. \tag{4.31}$$

Using separation of variables, the solution of the last ODE can be expressed as a quadrature:

$$q = \frac{1}{12\mu(l-z)}\int_0^{\mathfrak{u}(z)} \mathcal{R}(\mathfrak{u}')\,\mathrm{d}\mathfrak{u}', \tag{4.32}$$

where $\mathfrak{u}'$ is a "dummy" integration variable. Unfortunately, this integral appears to require numerical evaluation.

5. REDUCED MODELS OF FINITE-REYNOLDS-NUMBER FLOWS THROUGH COMPLIANT RECTANGULAR MICROCHANNELS AT STEADY STATE

SUMMARY

In this chapter, we analyze Newtonian fluid flow in a rectangular duct with a soft top wall at steady state. The resulting fluid–structure interaction (FSI) is formulated for both vanishing and finite flow inertia. At the leading-order in the small aspect ratio, the lubrication approximation implies that the pressure only varies in the streamwise direction. Meanwhile, the compliant wall's slenderness makes the fluid–solid interface behave like a Winkler foundation, with the displacement fully determined by the local pressure. Coupling flow and deformation and averaging across the cross-section leads to a one-dimensional reduced model. In the case of vanishing flow inertia, an effective deformed channel height is defined rigorously to eliminate the spanwise dependence of the deformation. It is shown that a previously-used averaged height concept is an acceptable approximation. From the one-dimensional model, a friction factor and the corresponding Poiseuille number are derived. Unlike the rigid duct case, the Poiseuille number for a compliant duct is not constant but varies in the streamwise direction. Compliance can increase the Poiseuille number by a factor of up to four. The model for finite flow inertia is obtained by assuming a parabolic vertical variation of the streamwise velocity. To satisfy the displacement constraints along the edges of the channel, weak tension is introduced in the streamwise direction to regularize the Winkler-foundation-like model. Matched asymptotic solutions of the regularized model are derived.

The material in this chapter was published as [X. Wang, I.C. Christov, "Reduced models of unidirectional flows in compliant rectangular ducts at finite Reynolds number", *Phys. Fluids*, vol. 33, art. 102004, 2021] [114], reproduced with the permission of AIP Publishing. Both authors contributed to the analysis of the problem and the derivation of the mathematical model. X.W. wrote the Python script and conducted all the case studies and data analysis. X.W. and I.C.C. jointly discussed the results, drafted and revised the manuscript.

5.1 Preliminaries: review on dominant effects

In this chapter, we take a step back to investigate the steady FSIs in the common rectangular microchannel with a deformable top wall, as section introduced in figure 3.1 of chapter 3. On one hand, as discussed in section 3.2, owing to the slenderness and shallowness of the channel, *i.e.*, $h(x,z) \ll w \ll \ell$, the lubrication approximation applies. Specifically, the dimensionless incompressible Navier–Stokes equations at the leading order in ϵ are written as

$$\frac{\partial V_X}{\partial X} + \frac{\partial V_Y}{\partial Y} + \frac{\partial V_Z}{\partial Z} = 0, \tag{5.1a}$$

$$-\frac{\partial P}{\partial X} = 0, \tag{5.1b}$$

$$-\frac{\partial P}{\partial Y} = 0, \tag{5.1c}$$

$$\hat{R}\mathrm{e}\left(V_X\frac{\partial V_Z}{\partial X} + V_Y\frac{\partial V_Z}{\partial Y} + V_Z\frac{\partial V_Z}{\partial Z}\right) = -\frac{\partial P}{\partial Z} + \frac{\partial^2 V_Z}{\partial Y^2}. \tag{5.1d}$$

The important observation from above is that, up to a reduced Reynolds number of $\hat{R}\mathrm{e} \sim \mathcal{O}(1)$, equation (5.1b) and equation (5.1c) indicate that the flow pressure P is shown to vary along the flowwise direction Z only.

On the other hand, as shown in section 3.3, since the wall is made slender with $d \ll \ell$ and $w \ll \ell$, the 3D linear elasticity problem can be reduced to a 2D plane strain problem. Then, the displacement at the fluid–solid interface at different z locations is fully determined by the local pressure $p(z)$ at the leading order (in ϵ), like a Winkler foundation. The general solution has a general form of equation (3.3), from which we can write the dimensionless deformed channel height $H(X,Z)$ as

$$H(X,Z) = \frac{h_0 + u_y(x,z)}{h_0} = 1 + \lambda F(X)P(Z), \tag{5.2}$$

where $\lambda := \mathcal{U}_c/h_0$, with $\mathcal{U}_c$ being the characteristic displacement of the top wall, is a dimensionless group that captures the compliance the top wall. The spanwise profile $F(X)$ is obtained by solving the corresponding elasticity problem in the (X,Y) cross-section of the duct [31], [33], [34], [101]. Also, note that equation (5.2) is *not* an assumption but a consequence of the asymptotic reduction of the elasticity problem for a long and slender microchannel. Since the analysis in section 3.3 only involves balancing the momentum equation in the solid, it holds for any boundary conditions. However, the boundary conditions play a role in determining the actual deformation field, leading to different expressions for $F(X)$.

Also note that equation (5.2) takes the form of the deformation of a soft layer on a Winkler foundation [117], [118], but now the foundation's (dimensionless) "spring stiffness" is given by $\lambda F(X)$. Winkler-foundation-like relations between pressure and deformation arise in a number of soft lubrication problems [64], [65], including particles near elastic substrates [141], [142], slider bearings [143], and rollers [144].

We will show how to realize fluid–solid coupling in this chapter. The following discussion begins with the case of $\hat{R}\mathrm{e} \to 0$ (in section 5.2), *i.e.*, flow with negligible inertia. In this case, we consider two different mechanical responses of the compliant microchannel's wall, for which analytical solutions, based on the notion of a slowly-varying [145] unidirectional flow solution, are available in the literature [31], [33], [34], [101], [135], [136]. (It is important to note that, unlike the case of unidirectional flows in rigid ducts, the solutions discussed herein are *not* exact solutions of the incompressible Navier–Stokes equations [146].) For both types of mechanical response, the previous solutions yield a 3D model, in which the dimensionless axial flow profile $V_Z = V_Z(X, Y, Z)$ and the top wall shape $H = H(X, Z)$ are coupled via the hydrodynamic pressure $P(Z)$. Our goal here is to first construct and validate reduced 2D models by "removing" the X dependence in a suitably rigorous way, so that $H = H(Z)$ only. Upon accomplishing this reduction, averaging the 2D model over Y yields a 1D model in which $H = H(Z)$ and $P = P(Z)$ are the remaining dependent variables. Therefore, when we extend the model to account for $\hat{R}\mathrm{e} = \mathcal{O}(1)$ (in section 5.3), *i.e.*, to flow with moderate inertia, it suffices to consider just one reduced model (instead of each mechanical response individually).

5.2 Negligible fluid inertia: $\hat{R}\mathrm{e} \to 0$

5.2.1 Effective deformed channel height

As already derived in section 4.2, neglecting the inertia of the flow by taking $\hat{R}\mathrm{e} \to 0$ in equation (5.1d), we find that the axial velocity V_Z, subject to the no-slip boundary condition at the walls, has a parabolic variation along the height of the duct (Y-direction):

$$V_Z(X, Y, Z) = -\frac{1}{2}\frac{\mathrm{d}P}{\mathrm{d}Z} Y[H(X, Z) - Y]. \tag{5.3}$$

At steady state, the flow rate is

$$Q := \int_{-1/2}^{+1/2} \int_{0}^{H(X,Z)} V_Z(X, Y, Z)\, \mathrm{d}Y\, \mathrm{d}X = \mathit{const.}, \tag{5.4}$$

and thus the pressure gradient is found from equations (5.3) and (5.4) to be

$$-\frac{\mathrm{d}P}{\mathrm{d}Z} = \frac{12Q}{\int_{-1/2}^{+1/2} H^3(X, Z)\, \mathrm{d}X}. \tag{5.5}$$

Equation (5.5) can satisfy either one or two pressure boundary conditions (BCs). On the one hand, if the flow rate is controlled, then we can enforce $Q = q/q = 1$ (*i.e.*, take $\mathcal{P}_c = \mu q \ell/(w h_0^3)$ in the nondimensionalization) and set the outlet pressure to gauge, *i.e.*, $P(Z = 1) = 0$. On the other hand, if the pressure drop $\Delta P = P(Z = 0) - P(Z = 1)$ is controlled, then enforcing $P(0) = p(0)/\Delta p = 1$ (*i.e.*, taking $\mathcal{P}_c = \Delta p$ in the nondimensionalization) is now also a BC, in addition to $P(Z = 1) = 0$, from which Q is determined like an eigenvalue. Thus, in principle, the dimensionless flow rate Q and the dimensionless pressure drop ΔP are not independent [31], and we do not specify the flow regime *a priori* to make our results general. Either way, the pressure distribution in the duct can be determined by integrating equation (5.5) in Z, as long as the shape of fluid–solid interface, *i.e.*, $H(X, Z)$, is known.

Before we introduce expressions for $H(X,Z)$, recall that, in a wide rigid rectangular duct, the relation between the pressure gradient and the flow rate is set by a Poiseuille-like law [115]:

$$-\frac{\mathrm{d}p}{\mathrm{d}z} = \frac{12\mu q}{wh_0^3}. \tag{5.6}$$

Thus, for a clearer comparison, it is helpful to transform equation (5.5) back into the dimensional form as

$$-\frac{\mathrm{d}p}{\mathrm{d}z} = \frac{12\mu q}{\int_{-w/2}^{+w/2} h^3(x,z)\,\mathrm{d}x}. \tag{5.7}$$

In order to consistently rewrite equation (5.7) in the form of a Poiseuille-like law (5.6), we define the effective channel height as

$$h_\mathrm{e}(z) := \left[\frac{1}{w}\int_{-w/2}^{+w/2} h^3(x,z)\,\mathrm{d}x\right]^{1/3}. \tag{5.8}$$

Then, equation (5.7) can be rewritten as

$$-\frac{\mathrm{d}p}{\mathrm{d}z} = \frac{12\mu q}{wh_\mathrm{e}^3(z)}. \tag{5.9}$$

Note that the corresponding dimensionless effective channel height is

$$H_\mathrm{e}(Z) := \frac{h_\mathrm{e}(z)}{h_0} = \left[\int_{-1/2}^{+1/2} H^3(X,Z)\,\mathrm{d}X\right]^{1/3}. \tag{5.10}$$

Equation (5.9) can be viewed as a generalization of the Poiseuille-like law (for a wide rigid rectangular duct) to a variable-height microchannel. From another perspective, using the axially varying height $h_\mathrm{e}(z)$ in equation (5.9) eliminates the spanwise x-dependence of $h(x,z)$. Then, since the velocity was already averaged across the cross-section (to introduce q), the original 3D model has been reduced to an effective 1D model. Note that h_e is meaningful only when speaking of the relation between q and $\mathrm{d}p/\mathrm{d}z$, both of which only vary with z. This fact does *not* mean that the velocity field is also 1D (it still depends on *both* y and z, thus remaining 2D). The effective height concept will be used to evaluate the accuracy of previous empirically-motivated reduced-order models.

In particular, in the original studies using 1D models, such as those proposed in [12] and [26], the *average* deformed channel height

$$\bar{h}(z) := \frac{1}{w}\int_{-w/2}^{+w/2} h(x,z)\,\mathrm{d}x \tag{5.11}$$

is used in equation (5.9) instead of $h_\mathrm{e}(z)$. The corresponding dimensionless averaged channel height is

$$\bar{H}(Z) := \frac{\bar{h}}{h_0} = \int_{-1/2}^{+1/2} H(X,Z)\,\mathrm{d}X. \tag{5.12}$$

It should be clear, however, that $\bar{h}$ (or $\bar{H}$) from equation (5.11) (or equation (5.12)) is *not* equal to h_e (or H_e) from equation (5.8) (or equation (5.10)). Importantly, the averaging approach (introducing $\bar{h}$ instead of h_e) leads to an inconsistency in the reduced model because if we replace $h_\mathrm{e}^3(z)$ with $\bar{h}^3(z)$ in equation (5.9), then it is no longer equivalent to equation (5.7), which was rigorously derived by integrating the leading-order iNS (5.1a)–(5.1d). In the present work, our goal is to determine how this inconsistency affects the hydraulic predictions.

Substituting equation (5.2) into equations (5.10) and (5.12), respectively, we obtain explicit expressions for $H_\mathrm{e}(Z)$ and $\bar{H}(Z)$ as

$$H_\mathrm{e}(Z) = \Big[1 + 3\mathcal{I}_1\lambda P(Z) + 3\mathcal{I}_2\lambda^2 P^2(Z) + \mathcal{I}_3\lambda^3 P^3(Z)\Big]^{1/3}, \tag{5.13}$$

and

$$\bar{H}(Z) = 1 + \mathcal{I}_1\lambda P(Z). \tag{5.14}$$

Then, from equation (5.14) the now-constant (dimensionless) spring stiffness in the analogy to a Winkler foundation is $\beta = \mathcal{I}_1\lambda$. Here, the coefficients $\mathcal{I}_i$ are defined as

$$\mathcal{I}_i := \int_{-1/2}^{+1/2} F^i(X)\,\mathrm{d}X, \quad i = 1, 2, \dots. \tag{5.15}$$

Interestingly, observe that $\bar{H}$ in equation (5.14) is simply the one-term Taylor-series approximation of H_e from equation (5.13) in terms of $\lambda \ll 1$. However, our analysis does not require $\lambda \ll 1$, in fact $\lambda = \mathcal{O}(1)$ is possible. Linear elasticity only requires that $\lambda \ll 1/\delta$

(as discussed in [101] and [33]). Thus, we would like to determine if the approximation in going from equation (5.13) to equation (5.14) is a valid one.

5.2.2 Flow rate–pressure drop relation

To obtain the general form of the flow rate–pressure drop relation in a soft hydraulic conduit, we return to the dimensionless form of equation (5.5), namely:

$$-\frac{\mathrm{d}P}{\mathrm{d}Z} = \frac{12Q}{H_{\mathrm{e}}^3(Z)}. \tag{5.16}$$

Since $Q = const.$ in steady flow, upon substituting equation (5.13) into equation (5.16), we obtain a separable first-order ordinary differential equation (ODE) for $P(Z)$. The solution, subject to $P(1) = 0$, is

$$12Q(1-Z) = P(Z)\left[1 + \frac{3}{2}\mathcal{I}_1\lambda P(Z) + \mathcal{I}_2\lambda^2 P^2(Z) + \frac{1}{4}\mathcal{I}_3\lambda^3 P^3(Z)\right]. \tag{5.17}$$

As discussed in section 5.2.1, previous empirical studies used $\bar{H}$ in place of H_{e}. In this case, substituting equation (5.14) into equation (5.16), and solving the corresponding ODE, yields an explicit expression for the pressure distribution:

$$P(Z) = \frac{1}{\mathcal{I}_1\lambda}\left\{[48\mathcal{I}_1\lambda Q(1-Z) + 1]^{1/4} - 1\right\}. \tag{5.18}$$

As mentioned in section 5.2.1, we may either consider a flow-controlled situation, in which $Q = 1$ and $\Delta P = P(0)$ is found from implicitly from equation (5.17) or explicitly from equation (5.18). Meanwhile in the pressure-controlled regime, we enforce $P(0) = 1$ and compute Q directly:

$$Q = \frac{1}{48} \times \begin{cases} 4 + 6\mathcal{I}_1\lambda + 4\mathcal{I}_2\lambda^2 + \mathcal{I}_3\lambda^3, & \text{from (5.17)}, \\ \dfrac{1}{\mathcal{I}_1\lambda}\left[(\mathcal{I}_1\lambda + 1)^4 - 1\right], & \text{from (5.18)}. \end{cases} \tag{5.19}$$

Equation (5.18) is essentially the same model derived in [12]. However, in said work, $\mathcal{I}_1\lambda$ was taken as an unknown parameter, denoted as α, which was calibrated against experiments. However, our equation (5.18) is parameter-free because both λ and $\mathcal{I}_1$ are known from solving a suitable elasticity problem. Therefore, our approach eliminates the ambiguity, pointed out in [26], of what unknown dependencies "hide" in α.

Note, however, that even if equation (5.14) is the one-term Taylor-series approximation to (5.13), this is not true for the flow rate–pressure drop relations (5.18) and (5.17), respectively. Therefore, we must determine how well $P(Z)$ based on the averaged channel height approximates $P(Z)$ based on the effective channel height. It is reasonable to conjecture that, due to the restriction to small strains required by linear elasticity, the two expressions should be in close agreement. To substantiate this conjecture, we proceed to quantify the difference between equations (5.17) and (5.18) to obtain insight into the error committed in the formulation based on the averaged channel height. To this end, we apply the methodology established in this subsection to two types of common microchannel wall deformations considered in the literature: a microchannel with a thick top wall (section 5.2.3) and a microchannel with a thinner, plate-like top wall (section 5.2.4).

5.2.3 Illustrated example I: Duct with thick compliant top wall

First, we analyze the case of chapter 4, an initially rectangular duct with three compliant walls embedded in a thick soft structure. The corresponding steady 3D FSI problem was solved in chapter 4. To summarize their key conclusions: although a solution was obtained for any d/w, it was shown that, for $d/w \gtrsim 1.5$, the "thick" limit ($d^2/w^2 \gg 1$) is achieved and a simple analytical Fourier series solution can be written down for the deformed channel's top wall:

$$h(x,z) = h_0\left[1 + \frac{wp(z)}{\bar{E}h_0}\tilde{\mathfrak{f}}(x)\right], \tag{5.20}$$

$$\tilde{\mathfrak{f}}(x) = \sum_{m=1}^{\infty} \frac{2A_m}{m\pi} \sin\left[m\pi\left(\frac{x}{w} + \frac{1}{2}\right)\right], \tag{5.21}$$

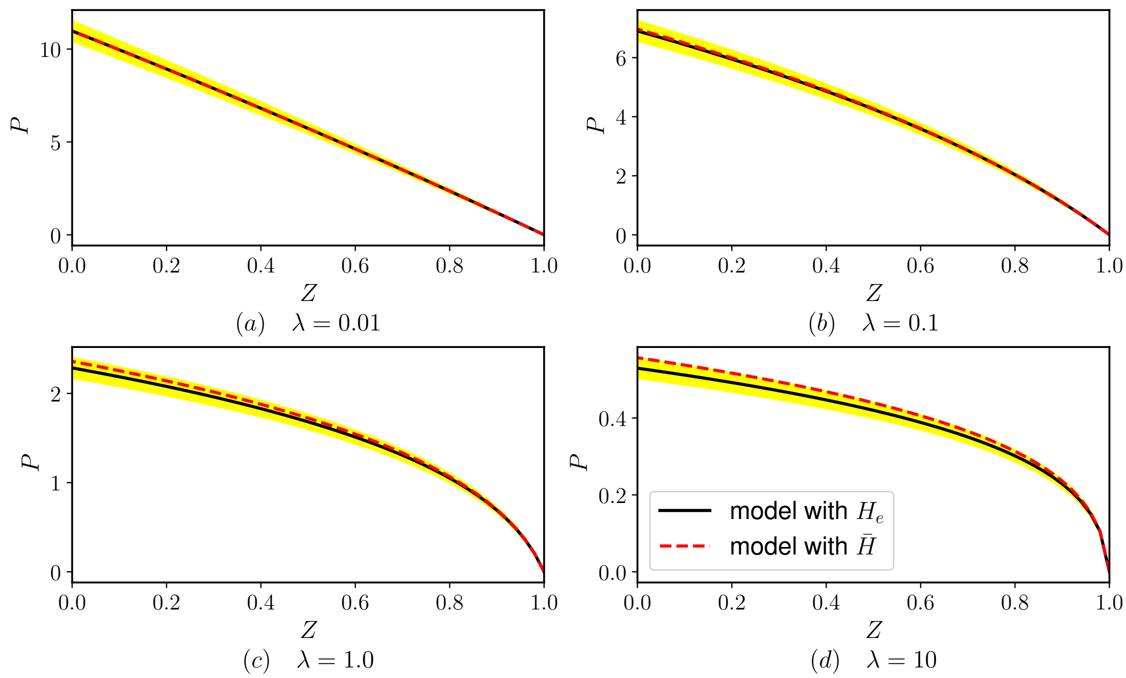

Figure 5.1. Thick top wall: Axial pressure distribution $P(Z)$ in a soft hydraulic conduit for $Q = 1$ and different λ: (a) $\lambda = 0.01$, (b) $\lambda = 0.1$, (c) $\lambda = 1.0$, and (d) $\lambda = 10$. The solid curve is computed from equation (5.17), in which the effective channel height (5.10) is employed, while the dashed curve is computed from equation (5.18), in which the averaged channel height (5.12) is employed. The shaded region represents $\pm 5\%$ of deviation from the solid curve, which is the baseline (or "truth") for this model.

where we have defined $A_m := \frac{2}{m\pi}[1-(-1)^m]$ and $\bar{E} := E/(1-\nu_s^2)$, with E being Young's modulus and ν_s the Poisson's ratio.

From equation (5.21), we can determine the function $F(X) \equiv F(x/w) = \widetilde{\mathfrak{f}}(x)$ introduced in equation (5.2). The corresponding values of $\mathcal{I}_i$, defined in equation (5.15), are computed in equation (4.20) and summarized as $\mathcal{I}_1 = 0.542754$, $\mathcal{I}_2 = 0.333333$ and $\mathcal{I}_3 = 0.215834$.

The compliance parameter λ emerges naturally from the nondimensionalization of equation (5.20):

$$\lambda = \frac{w\mathcal{P}_c}{h_0\bar{E}} = \begin{cases} \dfrac{\mu q \ell}{h_0^4 \bar{E}} & \text{(flow controlled)}, \\[2ex] \dfrac{w\Delta p}{h_0 \bar{E}} & \text{(pressure controlled)}. \end{cases} \tag{5.22}$$

Substituting λ and $\mathcal{I}_i$ into equation (5.17) and (5.18) respectively, we are ready to make a comparison between the two formulations. We observe that the pressure distribution depends nonlinearly upon λ, as illustrated in figure 5.1. The total pressure drop $\Delta P = P(0)$ decreases with λ, and a strong pressure gradient develops near the outlet. Notably, even with λ varying by three orders, the results computed with the two equation remain close to each other. The pressure distribution computed from equation (5.18), which employs the averaged channel height, is slightly higher than that from equation (5.17), which employs the effective channel height. However, the difference is no larger than 5% for almost the whole range of λ values considered. (The maximum deviation is found to be 5.14% in the case of $\lambda = 10$, which is pushing the limit of the applicability of the theory.) Having computed $P(Z)$, $H_\mathrm{e}(Z)$ and $\bar{H}(Z)$ can be found from equations (5.10) and (5.12), respectively. The largest deformed height is at the channel inlet (*i.e.*, at $Z = 0$), and we can expect the approximation of the effective channel height by the averaged one to be worst there. However, we determined that $\max_{0\le\lambda\le10} |H_\mathrm{e}(0) - \bar{H}(0)|/H_\mathrm{e}(0) < 5\%$, showing good agreement.

Now that the validity of the approximate prediction of the flow rate–pressure drop relation (5.18) has been established, it is worthwhile to provide a formula for the fitting parameter α introduced by Gervais *et al.* [12]. Recall the averaged channel height from the latter model is

$$\bar{h}(z) = h_0 \left[1 + \alpha \frac{wp(z)}{Eh_0}\right]. \tag{5.23}$$

For a clearer comparison, we transform equation (5.12) into its dimensional form:

$$\bar{h}(z) = h_0 \left[1 + \mathcal{I}_1(1-\nu_s^2)\frac{wp(z)}{Eh_0}\right]. \tag{5.24}$$

Then, comparing equations (5.23) and (5.24), it is readily recognized that

$$\alpha = \mathcal{I}_1(1-\nu_s^2) \approx 0.542754(1-\nu_s^2), \tag{5.25}$$

which we observe is a function of the Poisson's ratio, but no other material or geometric parameters related to the top wall, in this thick-wall limit ($d^2/w^2 \gg 1$). (This observation will be contrasted with the result in equation (5.32) below.) Furthermore, most microchannels are made from materials such as polydimethylsiloxane (PDMS) [4], [147], which is often considered a nearly incompressible material, *i.e.*, $\nu_s \approx 0.5$. Then, $\alpha \approx 0.4071$. A different solid mechanics model (and response) for the top wall would yield a different estimate of α (see section 5.2.4), showing that α is *not* a universal number that can be determined by a single set of experiments (even if this approach works for some set of geometries). Nevertheless, equation (5.25) provides a quantitative connection between the earlier scaling models [12] for flow-induced deformation and the later detailed elasticity calculations [101].

It is also relevant to mention that the results in this subsection also yield insight into the quality of approximation of another approach to the flow-induced deformation problem. For example, following [64], [65] and [141], in [63], the deformation at the fluid–solid interface of a thick-walled 2D duct was expressed as

$$h(z) = h_0 \left[1 + \frac{H_1 p(z)}{h_0 E_m}\right], \tag{5.26}$$

where the layer thickness H_1 and its "effective" Young's modulus E_m can be considered adjustable parameters. Such models have been found useful in analyzing the global inflation or relaxation time scale of a microchannel, which is relevant to the start-up problem and stop-flow lithography [61], [62]. In particular, H_1 represents the distance over which the vertical displacement varies, vanishing at $y = H_1$. Equation (5.26) is based on assuming no spanwise variation, reducing the flow and deformation problem to a 2D setting in the (y, z) plane, thus $h = h(z)$ *a forteriori* now (no averaging). The obvious question that arises is: what are suitable values of H_1 and E_m? As with equation (5.23), we simply compare equation (5.26) to (5.24) to obtain the answer. We conclude that

$$\frac{H_1}{E_m} = \mathcal{I}_1(1 - \nu_s^2)\frac{w}{E} \approx 0.542754(1 - \nu_s^2)\frac{w}{E}. \tag{5.27}$$

For example, if the 2D soft layer is taken to have the same elastic properties as the 3D one it approximates, $E_m = E$, then equation (5.27) provides its suitable thickness H_1 as a function of ν_s and w. Note that, separately, Essink *et al.* [148] surveyed a number of such two-dimensional elastohydrodynamic problems, while Chandler and Vella [149] critically addressed the 2D models' validity in the near-incompressible limit as $\nu_s \to 1/2^-$.

5.2.4 Illustrated Example II: Duct with plate-like compliant top wall

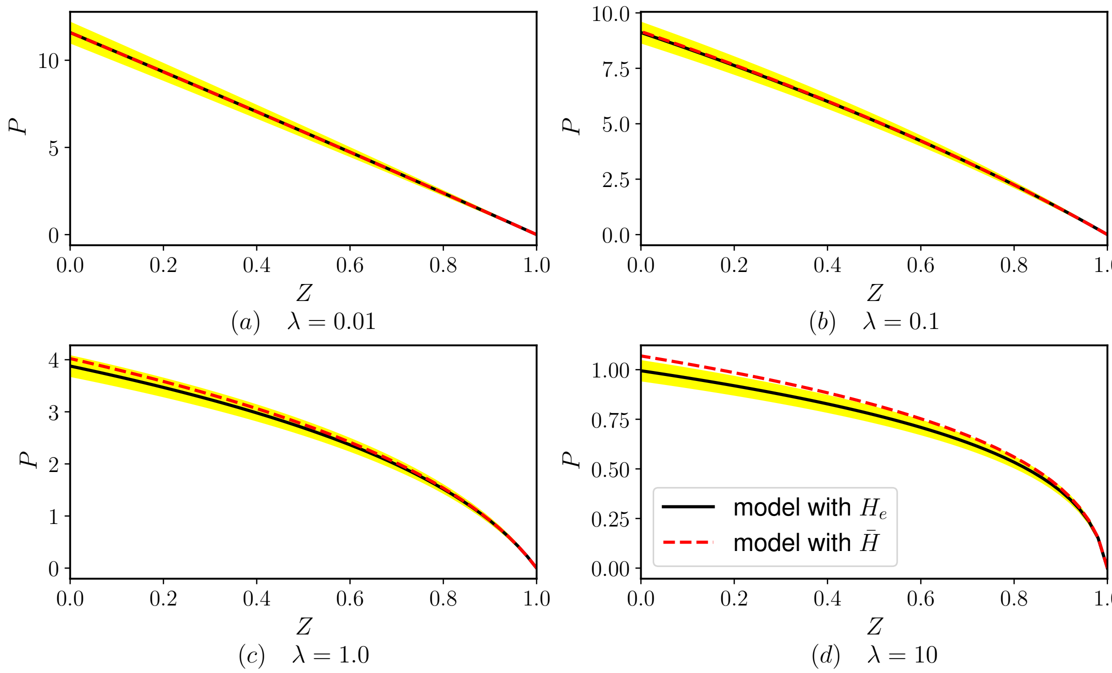

Figure 5.2. Plate-like top wall: Axial pressure distribution $P(Z)$ in a soft hydraulic conduit for $Q = 1$ and different λ: (a) $\lambda = 0.01$, (b) $\lambda = 0.1$, (c) $\lambda = 1.0$, and (d) $\lambda = 10$. The solid curve is computed from equation (5.17), in which the effective channel height (5.10) is employed, while the dashed curve is computed from equation (5.18), in which the averaged channel height (5.12) is employed. The shaded region represents $\pm 5\%$ of deviation from the solid curve, which is the baseline (or "truth") for this model. The top wall thickness-to-width ratio is $d/w = 0.5$.

Next, we analyze the case of a duct with a clamped thick-plate-like compliant top wall. As in section 5.2.3, the slenderness of the duct still results in the decoupling of the top wall deformation at each streamwise cross-section. However, the resulting shape of the

Table 5.1. Functional forms of the coefficients $\{\mathcal{I}_i\}_{i=1}^{3}$ defined by equation (5.15) for the plate-like-walled microchannel.

$\mathcal{I}_1$	$\frac{1}{30} + \frac{(d/w)^2}{3\kappa(1-\nu_s)}$
$\mathcal{I}_2$	$\frac{1}{630} + \frac{(d/w)^2}{35\kappa(1-\nu_s)} + \frac{2(d/w)^4}{15[\kappa(1-\nu_s)]^2}$
$\mathcal{I}_3$	$\frac{1}{12012} + \frac{(d/w)^2}{462\kappa(1-\nu_s)} + \frac{2(d/w)^4}{105[\kappa(1-\nu_s)]^2} + \frac{2(d/w)^6}{35[\kappa(1-\nu_s)]^3}$

deformed fluid–solid interface obtained by Shidhore and Christov [33] is quite different from equations (5.20)–(5.21). Specifically, now

$$h(x,z) = h_0\left[1 + \frac{w^4 p(z)}{24Bh_0}\tilde{\mathfrak{f}}(x)\right], \tag{5.28}$$

$$\tilde{\mathfrak{f}}(x) = \left[\frac{1}{4} - \left(\frac{x}{w}\right)^2\right]\left\{\frac{2(d/w)^2}{\kappa(1-\nu_s)} + \left[\frac{1}{4} - \left(\frac{x}{w}\right)^2\right]\right\}, \tag{5.29}$$

where $B = \bar{E}d^3/12$ is the plate's flexural rigidity [120], and κ is the "shear correction factor" [140]. For consistency with the theory of elasticity, $\kappa = 1$ should be imposed [150], but we leave it in the equations for the sake of completeness. The plate model considers bending deformation, as well as shear deformation, of the top wall, and it is applicable for $d \lesssim w$. If $d^2/w^2 \ll 1$, the first term in the inner curly brace in equation (5.29) is negligible, meaning the shear deformation is not important in this case. The model then reduces to the one derived earlier by Christov *et al.* [31], which only accounted for plate bending.

By making equation (5.28) dimensionless, we obtain

$$\lambda = \frac{w^4\mathcal{P}_c}{24h_0 B} = \begin{cases} \dfrac{\mu q w^3 \ell}{24h_0^4 B} & \text{(flow controlled)}, \\[2ex] \dfrac{w^4 \Delta p}{24h_0 B} & \text{(pressure controlled)}. \end{cases} \tag{5.30}$$

Again, we have $F(X) \equiv F(x/w) = \tilde{\mathfrak{f}}(x)$, but $\tilde{\mathfrak{f}}$ is now given by equation (5.29). Then, equation (5.28) takes the same form as equation (5.2). Next, the calculation of the $\mathcal{I}_i$ can be done explicitly for this case, yielding the functions of d/w, κ and ν_s summarized in table 5.1.

As in section5.2.3, we now substitute equation (5.30) into equations (5.10) and (5.12) respectively and compare the results. Figure 5.2 shows $P(Z)$ for different λ and $Q = 1$. The two formulations predict similar results. The error committed by replacing H_e with $\bar{H}$ is $< 8\%$. However, even with smaller or larger d/w ratios, the pressure distributions computed with each H expression do not differ much from each other. The maximum deviation is $< 9\%$. As in section 5.2.3, we computed the absolute difference between using $H_\mathrm{e}(0)$ and $\bar{H}(0)$, and found that $\max_{0\leq\lambda\leq 10} |H_\mathrm{e}(0) - \bar{H}(0)|/H_\mathrm{e}(0) < 5\%$.

Finally, we can also compare the model (5.18) (formulated with the averaged channel height) to equation (5.23) (the model derived by Gervais *et al.* [12]) to obtain an explicit expression for the fitting parameter α. Again, for convenience, we write the dimensional form of the averaged channel height as

$$\begin{aligned} \bar{h}(z) &= h_0 \left[1 + \mathcal{I}_1 \frac{w^4 p(z)}{24 B h_0}\right] \\ &= h_0 \left[1 + \mathcal{I}_1 \left(\frac{1-\nu_s^2}{2}\right) \left(\frac{w}{d}\right)^3 \frac{w p(z)}{E h_0}\right]. \end{aligned} \tag{5.31}$$

It follows, in this case, that

$$\begin{aligned} \alpha &= \mathcal{I}_1 \left(\frac{1-\nu_s^2}{2}\right) \left(\frac{w}{d}\right)^3 \\ &= \left(\frac{1-\nu_s^2}{60}\right) \left[\left(\frac{w}{d}\right)^3 + \frac{10}{\kappa(1-\nu_s)} \left(\frac{w}{d}\right)\right]. \end{aligned} \tag{5.32}$$

Observe that, unlike equation (5.25), α now depends upon w and d (with $w/d \gtrsim 1$), in addition to ν_s. The dependence on d, which equation (5.32) now quantitatively predicts, has been observed in experimental studies [26], [28].

5.2.5 A fiction factor for laminar flow in compliant ducts

Recently, it has been of interest to extend the textbook notion of a friction factor for various flows in microchannels. One idea is to take into account the shear-rate-dependent viscosity of non-Newtonian fluids [151]. Even for Newtonian fluids, updates are being sought to better understand (the previously considered "settled") wall roughness effects in both the laminar [152] and turbulent [153] portions of the Moody diagram (the visual representation of the friction factor [154]). A friction factor is needed for microfluidic system design [155], much like its use for analyzing pipe networks [156]. A frontier application is *microrheometry* [157], [158], in which an experimentally computed friction factor in a rectangular microchannel is compared to a theoretical value, in order to characterize the viscosity of a fluid [159]. An open problem in microrheometry [160] concerns whether measurements made in PDMS microchannels are affected by friction factor's implicit $\Delta p/E$ (or, in the present notation, λ) dependence. As the discussion above makes clear, the deformation of a compliant duct indeed changes the pressure drop characteristics. Thus, a salient application of our reduced-order flow and deformation model from section 5.2 is to interrogate the dependence of the friction factor on the elasticity-related parameters and variables.

To this end, we start from the reduced model with the averaged channel height as the effective channel height, *i.e.*, $h_\mathrm{e}(z) = \bar{h}(z) = h_0[1 + \eta p(z)]$. Note the compliance constant $\eta = \beta/\mathcal{P}_c$, with $\beta = \lambda\mathcal{I}_1$ being the dimensionless spring stiffness parameter introduced in section 5.2.1, is known from having solved a suitable solid mechanics problem. Then, from equation (5.18), we have

$$\eta p(z) = \beta P(Z) = [48\beta(1 - z/\ell) + 1]^{1/4} - 1, \tag{5.33}$$

where we have substituted $Q = 1$ and $Z = z/\ell$. Equation (5.33) indicates that ηp cannot be varied independently because it is fully determined by β. In the following discussion, we work with dimensional variables for convenience.

For $\hat{R}\mathrm{e} \to 0$, the pressure difference across an axial length of a duct is balanced by the viscous drag on the wall. Denote the area of the cross section as $a(z) = w\bar{h}(z)$, which takes into account the area change due to the deformation of the top wall. Then, the mean shear stress [115] can be written as

$$\begin{aligned}\bar{\tau}_w &= -\frac{1}{c_p}\left(\frac{\mathrm{d}p}{\mathrm{d}z}a + p\frac{\mathrm{d}a}{\mathrm{d}z}\right)\\ &= -\frac{wh_0}{c_p}\left(\frac{\mathrm{d}p}{\mathrm{d}z}(1+\eta p) + \eta p\frac{\mathrm{d}p}{\mathrm{d}z}\right)\\ &= \frac{D_{h_0}}{4}(1+2\eta p)\left(-\frac{\mathrm{d}p}{\mathrm{d}z}\right)\\ &= \frac{D_h}{4}\left(-\frac{\mathrm{d}p}{\mathrm{d}z}\right).\end{aligned} \tag{5.34}$$

Here, $c_p = 2(w+\bar{h})$ is the perimeter of the cross-section, and $c_p \approx 2(w+h_0)$ for $\bar{h} \ll w$. Additionally, $D_{h_0} = 4h_0w/[2(w+h_0)]$ is the *hydraulic diameter* of a rigid rectangular duct [115]. In the last equality in equation (5.34), we further defined the hydraulic diameter of the soft duct as

$$D_h := D_{h_0}(1+2\eta p), \tag{5.35}$$

where ηp captures the flow-induced deformation, meaning that D_h varies along the streamwise direction with p.

Next, consider the Fanning friction factor defined [115] as:

$$\begin{aligned}C_f &:= \frac{2\bar{\tau}_w}{\rho\bar{v}_z^2}\\ &= \frac{1}{2}D_h^2\left(-\frac{\mathrm{d}p}{\mathrm{d}z}\right)\left(\frac{\mu}{\rho\bar{v}_zD_h}\right)\left(\frac{1}{\mu\bar{v}_z}\right)\\ &= 6\left(\frac{D_h}{\bar{h}}\right)^2\frac{1}{Re_{D_h}},\end{aligned} \tag{5.36}$$

where we have substituted equation (5.9) with $h_\mathrm{e} = \bar{h}$ into the last step above. Also note that we have introduced the averaged velocity as $\bar{v}_z = q/(w\bar{h})$ and the hydraulic-diameter-based Reynolds number as

$$Re_{D_h} = \frac{\rho\bar{v}_zD_h}{\mu} = Re_{D_{h_0}}\left(1+\frac{\eta p}{1+\eta p}\right), \tag{5.37}$$

with $Re_{D_{h_0}} = \rho q D_{h_0}/(\mu w h_0)$ being the Reynolds number for the rigid rectangular duct.

Equation (5.36) has a form similar to the friction factor for a rigid rectangular duct. However, all of the three parameters, D_h, $\bar{h}$ and Re_{D_h}, depend on z due to FSI. To highlight this effect, we can re-write equation (5.36) as

$$C_f = \underbrace{6\left(\frac{D_{h_0}}{h_0}\right)^2 \frac{1}{Re_{D_{h_0}}}}_{\text{rigid duct } C_f} \left(1 + \frac{\eta p}{1+\eta p}\right). \tag{5.38}$$

The first term in equation (5.38) is C_f for a rigid rectangular duct, while the second term (in the parentheses) above captures the soft hydraulic effect. Furthermore, we can define the Poiseuille number as

$$Po := C_f Re_{D_h} = \underbrace{6\left(\frac{D_{h_0}}{h_0}\right)^2}_{\text{rigid duct } Po} \left(1 + \frac{\eta p}{1+\eta p}\right)^2. \tag{5.39}$$

We re-iterate that equation (5.39) is valid only for $h_0 \ll w$, and observe that the prefactor $6(D_{h_0}/h_0)^2 = 24$ for $h_0/w \to 0$. Furthermore, while $Po = const.$ in a non-circular *rigid* duct [115], Po from equation (5.39) becomes a function of z due to FSI. Further, the increase of the soft hydraulic Po is clearly demonstrated by the second term in the last parenthesis on the right-hand side of equation (5.39), which is bounded between 1 (as $\eta p \to 0$) and 4 (as $\eta p \to \infty$).

We highlight the novel dependence of Po on the compliance parameter ξ, beyond the usual geometric dependence on $(D_{h_0}/h_0)^2$, by plotting Po versus z/ℓ for given ξ, after eliminating ηp via equation (5.33). As predicted by equation (5.39), figure 5.3 shows that Po in a compliant duct is not a constant but rather a *decreasing* function along the streamwise direction (since $p(z)$ is as well). The shape is strongly influenced by the value of β, even if ultimately the correction factor due to compliance is bounded between 1 and 4.

5.3 Small but finite flow inertia: $\hat{Re} = \mathcal{O}(1)$

A feature of soft hydraulics problems is that the unidirectional flow solutions are derived under the lubrication approximation. As such, these solutions are *approximate* solutions

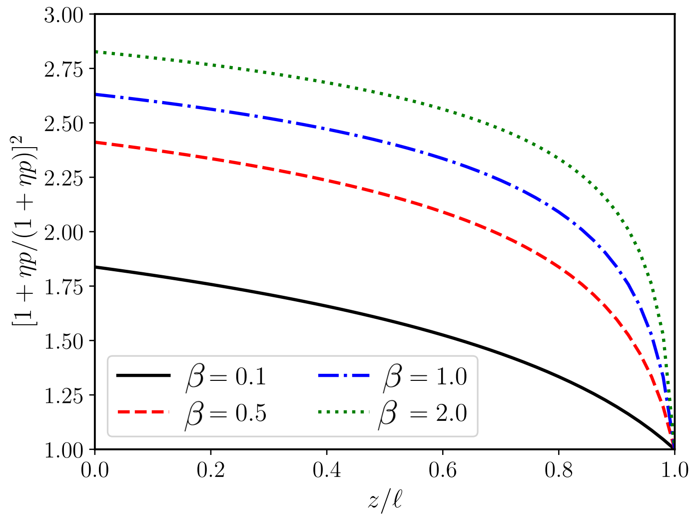

Figure 5.3. The variation of the reduced Poiseuille number, defined as $Po/(\text{rigid duct } Po) = [1 + \eta p/(1 + \eta p)]^2$ via equation (5.39), along the flow wise direction, z, for different β.

and, thus, are *not* valid for arbitrary Reynolds number, unlike classical unidirectional flow solutions in ducts [115]. Specifically, when the reduced Reynolds number, $\hat{R}\mathrm{e}$, is no longer vanishingly small, the inertial terms in equation (5.1d) are no longer negligible. However, equations (5.1b) and (5.1c) dictate that the pressure at each cross-section is still uniform at the leading order (in ϵ), hence we can still construct a 1D model relating the pressure $P(Z)$ to the flow rate Q.

Towards this end, as before, we can either introduce $H_\mathrm{e}(Z)$, by enforcing a Poiseuille-like law (5.16), or introduce the averaged channel height $\bar{H}(Z)$ as an approximation to $H_\mathrm{e}(Z)$ in the same relation. As shown in section 5.2 for $\hat{R}\mathrm{e} \to 0$, using $\bar{H}$ in place of H_e commits a controllable error, and both approaches lead to similar results (as long as the deformation gradient is small). Instead of treating both cases for $\hat{R}\mathrm{e} = \mathcal{O}(1)$, we refer the reader to the work by Wang and Christov [161], who implemented the calculation based on $H_\mathrm{e}(Z)$. In this section, we construct a 1D model using $\bar{H}(Z)$.

5.3.1 Pressure distribution using an averaged deformed channel height

To accomplish this task, the von Kármán–Pohlhausen approximation (see §4-6.5 of White's book [115]) is employed to enforce a shape of the streamwise velocity profile, V_Z^{2D}, so that the flow rate in the deformed fluid domain can be obtained [72], [86], [102]. That is, we assume a dimensionless parabolic axial velocity profile V_Z^{2D}, which is related to the dimensionless volumetric flow rate Q, as

$$V_Z^{2D}(Y, Z) = \frac{6QY[\bar{H}(Z) - Y]}{\bar{H}^3(Z)}. \tag{5.40}$$

As discussed in the section 5.2, a profile as in equation (5.40) is dictated by the Navier–Stokes equations for $\hat{R}\mathrm{e} \to 0$ (lubrication flow), and is generally valid for laminar flows [115]. An implicit assumption for using the velocity profile (5.40) for finite $\hat{R}\mathrm{e}$ is that flow inertia is weak: streamlines remain parallel and no recirculation occurs. Of course, this means that the theory developed herein is not valid in regimes in which transitional or turbulent flows occur. Indeed, the target application of our study is microfluidics, in which turbulent flows are not expected (or, generally possible) [2], [6], although laminar flow with $\hat{R}\mathrm{e} = \mathcal{O}(1)$ can be achieved [40], [162], [163].

Substituting equation (5.40) into equation (5.1d) and integrating over $Y \in [0, \bar{H}(Z)]$, we obtain

$$\frac{6}{5}\hat{R}\mathrm{e}\frac{\mathrm{d}}{\mathrm{d}Z}\left[\frac{Q^2}{\bar{H}(Z)}\right] = -\frac{\mathrm{d}P}{\mathrm{d}Z}\bar{H}(Z) - \frac{12Q}{\bar{H}^2(Z)}. \tag{5.41}$$

Observe that this expression, based on an equivalent 2D flow with $\bar{H}$ as the effective channel height, does not depend (or require integration) over X. It should be noted that in the thin films literature [164], [165] inertial corrections to lubrication theory are also formulated, going to higher orders. Instead of assuming a parabolic velocity profile as in equation (5.41), a polynomial is used, and the coefficients are determined by incorporating the cross-sectional momentum equations, with their relevant boundary conditions, as well as the necessary corrections to the pressure. This approach is beyond the scope of the present work, however, as we consider wide channels ($\delta \ll 1$), and there is no cross-sectional flow components (V_X or V_Y) at the leading order [31] in δ and ϵ.

Next, substituting $\bar{H}$ from equation (5.14) into equation (5.41), we once again obtain a separable first-order ODE for $P(Z)$. Imposing the outlet BC, $P(1) = 0$, equation (5.41) integrates to

$$P(Z) + \frac{3}{2}\beta P^2(Z) + \beta^2 P^3(Z) + \frac{1}{4}\beta^3 P^4(Z) - \frac{6}{5}\hat{R}\mathrm{e}\beta Q^2 P(Z) = 12Q(1 - Z), \tag{5.42}$$

where $\beta = \lambda\mathcal{I}_1$ as above. As before, in the flow-controlled regime, $Q = 1$, and ΔP is found implicitly from equation (5.42). Meanwhile, in the the pressure-controlled regime, after enforcing $P(0) = 1$, equation (5.42) becomes a quadratic in Q, and it has only one positive root:

$$Q = \sqrt{\frac{25}{\hat{R}\mathrm{e}^2\beta^2} + \frac{5}{24\hat{R}\mathrm{e}\beta}\left(4 + 6\beta + 4\beta^2 + \beta^3\right)} - \frac{5}{\hat{R}\mathrm{e}\beta}. \tag{5.43}$$

This expression generalizes equation (5.19) and shows the dependence on $\hat{R}\mathrm{e}$ explicitly in the inertial flow.

Since equation (5.42) is a polynomial in P, we can invert it to find the pressure distribution in the duct. Importantly, we expect $\mathrm{d}P/\mathrm{d}Z < 0$ strictly for all $X \in [0, 1]$ because of the assumption of laminar flow. Since $P(1) = 0$, then $P(Z) > 0$ for all $Z \in [0, 1)$, which actually imposes an upper bound on the allowed values of $\hat{R}\mathrm{e}$ and λ. To prove this bound, the leading-order term of the left-hand side of equation (5.42) is calculated to be $(1 - 6\hat{R}\mathrm{e}\beta Q^2/5)P$, as $Z \to 1^-$, while the right-hand side is positive. To ensure $P(Z) > 0$ as $Z \to 1^-$, we must require that

$$\hat{R}\mathrm{e}\lambda < \frac{5}{6\mathcal{I}_1 Q^2}. \tag{5.44}$$

Note that $\mathcal{I}_1$ is set by the solution of the corresponding elasticity problem.

5.3.2 An extension and regularization via weak tension

At first glance, the restriction (5.44) might be puzzling, but it actually ensures a continuous, and thus physical, pressure distribution and wall deformation at the leading order. Since the local deformed height is linearly proportional to the local pressure at the leading order, prominent local deformation can be expected for sufficiently inertial flows and/or sufficiently compliant ducts. In the case for which the restriction (5.44) is violated, the local deformation can be so large that it cannot transition smoothly near to zero at the outlet (to satisfy the boundary condition $P(1) = 0$, equivalently $\bar{H}(1) = 1$). Thus, the solution (5.42) breaks down for $\hat{Re}$ that violate the restriction (5.44).

In deriving equation (5.42), we used equation (5.14), which is a leading-order solution (in ϵ) based on a plane strain configuration of the elastic wall's deformation field. This solution does not take into account the reaction forces imposed by connectors at the inlet and outlet of the duct. In this sense, we can think of the solid mechanics problem as being essentially a boundary layer problem. The Winkler-foundation-like mechanism (equation (5.14)) is dominant outside the boundary layers, while some other mechanism plays a role within thin (boundary) layers near $Z = 0, 1$ to regularize the problem and account for the fact that the displacements in the vicinity of the inlet (or outlet) of the channel are usually restricted by external connections.

Since the bulging of the top wall unavoidably introduces stretching along Z in the solid, a simple extension of equation (5.14), which can circumvent the restriction (5.44), can be achieved by introducing weak constant tension into the formulation [73]. Note the tension has to be "weak" to ensure the dominance of the Winkler-foundation-like mechanism. Other regularization mechanisms are also possible. For example, in the setting of elastic structures on top of thin fluid films, Peng and Lister [166] considered bending and gravity in addition to tension as regularization mechanisms. However, weak tension is arguably the simplest mechanism related to microchannels.

Then, we may write down a governing equation for the deformed channel height:

$$-\theta_t \frac{\mathrm{d}^2 \bar{H}}{\mathrm{d}Z^2} + \bar{H} - 1 = \beta P. \tag{5.45}$$

As motivated above, the dimensionless tension parameter $\theta_t \ll 1$. In this way, equation (5.14) is precisely the outer solution of equation (5.45) with $\theta_t = 0$. To give a physical expression for θ_t^2, we transform equation (5.45) back into dimensional form:

$$\chi_t \frac{\mathrm{d}^2 \bar{h}}{\mathrm{d}z^2} + k(\bar{h} - h_0) = p(z), \tag{5.46}$$

where χ_t denotes the constant tension force per unit width ($\mathrm{N\,m^{-1}}$), and $k = \mathcal{P}_c/(\beta h_0)$ is the *effective* stiffness of the interface ($\mathrm{Pa\,m^{-1}}$). Then, clearly, $\theta_t^2 = \beta\chi_t h_0/(\mathcal{P}_c \ell^2)$. We postpone the modeling of χ_t until chapter 6.

Next, taking $\mathrm{d}/\mathrm{d}Z$ of both sides of equation (5.45) and substituting into equation (5.41), we obtain a nonlinear ODE for $\bar{H}(Z)$:

$$\frac{3}{5}\hat{R}\mathrm{e}\frac{\mathrm{d}}{\mathrm{d}Z}\left(\frac{Q^2}{\bar{H}^2}\right) = \frac{1}{\beta}\left(\theta_t \frac{\mathrm{d}^3\bar{H}}{\mathrm{d}Z^3} - \frac{\mathrm{d}\bar{H}}{\mathrm{d}Z}\right) - \frac{12Q}{\bar{H}^3}. \tag{5.47}$$

At the inlet and outlet, the top wall is restricted from moving, so the BCs for equation (5.47) are

$$\bar{H}(0) = \bar{H}(1) = 1, \tag{5.48}$$

$$\left.\frac{\mathrm{d}^2\bar{H}}{\mathrm{d}Z^2}\right|_{Z=1} = 0, \tag{5.49}$$

where the BC (5.49) is a restatement of the outlet BC $P(1) = 0$ in terms of $\bar{H}$ using equations (5.45) and (5.48). Equations (5.47), (5.48) and (5.49) constitute a nonlinear *two-point boundary-value problem* [167]. As before, in the flow-controlled situation, $Q = 1$ and equation (5.47) can be solved for $\bar{H}(Z)$ subject to the BCs (5.48)–(5.49). In the pressure-controlled situation, Q is found as an eigenvalue after imposing $P(0) = 1$ on equations (5.47), (5.48) and (5.49).

Now, the restriction (5.44) can be relaxed in the context of equation (5.47), in which the weak tension tends to restrain the wall deformation and, thus, regularizes the problem. Of course, the extent of regularization depends on the value of θ_t. For example, if $\lambda = 1.0$ and $\mathcal{I}_1 = 0.542754$ (for the thick-walled microchannel), then the upper bound of validity of the model is $\hat{R}\mathrm{e} \approx 1.5$ for $\theta_t = 0$. However, if $\theta_t = 10^{-4}$, equation (5.47) can be solved up to $\hat{R}\mathrm{e} \approx 2.0$. If θ_t is further increased to 10^{-3}, then equation (5.47) can be solved up to $\hat{R}\mathrm{e} \approx 3.0$. For such a large value of $\hat{R}\mathrm{e}$, one can interpret the breakdown of equation (5.47) as the breakdown of the lubrication theory and, potentially, as a sign that the "full" iNS equations need to be solved instead. Next, we illustrate these observations and explain how equation (5.47) was solved numerically.

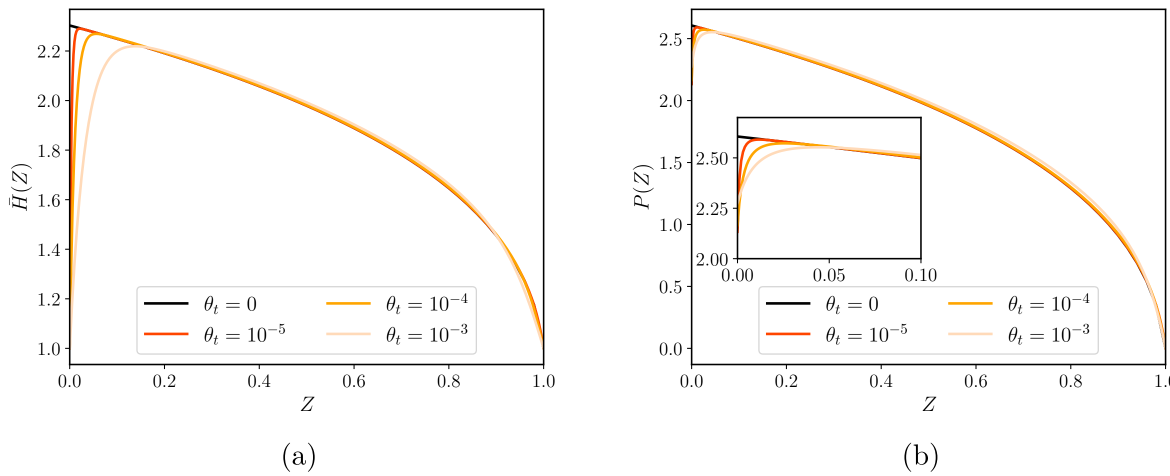

Figure 5.4. (a) The deformed channel height $\bar{H}(Z)$ for different values of the tension parameter θ_t. The black curves represent the outer solution of equation (5.41), while the other (lighter) curves are obtained using the "full" (numerical) solution of the two-point boundary-value problem consisting of equations (5.47), (5.48) and (5.49). (b) The corresponding pressure distribution $P(Z)$. The black curves are obtained by substituting the solution of equation (5.41) into equation (5.45), while the other (lighter) curves are similarly obtained from "full" (numerical) solution of equations (5.47), (5.48) and (5.48). In both panels, we fixed $Q = 1$, $\hat{R}\mathrm{e} = 1.0$, and $\xi = 0.5$.

5.3.3 Illustrated examples

Depending on the top wall's geometry, β in equations (5.41) and (5.47) will take different forms, such as the thick wall case and plate-like top wall case introduced in section 5.2.3 and section 5.2.4, respectively. To make our discussion general, instead of considering the two cases separately, we regard β and θ_t as characteristic system parameters and discuss the corresponding solutions of equations (5.41) and (5.47) to illustrate the regularization introduced in section 5.3.2. Equation (5.41) can be solved in two steps. First, invert equation (5.42) to get $P(Z)$. Second, substitute $P(Z)$ into equation (5.14) to get $\bar{H}$. As for equation (5.47), we use the `solve_bvp` routine from the SciPy stack [106] to obtain a numerical solution of the nonlinear two-point boundary value problem. After obtaining $\bar{H}(Z)$, equation (5.45) can be used to obtain $P(Z)$.

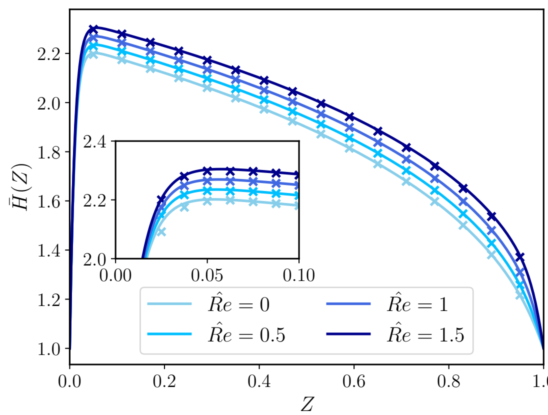

(a)

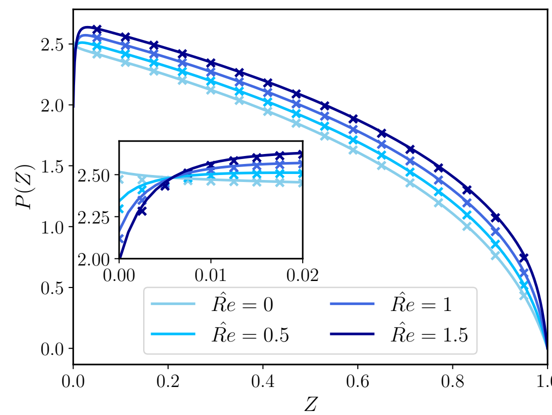

(b)

Figure 5.5. (a) The deformed channel height $\bar{H}(Z)$ for different values of the reduced Reynolds number $\hat{R}e$. The solid curves represent the numerical solution of equation (5.47), while the symbols represent the asymptotic solution (see equations (5.62) and (5.64)). (b) The corresponding pressure distributions $P(Z)$. The solid curves are obtained by substituting the solution of equation (5.47) into equation (5.45), while the symbols are the asymptotic solution (see equations (5.63) and (5.64)). The agreement between the asymptotic and numerical solutions is so good that the curves mostly overlap. In both panels, we fixed $Q = 1$, $\xi = 0.5$, and $\theta_t = 10^{-4}$.

First, we investigate the tension effect by varying θ_t in equation (5.41) while keeping Q, $\hat{R}e$ and β fixed. As shown in figure 5.4(a), with $\theta_t \ll 1$, the solutions to equations (5.41) and (5.47) do not differ much from each other along most of the domain $Z \in [0, 1]$, as required by the dominance of the Winkler-foundation-like mechanism of deformation. Since equation (5.41) only satisfies $\bar{H}(1) = 1$, in principle, two boundary layers could be expected near $Z = 0$ and $Z = 1$, respectively, to fulfill the remaining boundary conditions from equations (5.48)–(5.49). However, as we have discussed in section 5.3.1, with $\theta_t = 0$, equation (5.42) indicates that, P varies linearly with Z as $Z \to 1^-$. Since $\bar{H}$ is linearly proportional to P at the leading order in θ, $\bar{H}$ should be linear in Z as $Z \to 1^-$, hence $\mathrm{d}^2\bar{H}/\mathrm{d}Z^2 \to 0$ as $Z \to 1^-$. In other words, the outer solution actually satisfies the boundary condition (5.49). Therefore, there is no boundary layer located near $Z = 1$. This fact can also be seen in figure 5.4(a), where the left boundary layer is prominent (becoming thicker as θ_t is increased), while the outer solution agrees well with the full numerical solution near $Z = 1$ for all values of θ_t shown.

The effect of θ_t on $P(Z)$ is shown in figure 5.4(b). The key takeaway from this plot is that, while equation (5.41) always predicts $P(Z)$ to be a decreasing function of Z, a positive pressure gradient is observed near $Z = 0$ in the numerical solution to equation (5.47) for all $\theta_t \neq 0$ considered. The reason for this positive pressure gradient near the inlet is that, due to the restriction on the displacement at $Z = 0$, the area of the cross-section undergoes a sharp change near $Z = 0$. Since the flow rate is fixed at steady state, the axial velocity has to quickly reduce near $Z = 0$. The observed positive pressure gradient facilitates this deceleration of the flow.

Next, we address the effect of fluid inertia by varying $\hat{R}\mathrm{e}$. In this case, we fix $Q = 1$, $\beta = 0.5$ and $\theta_t = 10^{-4}$. As shown in figure 5.5(a), as $\hat{R}\mathrm{e}$ increases, larger deformation of the wall is observed. Also, the deformation gradient along Z is larger for higher $\hat{R}\mathrm{e}$ because the pressure displays sharper decrease with the increase of $\hat{R}\mathrm{e}$, which can be clearly seen in figure 5.5(b). Notably, $\mathrm{d}P/\mathrm{d}Z > 0$ is also observed for the three cases of $\hat{R}\mathrm{e} \neq 0$, which can be explained as before. However, $\mathrm{d}P/\mathrm{d}Z$ remains negative in the case of $\hat{R}\mathrm{e} = 0$. This is because, in this case of negligible fluid inertia, the deceleration of the flow near the inlet is not as large as the other cases, thus the positive pressure gradient is not necessary. Finally, we mention that instead of solving equation (5.47) numerically, we are able to obtain a uniformly valid asymptotic solution for $\bar{H}(Z)$ and $P(Z)$ using the method of matched asymptotic expansions [168]. In particular, for the special case of $\hat{R}\mathrm{e} = 0$, we are able to obtain explicit formulae for both $\bar{H}(Z)$ and $P(Z)$. The details of this calculation are provided in appendix 5.A. The dashed curves in figure 5.5(a) and figure 5.5(b) demonstrate that these asymptotic solution (equations (5.62) and (5.63) in appendix 5.A) agrees well with the numerical solution.

As a supplement to our discussion above, typical values of the dimensional and dimensionless variables of a microchannel with a thick top wall are summarized in table 5.2. Here $d^2/w^2 = 16 \gg 1$, thus equation (5.22) in section 5.2.3 is applicable. The steady responses of the system under different flow rates are calculated from equation (5.45) and tabulated in table 5.3. With the increase of the flow rate, the pressure drop, the maximum pressure within the channel, and the maximum deformation of the interface are increasing. As we

Table 5.2. Typical values of the dimensional and dimensionless parameters used in equation (5.45).

Name	Variable	Typical value	Unit
channel's length	ℓ	1.0	cm
channel's undeformed height	h_0	25	µm
channel's width	w	500	µm
top wall's thickness	t	2.0	mm
solid's Young's modulus	E	1.5	MPa
solid's Poisson's ratio	ν_s	0.5	–
fluid's dynamic viscosity	μ	1.0×10^{-3}	Pa s
fluid's density	ρ	1.0×10^{3}	$\mathrm{kg\,m^{-3}}$
inlet flow rate	q	See table 5.3	$\mathrm{\mu L\,min^{-1}}$
tension force per unit width	χ_t	400	$\mathrm{N\,m^{-1}}$
characteristic velocity scale	$\mathcal{V}_c = q/(wh_0)$	–	$\mathrm{m\,s^{-1}}$
characteristic pressure scale	$\mathcal{P}_c = \mu\mathcal{V}_c/(\epsilon h_0)$	–	kPa
pressure drop	$\Delta p = p(z=0)$	See table 5.3	kPa
maximum pressure	$p_{\max} = \max\limits_{0\le z\le\ell} p(z)$	See table 5.3	kPa
maximum channel's deformed height	$\bar{h}_{\max} = \max\limits_{0\le z\le\ell} \bar{h}(z)$	See table 5.3	µm
channel's height-to-length aspect ratio	$\epsilon = h_0/\ell$	0.0025	–
channel's height-to-width aspect ratio	$\delta = h_0/w$	0.05	–
reduced Reynolds number	$\hat{Re} = \epsilon\rho q/(w\mu)$	See table 5.3	–
dimensionless spring stiffness	$\beta = \lambda\mathcal{I}_1$	See table 5.3	–
tension coefficient	$\theta_t = \chi_t h_0 \xi/(\mathcal{P}_c \ell^2)$	5.42754×10^{-4}	–

have discussed, when the flow inertia is small (smaller $\hat{Re}$), the maximum pressure occurs at the inlet of the channel. However, if the flow inertia is prominent, there is a positive pressure gradient near the inlet and thus, the maximum pressure is "pushed" inwards, away from the inlet.

5.4 Discussion

To this end, we critically discussed weakly-unidirectional flows (under a lubrication scaling) in compliant ducts of initially rectangular cross-section, for both the vanishing and the finite Reynolds number cases. In doing so, we contributed to the recently developed theory of *soft hydraulics*. Attention was paid to the hydraulic resistance of such conduits during steady viscous flow (*i.e.*, the flow rate–pressure drop relations, which are now nonlinear). In

Table 5.3. Calculated steady-state responses of the microchannel system under different flow rate with the parameters specified in table 5.2.

q (μL min^{-1})	$\hat{Re}$ (–)	β (–)	Δp (kPa)	$p_{\max}$ (kPa)	$\bar{h}_{\max}$ (μm)
1500	0.125	0.1737	140.96	140.96	42.55
6000	0.5	0.6947	250.55	266.16	59.74
12000	1.0	1.3895	258.27	366.90	73.61

particular, we derived 1D reduced models from "full" 3D results on fluid–structure interaction. In doing so, we synthesized and unified a variety of previous models (some justified only by empirical considerations). This kind of reduction has been sought (and is of general interest [72]) for practical design considerations of microfluidic systems [138], [169]–[171], such as for calibrating optics-free non-contact measurement techniques [20].

For inertialess unidirectional flow in a compliant duct, the pressure varies nonlinearly along the streamwise direction due to the FSI between the viscous fluid flow and the compliant wall. Due to the slenderness and shallowness of the duct, we are able to relate the nonlinear pressure gradient $\mathrm{d}p/\mathrm{d}z$ to the flow rate q at steady state. By introducing the concept of an effective channel height, we recovered the form of the classical Poiseuille-like law and, at the same time, reduced the original 3D flow problem to an equivalent 2D one.

Although averaged deformed channel heights have been used in the literature, the validity of such models was not previously established. We found that the averaged channel height (5.11) can be a good approximation to the consistent effective height introduced in equation (5.8). This conclusion is important because the averaged-height models yield explicit flow rate–pressure drop relations, and are easily compared to other geometries such as axisymmetric cases. Interestingly, we showed that the averaged channel height has a universal expression as $\bar{H}(Z) = 1 + \beta P(Z)$, where $\beta = \lambda \mathcal{I}_1$, for *both* thick-walled and thinner, plate-like-walled top walls. Even though the formula for the dimensionless compliance coefficient β is different in the two cases, we have justified the observation (from the end of section 5.2.1) that a wide and shallow microchannel's top wall behaves like a Winkler foundation [117], [118], in which the averaged channel height is determined by the local pressure and a proportionality constant.

The reduction of the 3D FSI problem to a 1D model using the averaged height concept also allowed us to generalize the textbook concept of a friction factor [115], [156] to compliant ducts. We showed that the soft hydraulic system's Poiseuille number Po (product of the Fanning friction factor C_f and the Reynolds number) can be between 1 and 4 times larger than that for a rigid duct. Importantly, for the compliant duct, both C_f and Po depend on the streamwise coordinate due to the non-constant pressure gradient. This novel result extends the laminar portion of the Moody diagram, in which roughness is unimportant, via a new compliance parameter that is important in microfluidics.

Additionally, we showed how to incorporate weak but finite flow inertia in the previous $Re \to 0$ models. The finite-Re model breaks down beyond a certain value of the product of Re and a compliance parameter λ. Weak tension near the inlet and outlet of the reduced 1D model was introduced to regularize this breakdown and to obtain uniformly valid pressure distributions (in the sense of matched asymptotics).

5.A Appendix: Matched asymptotic solution for the 1D model with weak tension

For $\theta_t \ll 1$, equation (5.47) subject to the BCs (5.48)–(5.49) represents a singular perturbation problem [168]. The outer solution $\bar{H}_o(Z)$, which satisfies $\bar{H}_o(1) = 1$, is found by setting $\theta_t = 0$:

$$\frac{1}{\beta}\left[\frac{1}{4}(\bar{H}_o^4 - 1) - \frac{6}{5}\hat{R}\mathrm{e}\beta Q^2(\bar{H}_o - 1)\right] = 12Q(1 - Z). \tag{5.50}$$

Substituting equation (5.14) into the above, we recover equation (5.42) as the outer solution for the pressure.

For convenience, denote $\theta^2 = \theta_t$. In the boundary layer near $Z = 0$ ("left" boundary layer), we introduce the rescaled coordinate $\hat{Z} = Z/\theta$. Denote the left inner solution as $\bar{H}_l(\hat{Z})$. Then, in terms of these new variables, equation (5.47) is transformed into

$$\frac{3}{5}\hat{R}\mathrm{e}\frac{\mathrm{d}}{\mathrm{d}\hat{Z}}\left(\frac{Q^2}{\bar{H}_l^2}\right) = \frac{1}{\beta}\left(\frac{\mathrm{d}^3\bar{H}_l}{\mathrm{d}\hat{Z}^3} - \frac{\mathrm{d}\bar{H}_l}{\mathrm{d}\hat{Z}}\right) + \theta\frac{12Q}{\bar{H}_l^3}. \tag{5.51}$$

At the leading order, the last term in equation (5.51) is negligible, and we integrate once to obtain

$$\frac{3}{5}\hat{R}\mathrm{e}\beta\frac{Q^2}{\bar{H}_l^2} = \frac{\mathrm{d}^2\bar{H}_l}{\mathrm{d}\hat{Z}^2} - \bar{H}_l + C_1. \tag{5.52}$$

Now, consider the behavior of equation (5.52) in the phase plane $(\mathscr{H}, \mathscr{F})$, where we have defined $\mathscr{H} := \bar{H}_l$ and $\mathscr{F} := \mathrm{d}\bar{H}_l/\mathrm{d}\hat{Z}$; $\hat{Z}$ parametrizes integral curves (*i.e.*, solutions) in this plane. Equation (5.52) becomes

$$\frac{\mathrm{d}\mathscr{H}}{\mathrm{d}\hat{Z}} = \mathscr{F}, \tag{5.53}$$

$$\frac{\mathrm{d}\mathscr{F}}{\mathrm{d}\hat{Z}} = \frac{3}{5}\hat{R}\mathrm{e}\beta\frac{Q^2}{\mathscr{H}^2} + \mathscr{H} - C_1. \tag{5.54}$$

Fixed points of the system (5.53)–(5.54) are such that the right-hand sides vanish. Although the expression for the fixed point $(\mathscr{H}^\star, \mathscr{F}^\star)$ with and $\mathscr{H}^\star > 0$ and $\mathscr{F}^\star = 0$ is lengthy, it can be found. The solution of equation (5.52) as $\hat{Z} \to \infty$ and $\mathrm{d}\bar{H}_l/\mathrm{d}\hat{Z} \to 0$ should match the outer solution $\bar{H}_o$ as $Z \to 0$. Therefore, $\mathscr{H}^\star$ must be chosen to be precisely $\bar{H}_o(0)$, which is the positive real root of equation (5.50) with $Z = 0$. Consequently, without needing the explicit formula for $\mathscr{H}^\star$, we obtain:

$$C_1 = \frac{3}{5}\hat{R}\mathrm{e}\beta\frac{Q^2}{\bar{H}_o(0)^2} + \bar{H}_o(0). \tag{5.55}$$

Now, the inner solution in the left boundary layer is the integral curve in the $(\mathscr{H}, \mathscr{F})$ plane starting at $\mathscr{H} = 1$ and ending at $\mathscr{H} = \bar{H}_o(0)$. To construct this curve, multiply both sides of equation (5.52) by $\mathrm{d}\bar{H}_l/\mathrm{d}\hat{Z}$, and obtain a first integral:

$$\left(\frac{\mathrm{d}\mathscr{H}}{\mathrm{d}\hat{Z}}\right)^2 = -\frac{6}{5}\hat{R}\mathrm{e}\beta\frac{Q^2}{\mathscr{H}} + \mathscr{H}^2 - 2C_1\mathscr{H} + C_2. \tag{5.56}$$

To ensure that $\mathscr{H}^\star = \bar{H}_o(0)$ remains the desired fixed point of the ODE, the constant of integration must be

$$C_2 = \frac{12}{5}\hat{R}\mathrm{e}\beta\frac{Q^2}{\bar{H}_o(0)} + \bar{H}_o(0)^2. \tag{5.57}$$

Then, equation (5.56) can be rewritten as:

$$\left(\frac{\mathrm{d}\mathscr{H}}{\mathrm{d}\hat{Z}}\right)^2 = [\mathscr{H} - \bar{H}_o(0)]^2 \left\{1 - \frac{6}{5}\hat{R}\mathrm{e}\beta \frac{Q^2}{\mathscr{H}\bar{H}_o(0)^2}\right\}. \tag{5.58}$$

Equation (5.58) is separable, so its solution can be written as

$$\int_1^{\bar{H}_l} \frac{\mathrm{d}\mathscr{H}}{[\bar{H}_o(0) - \mathscr{H}]\sqrt{1 - \frac{6}{5}\hat{R}\mathrm{e}\beta\frac{Q^2}{\mathscr{H}\bar{H}_o(0)^2}}} = \hat{Z}, \tag{5.59}$$

where positive root is taken because it is expected that $\mathrm{d}\mathscr{H}/\mathrm{d}\hat{Z} > 0$ and thus, $\bar{H}_o(0) > \mathscr{H}$, in the boundary layer. Performing the integration in equation (5.59) yields an implicit solution:

$$\begin{aligned} &-2\left[\tanh^{-1}\left(\sqrt{1 - \frac{m}{\bar{H}_l}}\right) - \tanh^{-1}(\sqrt{1-m})\right] \\ &\quad + \frac{2}{\sqrt{1 - \frac{m}{\bar{H}_o(0)}}}\left[\tanh^{-1}\left(\sqrt{\frac{1 - \frac{m}{\bar{H}_l}}{1 - \frac{m}{\bar{H}_o(0)}}}\right) - \tanh^{-1}\left(\sqrt{\frac{1-m}{1 - \frac{m}{\bar{H}_o(0)}}}\right)\right] = \hat{Z}, \end{aligned} \tag{5.60}$$

where $m = 6\hat{R}\mathrm{e}\beta Q^2/[5\bar{H}_o(0)^2]$. Observe that if the criterion in equation (5.44) is satisfied then $m < 1$ follows, which is required for the solution (5.59) to exist. Therefore, the restriction (5.44) is needed to obtain a meaningful outer solution to equation (5.50). In the case for which the criterion (5.44) is violated, this asymptotic analysis will break down, which suggests that tension is no longer a sufficiently small effect. In that case, we can solve equation (5.47) numerically.

Inverting equation (5.60) to get an explicit expression for $\bar{H}_l(\hat{Z})$ is nontrivial. However, for the special case of $\hat{R}\mathrm{e} = 0$, equation (5.59) immediately gives an explicit solution:

$$\bar{H}_l(\hat{Z}) = \bar{H}_o(0) + [1 - \bar{H}_o(0)]\mathrm{e}^{-\hat{Z}} \qquad (\hat{R}\mathrm{e} = 0). \tag{5.61}$$

As for the right boundary, near $Z = 1$, the ODE does not exhibit a boundary layer structure for $\theta_t \to 0$, as we discussed in section 5.3.1. This fact is also shown by figure a, from which it is evident that the numerical solutions of the "full" ODE agree well with the leading-order outer solution (outside the left boundary layer), for any $\theta_t \ll 1$.

The composite solution is obtained after subtracting the common part between inner and outer solutions:

$$\bar{H}(Z) \sim \bar{H}_a(Z) = \bar{H}_l(Z/\theta) + \bar{H}_o(Z) - \bar{H}_o(0), \quad (\theta_t \ll 1) \tag{5.62}$$

with $\bar{H}_l$ and $\bar{H}_o$ given (implicitly) by equations (5.60) and (5.50), respectively. Equation (5.45) can be used to obtain the asymptotic solution for P. The leading-order terms are

$$\begin{aligned} P(Z) \sim P_a(Z) &= \frac{1}{\beta}\left(-\frac{\mathrm{d}^2\bar{H}_l}{\mathrm{d}\hat{Z}^2} + \bar{H}_a - 1\right) \\ &= \frac{1}{\beta}\left\{\bar{H}_o(Z) - 1 - \frac{3}{5}\hat{R}\mathrm{e}\xi Q^2\left[\frac{1}{\bar{H}_l(Z/\theta)^2} - \frac{1}{\bar{H}_o(0)^2}\right]\right\}, \qquad (\theta_t \ll 1) \end{aligned} \tag{5.63}$$

where we have used equation (5.52) to compute $\mathrm{d}^2\bar{H}_l/\mathrm{d}\hat{Z}^2$.

For $\hat{R}\mathrm{e} = 0$, using equation (5.61), the composite solution can be explicitly written as

$$\bar{H}(Z) \sim \bar{H}_a(Z) = \left[1 - (1 + 48Q\beta)^{1/4}\right]\mathrm{e}^{-Z/\theta} + [1 + 48Q\beta(1 - Z)]^{1/4} \qquad (\theta_t \ll 1,\ \hat{R}\mathrm{e} = 0). \tag{5.64}$$

Substituting equation (5.64) into equation (5.45) (or, setting $\hat{R}\mathrm{e} = 0$ in equation (5.63)), we obtain the matched asymptotic solution for the pressure distribution as well:

$$P(Z) \sim P_a(Z) = \frac{1}{\beta}\left\{[1 + 48\beta Q(1 - Z)]^{1/4} - 1\right\} \qquad (\theta_t \ll 1,\ \hat{R}\mathrm{e} = 0). \tag{5.65}$$

6. GLOBAL INSTABILITY OF FINITE-REYNOLDS-NUMBER FLOW IN COMPLIANT RECTANGULAR MICROCHANNELS

SUMMARY

Experiments have shown that flow in compliant microchannels can become unstable at a much lower Reynolds number than the corresponding flow in a rigid conduit. Therefore, it has been suggested that the wall's elastic compliance can be exploited towards new modalities of microscale mixing. While previous studies mainly focused on the local instability induced by the fluid–structure interactions (FSIs) in the system, in this chapter, we aim to provide new explanations for this phenomenon from the perspective of the global instability. In particular, we derive a new unsteady one-dimensional (1D) model that is tailored to long, shallow rectangular microchannels with a deformable top wall, similar to the experiments. Going beyond the usual lubrication flows analyzed in these geometries, we include finite fluid inertia and couple the reduced flow equations to a reduced 1D wall deformation equation. Although a quantitative comparison to previous experiments is quite difficult, the behaviors of the proposed derived model show qualitatively agreement with the experimental observations, and capture several key effects. Specifically, we find the critical conditions under which the inflated base state of the 1D FSI model is linearly unstable to infinitesimal perturbations. The critical Reynolds numbers predicted are in agreement with experimental observations. The unstable modes are highly oscillatory, with frequencies close to the natural frequency of the wall, suggesting that the observed instabilities are resonance phenomena. Furthermore, during the start-up from an undeformed initial state, self-sustained oscillations can be triggered by FSI.

The material in this chapter has been submitted for publication as [X. Wang, I.C. Christov, "Reduced modeling and global instability of finite-Reynolds-number flow in compliant rectangular channels"] [172]. Both authors contributed to the analysis of the problem and the derivation of the mathematical model, led by X.W. X.W. wrote the Python scripts and conducted all the case studies, numerical simulations, and data analysis. X.W. and I.C.C. jointly discussed the results, drafted and revised the manuscript for publication.

6.1 Model formulation

In this chapter, we investigate the experimentally observed unstable flows in compliant microchannels at finite but low Reynolds number. Similar to the experiments [41], we allow $Re \simeq 100$ with a corresponding "reduced" Reynolds number $\hat{R}e = \epsilon Re = h_0 Re/\ell = \mathcal{O}(1)$. We approach the unsteady FSI problem by reduced modeling. In particular, we synthesize the knowledge that we have obtained in the previous chapters and construct an unsteady reduced model for the finite-Reynolds-numbers flow within the long and shallow rectangular microchannels. The configuration of interest is depicted in figure 3.1, and the dominant mechanisms discussed in chapter 3 still apply. With the lubrication approximation, we have found that the flow pressure p varies along the flowwise direction z (or Z) mainly up to $\hat{R}e = \mathcal{O}(1)$. This observation actually motivates us to build a 1D model which can realize a coupling between the flow pressure, the flow rate and the wall deformation. Then, in chapter 5, we have shown that for such a reduced 1D model, we can introduce an effective deformed channel height by averaging the interface displacement over the channel width. This step removes the spanwise x-dependence, thus reducing the system from 3D as a 2D one, as shown in figure 6.1. However, chapter 5 is only focused on the steady state. Next, we show how to make appropriate extensions and give the complete formulation of the unsteady 1D FSI model.

6.1.1 Unsteady flow within a deformed channel

Since $h_0 \ll \ell$, using the scales tabulated in table 3.1 but applying in the 2D configuration of figure 6.1, we conclude that up to $\hat{R}e = \mathcal{O}(1)$, the leading-order terms left in the dimensional 2D incompressible Navier–Stokes equations are

$$\frac{\partial v_y}{\partial y} + \frac{\partial v_z}{\partial z} = 0, \tag{6.1a}$$

$$\frac{\partial p}{\partial y} = 0 \quad \Rightarrow \quad p = p(z,t), \tag{6.1b}$$

$$\frac{\partial v_z}{\partial t} + v_y \frac{\partial v_z}{\partial y} + v_z \frac{\partial v_z}{\partial z} = -\frac{1}{\rho_f}\frac{\partial p}{\partial z} + \frac{\mu}{\rho_f}\frac{\partial^2 v_z}{\partial y^2}. \tag{6.1c}$$

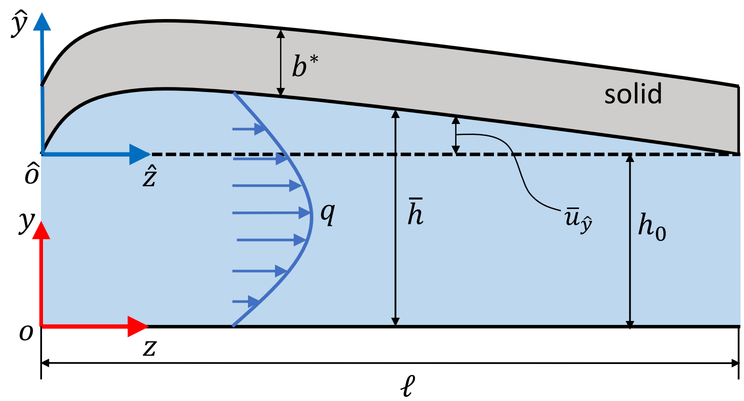

Figure 6.1. Schematic of the configuration of the reduced 2D problem obtained by width-averaging the interface displacement, with key dimensional labels labeled.

Importantly, the conservation of the linear momentum along y is reduced to $p = p(z,t)$. Like the 3D configuration, the momentum equation along z also indicates a balance between the finite fluid inertia, the pressure gradient and the dominant shear forces in the flow.

We can introduce the flow rate $q(z,t) = w \int_0^{\bar{h}(z,t)} v_z(y,z,t)\,\mathrm{d}y$ by integrating v_z along the deformed height, where the channel width w has to be used here for the consistency of units. However, our reduced modeling takes width-averaged quantities. Therefore, we define $\bar{q}(z,t) := q(z,t)/w$. Then, integrating equation (6.1a) and equation (6.1c) along y from 0 to $\bar{h}$, we get the following two equation:

$$\frac{\partial \bar{h}}{\partial t} + \frac{\partial \bar{q}}{\partial z} = 0, \tag{6.2a}$$

$$\frac{\partial \bar{q}}{\partial t} + \frac{6}{5}\frac{\partial}{\partial z}\left(\frac{\bar{q}^2}{\bar{h}}\right) = -\frac{\bar{h}}{\rho_f}\frac{\partial p}{\partial z} - \frac{12\mu\bar{q}}{\rho_f \bar{h}^3}. \tag{6.2b}$$

Note that in deriving equation (6.2a), we have applied the kinematic boundary condition:

$$v_y\big|_{y=\bar{h}} = \frac{\partial \bar{h}}{\partial t}, \tag{6.3}$$

and the no-slip boundary condition of $v_z(z = \bar{h}, t) = 0$. In deriving equation (6.2b), we have invoked a von Kármán–Pohlhausen approximation [173] (see also, *e.g.*, [115, §4-6.5] or

[104, p. 541]) to assume a parabolic velocity profile across any deformed cross-section of the channel:

$$v_z(y,z,t) = \frac{6\bar{q}y[\bar{h}(z,t)-y]}{\bar{h}^3(z,t)}, \tag{6.4}$$

which is the dimensional form equation (5.40) we have used in section 5.3.1. Note equations (6.2) were also previously derived by Stewart *et al.* [86] and Inamdar *et al.* [102].

To this end, equation (6.2) establishes a relationship between p, $\bar{q}$ and $\bar{h}$, as we have promised. However, we still need to put forward a solid mechanics model to solve for $\bar{h}$ to close the FSI system.

6.1.2 1D formulation of the compliant wall deformation

In section 5.3.2, we have already written out equation (5.46) for the width-averaged height $\bar{h}$ at steady state by combining the dominant Winkler-foundation-like mechanism with the weak tension effect. In this section, we will extend the steady state equation (5.46) into an unsteady one by considering the solid inertia.

For completeness, we first briefly review the logic of introducing the weak tension. If we only consider the dominant Winkler-foundation-like behavior as equation (3.3), we get the following equation by averaging the displacement of the fluid–solid interface over x:

$$\bar{u}_y(z,t) = \frac{1}{w}\int_{-w/2}^{+w/2} u_y(x,z,t)\,\mathrm{d}x = \underbrace{\left[\frac{1}{w}\int_{-w/2}^{+w/2} \mathfrak{f}(x)\,\mathrm{d}x\right]}_{1/k} p(z,t). \tag{6.5}$$

Recall that the salient assumption for equation (3.3) is that the square of the characteristic time scale for the solid deformation is much smaller the that of the flow, i.e., $\mathcal{T}_s^2 \ll \mathcal{T}_f^2$, the validity of which will be discussed when we make the 1D system dimensionless. With equation (6.5), the width-averaged height $\bar{h}$ of the channel is

$$\bar{h}(z,t) = \frac{1}{w}\int_{-w/2}^{+w/2} h_0 + u_y(x,z,t)\,\mathrm{d}x = h_0 + \frac{1}{k}p(z,t). \tag{6.6}$$

As in equation (5.46), the proportionality constant, k represents the *effective stiffness* of the interface.

However, the above two equations cannot satisfy the possible restrictions imposed at the inlet and the outlet (*i.e.*, at $z = 0$ and $z = \ell$). As shown in figure 6.1, the movement of the fluid–solid interface at both ends is often physically restricted. To satisfy these boundary conditions, we regard the wall deformation as a boundary layer problem. While the Winkler-foundation-like mechanism is dominant outside the "boundary layers" near the inlet and outlet, with equation (6.5) being the (outer) solution there, another mechanism plays a role within thin (boundary) layers near $z = 0, \ell$, each admitting inner solutions that regularize the problem and allow the enforcement of end constraints. The weak deformation effects we consider in this section is the weak constant tension. Then, the "regularized" governing equation for $\bar{u}_y$ with the solid inertia included is written as

$$\rho_s b^\star \frac{\partial^2 \bar{u}_y}{\partial t^2} + k\bar{u}_y - \chi_t \frac{\partial^2 \bar{u}_y}{\partial z^2} = p(z,t), \tag{6.7}$$

where ρ_s denotes the solid density, $b^\star$ represents the effective thickness of the interface (discussed in section 6.A.1), which is introduced so that the first term can represent the bulk inertial effects of the solid. Recalling that k is the effective stiffness introduced in equation (6.5), the second term represents the dominant Winkler-foundation effects. χ_t is the tension per unit width (discussed in section 6.A.2). In the case of χ_t being constant, the tension effects in terms of the transverse displacement $\bar{u}_y$ is written as the third term in equation (6.7) (see *e.g.*, [174, §4.3]). The weakness of the solid inertia and the tension is not obvious from equation (6.7), but will become clear after we introduce the dimensionless variables.

Equation (6.7) is essentially the equation of motion of a Kramer-type surface, which has been used extensively in the study of high-Re (boundary layer) flows over compliant coatings. The goal of the latter studies is to understand how to delay the laminar-turbulence transition [175]. However, microchannel flows cannot reach such high Re values. More surprisingly, the application of equation (6.7) in modeling soft microchannels leads to different conclusions from the compliant coating studies. Compliance of the wall can actually promote (instead of delay) the laminar-turbulence transition thanks to the FSI-induced instabilities. This effect can be successfully exploited for micromixing.

6.1.3 Nondimensionalization

We use the capitalized letters denote the corresponding dimensionless parameters. Using the scales tabulated in table 3.1, equation (6.2) is nondimensionalized as

$$\frac{\partial Q}{\partial Z} + \frac{\partial \bar{H}}{\partial T} = 0, \tag{6.8a}$$

$$\hat{R}\mathrm{e}\frac{\partial Q}{\partial T} + \hat{R}\mathrm{e}\frac{6}{5}\frac{\partial}{\partial Z}\left(\frac{Q^2}{\bar{H}}\right) = -\bar{H}\frac{\partial P}{\partial Z} - \frac{12Q}{\bar{H}^2}, \tag{6.8b}$$

where $Q = \bar{q}/\mathcal{V}_c h_0$.

As for the solid mechanics equations, the first step is to determine the characteristic scale, $\bar{\mathcal{U}}_c$, for the fluid–solid interface. The dominant deformation effect in equation (6.5), suggests that we should take $\bar{\mathcal{U}}_c = \mathcal{P}_c/k$, recalling that the scale for p is $\mathcal{P}_c$. Then, the dimensionless version of equation (6.5) is simply

$$\bar{U}_Y(Z,T) = P(Z,T). \tag{6.9}$$

Still using h_0 to scale $\bar{h}$, the dimensionless effective channel height (equation (6.6)) becomes

$$\bar{H}(Z,T) = 1 + \frac{\bar{\mathcal{U}}_c}{h_0}\bar{U}_Y(Z,T) = 1 + \beta\bar{U}_Y(Z,T). \tag{6.10}$$

Here, we have introduced another dimensionless parameter, $\beta = \bar{\mathcal{U}}_c/h_0 = \mathcal{P}_c/(kh_0)$. Note that this definition is consistent with that in equation (5.46). It is clear from equation (6.10) that β translates the interface displacement into the deformation of the fluid domain, capturing the "strength" of the fluid–solid coupling. Thus, β is the "FSI parameter" of our model.

The dependence of β on the system properties comes through $\mathcal{P}_c$ and k. While $\mathcal{P}_c$ is determined by the flow conditions (*i.e.*, the viscosity of the fluid, the flow rate, and the geometry of the undeformed channel), k is determined by the material properties, the geometry, and the boundary conditions on the compliant wall. To explicitly show this, we write

$$\frac{1}{k} = \frac{1}{w}\int_{-w/2}^{+w/2} \mathfrak{f}(x)\,\mathrm{d}x = \int_{-1/2}^{+1/2} \mathfrak{f}(wX)\,\mathrm{d}X = \frac{\xi}{\bar{E}} \underbrace{\int_{-1/2}^{+1/2} F(X)\,\mathrm{d}X}_{\mathcal{I}_1} = \frac{\xi \mathcal{I}_1}{\bar{E}}. \tag{6.11}$$

The definition of k from equation (6.5) is used in the first step. The second step is making the integral dimensionless. In the third step, the assumption of a linearly elastic solid has been invoked with $k \propto \bar{E}$ and $\mathfrak{f}(x) \propto 1/\bar{E}$. Here, $\bar{E} = E/(1-\nu_s^2)$, is used because of the plain-strain reduction, with E being the Young's modulus and ν_s being the Poisson's ratio, respectively. Then, $F(X)$ is introduced as the dimensionless self-similar deformation profile, and ξ is the resulting pre-factor after x is scaled by w. In the last step, $\mathcal{I}_1 = \int_{-1/2}^{+1/2} F(X)\,\mathrm{d}X$ was introduced to simplify the expression. While the effect of the material properties of the solid wall are captured by $\bar{E}$, the influence of the wall geometry and the boundary conditions are taken by both ξ and $\mathcal{I}_1$. As mentioned and illustrated in chapter 5, $\mathfrak{f}(x)$ takes different forms in different situations, thus giving different expressions of ξ and $\mathcal{I}_1$. For example, for the thick-walled microchannel considered by Wang and Christov [101], $\xi = w$ and $\mathcal{I}_1 \approx 0.542754$. Meanwhile, for the microchannels with thick-plate-like top walls considered by Shidhore and Christov [33], $\xi = w^4/(2d^3)$ and $\mathcal{I}_1 = \frac{1}{30} + \frac{(d/w)^2}{3\kappa(1-\nu_s)}$, with κ (typically, $\kappa = 1$) being a "shear correction factor." Nevertheless, the key point is that both ξ and $\mathcal{I}_1$ can be obtained *a priori*, by solving the corresponding elasticity problem, as analytical expressions.

Substituting the other scales from tables 3.1 and 3.2, the dimensionless version of equation (6.7) is

$$\theta_I \frac{\partial^2 \bar{U}_Y}{\partial T^2} + \bar{U}_Y - \theta_t \frac{\partial^2 \bar{U}_Y}{\partial Z^2} = P, \tag{6.12}$$

where $\theta_I = \rho_s b^\star \bar{\mathcal{U}}_c/(\mathcal{T}_f^2 \mathcal{P}_c)$ and $\theta_t = \chi_t \bar{\mathcal{U}}_c/(\ell^2 \mathcal{P}_c)$ are introduced above as the inertial coefficient and the tension coefficient, respectively. As discussed in section (6.1.2), $\theta_I \ll 1$ and $\theta_t \ll 1$ is expected because both the solid inertia and the tension effect are weak. Then, as expected, the leading-order solution (as $\theta_I, \theta_t \to 0$) of equation (6.12) is equation (6.9). Even though $\theta_I \ll 1$ and $\theta_t \ll 1$, as we will see in section 6.4.1, the inclusion of the solid inertia and tension is necessary because they have significant influence on the global instability of the system.

Let's justify $\theta_I \ll 1$ first. Recalling that $\mathcal{P}_c = \mu\mathcal{V}_c/(\epsilon h_0)$, $\hat{\mathrm{R}}\mathrm{e} = \epsilon\rho_f\mathcal{V}_c h_0/\mu$, and $\beta = \bar{\mathcal{U}}_c/h_0$, θ_I can be written as

$$\theta_I = \frac{\rho_s b^\star \bar{\mathcal{U}}_c}{\mathcal{T}_f^2\mathcal{P}_c} = \epsilon\frac{\rho_f\mathcal{V}_c h_0}{\mu}\frac{\bar{\mathcal{U}}_c}{h_0}\frac{b^\star h_0}{\ell^2}\frac{\rho_s}{\rho_f} = \epsilon\hat{\mathrm{R}}\mathrm{e}\beta\frac{b^\star}{\ell}\frac{\rho_s}{\rho_f}. \tag{6.13}$$

Since $\epsilon \ll 1$, $b^\star \leq d \ll \ell$, $\hat{\mathrm{R}}\mathrm{e} = \mathcal{O}(1)$, β is typically $\mathcal{O}(1)$ and $\rho_s \simeq \rho_f$ in the microchannel setting (because PDMS has a similar density to water), we have justified $\theta_I \ll 1$. Note time in equation (6.7) is scaled by $\mathcal{T}_f$, as before, to ensure the fluid–solid coupling. The limit $\theta_I \ll 1$ corresponds to $\mathcal{T}_s^2 \ll \mathcal{T}_f^2$, meaning that the solid does respond to the pressure change in the flow promptly. It is also helpful to note that, using equation (6.11), we can also write

$$\theta_I = \mathcal{I}_1\frac{\rho_s b^\star \xi}{\mathcal{T}_f^2\bar{E}}, \tag{6.14}$$

which indicates that, for a more rigid solid (*i.e.*, with the increase of $\bar{E}$), the solid deformation develops much faster than the flow.

Again using equation (6.11), the dimensionless tension coefficient can be written as

$$\theta_t = \frac{\chi_t\bar{\mathcal{U}}_c}{\ell^2\mathcal{P}_c} = \mathcal{I}_1\frac{\chi_t\xi}{\bar{E}\ell^2}. \tag{6.15}$$

If χ_t is deformation-induced (thus time-dependent), substituting equation (6.35) into equation (6.15), we obtain

$$\begin{aligned}\theta_t(T) &= \mathcal{I}_1\frac{\xi}{\bar{E}\ell^2}\frac{Eb^\star}{\ell}\int_0^\ell \frac{1}{2}\left(\frac{\partial\bar{u}_y}{\partial z}\right)^2 \mathrm{d}z \\ &= (1-\nu_s^2)\mathcal{I}_1\frac{\xi b^\star\bar{\mathcal{U}}_c^2}{\ell^4}\int_0^1 \frac{1}{2}\left(\frac{\partial\bar{U}_Y}{\partial Z}\right)^2 \mathrm{d}Z \\ &= \tilde{\theta}_t\int_0^1 \frac{1}{2}\left(\frac{\partial\bar{H}}{\partial Z}\right)^2 \mathrm{d}Z,\end{aligned} \tag{6.16}$$

Table 6.1. The dimensional and dimensionless parameters of the 1D FSI model.

Quantity	Notation	Typical value	Units
channel's length	ℓ	1.0	cm
channel's undeformed height	h_0	30	µm
channel's width	w	500	µm
top wall's thickness	t	2.0	mm
solid's Young's modulus	E	See table 6.2	MPa
solid's Poisson's ratio	ν	0.5	–
solid's density	ρ_s	1.0×10^3	$\mathrm{kg\,m^{-3}}$
fluid's density	ρ_f	1.0×10^3	$\mathrm{kg\,m^{-3}}$
fluid's dynamic viscosity	μ	1.0×10^{-3}	Pa s
inlet flow rate	q	See table 6.2	$\mathrm{\mu L\,min^{-1}}$
effective interface thickness	$b^\star$	$0.6141w = 307.05$	µm
channel's height-to-length ratio	$\epsilon = h_0/\ell$	0.003	–
channel's height-to-width ratio	$\delta = h_0/w$	0.06	–
reduced Reynolds number	$\hat{R}\mathrm{e} = \epsilon\rho q/(w\mu)$	See table 6.2	–
FSI parameter	$\beta = \mathcal{I}_1\mathcal{P}_c\xi/(\bar{E}h_0)$	See table 6.2	–
solid's inertia coefficient	$\theta_I = \epsilon\hat{R}\mathrm{e}\beta b^\star\rho_s/(\ell\rho_f)$	See table 6.2	–
tension coefficient	$\theta_t(T)$	Variable	–
(deformation-induced)	$= \tilde{\theta}_t \int_0^1 \frac{1}{2}\left(\frac{\partial \bar{H}}{\partial Z}\right)^2 \mathrm{d}Z$	($\tilde{\theta}_t$ in table 6.2)	–

where

$$\tilde{\theta}_t = \frac{1}{\beta^2} \times (1-\nu_s^2)\mathcal{I}_1 \frac{\xi b^\star \bar{\mathcal{U}}_c^2}{\ell^4} = (1-\nu_s^2)\mathcal{I}_1\epsilon^2\frac{\xi b^\star}{\ell^2}. \tag{6.17}$$

Note that we have used equation (6.10) in the last step of the manipulations in equation (6.16). Also, note that $\tilde{\theta}_t$ is not related to the flow conditions, and $\tilde{\theta}_t \ll 1$ for microchannels. Within linear elasticity, the integral in equation (6.16) is $\mathcal{O}(1)$, thus $\theta_t \ll 1$.

Finally, the key dimensional and dimensionless parameters are summarized in table 6.1. Typical values for microfluidic systems are given to justify the bigness/smallness assumptions made.

Table 6.2. The dimensional and dimensionless parameters for the exemplar cases considered.

Case	E (MPa)	q ($\mu\mathrm{L\,min^{-1}}$)	$\hat{R}\mathrm{e}$ (–)	β (–)	θ_I (–)	$\tilde{\theta}_t$ (–)
C1	1	1500	0.15	0.1256	1.7360×10^{-6}	5.6245×10^{-9}
C2	1	6000	0.60	0.5026	2.7775×10^{-5}	5.6245×10^{-9}
C3	1	9000	0.90	0.7538	6.2495×10^{-5}	5.6245×10^{-9}
C4	2	1500	0.15	0.0628	8.6798×10^{-7}	5.6245×10^{-9}
C5	2	6000	0.60	0.2513	1.3888×10^{-5}	5.6245×10^{-9}
C6	2	9000	0.90	0.3769	3.1247×10^{-5}	5.6245×10^{-9}

6.1.4 Initial and boundary conditions

Equations (6.8a), (6.8b), (6.12) and (6.10) define a 1D FSI model. In this work, we consider the case in which the flow rate at the inlet is fixed, while the pressure at the outlet is set to gauge, *i.e.*,

$$Q(0,T) = 1, \qquad P(1,T) = 0. \tag{6.18}$$

Also, there are no displacements at the inlet and the outlet of the channel:

$$\bar{U}_Y(0,T) = \bar{U}_Y(1,T) = 0 \quad \Rightarrow \quad \bar{H}_Y(0,T) = \bar{H}_Y(1,T) = 1. \tag{6.19}$$

Initially, we assume the wall is undeformed and the flow is uniform through the channel, *i.e.*,

$$Q(Z,0) = 1, \qquad \bar{U}_Y(Z,0) = 0 \quad \Rightarrow \quad \bar{H}_Y(Z,0) = 1. \tag{6.20}$$

6.2 Examplar cases and preview of results

The remainder of this paper is concerned with the steady-state features, the dynamic response, and also the linear stability of the non-flat steady state of the proposed 1D FSI model. To explore these issues, we have chosen exemplar cases with typical dimensional and dimensionless values given in table 6.1 and table 6.2. The values for the geometrical and material properties are taken and/or modified from [12]. The long and shallow microchannels

Table 6.3. Qualitative comparison between the experimental observations of [41] and the predictions of the proposed global 1D FSI model.

<table>
<tr><th></th><th>Experimental observation</th><th>Proposed 1D FSI model behavior</th></tr>
<tr><td>Steady</td><td>Wall deformation is nonuniform along the streamwise direction.
There is a sharp diverging section after the channel entrance, followed by a longer converging section tapering towards the outlet.</td><td>The steady-state pressure and deformation profiles vary along streamwise direction.
For weak axial tension, the channel expands sharply near the inlet, reaching a maximum deformation. Then, the deformation tapers out towards the outlet. This is due to the equation of the fluid–solid interface exhibiting a boundary-layer-like behavior for $\theta_t \ll 1$.</td></tr>
<tr><td>Dynamic</td><td>Dye injected in the flow oscillates/breaks up at $Re \simeq 100$ and $\hat{R}e \simeq 1$. The dye is observed to break up first in the converging section near the channel outlet.
In the mixing experiments, vigorous mixing is observed downstream in the converging section at $Re \simeq 100$ and $\hat{R}e \simeq 1$.
Under the same flow rate, the mixing in the more compliant channel is observed to be more complete.
The wall oscillates as the dye breakup (instability) is observed.</td><td>The base (steady) solution becomes linearly unstable to infinitesimal perturbations at $Re \simeq 100$ and $\hat{R}e \simeq 1$.
The global unstable modes are highly oscillatory, with frequencies close to the natural frequency of the wall. The eigenfunctions are highly oscillatory in space, with the shape changing more dramatically near the outlet than that near the inlet.
Under the same flow rate, the softer channel has larger growth rate for the most unstable mode.
Self-sustained wall oscillations can be triggered in the linearly unstable cases. The wall oscillations have a peak frequency close to the natural frequency of the wall, and are found to be more violent near the channel outlet.</td></tr>
</table>

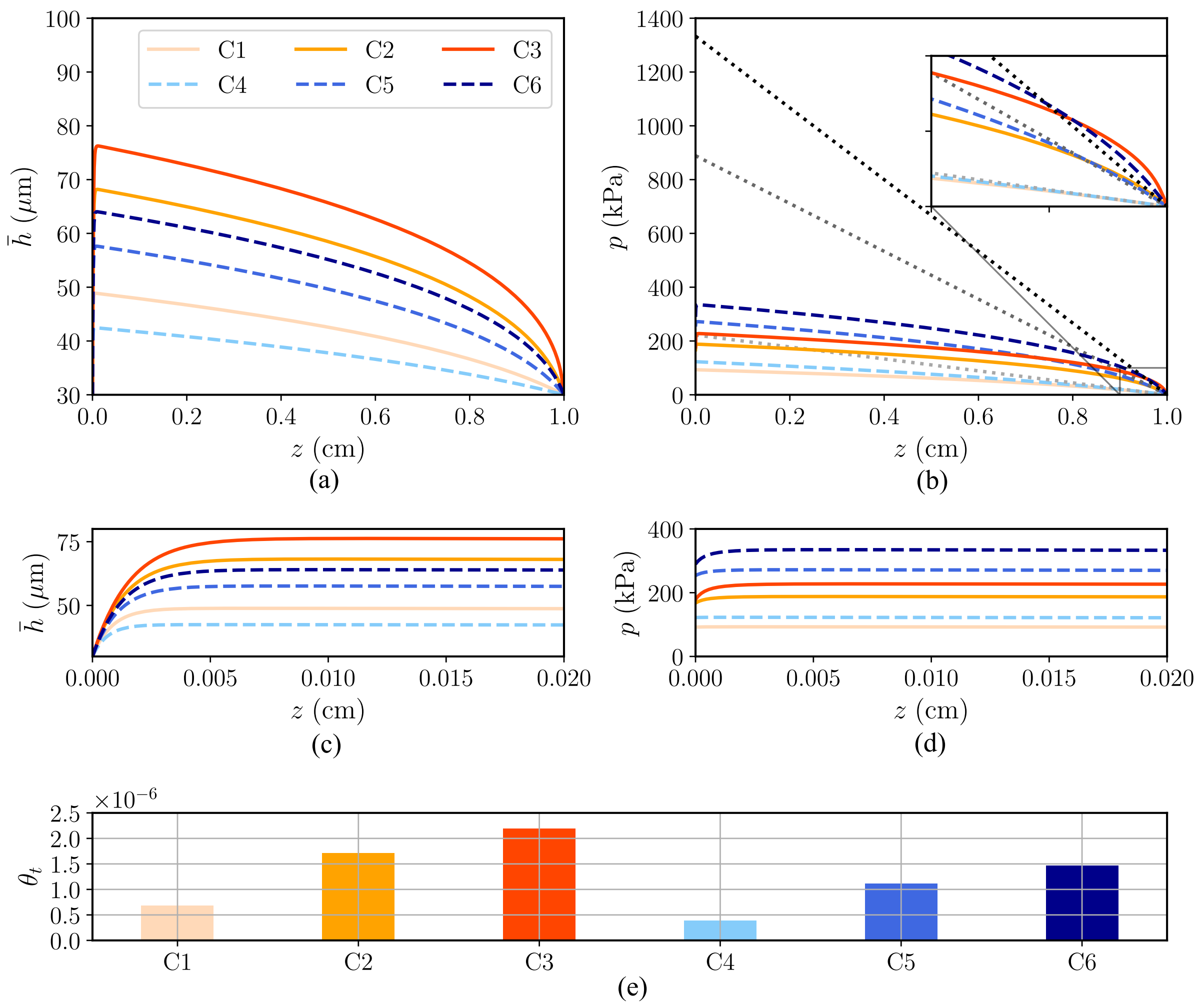

Figure 6.2. The steady-state response for the exemplar cases from table 6.2, for flow rates or $q = 1500,\ 6000,\ 9000\ \mu\mathrm{L\,min}^{-1}$ (higher q corresponds to darker curves). (a) The variation of the deformed channel height along z. (b) The pressure distribution along z, with the inset window showing a zoom-in view near the $z = \ell$. The dotted lines show the Hagen–Poiseuille law for a rigid channel (linearly variation or p along z). Panels (c) and (d) show zoomed-in views for $\bar{h}$ and p near the inlet, $z = 0$, respectively. (e) The computed θ_t of the exemplar cases from table 6.2.

are assumed fabricated via soft lithography, with a thick top wall. The leading-order steady response of such microchannels has been solved in chapter 4 [101], according to which, $\mathcal{I}_1 = 0.542754$ and $\xi = w$ for calculating β in table 6.2.

Similar to the experiments of Verma and Kumaran [41], cases C1 to C3 and C4 to C6 summarized in table 6.2 are each based on a single microchannel, operated under different flow conditions. As catalogued in table 6.3, the steady and dynamic responses of the new 1D FSI model match several experimental observations qualitatively, which indicates that the proposed model can provide unique insights into this unstable FSI problem. However, we cannot perform direct quantitative comparisons between our 1D model and the experiments of Verma and Kumaran [41], for the following reasons. First, the experiments' soft wall was compressed upon a rigid outer surface, unlike our model wherein a soft wall that bulges outwards in an unconstrained manner (being stress-free on its outer surface). Further, in the experiments, the wall thickness was comparable to the channel's width, with two side walls made rigid. Consequently, the deformation field within the compliant wall in the microchannels fabricated by Verma and Kumaran [41] is described by a different leading-order theory of the flow-induced deformation than the theories considered herein. At this time, it is not clear whether an exact solution (along the lines of chapter 4 [101]) could be obtained for the deformation in the configuration fabricated by Verma and Kumaran [41]. The main difference would be in the definition of β. Nevertheless, since the experiments did consider long and shallow microchannels with a slender deformable wall, the assumptions made in chapter 3 and section 6.1 apply. Therefore, the FSI *physics* in these experiments are expected to be captured by the theoretical framework proposed herein. Indeed, as discussed by Verma and Kumaran [41], the FSI-induced instabilities are generic, thus are not expected to be an "accidental" phenomenon occurring only in some specific experimental devices. It follows that our qualitative comparisons below are meaningful and useful for validating the proposed 1D FSI model.

6.3 Base state: features of the inflated microchannel at steady state

The steady response with weak tension effects included has been discussed in chapter 5. In this section, we will compute the steady state of the cases in table 6.2. Note that we consider the deformation induced tension computed by equation (6.16).

At steady state, all the time derivatives vanish. From equation (6.8a), we have $Q \equiv 1$, upon imposing the fixed-flux upstream boundary condition from equation (6.18). The remaining equations (6.12), (6.10) and (6.8b), together with the unsatisfied boundary con-

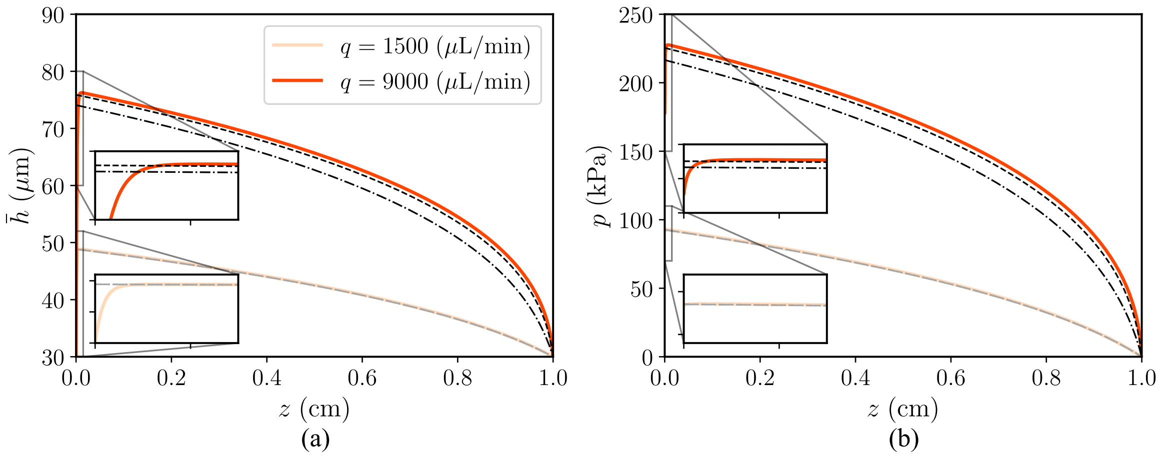

Figure 6.3. Comparison between the numerical solutions of the proposed 1D FSI model and previously reported analytical results for the exemplar cases of C1 and C3. (a) the deformed channel height along z. (b) the pressure distribution along z. The solid curves represent the numerical simulation of the 1D FSI model at steady state. The dash-dotted curves represent the results calculated by equation (6.23) with $\hat{R}\mathrm{e} = 0$ and $\theta_t = 0$. The dashed curves are calculated from equation (6.24), in which $\theta_t = 0$ but $\hat{R}\mathrm{e} = \mathcal{O}(1)$.

ditions from equations (6.18) and (6.19), constitute a nonlinear two-point boundary value problem [167]. This nonlinear system is solved using the `newton_krylov` routine from the SciPy stack [106], following the procedure described in section 6.B.

Also, note that equations (6.12), (6.10) and (6.8b) can be combined to form a single equation, in terms of the steady-state deformed height $\bar{H}_0$, written as

$$\frac{6}{5}\hat{R}\mathrm{e}\frac{1}{\bar{H}_0^3}\frac{\mathrm{d}\bar{H}_0}{\mathrm{d}Z} = \frac{1}{\beta}\left(\frac{\mathrm{d}\bar{H}_0}{\mathrm{d}Z} - \theta_t\frac{\mathrm{d}^3\bar{H}_0}{\mathrm{d}Z^3}\right) + \frac{12}{\bar{H}_0^3}. \tag{6.21}$$

Equation (6.21) is exactly the same as equation (5.47). The boundary conditions for this third-order nonlinear ordinary differential equation (ODE) are

$$\bar{H}_0(Z=0) = \bar{H}_0(Z=1) = 1, \qquad \left.\frac{\mathrm{d}^2\bar{H}_0}{\mathrm{d}Z^2}\right|_{Z=1} = 0, \tag{6.22}$$

which correspond to zero displacement imposed at $Z = 0, 1$, along with the gauge-pressure boundary condition at the outlet.

The steady responses of the exemplar cases from table 6.2 are shown in figure 6.2. The nonuniform deformation of the channel height is shown in figure 6.2(a), along with a zoom-in view near the inlet given in figure 6.2(c). The channel inflates more for larger flow rates and/or for softer walls (*i.e.*, with smaller E). For each case, there is a sharp diverging section near the channel inlet, and a much longer converging section connecting to the channel outlet, which agrees with the experimental observations of Verma and Kumaran [41]. As for the pressure distribution, figure 6.2(b) shows that the compliance of the wall leads to a non-uniform pressure gradient so that the pressure varies nonlinearly with z. Furthermore, compared to the case of flow in the rigid channel, the total pressure drop is reduced significantly due to the expanded cross-sectional area resulting from the deformation of the wall. This phenomenon has been addressed and analyzed, considering different geometrical configurations and elastic response, but typically limited to the case of $\hat{R}\mathrm{e} \to 0$ [see, *e.g.*, 30]. However, our proposed 1D FSI model pushes the limit to $\hat{R}\mathrm{e} = \mathcal{O}(1)$. Figure 6.2(d) also zooms into the neighborhood of the channel inlet. As the flow rate increases, a small region of positive pressure gradient appears. The reason for this effect is that, the sharp expansion of the channel's cross-section near the inlet makes the local velocity drop quickly (recall that $Q \equiv 1$ at steady state), and the positive pressure gradient aids in the deceleration of the flow [102], [114]. Finally, the deformation-induced weak tension coefficients of the exemplar cases are shown in figure 6.2(e). We observe that θ_t increases as the flow rate increases because higher flow rates induce larger deformations. Moreover, for the same flow conditions, it is observed that θ_t is larger when the wall is more compliant.

Next, to address the effect of $\hat{R}\mathrm{e}$ and θ_t, we compare the numerical results of the current 1D FSI model with the analytical results discussed in chapter ch:work3. At this stage, θ_t is fixed to be the corresponding values from figure 6.2(e). First, taking $\hat{R}\mathrm{e} \to 0$ and neglecting θ_t, the pressure distribution and the deformation at steady state [114] are

$$P_0(Z) = \frac{1}{\beta}\left\{[48\beta(1-Z)+1]^{1/4} - 1\right\}, \qquad \bar{H}_0(Z) = 1 + \beta P_0(Z). \tag{6.23}$$

Equation (6.23) is the essentially the same as the model proposed by Gevais *et al.* [12]. However, in the current theoretical framework, β is obtained by solving an appropriate linear elasticity problem, instead of being calibrated by an experiment. Second, if only θ_t is neglected but $\hat{R}\mathrm{e} = \mathcal{O}(1)$, the steady-state pressure distribution [114] is

$$P_0(Z)\left[1 + \frac{3}{2}\beta P_0(Z) + \beta^2 P_0^2(Z) + \frac{1}{4}\beta^3 P_0^3(Z) - \frac{6}{5}\hat{R}\mathrm{e}\beta\right] = 12(1-Z), \tag{6.24a}$$

$$\bar{H}_0(Z) = 1 + \beta P_0(Z). \tag{6.24b}$$

Observe that equation (6.24) reduces to equation (6.23) for $\hat{R}\mathrm{e} \to 0$. Finally, we mention that if both $\theta_t, \hat{R}\mathrm{e} \neq 0$, equation (6.21) is essentially a singular perturbation problem, which can be solved using the method of matched asymptotic expansions. Specifically, in section 5.A of chapter 5, we showed that there exists a boundary layer near $Z = 0$ of thickness $\mathcal{O}(\theta_t^{1/2})$, and obtained a matched asymptotic solution, which is too lengthy to summarize here.

In figure 6.3, we show a comparison between the steady-state solution obtained by numerical simulation of the 1D FSI model and the analytical results mentioned above. For a low flow rate, with $\hat{R}\mathrm{e} = 0.15$, the fluid inertia is not important, thus the numerical results agree well with the analytical results, except near the inlet. In contrast, for a high flow rate, with $\hat{R}\mathrm{e} = 0.9$, the results neglecting the effect of $\hat{R}\mathrm{e}$ (based on equation (6.23)) tend to underestimate the channel deformation and the pressure distribution. Since equations (6.23) and (6.24) do not take into account the weak tension effect, the no-displacement restriction at the inlet is not satisfied. With θ_t included, whether the flow rate is low or high, a short diverging section of the channel height emerges near the inlet, indicating the feature of a boundary layer problem described above.

6.4 Linear stability of the inflated base state

In this section, we address the linear stability of the base (steady-state) solutions obtained in section 6.3. We have shown, in figure 6.2, that both the deformation and the pressure gradient are nonuniform along z in the inflated (non-flat) base state. This observation makes the linear stability problem nontrivial, as the linearized operators have variable coefficients and are not self-adjoint. The key question that this section will address is: is the non-flat base state linearly stable to infinitesimal perturbations?

To answer this question, we perturb the base state with an infinitesimal disturbance as:

$$Q(Z,T) = Q_0 + \alpha\hat{Q}(Z,T), \qquad \bar{H}(Z,T) = \bar{H}_0(Z) + \alpha\hat{H}(Z,T), \tag{6.25}$$

with $\alpha \ll 1$. Note $Q_0 = 1$ for fixed flux upstream. Substituting the above into the governing equations (6.8) and (6.12), and keeping terms up to $\mathcal{O}(\alpha)$, we obtain the following linear evolution equations:

$$\frac{\partial\hat{H}}{\partial T} + \frac{\partial\hat{Q}}{\partial Z} = 0, \tag{6.26a}$$

$$\begin{aligned}\frac{\hat{R}\mathrm{e}\beta}{\bar{H}_0}\frac{\partial\hat{Q}}{\partial T} + \frac{6}{5}\hat{R}\mathrm{e}\beta\left[\left(\frac{3Q_0^2}{\bar{H}_0^4}\frac{\mathrm{d}\bar{H}_0}{\mathrm{d}Z} - \frac{Q_0^2}{\bar{H}_0^3}\frac{\partial}{\partial Z}\right)\hat{H} + \left(-\frac{2Q_0}{\bar{H}_0^3}\frac{\mathrm{d}\bar{H}_0}{\mathrm{d}Z} + \frac{2Q_0}{\bar{H}_0^2}\frac{\partial}{\partial Z}\right)\hat{Q}\right]& \\ + \theta_I\frac{\partial^3\hat{H}}{\partial Z\partial T^2} + \frac{\partial\hat{H}}{\partial Z} - \theta_t\frac{\partial^3\hat{H}}{\partial Z^3} + 12\beta\left(\frac{\hat{Q}}{\bar{H}_0^3} - \frac{3Q_0}{\bar{H}_0^4}\hat{H}\right) = 0.&\end{aligned} \tag{6.26b}$$

We further note that θ_t in the above equation is fixed to be the steady-state value rather than computed from equation (6.16), *i.e.*, we have neglected any modifications of θ_t introduced by the initial perturbations. It can be shown (see section 6.5.1) that this effect is negligible.

In this work, we only consider the asymptotic behavior of infinitesimal initial perturbations, *i.e.*, the modal analysis. To this end, we write

$$\hat{Q}(Z,T) = \widetilde{Q}(Z)\mathrm{e}^{-\mathrm{i}\omega_G T}, \qquad \hat{H}(Z,T) = \widetilde{H}(Z)\mathrm{e}^{-\mathrm{i}\omega_G T}. \tag{6.27}$$

Since the base state is non-flat, the eigenfunctions $\widetilde{Q}$ and $\widetilde{H}$ are not homogeneous in Z. Then, $\omega_G \in \mathbb{C}$ denotes the "global" growth/decay rate of the eigenmode [176].

For computational convenience, equation (6.26) is rewritten in matrix form as

$$\underbrace{\begin{pmatrix} 0 & \frac{\mathrm{d}}{\mathrm{d}Z} \\ \mathscr{L}_H & \mathscr{L}_Q \end{pmatrix}}_{\boldsymbol{A}} \underbrace{\begin{pmatrix} \widetilde{H} \\ \widetilde{Q} \end{pmatrix}}_{\boldsymbol{\psi}} = \mathrm{i}\omega_G \underbrace{\begin{pmatrix} 1 & 0 \\ 0 & \frac{\hat{R}\mathrm{e}\beta}{\bar{H}_0} - \theta_I\frac{\mathrm{d}^2}{\mathrm{d}Z^2} \end{pmatrix}}_{\boldsymbol{B}} \underbrace{\begin{pmatrix} \widetilde{H} \\ \widetilde{Q} \end{pmatrix}}_{\boldsymbol{\psi}}, \tag{6.28}$$

with the operators $\mathscr{L}_H$ and $\mathscr{L}_Q$ defined as

$$\mathscr{L}_H = \frac{6}{5}\hat{R}\mathrm{e}\beta\left(\frac{3Q_0^2}{\bar{H}_0^4}\frac{\mathrm{d}\bar{H}_0}{\mathrm{d}Z} - \frac{Q_0^2}{\bar{H}_0^3}\frac{\mathrm{d}}{\mathrm{d}Z}\right) + \frac{\mathrm{d}}{\mathrm{d}Z} - \theta_t\frac{\mathrm{d}^3}{\mathrm{d}Z^3} - \frac{36\beta Q_0}{\bar{H}_0^4}, \tag{6.29a}$$

$$\mathscr{L}_Q = \frac{6}{5}\hat{R}\mathrm{e}\beta\left(-\frac{2Q_0}{\bar{H}_0^3}\frac{\mathrm{d}\bar{H}_0}{\mathrm{d}Z} + \frac{2Q_0}{\bar{H}_0^2}\frac{\mathrm{d}}{\mathrm{d}Z}\right) + \frac{12\beta}{\bar{H}_0^3}. \tag{6.29b}$$

Note that $\mathscr{L}_H$ and $\mathscr{L}_Q$ are linear operators with *non-constant* coefficients, as a consequence of the non-flat base state. Also note in $\boldsymbol{B}$, $\theta_I\mathrm{d}^2\widetilde{Q}/\mathrm{d}Z^2$ originates from $\theta_I\partial^3\hat{H}/(\partial Z\partial T^2) = \theta_I\partial^3\hat{Q}/(\partial Z^2\partial T)$, using equation (6.26a).

Since the base state has satisfied all the boundary conditions from equations (6.18) and (6.19). The boundary conditions for the infinitesimal perturbations are homogeneous:

$$\widetilde{Q}|_{Z=0} = \left.\frac{\mathrm{d}\widetilde{Q}}{\mathrm{d}Z}\right|_{Z=0} = \left.\frac{\mathrm{d}\widetilde{Q}}{\mathrm{d}Z}\right|_{Z=1} = 0, \tag{6.30a}$$

$$\widetilde{H}|_{Z=0} = \widetilde{H}|_{Z=1} = \left.\frac{\mathrm{d}^2\widetilde{H}}{\mathrm{d}Z^2}\right|_{Z=1} = 0. \tag{6.30b}$$

The first boundary condition is deduced from the fixed flux upstream boundary condition, while the boundary conditions in terms of $\widetilde{H}$ correspond to the no-displacement restrictions at both ends and the outlet pressure set to gauge. The remaining two boundary conditions on $\widetilde{Q}$ are derived from the equation (6.8a) by imposing zero displacement at the channel inlet and outlet.

Equation (6.28) subject to equation (6.30) gives rise to a generalized eigenvalue problem, which can be solved numerically using the Chebyshev pseudospectral method (see section 6.C for details). For all the eigenmodes resolved, if the corresponding $\mathrm{Im}(\omega_G) > 0$, we say the non-flat base state of the 1D FSI model is linearly unstable to infinitesimal disturbances.

Table 6.4. Dimensionless eigenvalues, ω_G, for the pure decay modes and for the least unstable modes of the exemplar cases from table 6.2.

Case	Pure decay mode	Least stable mode
C1	-5.5501i	–
C2	-2.8538i	$202.3535 + 0.1393$i
C3	-1.9762i	$134.2670 + 1.3892$i
C4	-8.0068i	–
C5	-4.1750i	$284.8114 + 0.0637$i
C6	-3.0423i	$189.2292 + 0.5867$i

6.4.1 Eigenspectra of the exemplar cases

Here, it is illustrative to plot *dimensional* quantities to show how a corresponding physical system would behave. To this end, we write the dimensional frequency as

$$f_g = \frac{\omega_G}{2\pi\mathcal{T}_f} = \frac{\omega_G q}{2\pi \ell w h_0}. \tag{6.31}$$

Note that $f_g \in \mathbb{C}$, such that $\mathrm{Re}(f_g)$ is the oscillatory frequency of the corresponding eigenmode, *i.e.*, $[\widetilde{H}, \widetilde{Q}]^\top$ in our formulation, while $\mathrm{Im}(f_g)$ is the eigenmode's grow/decay time constant.

On the other hand, since equation (6.12) essentially represents a mechanical oscillator, the dimensionless and dimensional natural frequency of the oscillator, denoted as F_N and f_n respectively, can be approximated as

$$F_N = \frac{1}{2\pi\sqrt{\theta_I}}, \qquad f_n = \frac{F_N}{\mathcal{T}_f} = \frac{F_N q}{\ell w h_0}. \tag{6.32}$$

Unlike f_g, both $F_N, f_n \in \mathbb{R}$. Also note that, equation (6.32) does not take the tension effect into account, but since tension is weak, we believe equation (6.32) provides a good approximation to the natural frequency of the system.

In figure 6.4, we show the calculated eigenspectra for the six exemplar cases from table 6.2. First, observe that the eigenspectra are symmetric about the imaginary axis in the complex plane. This symmetry is a consequence of the formulation of the generalized eigenvalue

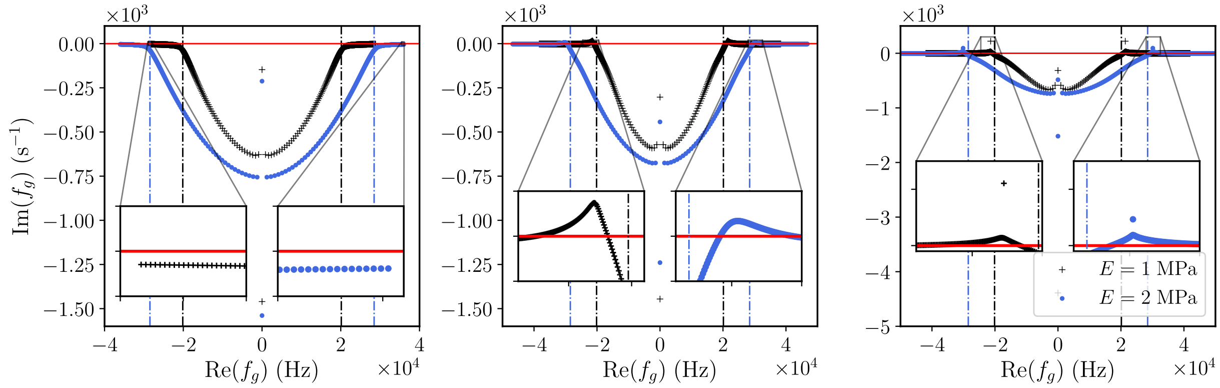

(a) (b) (c)

Figure 6.4. Eigenspectra of the exemplar cases from table 6.2: (a) $q = 1500$ µL min^{-1} (C1 and C4); (b) $q = 6000$ µL min^{-1} (C2 and C5); (c) $q = 9000$ µL min^{-1} (C3 and C6). The symbols represent the discrete eigenvalues for $E = 1$ MPa and $E = 2$ MPa respectively. The red horizontal line mark the position of real axis, *i.e.*, $\mathrm{Im}(f_g) = 0$. The dash-dotted lines mark the natural frequencies calculated by equation (6.32). The insets in each panel have the same vertical axes.

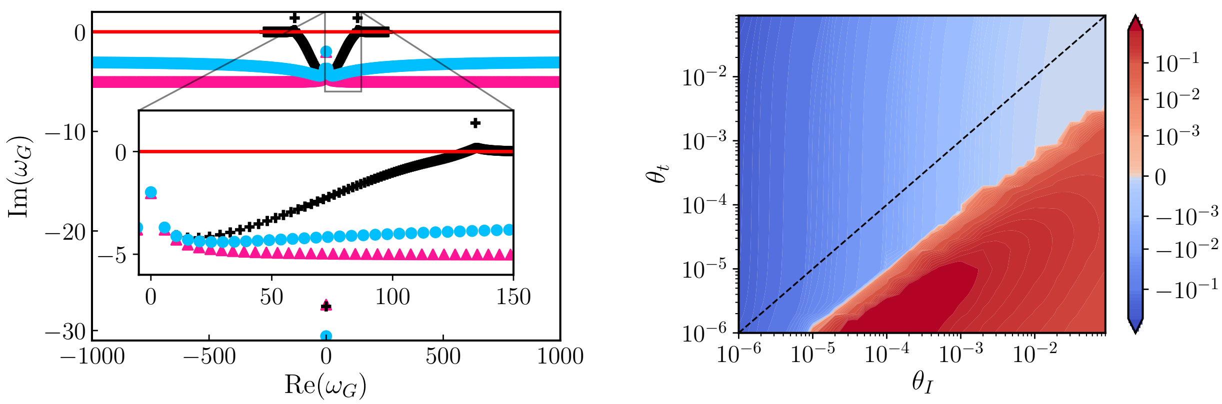

(a) (b)

Figure 6.5. (a) Comparison of the eigenspectra of the case with $\theta_I \ll 1$ and $\theta_t \ll 1$ (+), the case with $\theta_t \ll 1$ but $\theta_I = 0$ (●), and the case with $\theta_I = 0$ and $\theta_t = 0$ (▲). The dimensionless parameters are taken as per case C3 in table 6.2. (b) Contour plot of $\mathrm{Im}(\omega_G)$ of the least stable mode as a function of θ_I and θ_t, with $\hat{R}e$ and β taken from case C3 in table 6.2. The dashed line marks $\theta_I = \theta_t$.

problem (see equation (6.28)), as the matrix $\boldsymbol{A}$ on the left-hand side is purely real, while the matrix $\mathrm{i}\boldsymbol{B}$ on the right-hand side is purely imaginary. This symmetry is also a feature of the eigenvalue analyses in [102], [161].

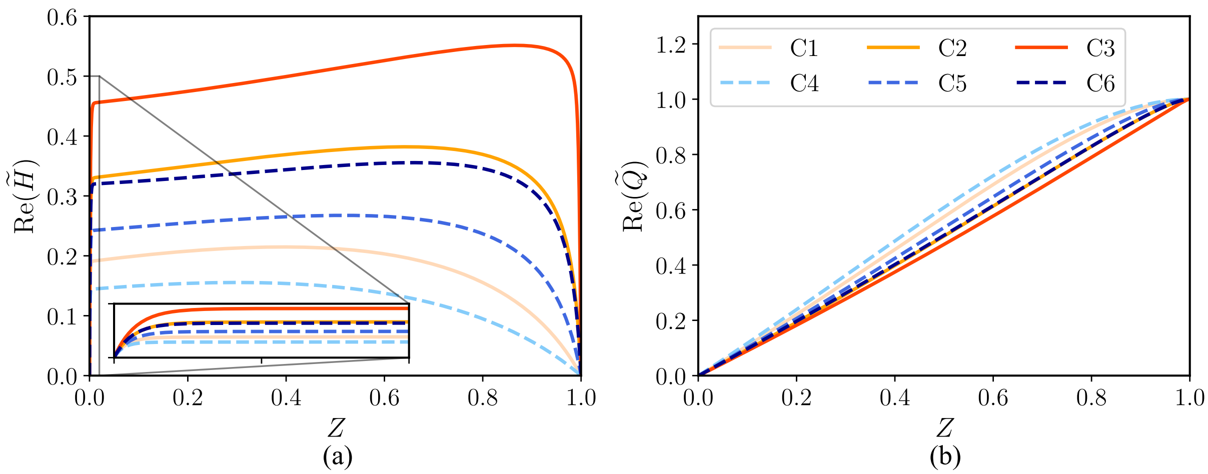

Figure 6.6. The eigenfunctions of the pure decay eigenmodes of the six exemplar cases from table 6.2. The eigenfunctions have been scaled by keeping $\max|\widetilde{Q}| = 1$.

Second, the 1D FSI system transitions from stability (panel (a)) to instability (panels (b) and (c)) as the flow rate is increased. The fluid inertia becomes more prominent as the flow rate is increased, indicated by the magnitude of $\hat{R}\mathrm{e}$, which is associated with the nonlinear terms on the left-hand side of equation (6.8b). For the six exemplar cases from table 6.2, we observe that the linear instability typically occurs for $\hat{R}\mathrm{e} \simeq 1$, or equivalently $R\mathrm{e} \simeq 100$, which is close to the values reported for the microchannel experiments showing instability [41].

Third, it is observed that the unstable regions in figure 6.4(b) and (c) are close to the natural frequency, indicating that the instabilities are related to the resonance of the wall. Due to the weak solid inertia, the natural frequency calculated from equation (6.32), as well as $\mathrm{Re}(f_g)$ in the unstable region, is as high as $\simeq 10^4$ Hz. This fact also matches the local linear stability analysis of Verma and Kumaran [41], who reported that the least stable mode oscillates at a frequency on the order of 10^4 Hz. Moreover, one of the common features of the eigenspectra in figure 6.4 is that, away from the unstable region where $|\mathrm{Re}(f_g)|$ is large, $\mathrm{Im}(f_g) \to 0^-$. This observation indicates that, apart from those modes that grow for the given flow conditions, the stable modes that oscillate with higher frequency will decay slowly, which highlights the *computational* stiffness of the 1D FSI system.

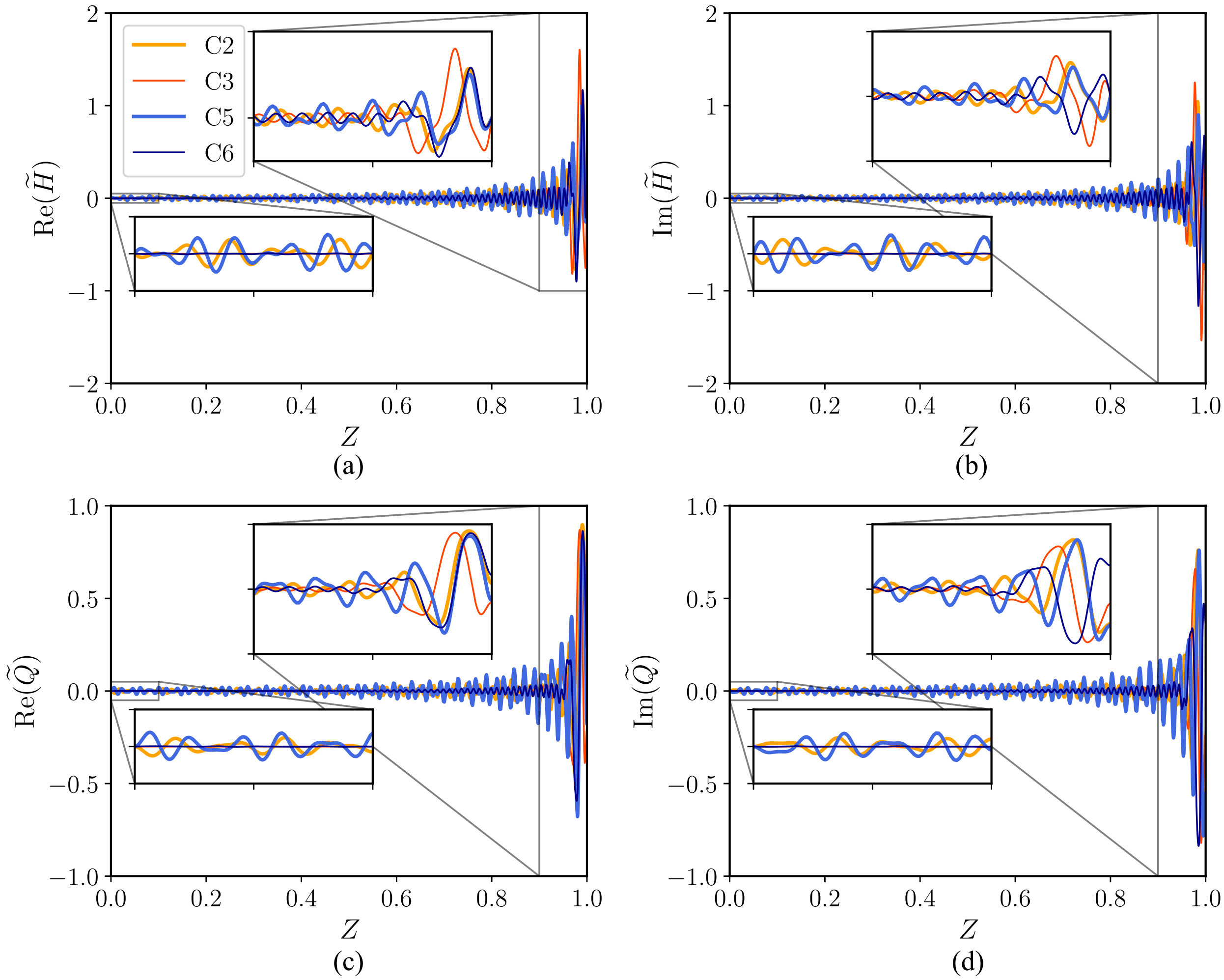

Figure 6.7. The eigenfunctions of the least stable modes for the linearly unstable cases, *i.e.*, C2, C3, C5 and C6 in table 6.2. The eigenfunctions have been scaled by keeping $\max|\widetilde{Q}| = 1$.

Lastly, the compliance of the wall does influence the shape of the eigenspectra. Since the stiffer wall has a larger natural frequency, its unstable region is located at higher frequencies than its softer counterpart. Note that in figure 6.4, the two zoom-in insets in each panel have the same range for the vertical axis. Then it can be shown that the more compliant wall has the larger growth rate (or the smaller decay rate in the linearly stable case) for the least stable mode, which could be related to the experimental observations that the softer microchannel is more prone to instabilities [41].

Since both θ_I and θ_t are small quantities in the solid mechanics equation (6.12), it would be interesting to show a comparison of the linear stability between cases either $\theta_I = 0$ or $\theta_t = 0$. We consider three different such cases: (i) $\theta_I \ll 1$ and $\theta_t \ll 1$; (ii) $\theta_I = 0$ and $\theta_t \ll 1$; (iii) $\theta_I = 0$ and $\theta_t = 0$. The base states of both case (i) and (ii) are the same, governed by equation (6.21). However, in case (iii), the system cannot satisfy $\bar{H}(0) = 0$, thus the corresponding base state should be taken from equation (6.24). As shown in figure 6.5(a), we observe that even though the solid inertia and tension are weak in the system, the inclusion of these weak effects changes the eigenspectrum fundamentally. The non-flat base state from equation (6.24) is shown to be linearly stable. With only $\theta_t \neq 0$, case (ii) can predict linear stability only while the case (i) with both $\theta_I, \theta_t \neq 0$ is linearly unstable. Furthermore, as shown in both case (ii) and (iii), for $\theta_I = 0$, the eigenmodes oscillate with higher frequencies. The reason is that, in this case, the natural frequency $F_N \to \infty$ as $\theta_I \to 0$.

To further investigate the effect of θ_I and θ_t, we calculated the growth/decay rate of the least stable mode by taking different combination of θ_I and θ_t, fixing $\hat{R}\mathrm{e}$ and β as the values corresponding to case C3. As shown in panel (b) of figure 6.5, for both θ_I and θ_t across five orders, linear instabilities are only observed when θ_I is at least one order larger than θ_t. Since the dimensionless phase speed of the transverse waves along the fluid–solid interface is $\sqrt{\theta_t/\theta_I}$, then the linear instability occurs when the transverse waves propagate (much) slower than the flow.

6.4.2 Eigenfunctions of the examplar cases

Each eigenvalue is associated with an eigenfunction pair, *i.e.*, $[\widetilde{H}, \widetilde{Q}]^\top$ via equation (6.28). For the eigenvalues with larger $|\mathrm{Re}(\omega_G)|$, the corresponding eigenfunctions are more oscillatory in space. For example, for the purely decay mode with $\mathrm{Re}(\omega_G) = 0$, the corresponding eigenfunctions are found to be purely real and non-oscillatory, as shown in figure 6.6. However, for the least stable modes of the linearly unstable cases from table 6.2, as shown in figure 6.7, with $|\mathrm{Re}(\omega_G)| \gg 1$, the corresponding eigenfunctions are highly oscillatory in space. The corresponding eigenvalues for the eigenfunctions in figure 6.6 and figure 6.7 are tabulated in table 6.4.

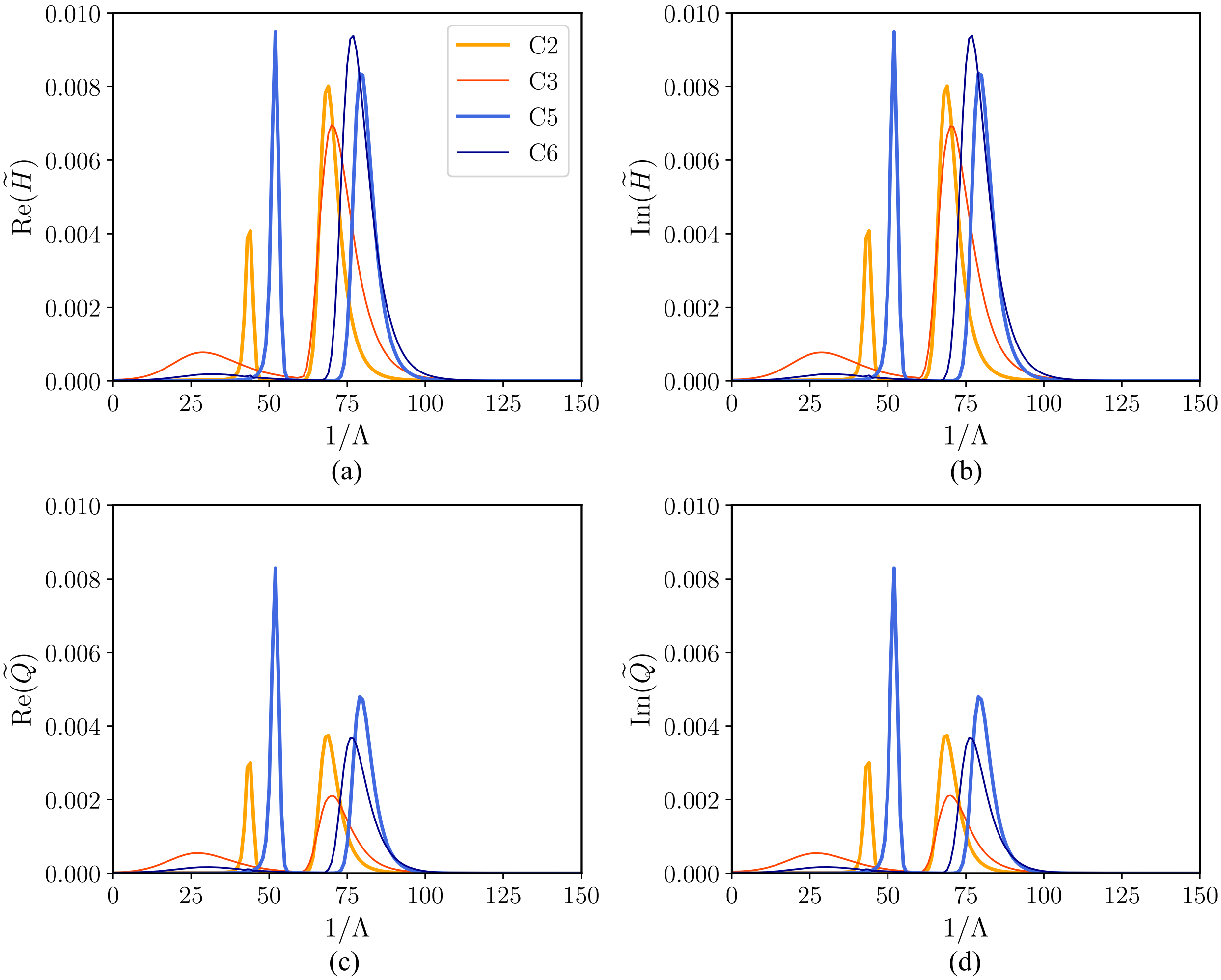

Figure 6.8. The spatial Fourier transform of the eigenfunctions from figure 6.7. Case C3 is scaled up by a factor of 10, while case C6 is scaled up a factor of 4.

We do not tabulate the least stable modes of the linearly stable cases in table 6.4 because it is hard to pick out the least stable mode due to the limitation of the numerical method. In that case, we observe that the least stable mode is always the farthest eigenvalue away from the imaginary axis, if computed with the Chebyshev pseudospectral method using different number of Gauss–Lobatto points N. In principle, there are infinite number of eigenvalues in the 1D FSI system, resolving all of which would require an infinite number of Gauss–Lobatto points. Unfortunately, N cannot be arbitrarily large because matrices in equation (6.28) will become ill-conditioned.

Let's take a closer look at the eigenfunctions of the least stable modes in figure 6.7. For all the cases, both $\widetilde{H}$ and $\widetilde{Q}$ exhibit much larger oscillations near the channel outlet ($Z = 1$), which echos the experimental observation that the instabilities were always first observed near the outlet in the converging section of the microchannel [41]. Furthermore, with larger growth rate, the difference in oscillations between the outlet and the inlet is more prominent (comparing C2 and C3, or C5 and C6).

The wavy forms of the eigenfunctions in figure 6.7 further inspire us to conduct a Fourier transform in space for each case. We have used the SciPy's `fft` routine with a Blackman window. The results are summarized in figure 6.8 and the abscissa represents the reciprocal of the dimensionless wave length, denoted by $\Lambda = \lambda/\ell$. Here, λ is the dimensional wave length. Interestingly, there are always two peaks for all the cases. The major peak is located at $1/\Lambda \simeq 100$, meaning the dominant wavelength is on the order of the channel height (recall $\ell/h_0 \approx 333$). This observation could be related to the results of the local linear stability analysis of Verma and Kumaran [41], who found that the most unstable modes have a wavelength comparable to the channel height.

6.5 Dynamic response of the microchannel

In this section, we solve the 1D FSI model, by discretizing the governing equations in space and time, to investigate the dynamic responses. The spatial discretization is based on the Chebyshev pseudospectral method [108], [110], while the "Newmark-β" method [177] is used for the time integration; see section 6.B for further details about the numerical method and its benchmarking.

6.5.1 Evolution from a perturbed inflated state

First, to validate the linear stability results from section 6.4, at $T = 0$, we perturb the steady-state solution of the 1D FSI model using the eigenfunction of a specific mode. Then, $\mathrm{Im}(\omega_G)$ indicates the decay/growth rate of the perturbation, while $2\pi/\mathrm{Re}(\omega_G)$ is the period of the perturbation's oscillations.

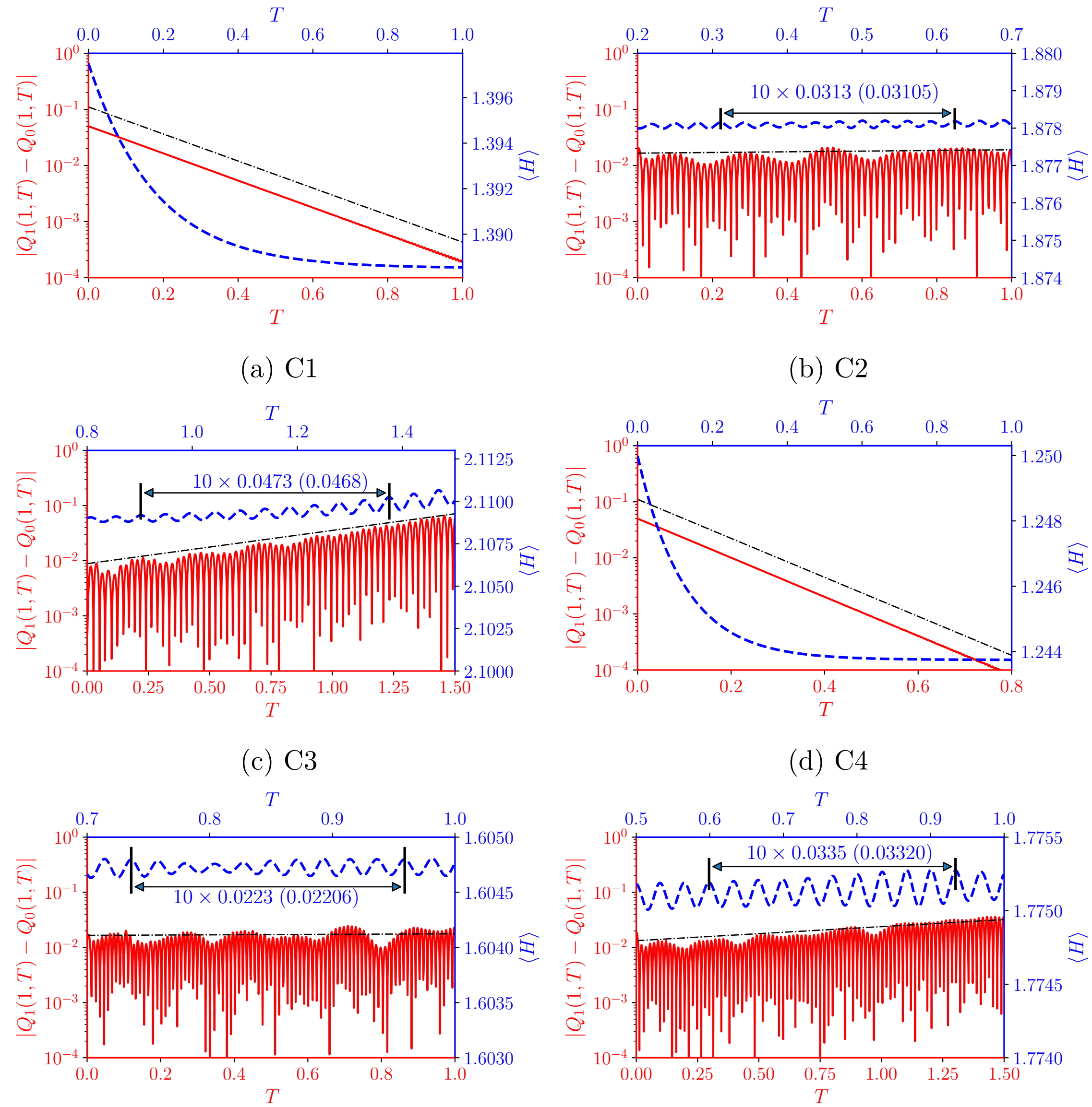

(a) C1 (b) C2

(c) C3 (d) C4

(e) C5 (f) C6

Figure 6.9. Time history of the difference between the instantaneous outlet flow rate and the steady one, *i.e.*, $|Q(1,T) - Q_0(1,T)|$ (solid, left axes), and the axially average deformed height, $\langle H \rangle = \int_0^1 \bar{H}\, \mathrm{d}Z$ (dashed, right axes). In (a) and (b), the steady state is perturbed using the eigenfunctions of the pure decay modes. In the other cases, the steady state is perturbed using the eigenfunctions of the most unstable modes. The dot-dashed trendlines represent the growth/decay of perturbations, based on the imaginary part of the eigenvalues from table 6.4. The corresponding computed periods of oscillations are marked in each panel. The value in parenthesis is from linear stability analysis, *i.e.*, $2\pi/\mathrm{Re}(\omega_G)$.

The first example is the linearly stable case C1 and $C4$ ($q = 1500\ \mu\mathrm{L\,min^{-1}}$) perturbed from the steady state with the eigenfunctions of the pure decay modes tabulated in table 6.4. The shapes of the corresponding eigenfunctions are shown in figure 6.6. The decay rate of the perturbation to the steady flow agrees well with the corresponding $\mathrm{Im}(\omega_G)$, as shown in figure 6.9(a). No oscillations are observed in the evolution of the perturbations because $\mathrm{Re}(\omega_G) = 0$ in this case.

The second example corresponds to the linearly unstable case C2, C3, C5 and C6. At $T = 0$, the steady state is perturbed at by the eigenfunction of the corresponding most unstable mode. The shape of the eigenfunctions are shown in figure 6.7, while the corresponding eigenvalues are given in table 6.4. Both the simulated growth rate and the oscillation period agree well with the linear stability analysis, as shown in figure 6.9(b). Here, note that the tension coefficient θ_t in equation (6.12) is estimated from the instantaneous wall deformation, thus it is time dependent. Meanwhile θ_t is fixed to be the steady-state value for the purposes of the linear stability analysis. The good agreement between the numerical simulation and the linear stability analysis indicates that neglecting the time dependence of θ_t for the linear stability analysis is valid.

The linear stability analysis only predicts the evolution of the perturbation in the vicinity of the steady state, *i.e.*, for early times. The simulations in section 6.5.1 are actually conducted for a longer time window. The results for cases C3 and C5 are shown in figures 6.10 and 6.11, respectively. For the time window shown, the numerical results are verified by time step refinement. All representative quantities shown in figures 6.10 and 6.11 experience high-frequency oscillations with nonlinear variations in their amplitudes. No saturated (periodic) state is found in any of the cases. Actually, beyond the given time window, the simulation results diverge when using different time step sizes, which suggests that this nonlinear dynamical system may exhibit chaotic behavior. However, pursing this possibility is beyond the scope of the present work. The most important conclusion from these simulations is that the perturbed steady state is unstable, and the system undergoes self-sustained oscillations, instead of returning to the inflated steady state.

In figure 6.10 and figure 6.11, the axially averaged deformed height (first rows), the inlet pressure and the axially averaged pressure (second rows) are observed to vary in a small

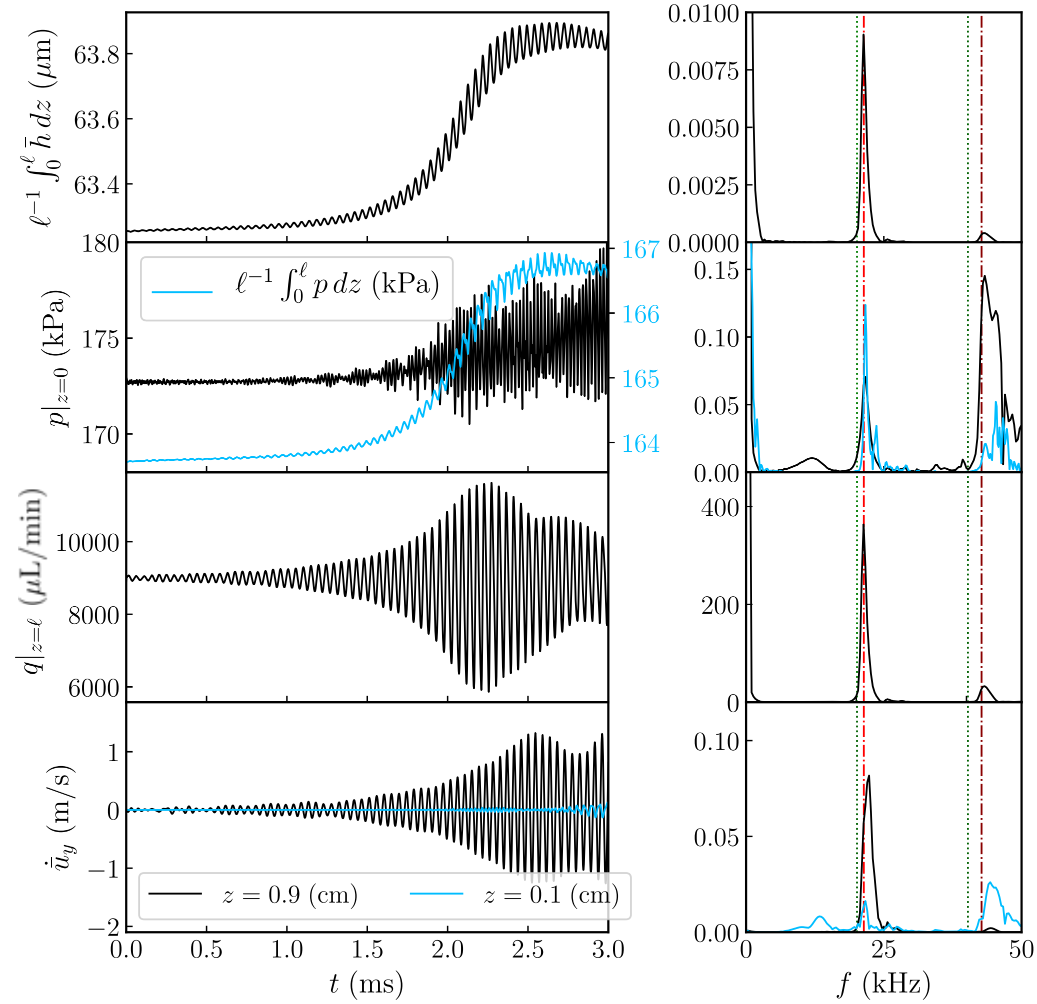

(a) (b)

Figure 6.10. Dynamic simulations of case C3, by perturbing the steady state with the eigenfunctions of the most unstable mode from table 6.4. (a) Time histories of representative quantities: the axially averaged deformed height, the inlet pressure and the axially averaged pressure, the outlet flow rate, and the vertical velocity of the interface at $z = 0.9$ cm and $z = 0.1$ cm, respectively, from top to below. (b) Fourier transform of the time signals from (a). Note that in the second and fourth rows, the vertical axis has been scaled for a clearer view. The dot-dashed lines mark f_g and $2f_g$ (see equation (6.31)), while the dotted lines mark f_n and $2f_n$ (see equation (6.32)).

range (< 1 µm for the axially averaged deformation and < 10 kPa for the pressure), which is consistent with the fact that no dramatic changes in the channel volume and the inlet pressure were reported in the experiments [41]. On the contrary, the outlet flow rate (third

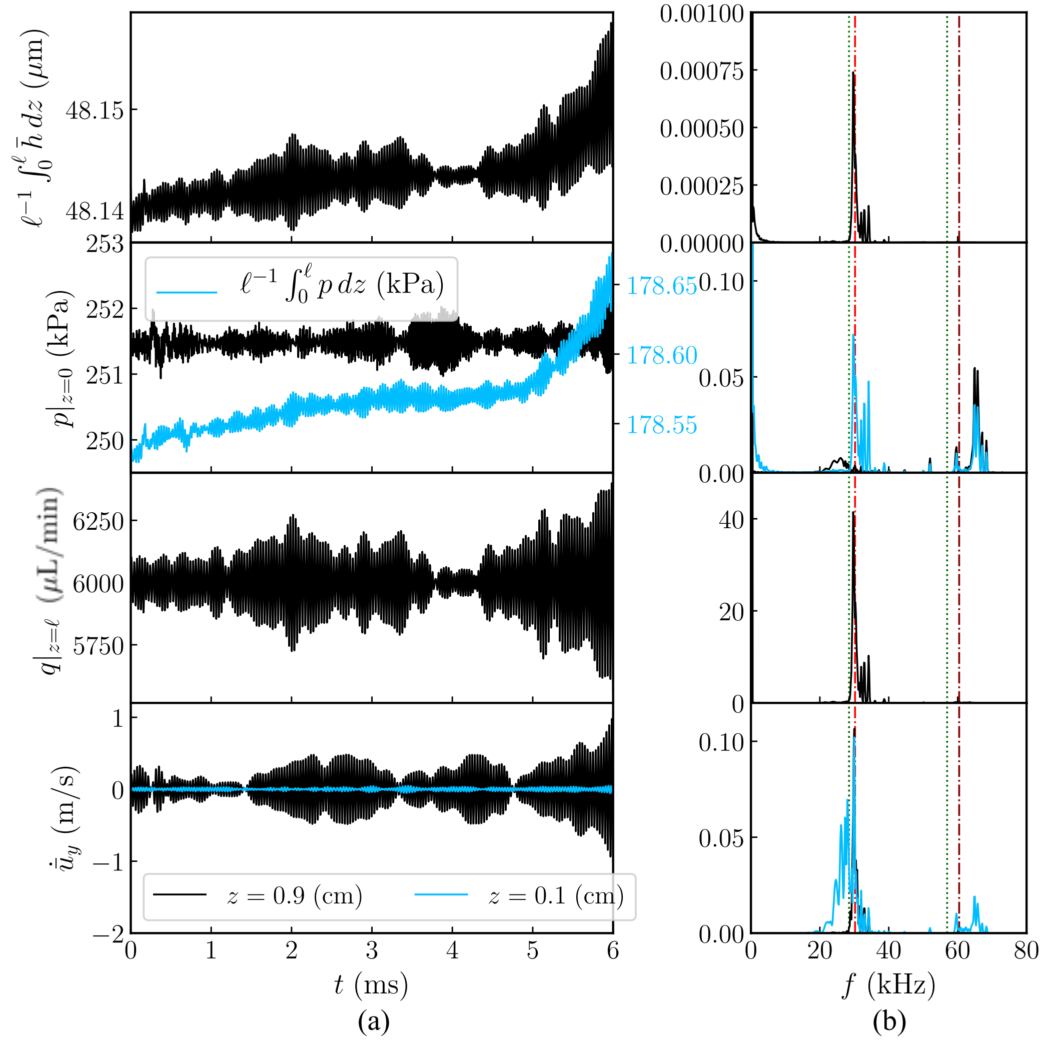

Figure 6.11. Dynamic simulations of case C5, by perturbing the steady state with the eigenfunctions of the most unstable mode from table 6.4. (a) Time histories of the representative quantities: the axially averaged deformed height, the inlet pressure and the axially averaged pressure, the outlet flow rate, and the vertical velocity of the interface at $z = 0.9$ cm and $z = 0.1$ cm, respectively, from top to below. (b) Fourier transform of the time signals from (a). Note that in the second and fourth rows, the vertical axis has been scaled to highlight the smaller-scale details. The dot-dashed lines mark f_g and $2f_g$ (see equation (6.31)), while the dotted lines mark f_n and $2f_n$ (see equation (6.32)).

rows) experiences more violent oscillations, which are prominent near the channel outlet, as shown in figure 6.7. In the fourth rows, the vertical velocity of the fluid–solid interface is shown. It is obtained based via equation (6.4) and conservation of mass (see section 6.B.2

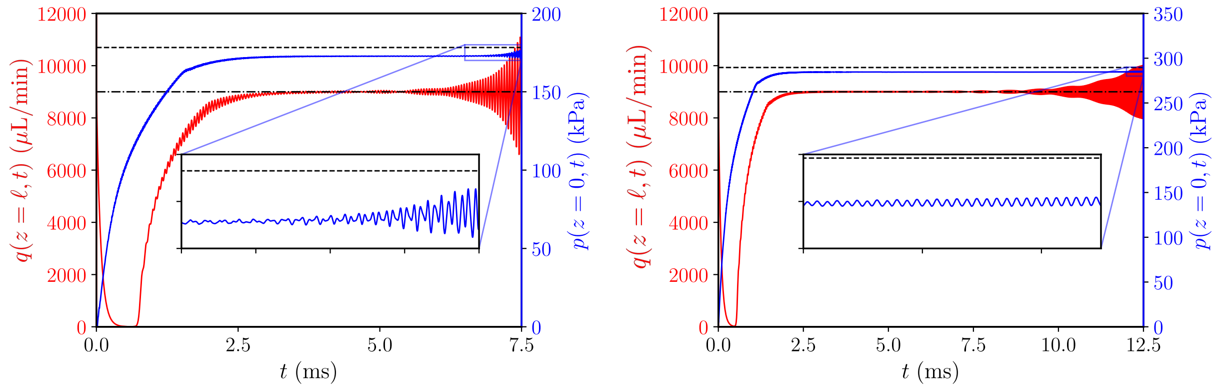

Figure 6.12. Time histories of the outlet flow rate and the inlet pressure for (a) case C3 and (b) case C6, respectively, with equation (6.20) being the initial condition. The dot-dashed lines mark the flow rate at steady state, while the dashed lines mark the inlet pressure at the steady state.

for further details). Like the flow rate, the vertical velocity of the interface is observed to experience larger oscillatory amplitude near the channel outlet than that near the channel inlet, which again matches the experimental observation that the instabilities initiate near the channel's outlet.

Figures 6.10(b) and 6.11(b) show the Fourier transform of the time history of the corresponding representative quantity. It is observed that there is a peak near f_g (see equation (6.31)), showing a good agreement with the linear stability analysis. Also observe that f_g is close to the natural frequency of the wall, f_n (see equation (6.32)), which indicates that the wall oscillations are a resonance phenomenon. Further, nonlinearity generates higher harmonics. In figure 6.10, there is another peak at $\approx 2f_g$, while in figure 6.11, the second peak is at a frequency higher than $2f_g$. The higher-frequency oscillations are more prominent near the channel inlet. For example, the second peak of the vertical velocity of the interface at $z = 0.1$ cm is taller than the first peak. Furthermore, the higher-frequency oscillations in the inlet pressure are more prominent than the lower-frequency oscillations as shown in both figures 6.10 and 6.11.

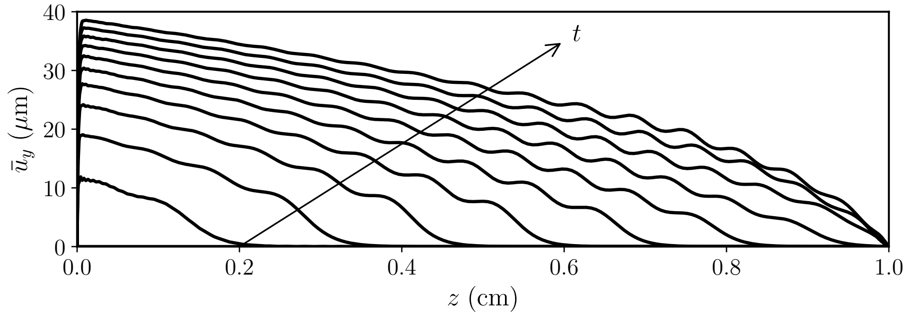

(a)

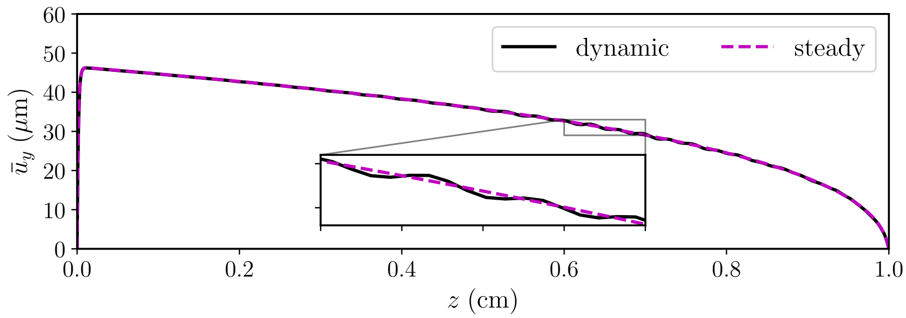

(b)

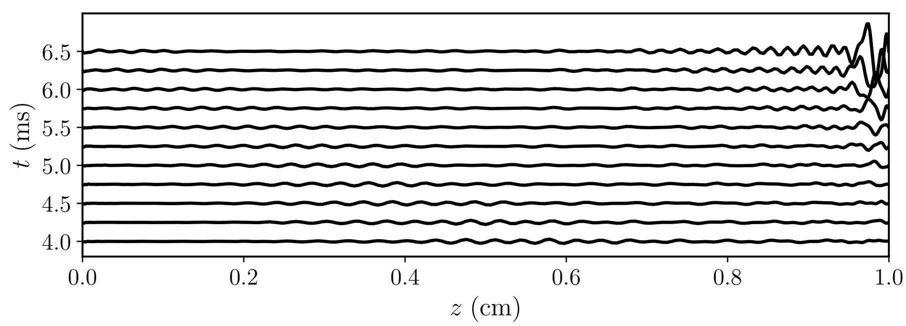

(c)

Figure 6.13. Evolution of the shape of the fluid–solid interface from the flat initial condition (6.20). (a) Shape of the interface for $0 \leq t \leq 1$ ms. (b) Comparison of the interface shape at $t = 3.5$ ms with the steady state. (c) Difference between the instantaneous interface shape $\bar{u}_y$ and the steady state $\bar{u}_y^s$, *i.e.*, $\bar{u}_y - \bar{u}_y^s$, for 4.0 ms $\leq t \leq$ 6.5 ms.

6.5.2 Evolution from a flat initial state

Starting the simulations with an undeformed channel initial condition (as in equation (6.20)) would be more realistic of how a microfluidic device might be operated. With equation

(6.20) as the initial condition, cases C1 and C4 are linearly stable and reach the steady state without detectable oscillations. The evolution of the representative quantities for case C4 are shown in figure 6.18 in section 6.B.2. In this subsection, we focus on the two linearly unstable cases C3 and C6. All of the results shown below have been verified by time step refinement (see section 6.B.2 and figure 6.19, for example).

First, the evolution of the outlet flow rate and the inlet pressure for cases C3 and C6 are shown in figure 6.12. In both cases, the outlet flow rate first decreases and then increases, reaching a value close to the imposed flow rate at late times. Meanwhile, the inlet pressure increases to a value slightly below the steady-state inlet pressure. Small-amplitude oscillations are observed in the evolution of both quantities. More importantly, the oscillations become magnified in at later times in the simulation, which suggests that these unstable cases will not reach the steady state. It can be shown (by running longer-time simulations) the that these oscillations are not unbounded. Nevertheless, similar to the cases discussed in section 6.5.1, no saturated periodic state appears to emerge during the time window of the simulations shown in this subsection.

It is more enlightening to contrast the two simulations shown in figure 6.12. For these two cases, all system parameters are the same, except that the Young's modulus for case C3 is half of that for case C6. With a more compliant wall, the instabilities under case C3 develop more quickly. Specifically, more "violent" oscillations are observed in case C3 for the outlet flow rate and the inlet pressure than in case C6. These oscillation amplitudes could be, qualitatively, representative of the observations in dye-stream experiments. In other words, dye breakup could be expected when more violent oscillations occur in softer channels, while the dye steam may just oscillate (without breaking up) if the channel is less compliant (thus, the oscillations in the flow rate and pressure are milder). Indeed, it was observed in the experiments that the dye breaks up at lower Re in softer channels [41].

Next, let us take a closer look at the evolution of the fluid–solid interface. The example in figure 6.13 corresponds to case C3 in figure 6.12 (a), while the evolution under case C6 is qualitatively similar. Initially, for $0 \leq t \leq 1$ ms as shown in figure 6.13(a), the interface bulges near the channel inlet first because the pressure is relatively high there. At the same time, transverse waves are shed and propagate from the inlet to the outlet until they are reflected at the downstream boundary of the domain. There is a dramatic increase in the total volume of fluid in the channel at this stage. Thereafter, the deformation of the wall stops growing, but the transverse waves still propagate back and forth along the fluid–solid interface. Compared with figure 6.13(a), the transverse waves have smaller wave length and amplitudes. Furthermore, the interface shape at this stage is close to the steady-state shape, as seen in figure 6.13(b). The deviation of the interface's dynamic deformation from the steady one is plotted for 4.0 ms $\leq t \leq$ 6.5 ms in figure 6.13(c), where the wave propagation can be clearly observed. Interestingly, after a while, the oscillations near the channel's outlet continue to grow and become larger than the oscillations anywhere else along the channel, which explains why the variations of the outlet flow rate appear more prominent compared than that of the inlet pressure in figure 6.12. This observation is also corroborated by the experimental observation that the instabilities always initiate near the channel's outlet.

To better emphasize the difference in the wall motions near the inlet versus near the outlet, the vertical velocities of the fluid–solid interface at $z = 0.9\ell$ (near the outlet) and $z = 0.1\ell$ (near the inlet) of case C3 and C6 are plotted in figures 6.14 and 6.14, respectively (see section 6.B.2 for the details of reconstructing the velocities). The three stages discussed in figure 6.13 can also be identified from the time histories of the vertical velocities shown in these two figures. At early times, since the wall bulges first near the channel inlet, the vertical velocity at $z = 0.1\ell$ is larger. The motion at $z = 0.9\ell$ starts after the transverse waves reach the channel outlet. In the intermediate stage, during which the channel volume does not change significantly, the oscillations at both positions remain relatively small, until the motion near the outlet becomes amplified and leads to a striking difference in the oscillatory amplitudes at the two positions.

Figures 6.14(b) 6.15(b) show the corresponding time histories in the frequency (Fourier) domain. We observe that the peak is near the natural frequency of the wall (predicted by equation (6.32)), indicating a resonant phenomenon. Due to the FSI, which gives rise to the transverse waves along the fluid–solid interface, the pressure oscillations exhibit a frequency close to the natural frequency of the wall as well, causing a feedback. Note that, the resonances are *self-excited* as no oscillatory components are introduced in the initial condition (6.20). Further, the oscillations are self-sustained as they do not die out during

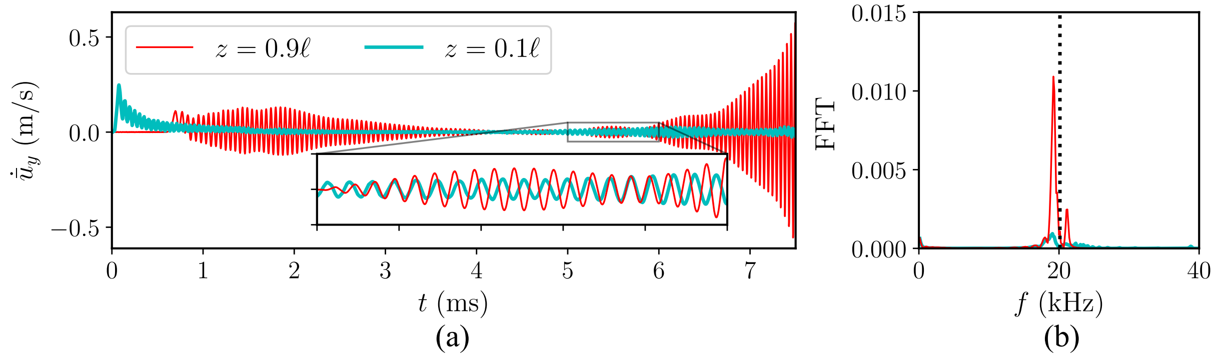

Figure 6.14. (a) Time histories of the vertical velocity of the fluid–solid interface of case C3 at $z = 0.9\ell$ (near the outlet) and $z = 0.1\ell$ (near the inlet), respectively. (b) Fourier transform of the corresponding time histories from (a). The dotted line marks the natural frequency calculated from equation (6.32).

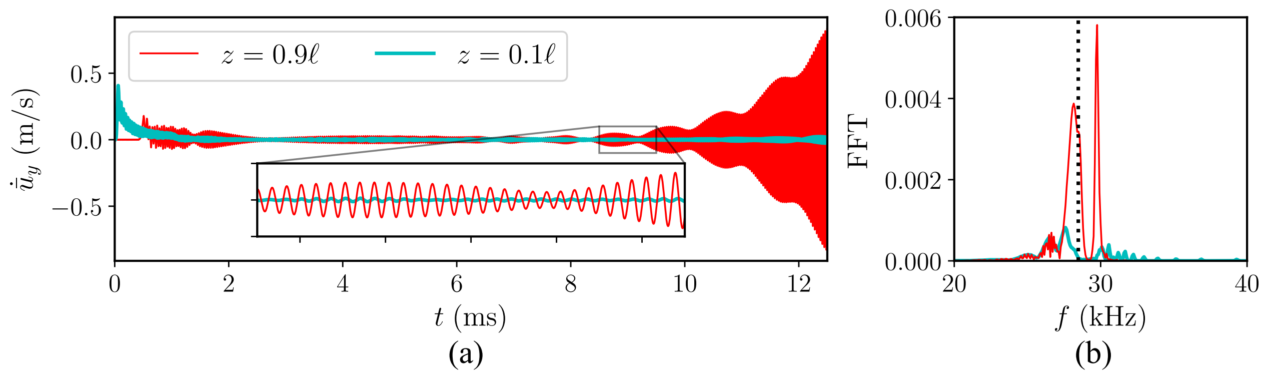

Figure 6.15. (a) Time histories of the vertical velocity of the fluid–solid interface of case C6 at $z = 0.9\ell$ (near the outlet) and $z = 0.1\ell$ (near the inlet), respectively. (b) Fourier transform of the corresponding time histories from (a). The dotted line marks the natural frequency calculated from equation (6.32).

the entire simulation time window. Consequently, the demonstrated FSI-induced instabilities could be an effective and inexpensive way of enhancing mixing at the microscale.

6.6 Discussion

We have derived a new 1D (reduced) FSI model for the physics underlying FSI-induced instabilities of flows conveyed in long and shallow microchannels with a deformable top wall.

The key advance in our 1D FSI model, compared to previous work, lies in the accurate modeling of the wall deformation due to two-way FSI. For collapsible tubes, a constant large tension is always included, though bending was also considered in some computational studies [77], [79], [80]. Similarly, the 1D FSI model of Inamdar, Wang, and Christov [102] considered the top wall as a beam and took large-deformation-induced tension and bending into account. However, in a typical long and shallow rectangular microchannel, previous studies have demonstrated that, under linear elasticity, at the leading order, the soft wall deforms more like a Winkler foundation, *i.e.*, the deformation of the channel's cross-section at different streamwise locations is fully determined by the local pressure [31], [33], [101]. Hence, in contrast to other 1D models, the 1D FSI model proposed herein maintains the dominance of the Winkler-foundation-like behavior of the soft wall. Weak tension was introduced only to take account into the boundary effects near the inlet and outlet of the channel. Moreover, the inertia of the solid was also modelled consistently, just like the inertia of the fluid was take into account by lubrication theory at low, but finite, Reynolds number, following [114]. Our proposed 1D model establishes how the unsteady flow rate, the pressure and the channel deformation evolve together in a tightly coupled manner.

Importantly, we found that the predictions of the proposed 1D FSI model agree qualitatively with key experiments [41] (summarized in table 6.3). Consequently, we believe that the present analysis leads to significant, novel insight into the experimentally observed low-Re FSI-induced instabilities in compliant microchannels. In short, the physical insight provided by our new model is that FSI causes wall resonances, giving rise to self-sustained oscillations of the fluid–solid interface. These resonances are triggered thanks to the combined effect of weak axial tension and finite solid inertia, which renders the local pressure varying at frequencies close to the natural frequency of the wall. Further, the experimentally observed dye breakup (and "ultrafast" mixing) are explained by the global instability of non-flat (deformed) base state of our model, which was not accurately accounted for in previous work. Our proposed 1D FSI model allows for the identification (computationally) of the critical conditions for instability of this coupled system. The predicted critical Reynolds number is in agreement with the value suggested by experiments.

To the experimentalist, our proposed 1D FSI model provides a tool through which different microchannel designs can be rapidly prototyped and evaluated. Beyond that, our model provides a convenient way to evaluate operating conditions that might lead to instability and mixing. Extending the present results, the pressure drop could be prescribed across the channel (instead of fixing the flux at the inlet), similarly to the works of Stewart *et al.* [86] and Stewart *et al.* [87]. Further, the proposed 1D modeling framework can be easily used to analyze soft conduits of different cross-sectional geometries and other boundary conditions, as long as the basic assumptions on the separation of scales (and weak versus dominant effects in the solid) are not violated.

6.A Modeling of weak deformation effects

6.A.1 Effective interface thickness

The goal of previous studies was to find a solution for the fluid–solid interface displacement, $\bar{u}_y$, from which to determine the cross-sectional area of the deformed fluidic channel. To illustrate this point, consider the microchannel studied by Wang and Christov [101], which has a similar configuration to figure 3.1. In this case, the theory of the flow-induced deformation predicts that the vertical displacement of the solid, $U_Y^s = u_y^s(x,\hat{y},z)/\mathcal{U}_c$, varies with the vertical distance from the fluid–solid interface ($\hat{y} = 0$)), as shown in figure 6.16. For the unsteady motion in this work, however, we must properly connect the motion of the fluid–solid interface to the non-uniform motion of the entire top wall. Since this variation is rapidly decaying, it is reasonable to expect that a suitable *effective thickness* of the fluid–solid interface, $b^\star$, can be introduced and used in equation (6.7). In doing so, the unsteady motion of the *whole* solid (of nonuniform vertical displacements) will be captured by the vertical motion of an *interface* of "virtual" thickness $b^\star$.

In analogy to the definition of boundary layer thickness [104], [115], we define $b^\star$ by requiring that the momentum of the solid wall's motion is equivalent to the momentum of the reduced interface's motion, *i.e.*,

$$\rho_s \int_0^d \int_{-w/2}^{+w/2} \dot{u}_y^s(x,\hat{y},z)\,\mathrm{d}x\,\mathrm{d}\hat{y} = \rho_s w b^\star \dot{\bar{u}}_y(z). \tag{6.33}$$

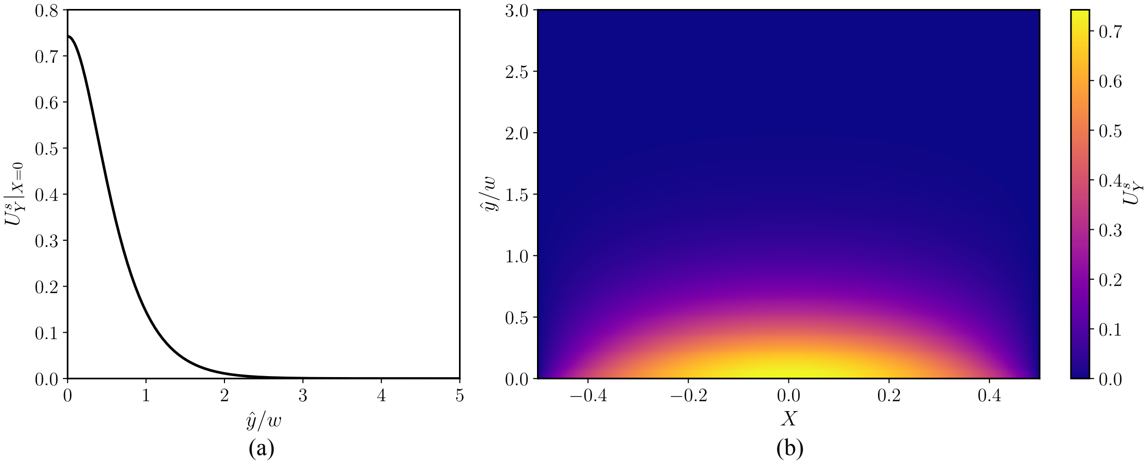

Figure 6.16. Illustration of the displacement field in a thick wall predicted by equation (4.13) from chapter 4. (a) Centerline displacement at $x/w = X = 0$ versus dimensionless vertical distance from the fluid–solid interface, $\hat{y}/w$. (b) Contour plot of the displacement field. Here, $\hat{y} = y + h_0$ and $\mathcal{U}_c = w\mathcal{P}_c/(h_0\bar{E})$.

Since we have assumed that the solid deformation is governed by linear elasticity, the domain of integration is unchanged after deformation. Then, we can take the time derivative out of the integral. Substituting the definition of $\bar{u}_y$, we obtain

$$b^\star = \frac{\int_0^d \int_{-w/2}^{+w/2} u_y^s(x,\hat{y},z)\,\mathrm{d}x\,\mathrm{d}\hat{y}}{w\bar{u}_y} = \frac{\int_0^d \int_{-w/2}^{+w/2} u_y^s(x,\hat{y},z)\,\mathrm{d}x\,\mathrm{d}\hat{y}}{\int_{-w/2}^{+w/2} u_y^s(x,0,z)\,\mathrm{d}x}. \tag{6.34}$$

Substituting equation (3.14) from [101] into equation (6.34), we find that $b^\star \approx 0.6141w$ for thick-walled microchannel ($d^2/w^2 \gg 1$). However, if the top wall is thin ($d \simeq w$), plate theory can be invoked, and the mid-plane displacement can represent the bulk motion of the interface; in this case, $b^\star = d$.

6.A.2 Weak tension

Having introduced $b^\star$, we are ready to give an expression for the weak tension, χ_t. One possible scenario is that χ_t arises from the bulging of the wall. In principle, the deformation-induced tension is nonuniform along z. However, as mentioned, the variation of tension in z is balanced with the shear stress in the flow, and thus can be neglected. Then, assuming the in-plane displacement (along z) is negligible, χ_t can be estimated by the average stretch of the wall [178], written as

$$\chi_t = \frac{Eb^\star}{\ell} \int_0^\ell \frac{1}{2} \left(\frac{\partial \bar{u}_y}{\partial z} \right)^2 \mathrm{d}z. \tag{6.35}$$

Deformation-induced tension is expected to occur when the outlet of the channel is open to air, as in [12], [41], or the pre-tension provided by external connectors is negligible. In the unsteady case, χ_t is time-dependent.

Another possible situation is that the microchannel is pre-stretched and installed between an upstream and downstream section, as in the research on collapsible tubes mentioned in chapter 1. With the increase of the flow rate, the bulging of the wall is more prominent, leading to larger χ_t. However, beyond a certain flow rate, the deformation-induced tension will not be sufficient to hold the channel at the inlet and the outlet. In other words, the boundary conditions cannot be satisfied. The upper bound on the flow rate before the model breaks down is related to and found to increase with χ_t [114]. Therefore, in this case when the deformation-induced tension is not sufficient, if the system is still to operate at such a high flow rate, external pre-tension needs to be provided. Nevertheless, for the validity of equation (6.7), the pre-tension in this case should be much larger than the deformation-induced tension. On the other hand, the third term in equation (6.7) needs to be small compared with the second term, to ensure the dominance of the Winkler-foundation-like mechanism.

Apart from weak tension, other elastic forces might also be relevant. For example, if the top wall is thin, bending could play a role. Another example comes from the elastic structures on top of thin fluid films, wherein (in addition to tension) bending and gravity are invoked to regularize the problem [166]. However, in the present work, we consider only the weak tension effect.

6.B Numerical scheme for the 1D FSI model

Here, we introduce a numerical scheme to solve the coupled problem of deformation-induced tension, wall deformation, and flow. This scheme is also applied to the simpler case of constant tension with given θ_t. The spatial domain is discretized using the pseudospectral method [108], with which the governing equations are satisfied at preassigned Gauss-type-quadrature nodes. In our case, the Gauss–Lobatto points are chosen. Therefore, the method is also referred to as "Chebyshev pseudospectral method" or "Chebyshev collocation method." Note that in some literature [110], the pseudospectral method is specifically referred to as a Galerkin-type method with the numerical integration using a Gauss-type quadrature, which is not the case for the present method.

The Gauss–Lobatto points

$$\tilde{Z}_j = -\cos\left(\frac{j\pi}{N}\right), \quad j = 0, 1, \ldots, N \tag{6.36}$$

are defined on the domain $[-1, 1]$. (Note that $\tilde{Z}_0 = -1$ and $\tilde{Z}_N = 1$.) Consequently, we use a change of variables, $\tilde{Z} = 2Z - 1$, to transform the computational domain from $\{Z \,|\, Z \in [0, 1]\}$ to $\{\tilde{Z} \,|\, \tilde{Z} \in [-1, 1]\}$. Then, $\mathrm{d}^m/\mathrm{d}Z^m = 2^m \mathrm{d}^m/\mathrm{d}\tilde{Z}^m$. There are two major advantages of choosing the Gauss–Lobatto points as the collocation points. First, the Gauss–Lobatto points are nonuniformly distributed and clustered near the endpoints $\tilde{Z} = \pm 1$, with the spacing scaling as $\mathcal{O}(N^{-2})$, which helps resolve the deformation boundary layer near the channel outlet. Second, it is convenient to compute derivatives at the Gauss–Lobatto points. Essentially, the Chebyshev pseudospectral method finds a high-order polynomial-based, valid in the whole domain, to approximate the actual solution. As long as the functional values are known at the $N+1$ collocated points, an N-order polynomial can be uniquely determined.

The Lagrange basis, $l_j(Z)$ ($j = 0, 1, \ldots, N$), is a convenient choice for the interpolating polynomial since the coefficients are just the functional values. Here, l_j denotes the Lagrange polynomial which takes the value of 1 at $\tilde{Z} = Z_j$ while being 0 for Z_k with $k \neq j$. Importantly, the derivatives of the Lagrange basis at the Gauss–Lobatto points are known analytically.

For example, taking $Q_k \approx Q|_{\tilde{Z}=\tilde{Z}_k}$, $k = 0, 1, \dots, N$, then $\mathrm{d}Q/\mathrm{d}\tilde{Z}|_{\tilde{Z}=\tilde{Z}_k} \approx \sum_{j=0}^{N} D_{kj}^{(1)} Q_j$. Here, the components of the first-order differentiation matrix $\boldsymbol{D}^{(1)}$ are:

$$D_{kj}^{(1)} = \left.\frac{\mathrm{d}l_j}{\mathrm{d}\tilde{Z}}\right|_{\tilde{Z}=\tilde{Z}_k} = \begin{cases} -\dfrac{2N^2+1}{6}, & k = j = 0, \\ \dfrac{\widetilde{c}_k}{\widetilde{c}_j}\dfrac{(-1)^{k+j}}{\tilde{Z}_k - \tilde{Z}_j}, & k \neq j, \ \ 0 \leq k, j \leq N, \\ -\dfrac{\tilde{Z}_k}{2(1-\tilde{Z}_k^2)}, & k = j, \ \ 1 \leq k, j \leq N-1, \\ \dfrac{2N^2+1}{6}, & k = j = N, \end{cases} \tag{6.37}$$

where $\widetilde{c}_0 = \widetilde{c}_N = 2$ and $\widetilde{c}_j = 1$ for $1 \leq j \leq N-1$. The higher-order differentiation matrix is just the matrix multiplication of the lower ones, *i.e.*, $\mathrm{d}^m/\mathrm{d}\tilde{Z}^m|_{\tilde{Z}=\tilde{Z}_k} \approx \boldsymbol{D}^{(m)} = [\boldsymbol{D}^{(1)}]^m = \boldsymbol{D}^{(1)} \times \boldsymbol{D}^{(1)} \times \cdots \times \boldsymbol{D}^{(1)}$.

As for the time integration, a second-order backward-difference formula is used for the flow equations. Let the time step be ΔT, and a subscript denote the functional value at the corresponding grid point, while a superscript indicates the time step. Then, equations (6.8a) and (6.8b) are discretized as:

$$Q_j^{n+1} = 1 - \int_{-1}^{\tilde{Z}_j} \frac{1}{2}\beta \left(\dot{\bar{U}}_Y\right)^{n+1} \mathrm{d}\tilde{Z}, \tag{6.38}$$

$$P_j^{n+1} = \int_{1}^{\tilde{Z}_j} \frac{1}{2} \left\{ -\frac{\hat{R}\mathrm{e}}{\bar{H}^{n+1}} \frac{3Q^{n+1} - 4Q^n + Q^{n-1}}{2\Delta T} - \frac{6\hat{R}\mathrm{e}}{5\bar{H}^{n+1}} 2D^{(1)} \frac{(Q^{n+1})^2}{\bar{H}^{n+1}} - \frac{12Q^{n+1}}{(\bar{H}^{n+1})^3} \right\} \mathrm{d}\tilde{Z}. \tag{6.39}$$

Both of these equations have been integrated in space, with $Q_0 \equiv Q|_{Z=0} = 1$ imposed in equation (6.38) and $P_N \equiv P|_{Z=1} = 0$ imposed in equation (6.39). The integral is to be evaluated numerically using the trapezoidal rule. Note $\mathrm{d}\tilde{Z} = 2\mathrm{d}Z$ due to the change of variables introduced above. Also, in equation (6.38), $\dot{\bar{U}}_Y$ denotes the velocity of the interface, which can be obtained from equation (6.42b) below.

The so-called Newmark–β method is applied to the governing solid equation (6.12). Then, the spatially discretized equation (6.12) is written as

$$\boldsymbol{M}\ddot{\bar{U}}_Y + \boldsymbol{K}\bar{U}_Y = P, \tag{6.40}$$

with

$$\boldsymbol{M} = \theta_I \boldsymbol{I}, \quad \boldsymbol{K} = \boldsymbol{I} - \theta_t \boldsymbol{D}^{(2)}. \tag{6.41}$$

Here, θ_t is evaluated from equation (6.16). To ensure the accuracy of the numerical integration required to evaluate θ_t, the kernel, $(\mathrm{d}\bar{H}/\mathrm{d}Z)^2 \approx (2\boldsymbol{D}^{(1)}\bar{H})^2$, is interpolated on the finer grid of $N = 1024$ using the `barycentric_interpolate` subroutine in SciPy. Then, a Gauss–Lobatto quadrature is applied on the finer grids to calculate the integral in equation (6.16).

With the coefficients in equation (6.40) determined, the acceleration, velocity and displacement of the interface are calculated as

$$\ddot{\bar{U}}_Y^{n+1} = \left(\boldsymbol{M} + \phi_2 \Delta T^2 \boldsymbol{K}\right)^{-1} \left\{P^{n+1} - \boldsymbol{K}\left[\bar{U}_Y^n + \Delta T \dot{\bar{U}}_Y^n + \left(\frac{1}{2} - \phi_2\right)\Delta T^2 \ddot{\bar{U}}_Y^n\right]\right\}, \tag{6.42a}$$

$$\dot{\bar{U}}_Y^{n+1} = \dot{\bar{U}}_Y^n + (1-\phi_1)\Delta T \ddot{\bar{U}}_Y^n + \phi_1 \Delta T \ddot{\bar{U}}_Y^{n+1}, \tag{6.42b}$$

$$\bar{U}_Y^{n+1} = \bar{U}_Y^n + \Delta T \dot{\bar{U}}_Y^n + \left(\frac{1}{2} - \phi_2\right)\Delta T^2 \ddot{\bar{U}}_Y^n + \phi_2 \Delta T^2 \ddot{\bar{U}}_Y^{n+1}, \tag{6.42c}$$

where ϕ_1 and ϕ_2 are two adjustable parameters. The Newmark–β scheme is unconditionally stable and second-order accurate if $\phi_1 = 1/2$ and $\phi_2 = 1/4$. However, to damp out numerically-induced high-frequency oscillations, $\phi_1 > 1/2$ is usually needed [177]. In our simulations, we use $\phi_1 = 1.0$ and $\phi_2 = 0.5625$.

Finally, the discretized interface equation (6.10) is simply

$$\bar{H}_j^{n+1} = 1 + \beta(\bar{U}_Y)_j^{n+1}. \tag{6.43}$$

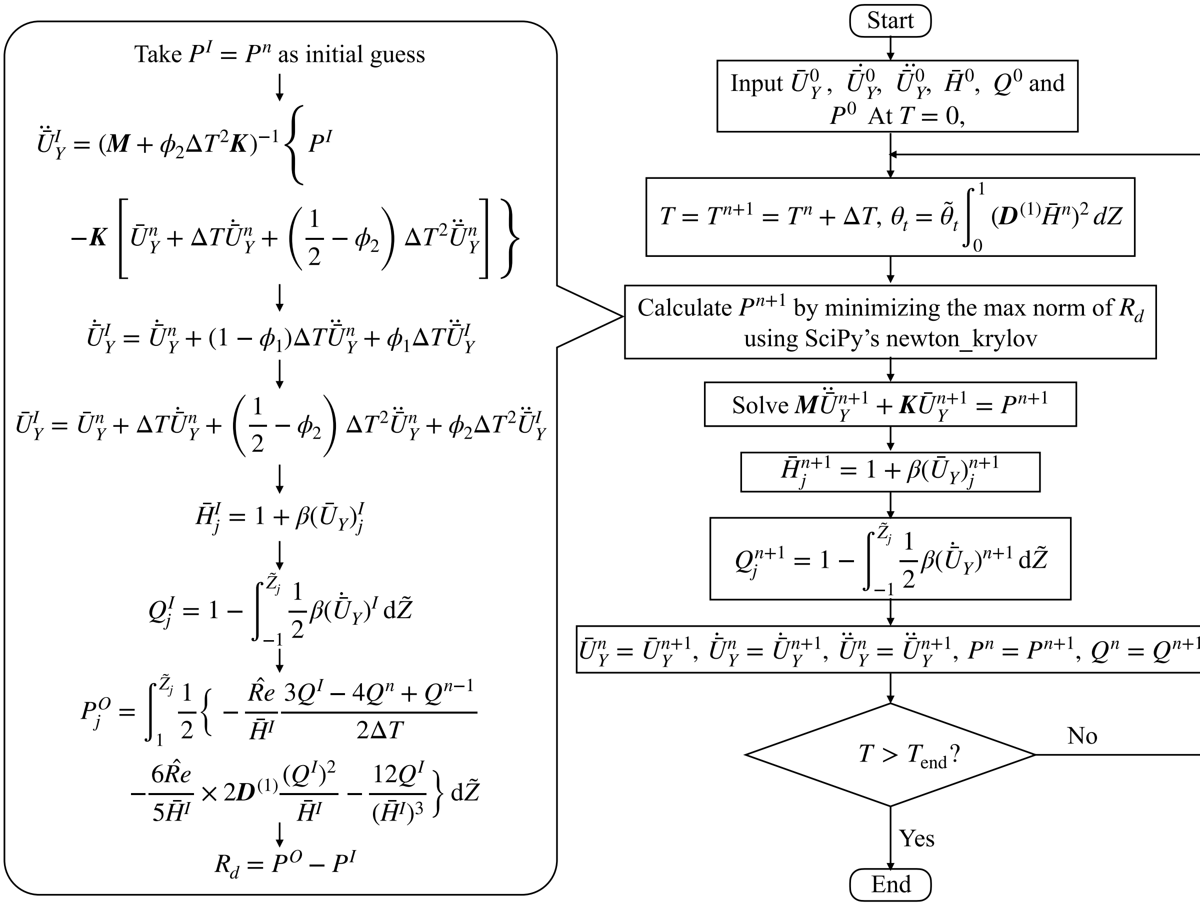

Figure 6.17. Flow chart of the numerical scheme for the dynamic simulations. To the left of the cell where SciPy's `newton_krylov` solver is called, the details of the construction of the residual, R_d, is shown. The superscript I indicates that the quantity is calculated based on P^I.

6.B.1 Steady-state simulation

As mentioned in the main text, the case with given constant tension can be easily solved using SciPy's `solve_bvp`. However, in the case of the deformation-dependent tension, since θ_t is unknown, `solve_bvp` is not as robust and usually has difficulty reaching convergence. Instead, SciPy's `newton_krylov` method is applied to resolve the steady-state solution.

At steady state, all of the terms involving ΔT can be neglected. Further, we drop the subscripts on the spatial discretizations for convenience. Then, equations (6.38), (6.39), (6.40) and (6.43) comprise a nonlinear algebraic problem. Then, given $\bar{U}_Y$, equations (6.43) and (6.39) allow us to evaluate the pressure, denoted as P^F. At the same time, equation (6.40) can also be used to evaluate the pressure, denote as P^S. Now, we define a residual as

$$R_s = P^F - P^S. \tag{6.44}$$

SciPy's `newton_krylov` solver is used to minimize the max-norm of R_s, which yields an approximate evaluation for $\bar{U}_Y$ at steady state. The tolerance used was 6×10^{-6}.

With $\bar{U}_Y$ obtained, θ_t is calculated from equation (6.16) using the Gauss–Lobatto quadrature, as discussed before. The steady-state solution is then validated with `solve_bvp` by solving equation (6.21), where both the initial guess and θ_t are based on the outputs of `newton_krylov`.

6.B.2 Dynamic simulation

The dynamic problem is solved in a similar manner. At each time step, the nonlinear system of equations (6.38), (6.39), (6.40) and (6.43) must be solved. However, to get the Newmark–β time integration (6.42) involved, the residual, R_d, is defined with the pressure as the input, denoted as P^I. Then, starting from equation (6.40), solved with the scheme (6.42), $\bar{U}_Y$ and $\dot{\bar{U}}_Y$ are obtained. Then, $\bar{H}$ and Q are evaluated from equations (6.43) and (6.38), respectively. Equation (6.39) gives another evaluation of the pressure, denoted as, P^O. The residual is thus evaluated as

$$R_d = P^O - P^I. \tag{6.45}$$

At each time step, SciPy's `newton_krylov` is used to minimize the max-norm of R_d. The details of this numerical procedure are summarized in the flow chat in figure 6.17.

Note that at time step $n+1$, θ_t is evaluated as $\theta_t = \tilde{\theta}_t \int_0^1 (\boldsymbol{D}^{(1)} \bar{H}^n)^2 \, \mathrm{d}Z$. The integral is approximated using the Gauss–Lobatto quadrature after interpolating the kernel on the finer grid of $N = 1024$. Here, we use $\bar{H}^n$ instead of $\bar{H}^{n+1}$ in order to avoid another nonlinear problem requiring "internal iterations" on θ_t^{n+1}. We have verified that the results using $\bar{H}^n$

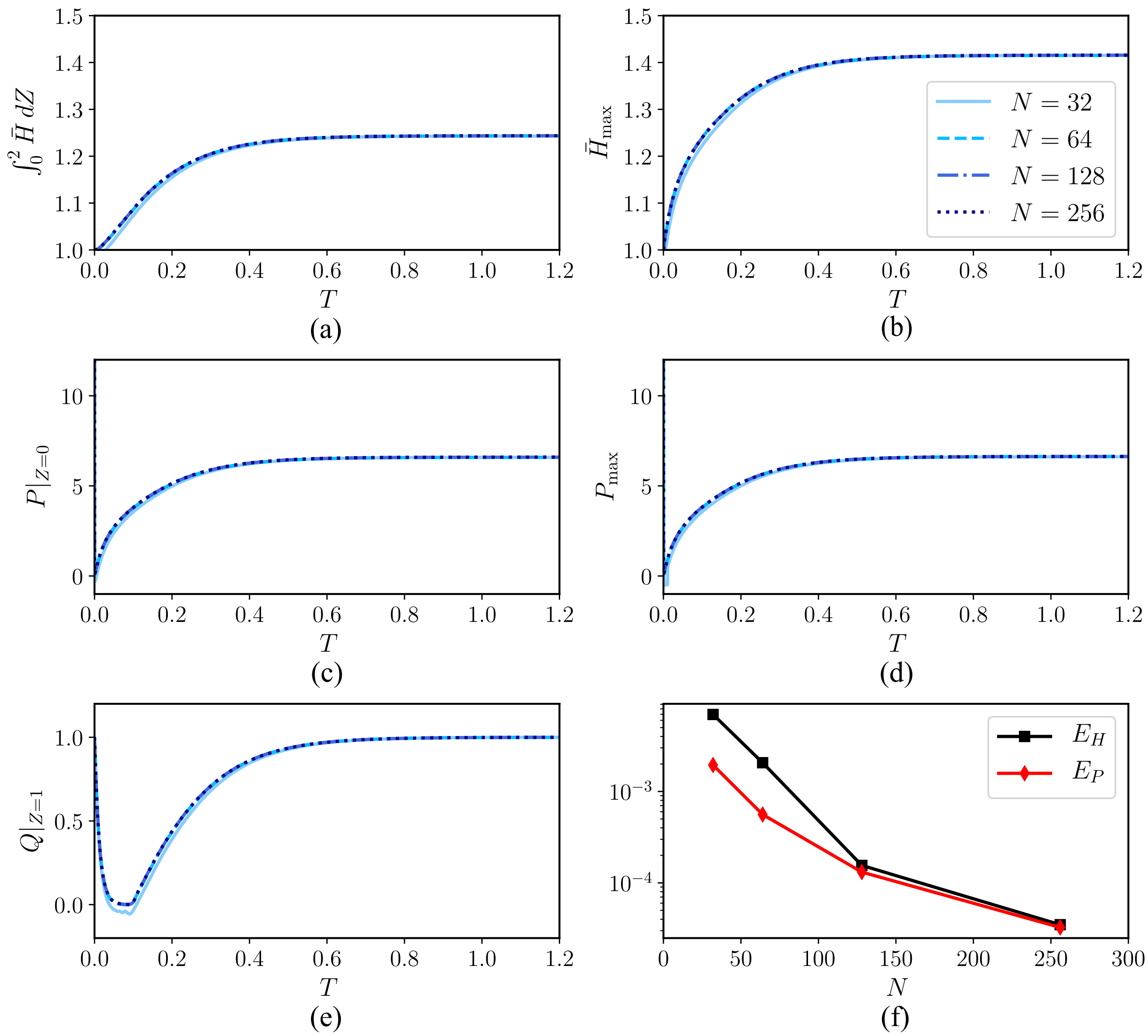

Figure 6.18. Grid independence study for the dynamic simulations of FSI in the microchannel with $E = 2$ MPa under a flow rate of $q = 1500$ µL min^{-1} (case C4). The time histories of the representative quantities in the system are shown in panels (a) to (e). Panel (f) shows the two-norm of the difference between the simulated steady state solution and the "exact" solution, which is computed from the steady simulation with $N = 2048$ Gauss–Lobatto points using the scheme described in section 6.B.1. The tolerance used in SciPy's `newton_krylov` was 10^{-8}. The errors E_H and E_P are computed via equation (6.46).

instead of $\bar{H}^{n+1}$ do not differ from those evaluated based on more involved method using $\bar{H}^{n+1}$.

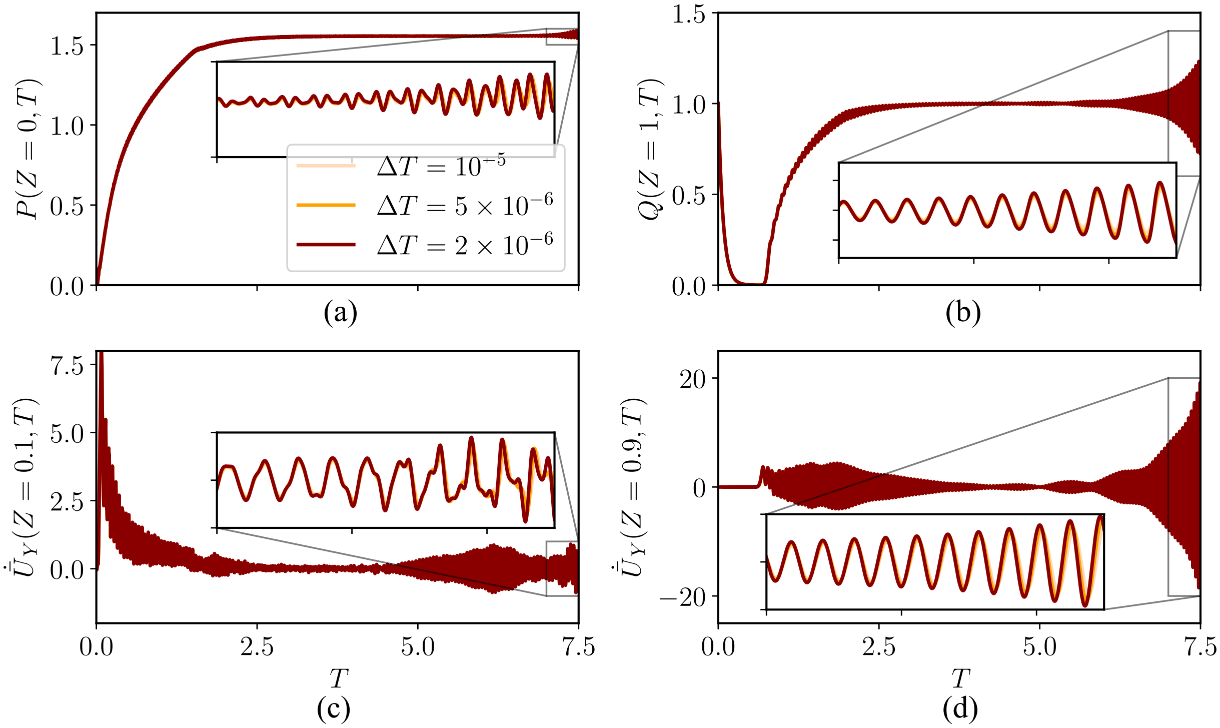

Figure 6.19. Time histories of (a) inlet pressure $P(0,T)$, (b) outlet flow rate $Q(1,T)$, the vertical velocity $\dot{\bar{U}}_Y$ of the fluid–solid interface at (c) $Z=0.1$ and (d) $Z=0.9$. All panels are for case C3 but using different time step sizes ΔT. The spatial grid is fixed to have $N=128$ nodes.

Next, we verify the grid independence of the numerical results shown in the main text. The case chosen to perform the grid independence study is C4 from table 6.2 (corresponding to $E = 2$ MPa and $q = 1500$ µL min^{-1}). For case C4, we have shown in section 6.4 that the inflated steady state is linearly stable to infinitesimal perturbations. If the flat initial condition (6.20) is used, then the system will reach the steady state eventually.

The end time for the simulation is $T_{\text{end}} = 2.0$. However, for the clarity of the presentation, only the results between $T = 0$ and $T = 1.2$ are shown. Furthermore, the ratio of the smallest grid size to the time step is fixed for every simulation. Since the smallest spacing of the Gauss–Lobatto grid points goes as $\mathcal{O}(N^{-2})$, then as N is doubled, ΔT is decreased by a factor 4 accordingly. The time step for $N = 32$ is $\Delta T = 4\times10^{-4}$. As shown figure 6.18(a) and (e), all of the representative quantities agree well with each other as ΔT is refined, except on the courses grid with $N = 32$, After the simulation has reached $T = T_{\text{end}}$, the deformed interface shape, $\bar{H}^{\text{end}}(Z)$, and the pressure distribution within the channel, $P^{\text{end}}(Z)$ are compared with an "exact" steady-state solution.

The latter are denoted as $\bar{H}^{\text{e}}(Z)$ and $P^{\text{e}}(Z)$, respectively. The "exact" solution is taken to be the steady state of the simulation with $N = 2048$, and tolerance for SciPy's `newton_krylov` set to 10^{-8}. We define two L^2-norm based error estimates:

$$E_H = \left(\frac{1}{2} \sum_{j=1}^{N-1} (\bar{H}_j^{\text{end}} - \bar{H}_j^{\text{e}}) \mathfrak{w} \sqrt{1 - \tilde{Z}_j^2} \right)^{1/2}, \tag{6.46a}$$

$$E_P = \left(\frac{1}{2} \sum_{j=1}^{N-1} (P_j^{\text{end}} - P_j^{\text{e}}) \mathfrak{w} \sqrt{1 - \tilde{Z}_j^2} \right)^{1/2}, \tag{6.46b}$$

which are written in the discrete form using the Gauss–Lobatto quadrature. Here, $\mathfrak{w} = \pi/N$ are the weights, and we choose $N = 2048$. Figure 6.18(f) shows that the error decreases with the increase of N. The cases of $N = 32,\ 64$ and even 128 display an exponential decay for E_H. However, since the "exact" solution is not really exact, both error estimates tend to "saturate" for $N = 256$.

As for the linearly unstable cases, the errors defined in equation (6.46) are not applicable because the system will not reach steady state. In these cases, each simulation is tested with different time step sizes, and only the converged results are shown. The spatial grid is typically fixed as $N = 128$ for satisfactory accuracy (as shown in figure 6.18). One example for case C3 is shown in figure 6.19. In panel (c) and (d), the vertical velocity of the fluid–solid interface is obtained as follows. First, we substitute the simulated $\bar{H}$ into equation (5.40) to obtain V_Z^{2D}. Then, we compute V_Y^{2D} based on conservation of mass, *i.e.*, $\partial V_Z^{2D}/\partial Z + \partial V_Y^{2D}/\partial Y = 0$. Lastly, we obtain $\dot{\bar{U}}_Y = \beta^{-1} V_Y^{2D}|_{Y=\bar{H}}$ using equations (6.3) and (6.10). The actual simulation time is longer than the time window shown for each case. However, it is observed that after a certain T, the results with different time step sizes begin to diverge, indicating this nonlinear 1D FSI model's dynamic behavior may be chaotic. Understanding such an interesting possibility is beyond of the scope of the current work.

6.C A Chebyshev pseudospectral method for the generalized eigenvalue problem

We solve the generalized eigenvalue problem (6.28) using the approach proposed in section 2.4.2 of chapter 2. However, since the boundary conditions for equation (6.28) are different from the boundary conditions of section 2.4.2, we employ another modified Lagrange polynomial basis, now written as

$$\widetilde{Q}(\tilde{Z}) \approx (1+\tilde{Z})\sum_{j=1}^{N}\tilde{Q}_j\frac{\ell_j(\tilde{Z})}{1+\tilde{Z}_j}, \qquad \widetilde{H}(\tilde{Z}) \approx \sum_{j=1}^{N-1}\widetilde{H}_j\ell_j(\tilde{Z}) + \widetilde{H}_N(1-\tilde{Z}^2). \tag{6.47}$$

It is easy to check that $\widetilde{Q}(\tilde{Z}_j) = \tilde{Q}_j$ and $\widetilde{H}(\tilde{Z}_j) = \widetilde{H}_j$, except that $\widetilde{H}(\tilde{Z}_N) = 0 \neq \widetilde{H}_N$, meaning that $\widetilde{Q}_j$ and $\widetilde{H}_j$ are the collocated function values; $\widetilde{H}_N$ is introduced ensure the satisfaction of the boundary condition. Also note j starts from 1 instead of 0, because equation (6.47) has already satisfied the conditions that $\widetilde{Q} = \mathrm{d}\widetilde{Q}/\mathrm{d}\tilde{Z} = 0$ at $\tilde{Z} = -1$, and $\widetilde{H} = 0$ at $\tilde{Z} = \pm 1$. The two remaining boundary conditions at $\tilde{Z} = 1$ in equation (6.30) are enforced manually.

Next, the generalized eigenvalue problem (6.28) is collocated at the Gauss–Lobatto points from $j = 1, 2, \dots, N-1$, with the unsatisfied boundary conditions enforced at $j = N$. This approach gives rise to the $2N \times 2N$ matrices $\boldsymbol{A}$ and $\boldsymbol{B}$ in equation (6.28). Due to the imposition of the boundary conditions at $\tilde{Z} = 1$, $\boldsymbol{B}$ is singular. Thus, we invert $\boldsymbol{A}$ to obtain a regular eigenvalue problem, $\boldsymbol{A}^{-1}\boldsymbol{B}\boldsymbol{\psi} = (\mathrm{i}\omega_G)^{-1}\boldsymbol{\psi}$, which can be solved using SciPy's `eig`.

Finally, to filter out any spurious modes, each calculation has been performed with $N = 600$ and $N = 800$ grid points and cross-checked. Only the converged modes are reported in the text.

7. LINEAR NON-NORMALITY OF THE REDUCED FLUID–STRUCTURE INTERACTION MODEL

SUMMARY

In this chapter, we study the linear non-normality of the linearization of the one-dimensional fluid–structure interaction model (specifically for perturbations about its steady, deformed base state). We derive a theoretical framework for investigating the eigenvalue sensitivity and the maximum transient energy amplification of infinitesimal initial perturbations in the linearized problem. We find that the eigenspectrum is typically not very sensitive to perturbations imposed on the linear operator. Therefore, even though the linear operator is approximated numerically, with some errors unavoidably being introduced by discretization, the computed eigenvalues are trustworthy. The transient energy growth of initial disturbances is a more meaningful quantity associated with the non-normality of the linear operator than the eigenvalue sensitivity. Thus, we study the maximum transient energy growth of the linearized system and find that it is can exhibit different behaviors depending on the exemplar system/case considered. This finding indicates that the system's parameters can significantly influence the non-normality of the linearized problem. The solid kinetic energy is found to be the largest portion of the total energy of growing infinitesimal disturbances. In the case in which the initial disturbances contain many slowly-decaying oscillatory eigenmodes, the solid kinetic energy can experience substantial transient amplification, which could impose extra challenges on the numerical simulations. The proposed non-normality framework (and the case studies considered) have implications for designing novel microscale mixing systems that exploit the interplay between (in)stability and transient growth due to FSIs in compliant microchannels.

7.1 Problem statement

In chapter 6, we perturbed the steady state of the 1D FSI model with infinitesimal initial disturbances. By linearizing the governing equations around the base state, we obtained a linear evolution equation (6.26) for these initial disturbances. Then, the stable and unstable eigenmodes were identified through an eigenvalue analysis (recall section 6.4 for details). However, the eigenvalues only predict the asymptotic behavior of the linearized system, as $T \to \infty$. In equation (6.26), the linearized operator is not normal (*i.e.*, $\boldsymbol{A}\boldsymbol{A}^{+} \neq \boldsymbol{A}^{+}\boldsymbol{A}$, with $\boldsymbol{A}^{+}$ being the adjoint of $\boldsymbol{A}$), thus its eigenfunctions are not orthogonal to each other. Consequently, it is possible for initially infinitesimal perturbations to experience transient amplification during a short time window, say $0 \leq T \leq T_{\mathrm{e}}$. In particular, if the linearized operator is "highly" non-normal, the transient amplification can be so large that the nonlinearities of the system "take over." Consequently, the finite-time evolution of such disturbances would be significantly different from what the corresponding linearized problem predicts. Importantly, it may even be the case that these disturbances do not exhibit the asymptotic behavior suggested by the eigenvalue analysis, as $T \to \infty$.

In this chapter, to complement the eigenvalue analysis in section 6.4, we address the linear non-normality of the linear evolution equation (6.26). Specifically, we investigate the sensitivity of the eigenspectra (section 7.2) and compute the maximum energy amplification of infinitesimal initial perturbations (section 7.3). The larger these two quantities are, the "more non-normal" the corresponding operator is.

7.2 Sensitivity of the linearized operator's eigenvalues

7.2.1 The eigenvalue problem and its adjoint

In equation (6.26), we have derived a generalized eigenvalue problem (6.28) in the form of $\boldsymbol{A}\boldsymbol{\psi} = \mathrm{i}\omega_G \boldsymbol{B}\boldsymbol{\psi}$. Since the operator $\boldsymbol{A}$ is not self-adjoint, we need to find another set of functions that are orthogonal to the eigenfunctions $\boldsymbol{\psi}$. To do so, we derive the adjoint of the eigenvalue problem. Denote $\boldsymbol{\psi}^+ = (\widetilde{H}^+, \widetilde{Q}^+)^\top$ and $\boldsymbol{A}^+$ as the adjoint eigenfunctions and the adjoint operator, respectively. By definition,

$$\int_0^1 (\boldsymbol{\psi}^+)^* \boldsymbol{A}\boldsymbol{\psi}\,\mathrm{d}Z = \int_0^1 (\boldsymbol{A}^+\boldsymbol{\psi}^+)^* \boldsymbol{\psi}\,\mathrm{d}Z, \tag{7.1}$$

where the * superscript denotes the complex conjugate.

Deriving the adjoint eigenvalue problem is an exercise in integration by parts, the details of which are found in section 7.A. Ultimately, the adjoint eigenvalue problem is found to be

$$\underbrace{\begin{pmatrix} 0 & \mathscr{L}_1^+ \\ -\frac{\mathrm{d}}{\mathrm{d}Z} & \mathscr{L}_2^+ \end{pmatrix}}_{\boldsymbol{A}^+} \underbrace{\begin{pmatrix} \widetilde{H}^+ \\ \widetilde{Q}^+ \end{pmatrix}}_{\boldsymbol{\psi}^+} = -\mathrm{i}\omega_G^* \underbrace{\begin{pmatrix} 1 & 0 \\ 0 & \frac{\hat{R}\mathrm{e}\beta}{\bar{H}_0} - \theta_I \frac{\mathrm{d}^2}{\mathrm{d}Z^2} \end{pmatrix}}_{\boldsymbol{B}^+} \underbrace{\begin{pmatrix} \widetilde{H}^+ \\ \widetilde{Q}^+ \end{pmatrix}}_{\boldsymbol{\psi}^+}, \tag{7.2}$$

where

$$\mathscr{L}_1^+ = -\frac{36\beta Q_0}{\bar{H}_0^4} - \left(1 - \frac{6}{5}\hat{R}\mathrm{e}\beta\frac{Q_0^2}{\bar{H}_0^3}\right)\frac{\mathrm{d}}{\mathrm{d}Z} + \theta_t\frac{\mathrm{d}^3}{\mathrm{d}Z^3}, \tag{7.3a}$$

$$\mathscr{L}_2^+ = \frac{12}{5}\hat{R}\mathrm{e}\beta\frac{Q_0}{\bar{H}_0^3}\frac{\mathrm{d}\bar{H}_0}{\mathrm{d}Z} + \frac{12\beta}{\bar{H}_0^3} - \frac{12}{5}\hat{R}\mathrm{e}\beta\frac{Q_0}{\bar{H}_0^2}\frac{\mathrm{d}}{\mathrm{d}Z}. \tag{7.3b}$$

Note that $\boldsymbol{B} = \boldsymbol{B}^+$. The adjoint problem (7.2) is subject to the following boundary conditions:

$$\widetilde{Q}^+\Big|_{Z=0} = 0, \quad \frac{\mathrm{d}\widetilde{Q}^+}{\mathrm{d}Z}\bigg|_{Z=0} = \frac{\mathrm{d}\widetilde{Q}^+}{\mathrm{d}Z}\bigg|_{Z=1} = 0, \quad \widetilde{H}^+ + \frac{12}{5}\hat{R}\mathrm{e}\beta\frac{Q_0}{\bar{H}_0^2}\widetilde{Q}^+\bigg|_{Z=1} = 0. \tag{7.4}$$

The first three boundary conditions for $\widetilde{Q}^+$ are the same as those for $\widetilde{Q}$. However, unlike the case for $\widetilde{H}$, we only have one mixed boundary condition for $\widetilde{H}^+$.

It is clear that $\boldsymbol{A}\boldsymbol{A}^+ \neq \boldsymbol{A}^+\boldsymbol{A}$. Therefore, we say that the eigenvalue problem (6.28) is non-normal, and its eigenfunctions are not orthogonal to each other.

7.2.2 Biorthogonality condition and the definition of the energy norm

Substituting $\boldsymbol{A}\boldsymbol{\psi} = \mathrm{i}\omega_G \boldsymbol{B}\boldsymbol{\psi}$ and $\boldsymbol{A}^+\boldsymbol{\psi}^+ = -\mathrm{i}\omega_G^* \boldsymbol{B}\boldsymbol{\psi}^+$ into equation (7.1), we obtain the following equivalent equation:

$$\left[\mathrm{i}\omega_G^i - (\mathrm{i}\omega_G^j)\right] \int_0^1 (\boldsymbol{\psi}_j^+)^* \boldsymbol{B}\boldsymbol{\psi}_i \,\mathrm{d}Z = 0, \tag{7.5}$$

where $\boldsymbol{\psi}_j$ and $\boldsymbol{\psi}_j^+$ denote the jth eigenmode and adjoint eigenmode, respectively. If $i = j$, then equation (7.5) is satisfied. However, if $i \neq j$, the integral in equation (7.5) has to vanish instead. Therefore, the biorthogonality condition for the eigenfunctions is

$$\int_0^1 (\boldsymbol{\psi}_j^+)^* \boldsymbol{B}\boldsymbol{\psi}_i \,\mathrm{d}Z = \int_0^1 (\widetilde{H}_j^+)^* \widetilde{H}_i + \frac{\hat{R}\mathrm{e}\beta}{\bar{H}_0} (\widetilde{Q}_j^+)^* \widetilde{Q}_i + \theta_I \left(\frac{\mathrm{d}\widetilde{Q}_j^+}{\mathrm{d}Z}\right)^* \frac{\mathrm{d}\widetilde{Q}_i}{\mathrm{d}Z} \,\mathrm{d}Z = \mathcal{C}\delta_{ij}, \tag{7.6}$$

where $\mathcal{C}$ is a constant, δ_{ij} is the Kronecker delta, and $\boldsymbol{B}$ is the "weight operator."

Let $\Psi = (\mathcal{H}, \mathcal{Q})^\top$ denote an arbitrary infinitesimal disturbance. We define the (induced) energy norm $\|\cdot\|_E^2$ of the disturbance Ψ as

$$\|\Psi\|_E^2 = \langle \Psi, \Psi \rangle_E^2, \tag{7.7}$$

where the energy inner product arises from the biorthogonality condition:

$$\begin{aligned} \langle \Psi_1, \Psi_2 \rangle_E = \langle \Psi_1, \boldsymbol{B}\Psi_2 \rangle &= \int_0^1 \Psi_1^* \boldsymbol{B} \Psi_2 \,\mathrm{d}Z \\ &= \int_0^1 \mathcal{H}_1^* \mathcal{H}_2 + \frac{\hat{R}\mathrm{e}\beta}{\bar{H}_0} \mathcal{Q}_1^* \mathcal{Q}_2 + \theta_I \left(\frac{\mathrm{d}\mathcal{Q}_1}{\mathrm{d}Z}\right)^* \frac{\mathrm{d}\mathcal{Q}_2}{\mathrm{d}Z} \,\mathrm{d}Z. \end{aligned} \tag{7.8}$$

The definition of the energy norm (7.7) based on the energy inner product (7.8) also has a physical interpretation. The integral of $\mathcal{H}^*\mathcal{H}$ can be interpreted as the elastic energy density. As for the second term associated with $\mathcal{Q}$, recalling that $V_Z^{\mathrm{2D}} = 6QY(\bar{H} - Y)/\bar{H}^3$, we deduce that $\mathcal{Q}^*\mathcal{Q}/\bar{H}_0 \propto \int_0^{\bar{H}_0} (V_Z^{2D})^2 \mathrm{d}Y$ is the kinetic energy of the flow disturbance (evaluated at the unperturbed base state). Lastly, since $\partial Q/\partial Z = -\partial \bar{H}/\partial T$, the integral associated with $\mathrm{d}\mathcal{Q}/\mathrm{d}Z$ represents the kinetic energy of the wall motion.

7.2.3 Quantitative estimate of the eigenvalues' sensitivity

Letting $\boldsymbol{L} = \boldsymbol{B}^{-1}\boldsymbol{A}$, the generalized eigenvalue problem (6.28) can be transformed to the regular eigenvalue problem $\boldsymbol{L}\boldsymbol{\psi} = \mathrm{i}\omega_G\boldsymbol{\psi}$. Similarly, $\boldsymbol{L}^+ = \boldsymbol{B}^{-1}\boldsymbol{A}^+$. We still have $\boldsymbol{L}\boldsymbol{L}^+ \neq \boldsymbol{L}^+\boldsymbol{L}$, indicating that the operator $\boldsymbol{L}$ is non-normal. The non-normality of an operator can be assessed via the sensitivity of its eigenvalues [107]. Basically, the eigenvalue sensitivity is introduced to answer the following question: when the linear operator $\boldsymbol{L}$ is perturbed by small amount, by how much will the corresponding eigenvalues change? Formulated in a mathematical way, we seek to find the magnitude of the eigenvalue perturbation, $|\delta\omega_G^j|$ of the perturbed eigenvalue problem

$$(\boldsymbol{L} + \boldsymbol{P})(\boldsymbol{\psi}_j + \boldsymbol{\delta\psi}_j) = \mathrm{i}(\omega_G^j + \delta\omega_G^j)(\boldsymbol{\psi}_j + \boldsymbol{\delta\psi}_j), \tag{7.9}$$

where $\|\boldsymbol{P}\| = \varepsilon \ll 1$ (evaluated under an appropriate norm).

Assuming that the resulting $\|\boldsymbol{\delta\psi}_j\|, |\delta\omega_G^j| \sim \varepsilon \ll 1$ as well, and neglecting terms of $\mathcal{O}(\varepsilon^2)$, equation (7.9) is simplified as

$$(\boldsymbol{L} - \mathrm{i}\omega_G^j\boldsymbol{I})\boldsymbol{\delta\psi}_j + \boldsymbol{P}\boldsymbol{\psi}_j = \mathrm{i}\delta\omega_G^j\boldsymbol{\psi}_j. \tag{7.10}$$

If we assume that $\boldsymbol{\delta\psi}_j$ can be expanded in terms of the eigenfunction $\{\boldsymbol{\psi}_j\}_{j=1,2,\ldots}$, then the first term is identically zero. Multiplying the rest of equation (7.10) by $\boldsymbol{B}\boldsymbol{\psi}_j^+$, and taking the inner product over $Z \in [0,1]$, we obtain an estimate of $|\delta\omega_G^j|$ based on the energy norm defined in equation (7.7):

$$\begin{aligned}|\delta\omega_G^j|_E = \frac{\langle \boldsymbol{B}\boldsymbol{\psi}_j^+, \boldsymbol{P}\boldsymbol{\psi}_j\rangle}{\langle \boldsymbol{B}\boldsymbol{\psi}_j^+, \boldsymbol{\psi}_j\rangle} &= \langle \boldsymbol{B}\boldsymbol{\psi}_j^+, \boldsymbol{P}\boldsymbol{\psi}_j\rangle = \langle \boldsymbol{F}^{\mathrm{H}}\boldsymbol{F}\boldsymbol{\psi}_j^+, \boldsymbol{P}\boldsymbol{\psi}_j\rangle = \langle \boldsymbol{F}\boldsymbol{\psi}_j^+, \boldsymbol{F}\boldsymbol{P}\boldsymbol{F}^{-1}\boldsymbol{F}\boldsymbol{\psi}_j\rangle \\ &\leq \|\boldsymbol{F}\boldsymbol{\psi}_j^+\|\|\boldsymbol{F}\boldsymbol{\psi}_j\|\|\boldsymbol{F}\boldsymbol{P}\boldsymbol{F}^{-1}\| = \|\boldsymbol{\psi}_j^+\|_E\|\boldsymbol{\psi}_j\|_E\|\boldsymbol{P}\|_E.\end{aligned} \tag{7.11}$$

In the above equation, we have assumed that $\boldsymbol{\psi}_j$ and $\boldsymbol{\psi}_j^+$ have been properly normalized so that $\langle \boldsymbol{B}\boldsymbol{\psi}_j^+, \boldsymbol{\psi}_j\rangle = 1$. Furthermore, we have utilized the fact that $\boldsymbol{B}$ is positive definite, and thus it can be factored into $\boldsymbol{B} = \boldsymbol{F}^{\mathrm{H}}\boldsymbol{F}$ (the $^{\mathrm{H}}$ superscript denotes the conjugate transpose). Further, $\|\boldsymbol{P}\|_E := \|\boldsymbol{F}\boldsymbol{P}\boldsymbol{F}^{-1}\|$ is the energy norm of the operator perturbations.

This definition will become clear after the discrete formulation of $\boldsymbol{B}$ and $\boldsymbol{F}$ is introduced in section 7.3.2.

From the inequality (7.11), we can define the sensitivity of the eigenvalue ω_G^j as

$$s := \|\boldsymbol{\psi}_j^+\|_E \|\boldsymbol{\psi}_j\|_E. \tag{7.12}$$

If the eigenfunctions of $\boldsymbol{L}$ are orthogonal to each other, *i.e.*, $\boldsymbol{L}$ is a normal operator, then $s \equiv 1$. In this case, small perturbations of $\boldsymbol{L}$ do not affect the eigenspectrum. However, if $\boldsymbol{L}$ is non-normal, then $s > 1$. When $\boldsymbol{L}$ is "highly non-normal," such that $s \gg 1$, small perturbations of $\boldsymbol{L}$ can result in large changes of the eigenspectrum. In this case, computing the eigenvalues numerically will be challenging, since any numerical method used to approximate the linear operator will unavoidably introduce errors in the eigenvalues, which are then amplified by the non-normality.

7.2.4 Results

First, let us check the validity of the derived adjoint eigenvalue problem (7.2). We numerically solve equation (7.2) using the Chebyshev pseudospectral method, similar to how equation (6.28) was solved in section 6.C. However, due to the different boundary conditions (7.4), we need to use a different modified Lagrange polynomial basis. Now, the expansion is written as

$$\widetilde{Q}(\tilde{Z}) \approx (1+\tilde{Z}) \sum_{j=1}^{N} \widetilde{Q}_j \frac{\ell_j(\tilde{Z})}{1+\tilde{Z}_j}, \qquad \widetilde{H}(\tilde{Z}) \approx \sum_{j=0}^{N} \widetilde{H}_j \ell_j(\tilde{Z}). \tag{7.13}$$

Recall, as before, that $\tilde{Z}_j,\ j = 0, 1, \ldots, N$ are the Gauss–Lobatto points on $[-1, 1]$, with $\tilde{Z}_0 = -1$ and $\tilde{Z}_N = +1$.

In figure 7.1, we take case C3 from table 6.2 as an example, and show the eigenspectrum for the original eigenvalue problem (6.28) and its adjoint (7.2), respectively. As expected, the two eigenspectra are symmetric about the real axis, with the eigenvalues of the adjoint problem being the complex conjugates of the eigenvalues the original problem. Therefore, our formulation of the adjoint eigenvalue problem (7.2) has been validated.

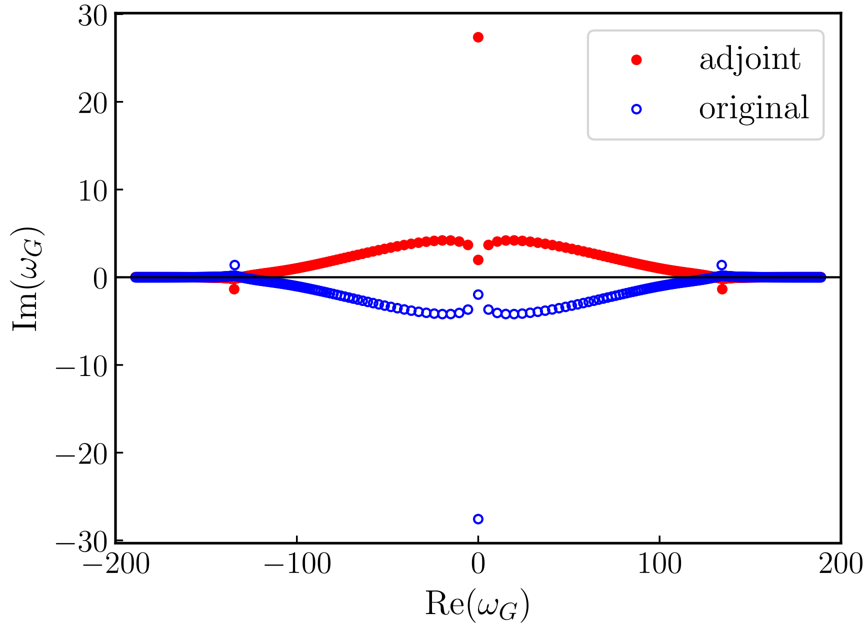

Figure 7.1. The eigenvalues of the original eigenvalue problem (6.28) and its adjoint (7.2) for case C3 from table 6.2.

Table 7.1. Dimensionless parameters for the newly introduced cases S1 and S2.

Case	$\hat{R}e$	β	θ_I	θ_t
S1	1.0	0.5	0.001	0.1
S2	1.0	0.5	0.001	0.001

In figure 7.2, we plot the eigenfunctions of the most unstable mode of case C3 and the corresponding adjoint eigenfunctions. It is clear that the eigenmode is different from its adjoint as the eigenvalue problem (6.28) is non-self-adjoint.

Next, we show the eigenvalue sensitivity defined by equation (7.12) in figure 7.3. We choose two example cases, C1 and C3, from table 6.2. As shown in figure 7.3 (also discussed in section 6.4), C1 is the linearly stable case while C3 is linearly unstable. For both cases, the sensitivity of the eigenvalues is $\mathcal{O}(1)$. Thus, we say the eigenspectra for cases C1 and C3 are not very sensitive to perturbations imposed on the linear operator.

In addition to C1 and C3, we have also computed spectra for another two cases, S1 and S2, with the system's dimensionless parameters given in table 7.1. The eigenspectra, colored

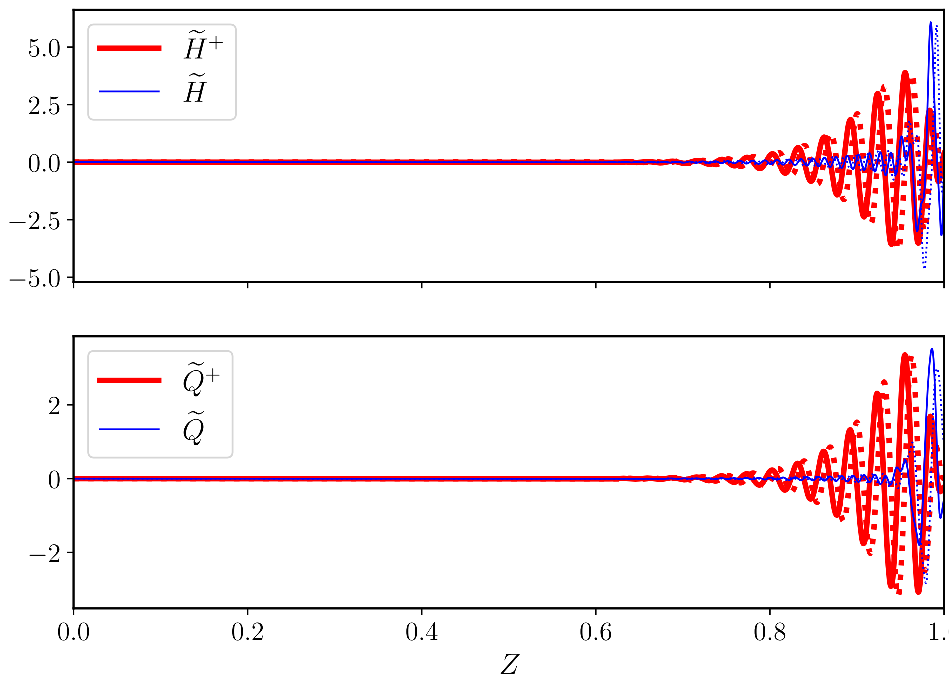

Figure 7.2. The eigenfunctions of the most unstable mode of the original eigenvalue problem (6.28) and the corresponding adjoint eigenfunctions for case C3 from table 6.2. The solid curves represent the real part of the eigenfunctions while the dotted curves represent the imaginary part.

with the eigenvalue sensitivity, for the two cases are shown in figure 7.4. We can see that S1 is linearly unstable, while S2 is linearly stable. Similar to the cases in figure 7.3, the eigenspectra for S1 and S2 display weak sensitivity to small perturbations imposed on the linear operator.

Due to the low sensitivity of the eigenspectra in the four cases considered, we do not need to worry that the discretization errors introduced in computing the eigenvalues with the Chebyshev pseudospectral method could lead to inaccurate results. It is worth emphasizing that the eigenvalue sensitivity is an intrinsic property of the linear operator. However, if the eigenvalue sensitivity of a linear operator is found to be high, then computing the eigenspectrum numerically might be challenging.

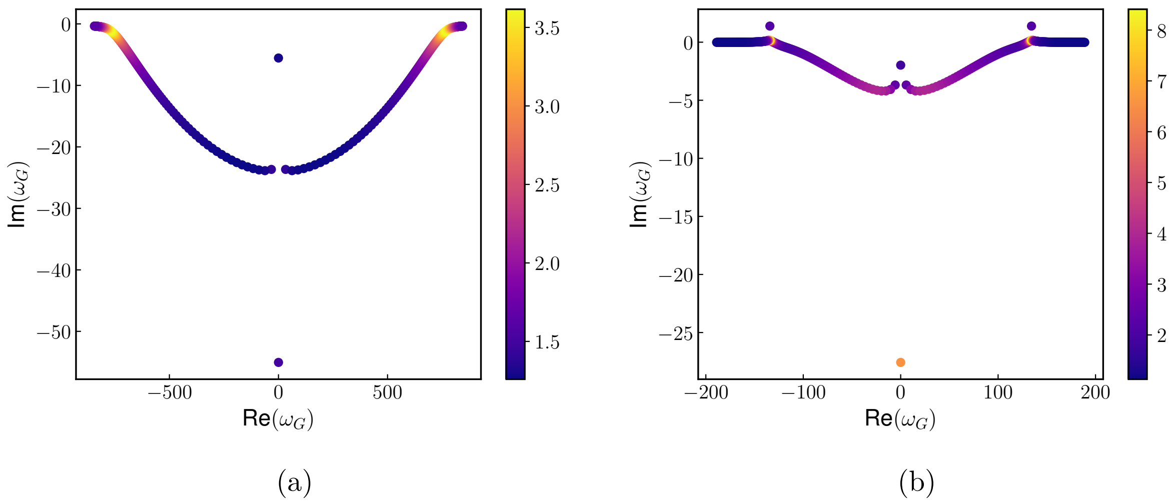

Figure 7.3. The eigenvalue sensitivity defined by equation (7.12) for (a) case C1 and (b) case C3 from table 6.2.

Nevertheless, it would be an unjustified conclusion to say that the linear problem (6.26) is weakly non-normal simply because the eigenvalue sensitivity is low. The eigenvalue sensitivity only sets the *upper bound* of how much a single eigenvalue can drift in the complex plane in response to a perturbation of the linear operator. In reality, the linear operator is acting on specific initial disturbances, and the non-normality of the operator directly determines how much the initial disturbances can grow. However, the eigenvalue sensitivity cannot provide such a quantitative estimate. From a practical point of view, computing the maximum transient energy amplification over *all* possible initial disturbances is more meaningful, which we now pursue in section 7.3.

7.3 Transient energy growth of infinitesimal initial perturbations

In this section, we compute the transient energy growth of the linear equation (6.26) quantitatively, following the framework outlined in [107].

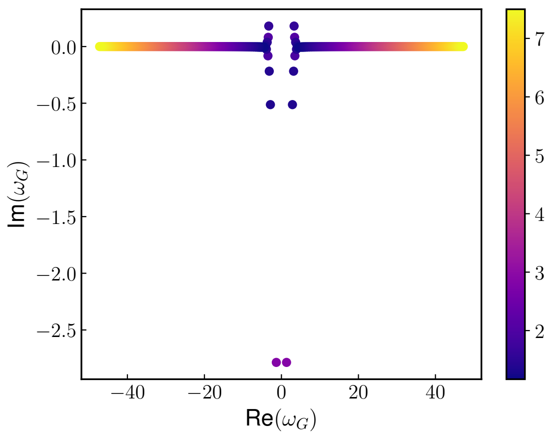

(a)

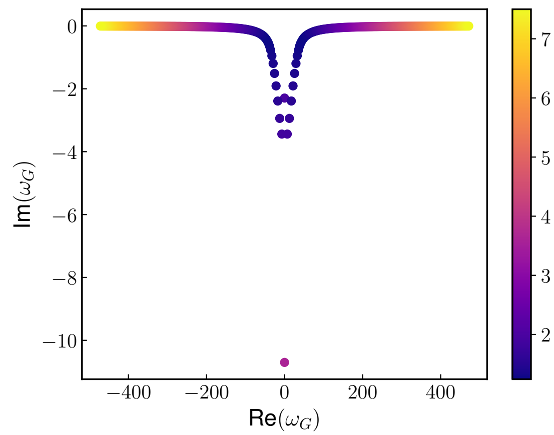

(b)

Figure 7.4. The eigenvalue sensitivity defined by equation (7.12) for (a) case S1 and (b) case S2 from table 7.1.

7.3.1 The linearized initial value problem

Let us introduce $\boldsymbol{\phi}(Z, T)$ as an infinitesimal disturbance superimposed onto the base state of the 1D FSI system described by equations (6.8), (6.12) and (5.12). Here, $\boldsymbol{\phi}$ satisfies the following initial-value problem (IVP):

$$\frac{\partial \boldsymbol{\phi}}{\partial T} = -\boldsymbol{L}\boldsymbol{\phi}, \quad \boldsymbol{\phi}(Z, 0) = \boldsymbol{\phi}_0(Z). \tag{7.14}$$

Recall that $\boldsymbol{L} = \boldsymbol{B}^{-1}\boldsymbol{A}$. Writing $\boldsymbol{\phi} = \boldsymbol{\psi}\mathrm{e}^{-\mathrm{i}\omega_G T}$, we obtain the eigenvalue problem (6.28). Formally, the solution of equation (7.14) is

$$\boldsymbol{\phi}(Z, T) = \boldsymbol{\phi}_0(Z)\mathrm{e}^{-\boldsymbol{L}T}. \tag{7.15}$$

While the long-time behavior of $\boldsymbol{\phi}$ is determined by the eigenvalues of $\boldsymbol{L}$, the energy of $\boldsymbol{\phi}$ during a short (finite) time window is related to the non-normality of $\boldsymbol{L}$. Our goal is to find an “optimal” $\boldsymbol{\phi}_0$ that gives rise to maximum transient energy amplification.

7.3.2 Eigenfunction expansion and discrete formulation

We only consider the disturbances that belong to the vector space spanned by the eigenfunctions of the linear operator:

$$\mathbb{S}^N = \mathrm{span}\{\boldsymbol{\psi}_1, \boldsymbol{\psi}_2, \cdots, \boldsymbol{\psi}_N\}. \tag{7.16}$$

Then $\forall \boldsymbol{\phi} \in \mathbb{S}^N$, we can write

$$\boldsymbol{\phi}(Z,T) = \sum_{i=0}^{N} c_i(T)\boldsymbol{\psi}_i(Z), \tag{7.17}$$

where $\boldsymbol{c} = (c_1, c_2, \ldots, c_N)^\top$ is the corresponding vector of coefficients in the expansion. Substituting equation (7.17) into equation (7.14), and using the fact that $\boldsymbol{L}\boldsymbol{\psi}_j = \mathrm{i}\omega_G^j \boldsymbol{\psi}_j$, we can rewrite the IVP (7.14) and its solution in terms of $\boldsymbol{c}$ as

$$\frac{\mathrm{d}\boldsymbol{c}}{\mathrm{d}T} = -\mathrm{i}\boldsymbol{\Lambda}\boldsymbol{c} \quad \Rightarrow \quad \boldsymbol{c} = \boldsymbol{c}_0 \mathrm{e}^{-\mathrm{i}\boldsymbol{\Lambda} T}, \tag{7.18}$$

where $\boldsymbol{c}(0) = \boldsymbol{c}_0$ and $\boldsymbol{\Lambda} = \mathrm{diag}\{\omega_G^1, \omega_G^2, \ldots, \omega_G^N\}$ is the diagonal matrix consisting of the eigenvalues.

We proceed by deriving the discrete formulation of the energy inner product defined in equation (7.8). Consider two arbitrary functions expanded in terms of the eigenfunction as $\boldsymbol{\phi}_1 = \boldsymbol{\psi}\boldsymbol{c}_1$ and $\boldsymbol{\phi}_2 = \boldsymbol{\psi}\boldsymbol{c}_2$, respectively. Here, $\boldsymbol{\psi}\boldsymbol{c}_{1,2}$ is a matrix multiplication because $\boldsymbol{\psi} = (\psi_1, \psi_2, \ldots, \psi_N)$ is a row vector while $\boldsymbol{c} = (c_1, c_2, \ldots, c_N)^\top$ is a column vector. Recalling that $\boldsymbol{\psi} = (\widetilde{\boldsymbol{H}}, \widetilde{\boldsymbol{Q}})^\top$, with $\widetilde{\boldsymbol{H}} = (\widetilde{H}_1, \widetilde{H}_2, \ldots, \widetilde{H}_N)$ and $\widetilde{\boldsymbol{Q}} = (\widetilde{Q}_1, \widetilde{Q}_2, \ldots, \widetilde{Q}_N)$, the energy inner product of $\boldsymbol{\phi}_1$ and $\boldsymbol{\phi}_2$ can be computed as

$$\begin{aligned}
\langle \boldsymbol{\phi}_1, \boldsymbol{\phi}_2 \rangle_E &= \int_0^1 (\widetilde{\boldsymbol{H}}\boldsymbol{c_1})^{\mathrm{H}} \widetilde{\boldsymbol{H}}\boldsymbol{c_2} + \frac{\hat{R}\mathrm{e}\beta}{\bar{H}_0} (\widetilde{\boldsymbol{Q}}\boldsymbol{c}_1)^{\mathrm{H}} \widetilde{\boldsymbol{Q}}\boldsymbol{c}_2 + \theta_I \left(\frac{\mathrm{d}\widetilde{\boldsymbol{Q}}}{\mathrm{d}Z}\boldsymbol{c}_1\right)^{\mathrm{H}} \frac{\mathrm{d}\widetilde{\boldsymbol{Q}}}{\mathrm{d}Z}\boldsymbol{c}_2 \,\mathrm{d}Z \\
&= \boldsymbol{c}_1^{\mathrm{H}} \underbrace{\int_0^1 (\widetilde{\boldsymbol{H}}^{\mathrm{H}}\widetilde{\boldsymbol{H}} + \frac{\hat{R}\mathrm{e}\beta}{\bar{H}_0} (\widetilde{\boldsymbol{Q}})^{\mathrm{H}} \widetilde{\boldsymbol{Q}} + \theta_I \left(\frac{\mathrm{d}\widetilde{\boldsymbol{Q}}}{\mathrm{d}Z}\right)^{\mathrm{H}} \frac{\mathrm{d}\widetilde{\boldsymbol{Q}}}{\mathrm{d}Z} \,\mathrm{d}Z}_{\boldsymbol{B}} \,\boldsymbol{c}_2 \\
&= \boldsymbol{c}_1^{\mathrm{H}} \boldsymbol{F}^{\mathrm{H}} \boldsymbol{F} \boldsymbol{c}_2.
\end{aligned} \tag{7.19}$$

Also note that the expression of $\boldsymbol{B}$ has been labeled. Recall that $\boldsymbol{B}$ is a $N \times N$ Hermitian matrix, thus we can write $\boldsymbol{B} = \boldsymbol{F}^{\mathrm{H}}\boldsymbol{F}$. With this formulation, the computation of the energy inner product is converted to matrix multiplication in terms of the associated coefficient vectors.

Then, $\forall \boldsymbol{\phi} \in \mathbb{S}^N$ with expansion coefficients $\boldsymbol{c}$, its energy norm, following the definition (7.7), can be computed as

$$\|\boldsymbol{\phi}\|_E = \sqrt{\langle \boldsymbol{\phi}, \boldsymbol{\phi} \rangle_E} = \sqrt{\boldsymbol{F}\boldsymbol{c}^{\mathrm{H}}\boldsymbol{F}\boldsymbol{c}} = \|\boldsymbol{F}\boldsymbol{c}\|_2. \tag{7.20}$$

Finally, for an $N \times N$ matrix $\boldsymbol{M}$, its induced energy matrix norm can be calculated as

$$\|\boldsymbol{M}\|_E = \max_{\boldsymbol{\phi}} \frac{\|\boldsymbol{M}\boldsymbol{\phi}\|_E}{\|\boldsymbol{\phi}\|_E} = \max_{\boldsymbol{\phi}} \frac{\|\boldsymbol{F}\boldsymbol{M}\boldsymbol{\phi}\|_2}{\|\boldsymbol{F}\boldsymbol{\phi}\|_2} = \max_{\boldsymbol{\phi}} \frac{\|\boldsymbol{F}\boldsymbol{M}\boldsymbol{F}^{-1}\boldsymbol{F}\boldsymbol{\phi}\|_2}{\|\boldsymbol{F}\boldsymbol{\phi}\|_2} = \|\boldsymbol{F}\boldsymbol{M}\boldsymbol{F}^{-1}\|_2. \tag{7.21}$$

7.3.3 Quantitative description of the transient energy amplification

Next, for the IVP (7.14), reduced to the IVP (7.18), we investigate the possible maximum finite-time energy growth in $\mathbb{S}^N$. To this end, the growth factor G is introduced, which is defined as

$$G(T) = \max_{\boldsymbol{\phi}_0 \neq 0} \frac{\|\boldsymbol{\phi}\|_E^2}{\|\boldsymbol{\phi}_0\|_E^2} = \max_{\boldsymbol{c}_0 \neq 0} \frac{\|\boldsymbol{c}\|_E^2}{\|\boldsymbol{c}_0\|_E^2 S} = \max_{\boldsymbol{c}_0 \neq 0} \frac{\|\mathrm{e}^{-\mathrm{i}\boldsymbol{\Lambda}T}\boldsymbol{c}_0\|_E^2}{\|\boldsymbol{c}_0\|_E^2} = \|\mathrm{e}^{-\mathrm{i}\boldsymbol{\Lambda}T}\|_E^2 = \|\boldsymbol{F}\mathrm{e}^{-\mathrm{i}\boldsymbol{\Lambda}T}\boldsymbol{F}\|_2^2. \tag{7.22}$$

Note that we have utilized equation (7.21) above to re-express the energy norm in terms of the 2-norm.

Over a finite time window of $T \in [0, T_{\mathrm{e}}]$, the maximum transient energy amplification $G(T)$ computed by equation (7.22) may correspond to different initial disturbances (with different expansion coefficients $\boldsymbol{c}_0$). Therefore, the curve of $G(T)$ is the *envelope* that wraps all the possible energy growth paths of disturbances in $\boldsymbol{\phi} \in \mathbb{S}^N$.

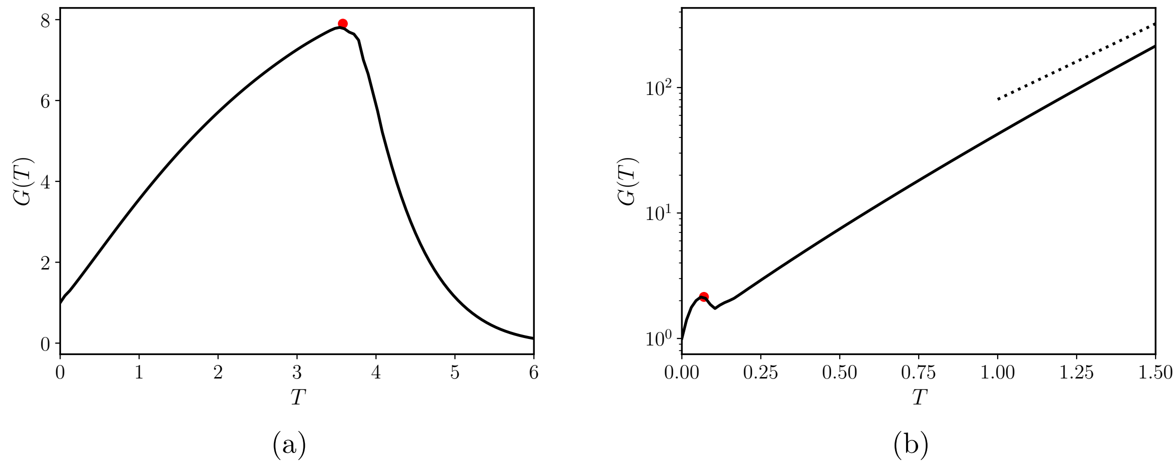

Figure 7.5. The maximum energy amplification of infinitesimal initial disturbances $G(T)$ of (a) case C1 and (b) case C3 from table 6.2. The dotted trendline in panel (b) indicates the growth rate, $[\mathrm{Im}(\omega_G)]^2$, of the most unstable eigenmode of C3. The red dots mark the local maxima in each panel.

7.3.4 Results

In figure 7.5, we show the maximum transient energy amplification of infinitesimal initial perturbations for cases C1 and C3. As shown in figure 7.5(a), for C1, the transient energy growth is at most $\mathcal{O}(1)$. The maximum energy amplification of the initial disturbances increases in a short time window near $T = 0$. After that, the maximum energy amplification decays, which is consistent with the fact that case C1 is a linearly stable. For case C3, shown in figure 7.5(b), the transient energy amplification is also not prominent. However, since C3 is linearly unstable, the most unstable eigenmode will dominate the evolution of the disturbance after a short time, and the maximum transient energy growth rate agrees with this mode's eigenvalue, $[\mathrm{Im}(\omega_G)]^2$. Here, we take the square of $\mathrm{Im}(\omega_G)$ because G is defined based on the square of the energy norm (see equation (7.22)). Since in both cases the transient energy amplification of initial disturbances is not significant, we conclude that, for C1 and C3, the eigenvalue analysis is adequate to study the linear stability of the corresponding steady state of the 1D FSI model.

However, the situation changes for cases S1 and S2. As shown in figure 7.6, the predicted maximum transient energy amplification is up to 10^2 for both cases, which is much

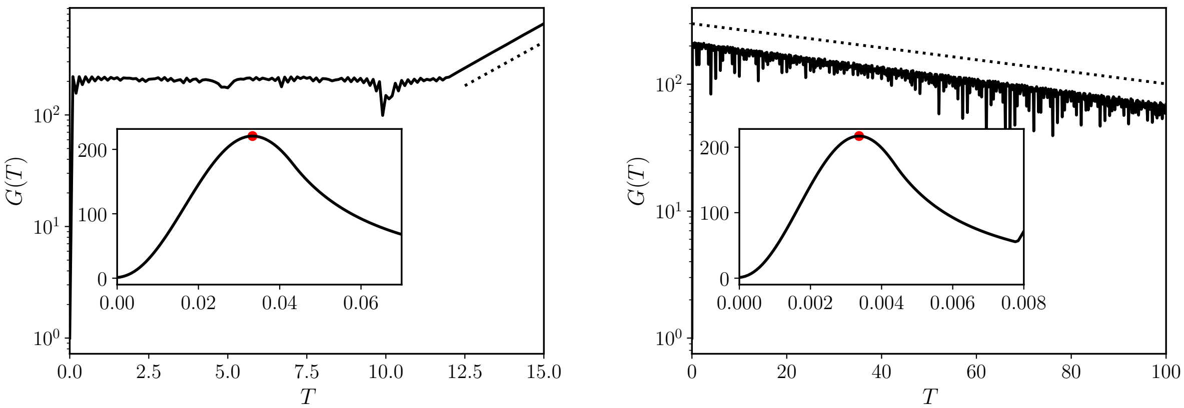

(a) (b)

Figure 7.6. The maximum energy amplification of infinitesimal initial disturbances $G(T)$ of (a) case S1 and (b) case S2 from table 7.1. The dotted trendlines in panel (a) and (b) indicate the growth/decay rate *i.e.*, $[\mathrm{Im}(\omega_G)]^2$, of the corresponding least stable eigenmodes of S1 and S2, respectively. The red dots mark the local maxima in each panel.

more prominent than for cases C1 and C3. In the linearly unstable case S1, as shown in figure 7.6(a), the energy of the initial disturbances can experience a sharp initial growth. However, for a relatively long time window of $0 \leq T \leq 12$ (before the most unstable eigenmode takes over), the maximum transient energy amplification that the linear system can achieve remains almost constant, save for some small oscillations. Note that, at each T, the corresponding initial disturbance that led to this state is different. Similarly, for the linearly stable case S2 shown in figure 7.6(b). For this case, the maximum transient energy amplification G decays slowly, at a rate close to the decay rate of the least stable eigenmode, although it does so over a must longer time window and oscillates. Note that, for both S1 and S2, there are many stable eigenmodes with very small and similar decay rates, as shown in figure 7.4. These eigenmodes are typically highly oscillatory in both space and time. Noting that such modes are much fewer for cases C1 and C3 (see figure 7.3), this might explain why the curves of G for cases C1 and C3 are much smoother than those for cases S1 and S2.

As discussed in section 7.2.2, the total energy of the disturbances includes the wall's elastic energy, the flow's kinetic energy and the wall's kinetic energy, which correspond to

Table 7.2. The components of and their percentage in the total energy of the disturbances for C1, C3, S1 and S3 at a specific time (indicated by the red dots in figures 7.5 and 7.6, respectively).

Case	Wall's elastic energy	Flow's kinetic energy	Wall's kinetic energy
C1	2.8811 (36.20%)	0.1959 (2.46%)	4.8819 (61.33%)
C3	0.0016 (0.07%)	0.0181 (0.84%)	2.1246 (99.08%)
S1	5.4461 (2.41%)	0.0051 (0.002%)	220.6665 (97.59%)
S2	8.6300 (3.83%)	0.2710 (0.12%)	216.7186 (96.05%)

the integrals of the first, the second and the third term in equation (7.8), respectively. We computed the three components of the total energy for each case in figures 7.5 and 7.6 at its corresponding local maximum of G (labeled with a red dot in the figures), and summarize the results in table 7.2. We find that the wall's kinetic energy makes up the largest portion of the disturbance's energy in all four cases. In particular, for cases C3, S1 and S2, the wall's kinetic energy is over 95% of the total energy. More interestingly, the wall's kinetic energy in cases S1 and S2 is much larger than that in cases C1 and C3, which makes the transient energy growth more prominent for cases S1 and S2. This observation might also relate to the fact that there are many highly oscillatory (but slowly decaying) eigenmodes for cases S1 and S2.

7.4 Discussion

In this chapter, we studied the non-normality of the linearized problem (6.26), which is obtained from imposing infinitesimal perturbations on the base state of the 1D FSI model (derived in chapter 6) and linearizing the governing equations. We computed two key quantities related to non-normality: the eigenvalue sensitivity s and the maximum transient energy amplification G. These quantities allow us to judge the "degree" of non-normality of the linearized problem.

In the four exemplar cases that we discussed, we found that the eigenspectra are not sensitive to perturbations of the linear operator of the problem (6.26). This observation is, in fact, good news because it means that we can trust our eigenvalue calculations, and that the numerical errors in approximating the linear operator will not result in inaccurate results.

If the eigenspectrum were sensitive, special care would need to be taken when approximating the eigenvalues numerically.

However, eigenvalue sensitivity is not a direct indicator of the non-normality of the linear operator. Even though the sensitivity of the eigenspectra (of the cases considered) is low, the predicted maximum transient energy amplification is different in each of the four cases. The infinitesimal initial disturbances in cases C1 and C3 only experience mild energy amplification, while the transient energy amplification of disturbances in cases S1 and S2 is much more prominent up to $\mathcal{O}(10^2)$. This indicates that the system parameters, $\hat{R}\mathrm{e}$, β, θ_I and θ_t (defined in chapter 6) can significantly affect the non-normality of the linear operator.

Moreover, in the evolution of the infinitesimal disturbances, the solid's kinetic energy is amplified to take the largest portion of the disturbance energy. In cases S1 and S2, where many highly oscillatory eigenmodes decay very slowly, this amplification is even stronger, and there exists a long time window over which the system can achieve substantial energy growth. As discussed in chapter 2 (and in [102]), the existence of these highly oscillatory modes relates to the stiffness of these FSI problems. If the wall oscillates at a high frequency, experiences substantial transient growth, and the transients decay very slowly, then the corresponding unsteady numerical simulations will be particularly challenging. Specifically, a rather long simulation time would be needed to capture and resolved the unsteady dynamics.

7.A Derivation of the adjoint eigenvalue problem

Denote the generalized eigenvalue problem (6.28) as $\mathscr{L}\boldsymbol{\psi} = \mathbf{0}$, with $\mathscr{L} = \boldsymbol{A} - \mathrm{i}\omega_G\boldsymbol{B}$. Then, by definition, the adjoint problem problem is $\mathscr{L}^+\boldsymbol{\psi}^+ = \mathbf{0}$, where

$$\int_0^1 (\boldsymbol{\psi}^+)^* \mathscr{L}\boldsymbol{\psi}\,\mathrm{d}Z = \int_0^1 (\mathscr{L}^+\boldsymbol{\psi}^+)^*\boldsymbol{\psi}\,\mathrm{d}Z. \tag{7.23}$$

Here, the * superscript denotes the complex conjugate. Also, recall that $\boldsymbol{\psi} = (\widetilde{H},\ \widetilde{Q})^\top$ and $\boldsymbol{\psi}^+ = (\widetilde{H}^+,\ \widetilde{Q}^+)^\top$. Substituting equation (6.28) into equation (7.1), the left hand side (LHS) can be written as

$$
\begin{aligned}
\mathrm{LHS} = \int_0^1 &\underbrace{(\widetilde{H}^+)^* \frac{\mathrm{d}\widetilde{Q}}{\mathrm{d}Z}}_{\mathrm{L1}} + \underbrace{(\widetilde{Q}^+)^* \mathscr{L}_H \widetilde{H}}_{\mathrm{L2}} + \underbrace{(\widetilde{Q}^+)^* \mathscr{L}_Q \widetilde{Q}}_{\mathrm{L3}} \\
&- \underbrace{\mathrm{i}\omega_G \left[(\widetilde{H}^+)^* \widetilde{H} + (\widetilde{Q}^+)^* \frac{\hat{R}\mathrm{e}\beta}{\bar{H}_0} \widetilde{Q} - \theta_I (\widetilde{Q}^+)^* \frac{\mathrm{d}^2\widetilde{Q}}{\mathrm{d}Z^2} \right]}_{\mathrm{R}} \mathrm{d}Z.
\end{aligned} \tag{7.24}
$$

For convenience in the upcoming derivation, several terms in this expression have been denoted by symbols in the braces below them.

The derivation of the adjoint is essentially an exercise in integration by parts. First, the term L1 can be written as

$$
\begin{aligned}
\mathrm{L1} = \int_0^1 (\widetilde{H}^+)^* \mathrm{d}\widetilde{Q} &= (\widetilde{H}^+)^* \widetilde{Q} \Big|_0^1 - \int_0^1 \left(\frac{\mathrm{d}\widetilde{H}^+}{\mathrm{d}Z} \right)^* \widetilde{Q}\, dZ \\
&= (\widetilde{H}^+)^* \widetilde{Q} \Big|_{Z=1} - \int_0^1 \left(\frac{\mathrm{d}\widetilde{H}^+}{\mathrm{d}Z} \right)^* \widetilde{Q}\, dZ,
\end{aligned} \tag{7.25}
$$

where we have employed the boundary condition $\widetilde{Q}(0) = 0$ from equation (6.30).

Similarly,

$$
\begin{aligned}
\mathrm{L2} = \int_0^1 (\widetilde{Q}^+)^* &\left[\left(\frac{18}{5} \hat{R}\mathrm{e}\beta \frac{Q_0^2}{\bar{H}_0^4} \frac{\mathrm{d}\bar{H}_0}{\mathrm{d}Z} - \frac{36\beta Q_0}{\bar{H}_0^4} \right) \widetilde{H} + \left(1 - \frac{6}{5} \hat{R}\mathrm{e}\beta \frac{Q_0^2}{\bar{H}_0^3} \right) \frac{\mathrm{d}\widetilde{H}}{\mathrm{d}Z} - \theta_t \frac{\mathrm{d}^3\widetilde{H}}{\mathrm{d}Z^3} \right] \mathrm{d}Z \\
= \int_0^1 &\left[\left(\frac{18}{5} \hat{R}\mathrm{e}\beta \frac{Q_0^2}{\bar{H}_0^4} \frac{\mathrm{d}\bar{H}_0}{\mathrm{d}Z} - \frac{36\beta Q_0}{\bar{H}_0^4} \right) \widetilde{Q}^+ \right]^* \widetilde{H}\, \mathrm{d}Z \\
&+ (\widetilde{Q}^+)^* \left(1 - \frac{6}{5} \hat{R}\mathrm{e}\beta \frac{Q_0^2}{\bar{H}_0^3} \right) \widetilde{H} \Bigg|_0^1 - \int_0^1 \left\{ \frac{\mathrm{d}}{\mathrm{d}Z} \left[\left(1 - \frac{6}{5} \hat{R}\mathrm{e}\beta \frac{Q_0^2}{\bar{H}_0^3} \right) \widetilde{Q}^+ \right] \right\}^* \widetilde{H}\, \mathrm{d}Z \\
&- \theta_t (\widetilde{Q}^+)^* \frac{\mathrm{d}^2\widetilde{H}}{\mathrm{d}Z^2} \Bigg|_0^1 + \theta_t \left(\frac{\mathrm{d}\widetilde{Q}^+}{\mathrm{d}Z} \right)^* \frac{\mathrm{d}\widetilde{H}}{\mathrm{d}Z} \Bigg|_0^1 - \theta_t \left(\frac{\mathrm{d}^2\widetilde{Q}+}{\mathrm{d}Z^2} \right)^* \widetilde{H} \Bigg|_0^1 + \int_0^1 \left(\theta_t \frac{\mathrm{d}^3\widetilde{Q}^+}{\mathrm{d}Z^3} \right)^* \widetilde{H}\, \mathrm{d}Z \\
= \theta_t &(\widetilde{Q}^+)^* \frac{\mathrm{d}^2\widetilde{H}}{\mathrm{d}Z^2} \Bigg|_{Z=0} + \theta_t \left(\frac{\mathrm{d}\widetilde{Q}^+}{\mathrm{d}Z} \right)^* \frac{\mathrm{d}\widetilde{H}}{\mathrm{d}Z} \Bigg|_0^1 \\
&+ \int_0^1 \left\{ \left[-\frac{36\beta Q_0}{\bar{H}_0^4} - \left(1 - \frac{6}{5} \hat{R}\mathrm{e}\beta \frac{Q_0^2}{\bar{H}_0^3} \right) \frac{\mathrm{d}}{\mathrm{d}Z} + \theta_t \frac{\mathrm{d}^3}{\mathrm{d}Z^3} \right] \widetilde{Q}^+ \right\}^* \widetilde{H}\, \mathrm{d}Z,
\end{aligned} \tag{7.26}
$$

where we have employed the boundary conditions $\widetilde{H}(0) = \widetilde{H}(1) = 0$ and $(\mathrm{d}^2\widetilde{H}/\mathrm{d}Z^2)|_{Z=1} = 0$ from equation (6.30).

Next,

$$
\begin{aligned}
\mathrm{L3} &= \int_0^1 (\widetilde{Q}^+)^* \left[\left(-\frac{12}{5}\hat{R}\mathrm{e}\beta \frac{Q_0}{\bar{H}_0^3}\frac{\mathrm{d}\bar{H}_0}{\mathrm{d}Z} + \frac{12\beta}{\bar{H}_0^3} \right) \widetilde{Q} + \frac{12}{5}\hat{R}\mathrm{e}\beta \frac{Q_0}{\bar{H}_0^2}\frac{\mathrm{d}\widetilde{Q}}{\mathrm{d}Z} \right] \mathrm{d}Z \\
&= \int_0^1 \left[\left(-\frac{12}{5}\hat{R}\mathrm{e}\beta \frac{Q_0}{\bar{H}_0^3}\frac{\mathrm{d}\bar{H}_0}{\mathrm{d}Z} + \frac{12\beta}{\bar{H}_0^3} \right) \widetilde{Q}^+ \right]^* \widetilde{Q}\,\mathrm{d}Z \\
&\quad + (\widetilde{Q}^+)^* \frac{12}{5}\hat{R}\mathrm{e}\beta \frac{Q_0}{\bar{H}_0^2}\widetilde{Q}\bigg|_0^1 - \int_0^1 \left[\frac{\mathrm{d}}{\mathrm{d}Z}\left(\frac{12}{5}\hat{R}\mathrm{e}\beta \frac{Q_0}{\bar{H}_0^2}\widetilde{Q}^+ \right) \right]^* \widetilde{Q}\,\mathrm{d}Z \\
&= (\widetilde{Q}^+)^* \frac{12}{5}\hat{R}\mathrm{e}\beta \frac{Q_0}{\bar{H}_0^2}\widetilde{Q}\bigg|_{Z=1} \\
&\quad + \int_0^1 \left\{ \left[\frac{12}{5}\hat{R}\mathrm{e}\beta \frac{Q_0}{\bar{H}_0^3}\frac{\mathrm{d}\bar{H}_0}{\mathrm{d}Z} + \frac{12\beta}{\bar{H}_0^3} - \frac{12}{5}\hat{R}\mathrm{e}\beta \frac{Q_0}{\bar{H}_0^2}\frac{\mathrm{d}}{\mathrm{d}Z} \right] \widetilde{Q}^+ \right\}^* \widetilde{Q}\,\mathrm{d}Z,
\end{aligned}
\tag{7.27}
$$

where we have employed the boundary condition $\widetilde{Q}(0) = 0$ from equation (6.30).

Lastly,

$$
\begin{aligned}
\mathrm{R} &= \int_0^1 \mathrm{i}\omega_G \left[(\widetilde{H}^+)^*\widetilde{H} + \left(\frac{\hat{R}\mathrm{e}\beta}{\bar{H}_0}\widetilde{Q}^+ \right)^* \widetilde{Q} - \theta_I (\widetilde{Q}^+)^* \frac{\mathrm{d}^2\widetilde{Q}}{\mathrm{d}Z^2} \right] \mathrm{d}Z \\
&= \int_0^1 \mathrm{i}\omega_G \left[(\widetilde{H}^+)^*\widetilde{H} + \left(\frac{\hat{R}\mathrm{e}\beta}{\bar{H}_0}\widetilde{Q}^+ \right)^* \widetilde{Q} \right] \mathrm{d}Z \\
&\quad - \mathrm{i}\omega_G \left[\theta_I (\widetilde{Q}^+)^* \frac{\mathrm{d}\widetilde{Q}}{\mathrm{d}Z}\bigg|_0^1 - \theta_I \left(\frac{\mathrm{d}\widetilde{Q}^+}{\mathrm{d}Z} \right)^* \widetilde{Q}\bigg|_0^1 + \int_0^1 \theta_I \left(\frac{\mathrm{d}^2\widetilde{Q}^+}{\mathrm{d}Z^2} \right)^* \widetilde{Q}\,\mathrm{d}Z \right] \\
&= \mathrm{i}\omega_G\,\theta_I \left(\frac{\mathrm{d}\widetilde{Q}^+}{\mathrm{d}Z} \right)^* \widetilde{Q}\bigg|_{Z=1} + \int_0^1 (-\mathrm{i}\omega_G^*\widetilde{H}^+)^*\widetilde{H} + \left[-\mathrm{i}\omega_G^* \left(\frac{\hat{R}\mathrm{e}\beta}{\bar{H}_0} - \theta_I \frac{\mathrm{d}^2}{\mathrm{d}Z^2} \right) \widetilde{Q}^+ \right]^* \widetilde{Q}\,\mathrm{d}Z,
\end{aligned}
\tag{7.28}
$$

where we have employed the boundary conditions $\widetilde{Q}(0) = 0$ and $(\mathrm{d}\widetilde{Q}/\mathrm{d}Z)|_{Z=0,1} = 0$. Also note that $(\mathrm{i}\omega_G)^* = -\mathrm{i}\omega_G^*$.

Adding equations (7.25), (7.26), (7.27) and (7.28) together, in order to eliminate the boundary terms, we obtain the boundary conditions for $\widetilde{H}^+$ and $\widetilde{Q}^+$ given in equation (7.4). Then, the remaining terms can be written in a matrix form as equation (7.2).

8. SUMMARY AND OUTLOOK

8.1 Thesis summary

In this thesis, we have investigated the interaction between internal low-Reynolds-number flow and compliant boundaries at the microscale by combining mathematical modeling with numerical simulations. We have discovered the key mechanisms governing the steady response, the dynamics and the stability of these microscale fluid–structure interactions (FSIs). Inertial and unsteady effects have been of particular interest, constituting key contributions of this thesis to the modeling and stability of flows in compliant microchannels. Specifically, the chapter-wise accomplishments of this thesis are:

- **Chapter 2:** We studied the steady state and the linear stability of a previously derived 1D FSI model, which describes flow through a 2D channel with a beam-like compliant wall on its top. At steady state, there are two pairs of competing mechanisms, *i.e.*, the inertial and viscous forces in the flow, and the bending and tension effect in the wall deformation. We identified two scaling regimes for the axially averaged pressure in the flow, and four different regimes for the maximum deformation of the top wall. Each of these scaling regimes was validated against steady-state numerical simulations. We then investigated the linear stability of the non-flat steady state of the 1D model. We computed its eigenvalues with the Chebyshev pseudospectral method, and found that the 1D FSI problem is linearly stable to infinitesimal perturbations. Many eigenmodes were found to be highly oscillatory and decay slowly in time, which highlights the computational challenges of simulating unsteady FSIs.

- **Chapter 3:** Starting from this chapter, we turned to a more realistic problem of flow through a 3D long and shallow rectangular microchannel with a deformable top wall. In this chapter, we provided a general discussion of the dominant mechanisms in both the flow and the elastic deformation of the wall. Specifically, through a scaling analysis taking advantage of the channel being long and shallow, we found that, even with finite fluid inertia included (up to a reduced Reynolds number of order unity), the flow is unidirectional with the hydrodynamic pressure varying only along the flowwise direction at the leading order. The inertial forces in the flow are balanced by the dominant pressure gradient and the viscous forces. We also conducted a scaling analysis of the linear elastodynamic equations that govern the solid deformation. Unlike previous studies, we did not assume the top wall to be thin, but required that it is slender (*i.e.*, its thickness is much smaller than its channel length). We found that the balance of the dominant Cauchy stresses always occurs in a cross-sectional plane perpendicular to the flow, which reduces the 3D elasticity problem to a 2D plane-strain problem. This plane-strain reduction indicated that the deformation of the cross-sections at different streamwise locations decouple from each other, and thus the deformation is fully determined by the local pressure at the leading order, yielding a separation of variables solution for the interface displacement (at the leading order in the slenderness parameter).

- **Chapter 4:** We investigated a specific example of inertialess flows through a long, shallow rectangular microchannel embedded in a thick elastic slab. The Winkler-foundation-like dominant mechanism of the wall deformation discovered in chapter 3 applies in this case. Specifically, we found that each cross-section deforms like a simply supported rectangle subjected to a uniform pressure at its bottom. The solution of this 2D elasticity problem was found in terms of a Fourier series. By integrating the axial velocity across the deformed channel's cross-section, we derived a parameter-free flow rate–pressure drop relation. We validated this newly derived relation against previous experiments and found satisfactory agreement, whereas previous models did not (or required fitting parameters).

- **Chapter 5:** We introduced the width-averaged deformed channel height as the *effective* deformed height, with which we recovered the same expression for the empirical flow rate–pressure drop relation derived in [12]. In the inertialess flow regime, we found that this width-averaged approach introduced controllable errors into the resulting flow rate–pressure drop relation, compared to the approach based on the full leading-order solution of the solid deformation. Then, we extended the use of the width-averaged effective deformed height into the inertial flow regime, and derived a 1D reduced model that relates the flow rate and pressure to the wall deformation at steady state. The model not only includes the dominant Winkler-foundation-like mechanism for the wall deformation, but also captures weak deformation effects as regularizations to allow the system to satisfy displacement constraints imposed at the channel's inlet and outlet. For weak tension effect, we found a matched-asymptotic analytical solution for the deformation.

- **Chapter 6:** We extended the steady-state 1D reduced model derived in chapter 5 into an unsteady model by including the flow unsteadiness and the solid's inertia into the formulation. The proposed 1D solid mechanics model combines the dominant Winkler-foundation-like mechanism with weak tension (as in chapter 5) with weak inertia of the wall. We showed that the reduced model can capture key features observed in experiments, both for the steady and dynamic responses. More importantly, we explained the observed FSI-induced hydrodynamic instability in compliant microchannels from a *global* perspective, providing improved physical understanding. Specifically, we have found that the non-flat steady state of the 1D FSI problem can become linearly unstable, typically at finite Reynolds number (corresponding to a reduced Reynolds number at $\mathcal{O}(1)$, similar to the experimental observations). Furthermore, the unstable eigenmodes oscillate at frequencies close to the natural frequency of the wall, indicating that the global instability is related to wall-mode resonances. Also, in our numerical simulations of the 1D reduced model, we observed that a wall resonance can be triggered by FSIs, with the system subsequently undergoing self-sustained oscillations.

- **Chapter 7:** We investigated the linear non-normality of the linear problem governing the evolution of infinitesimal perturbations around the base state of the 1D FSI system derived in chapter 7. We considered four exemplar cases (choices of parameters) and found that the eigenspectra of the linear system are not very sensitive to perturbations of the linear operator. However, the results for the maximum transient energy amplification differed from case to case, which indicated that the system parameters can significantly affect the linear non-normality of the system. In particular, we observed large transient energy amplification in the case with many slowly decaying but highly oscillatory eigenmodes. In such cases, the solid kinetic energy can experience substantial transient growth, which would make the corresponding numerical simulations challenging. These observations can have implications for designing novel microscale mixing systems that exploit the interplay between (in)stability and transient growth in microscale FSIs.

8.2 Future work

In chapters 3 to 6, we showed that the interface deformation can be modeled as the combination of a dominant Winkler-foundation-like mechanism and weak effects (such as tension). Specifically, the Winkler-foundation-like behavior is captured by the constant (dimensionless) spring stiffness β, which can be obtained by solving the corresponding 2D plane-strain problem at the leading order. In chapters 4 and 5, we considered thick-walled and the plate-like microchannels as two examples and derived the expressions of β. However, in different configurations, both the wall thickness and the constraints of the side walls, as well as those on the upper surface of the compliant wall, can influence the derived expression for β. For example, in section 4.A (see also [101]), we discussed the plane-strain solution in a similar configuration to that of chapter 4, but the wall thickness is moderate with $d \lesssim w$. Also, in the experiments of Verma and Kumaran [41], the compliant wall with a thickness of $d \sim w$ is pressed upon a rigid surface. Apparently, the boundary conditions of this configuration need careful modeling, and the resulting β should have a different form from that in the existing literature. Providing an exhaustive survey of different β expressions for different configurations and boundary conditions is important for the design of microfluidic systems.

Apart from the dominant Winkler-foundation-like behavior, the formulation of the weak deformation effects also depends on the configuration of the microchannel. In this thesis, we only discussed the weak tension effect. However, if the compliant wall is plate-like or beam-like, bending could also play a role as another weak effect. In studies on collapsible tubes, it has been shown that various deformation effects, such as bending, pre-tension and stretching, can lead to a rich phenomenology of FSI instabilities [74], [179], but the discussions are limited to the high-Reynolds-number flows which are not relevant to the microfluidic setting. On the other hand, in the low-Reynolds-number regime, even though the bending effect was discussed in chapter 2, it was considered in a 2D channel and bending was not a weak effect in this case. In other works, weak bending [38] and pre-tension [34] have only been considered under steady flow. How such further (weak) deformation effects would couple with the flow and affect the *dynamics* and stability of the FSIs in the regime of low-Reynolds number remains to be determined in future work.

It is also worthwhile to extend the results in this thesis by considering different flow operating conditions in different conduit geometries. In this thesis, we have only discussed the situation in which the volumetric flux is fixed at the channel's inlet, and the channel's outlet is open to the atmosphere. Alternatively, the pressure drop could be prescribed across the channel, similarly to the works of Stewart *et al.* [86], [87]. Further, soft conduits are not necessarily rectangular. For example, a microtube is also common in experiments [134], [180], [181]. However, as long as the basic assumptions on the separation of scales (and weak versus dominant effects in the solid) are not violated, the current 1D modeling framework can be applied to such FSIs as well [39].

The construction of the 1D FSI model in this thesis was motivated by microfluidic experiments and aimed to provide new qualitative and quantitative physical insights into the hydrodynamics in compliant microchannels. Nevertheless, further work is needed to understand the full range of dynamic behaviors possible under the proposed 1D FSI model. For example, in the linearly unstable case, the numerical simulations of the model using different time step sizes begin to diverge after a certain (long) integration time. This observation reminds us of the similarly chaotic behavior observed in a 1D FSI model derived by Jensen [84] in the context of collapsible tubes. Similar to our 1D FSI model, Jensen's model also exhibits multiple unstable modes, and its dynamics may be sensitive to initial conditions (due to the interactions of multiple unstable modes). Therefore, understanding the nonlinear dynamics of the proposed 1D FSI model could be a fruitful avenue for future work. Further, since the observed oscillations are low-amplitude and high-frequency, asymptotic analysis could yield the stability boundaries [91]. On the other hand, an Orr–Sommerfeld-type local stability analysis (similarly to the Kumaran family of studies, recall chapter 1) could once again be conducted on the proposed model to complement to the global stability analysis from chapter 6. Investigating the connections between the local and global instabilities could provide insight regarding what types of excitations trigger unstable global modes [86], [87], opening the door towards more controllable "ultrafast mixing" due to FSIs in compliant microchannels.

Finally, as a complement to the linear stability and the linear non-normality analysis of the reduced, 1D unsteady FSI model, *nonlinear* non-normal analysis could provide a more complete picture of the transient growth of initial disturbances. This understanding may be more helpful in guiding the design and control of the dynamics of various compliant microsystems. The standard approach to the nonlinear non-normality analysis is the so-called direct-adjoint looping method [182], which searches for optimal initial perturbations that lead to maximum energy amplification within a given finite time window. Previous studies showed that nonlinearities lead to disturbances evolving differently from the predictions of linear theory [183], [184]. Furthermore, since the nonlinear theory reduces to the linear theory, when the initial perturbation's energy is sufficiently small, then as argued by Kerswell [185], the nonlinear non-normality analysis "bridges the conceptual gap" between the standard linear approach to infinitesimal perturbations and the more advanced dynamical system approach to the nonlinear behaviors, including transient growth and instability.

REFERENCES

[1] T. M. Squires and S. R. Quake, "Microfluidics: Fluid physics at the nanoliter scale," *Rev. Mod. Phys.*, vol. 77, pp. 977–1026, 2005, DOI: 10.1103/RevModPhys.77.977.

[2] H. Bruus, *Theoretical Microfluidics*, ser. Oxford Master Series in Condensed Matter Physics. Oxford, UK: Oxford University Press, 2008.

[3] Y. Xia and G. M. Whitesides, "Soft lithography," *Annu. Rev. Mater. Sci.*, vol. 28, pp. 153–184, 1998, DOI: 10.1146/annurev.matsci.28.1.153.

[4] J. C. McDonald and G. M. Whitesides, "Poly(dimethylsiloxane) as a material for fabricating microfluidic devices," *Acc. Chem. Res.*, vol. 35, pp. 491–499, 2002, DOI: 10.1021/ar010110q.

[5] E. Sollier, C. Murray, P. Maoddi, and D. Di Carlo, "Rapid prototyping polymers for microfluidic devices and high pressure injections," *Lab Chip*, vol. 11, pp. 3752–3765, 2011, DOI: 10.1039/c1lc20514e.

[6] H. A. Stone, A. D. Stroock, and A. Ajdari, "Engineering flows in small devices: Microfluidics toward a Lab-on-a-Chip," *Annu. Rev. Fluid Mech.*, vol. 36, pp. 381–411, 2004, DOI: 10.1146/annurev.fluid.36.050802.122124.

[7] S. Chakraborty, Ed., *Microfluidics and Microscale Transport Processes*, ser. IIT Kharagpur Research Monograph Series. Boca Raton, FL: CRC Press, 2013, DOI: 10.1201/b12976.

[8] H. Fallahi, J. Zhang, H.-P. Phan, and N.-T. Nguyen, "Flexible microfluidics: Fundamentals, recent developments, and applications," *Micromachines*, vol. 10, p. 830, 2019, DOI: 10.3390/mi10120830.

[9] D. Huh, B. D. Matthews, A. Mammoto, M. Montoya-Zavala, H. Y. Hsin, and D. E. Ingber, "Reconstituting organ-level lung functions on a chip," *Science*, vol. 328, pp. 1662–1668, 2010, DOI: 10.1126/science.1188302.

[10] S. K. Sia and G. M. Whitesides, "Microfluidic devices fabricated in poly(dimethylsiloxane) for biological studies," *Electrophoresis*, vol. 24, pp. 3563–3576, 2003, DOI: 10.1002/elps.200305584.

[11] I. D. Johnston, D. K. McCluskey, C. K. L. Tan, and M. C. Tracey, "Mechanical characterization of bulk Sylgard 184 for microfluidics and microengineering," *J. Micromech. Microeng.*, vol. 24, p. 35 017, 2014, DOI: 10.1088/0960-1317/24/3/035017.

[12] T. Gervais, J. El-Ali, A. Günther, and K. F. Jensen, "Flow-induced deformation of shallow microfluidic channels," *Lab Chip*, vol. 6, pp. 500–507, 2006, DOI: 10.1039/b513524a.

[13] D. Chakraborty, J. R. Prakash, J. Friend, and L. Yeo, "Fluid-structure interaction in deformable microchannels," *Phys. Fluids*, vol. 24, p. 102 002, 2012, DOI: 10.1063/1.4759493.

[14] E. Delamarche, H. Schmid, B. Michel, and H. Biebuyck, "Stability of molded polydimethylsiloxane microstructures," *Adv. Mat.*, vol. 9, pp. 741–746, 1997, DOI: 10.1002/adma.19970090914.

[15] C. Y. Hui, A. Jagota, Y. Y. Lin, and E. J. Kramer, "Constraints on microcontact printing imposed by stamp deformation," *Langmuir*, vol. 18, pp. 1394–1407, 2002, DOI: 10.1021/la0113567.

[16] T. Thorsen, S. J. Maerkl, and S. R. Quake, "Microfluidic large-scale integration," *Science*, vol. 298, pp. 580–584, 2002, DOI: 10.1126/science.1076996.

[17] M. Gomez, D. E. Moulton, and D. Vella, "Passive control of viscous flow via elastic snap-through," *Phys. Rev. Lett.*, vol. 119, p. 144 502, 2017, DOI: 10.1103/PhysRevLett.119.144502.

[18] K. Hosokawa, K. Hanada, and R. Maeda, "A polydimethylsiloxane (PDMS) deformable diffraction grating for monitoring of local pressure in microfluidic devices," *J. Microelectromechan. Syst.*, vol. 12, pp. 1–6, 2002, DOI: 10.1088/0960-1317/12/1/301.

[19] O. Ozsun, V. Yakhot, and K. L. Ekinci, "Non-invasive measurement of the pressure distribution in a deformable micro-channel," *J. Fluid Mech.*, vol. 734, R1, 2013, DOI: 10.1017/jfm.2013.474.

[20] C. Dhong, S. J. Edmunds, J. Ramírez, *et al.*, "Optics-free, non-contact measurements of fluids, bubbles, and particles in microchannels using metallic nano-islands on graphene," *Nano Lett.*, vol. 18, pp. 5306–5311, 2018, DOI: 10.1021/acs.nanolett.8b02292.

[21] P. Niu, B. J. Nablo, K. Bhadriraju, and D. R. Reyes, "Uncovering the contribution of microchannel deformation to impedance-based flow rate measurements," *Anal. Chem.*, vol. 89, pp. 11 372–11 377, 2017, DOI: 10.1021/acs.analchem.7b02287.

[22] K. Shiba, G. Li, E. Virot, G. Yoshikawa, and D. A. Weitz, "Microchannel measurements of viscosity for both gases and liquids," *Lab Chip*, vol. 21, pp. 2805–2811, 2021, DOI: 10.1039/D1LC00202C.

[23] P. Karan, J. Chakraborty, S. Chakraborty, S. T. Wereley, and I. C. Christov, "Profiling a soft solid layer to passively control the conduit shape in a compliant microchannel during flow," *Phys. Rev. E*, vol. 104, p. 015 108, 2021, DOI: 10.1103/PhysRevE.104.015108.

[24] C. Duprat and H. A. Stone, Eds., *Fluid–Structure Interactions in Low-Reynolds-Number Flows*. Cambridge, UK: The Royal Society of Chemistry, 2016, DOI: 10.1039/9781782628491.

[25] P. Karan, J. Chakraborty, and S. Chakraborty, "Small-scale flow with deformable boundaries," *J. Indian Inst. Sci.*, vol. 98, pp. 159–183, 2018, DOI: 10.1007/s41745-018-0073-5.

[26] B. S. Hardy, K. Uechi, J. Zhen, and H. Pirouz Kavehpour, "The deformation of flexible PDMS microchannels under a pressure driven flow," *Lab Chip*, vol. 9, pp. 935–938, 2009, DOI: 10.1039/B813061B.

[27] P. Cheung, K. Toda-Peters, and A. Q. Shen, "In situ pressure measurement within deformable rectangular polydimethylsiloxane microfluidic devices," *Biomicrofluidics*, vol. 6, p. 026 501, 2012, DOI: 10.1063/1.4720394.

[28] M. K. Raj, S. DasGupta, and S. Chakraborty, "Hydrodynamics in deformable microchannels," *Microfluid. Nanofluid.*, vol. 21, p. 70, 2017, DOI: 10.1007/s10404-017-1908-5.

[29] E. Seker, D. C. Leslie, H. Haj-Hariri, J. P. Landers, M. Utz, and M. R. Begley, "Nonlinear pressure-flow relationships for passive microfluidic valves," *Lab Chip*, vol. 9, pp. 2691–2697, 2009, DOI: 10.1039/B903960K.

[30] I. C. Christov, "Soft hydraulics: from Newtonian to complex fluid flows through compliant conduits," *J. Phys.: Condens. Matter*, vol. 34, p. 063 001, 2022, DOI: 10.1088/1361-648X/ac327d.

[31] I. C. Christov, V. Cognet, T. C. Shidhore, and H. A. Stone, "Flow rate–pressure drop relation for deformable shallow microfluidic channels," *J. Fluid Mech.*, vol. 814, pp. 267–286, 2018, DOI: 10.1017/jfm.2018.30.

[32] E. Boyko, H. A. Stone, and I. C. Christov, "Flow rate-pressure drop relation for deformable channels via fluidic and elastic reciprocal theorems," *preprint, arXiv:2203.14112*, 2022, DOI: 10.48550/arXiv.2203.14112.

[33] T. C. Shidhore and I. C. Christov, "Static response of deformable microchannels: a comparative modelling study," *J. Phys.: Condens. Matter*, vol. 30, p. 054 002, 2018, DOI: 10.1088/1361-648X/aaa226.

[34] V. Anand, S. C. Muchandimath, and I. C. Christov, "Hydrodynamic Bulge Testing: Materials Characterization Without Measuring Deformation," *ASME J. Appl. Mech.*, vol. 87, p. 051 012, 2020, DOI: 10.1115/1.4046297.

[35] E. Boyko, D. Ilssar, M. Bercovici, and A. D. Gat, "Interfacial instability of thin films in soft microfluidic configurations actuated by electro-osmotic flow," *Phys. Rev. Fluids*, vol. 5, p. 104 201, 2020, DOI: 10.1103/PhysRevFluids.5.104201.

[36] V. Anand, J. D. J. Rathinaraj, and I. C. Christov, "Non-Newtonian fluid–structure interactions: Static response of a microchannel due to internal flow of a power-law fluid," *J. Non-Newtonian Fluid Mech.*, vol. 264, pp. 62–72, 2019, DOI: 10.1016/j.jnnfm.2018.12.008.

[37] L. Ramos-Arzola and O. Bautista, "Fluid-structure interaction in a deformable microchannel conveying a viscoelastic fluid," *J. Non-Newtonian Fluid Mech.*, vol. 296, p. 104 634, 2021, DOI: 10.1016/j.jnnfm.2021.104634.

[38] V. Anand and I. C. Christov, "Revisiting steady viscous flow of a generalized Newtonian fluid through a slender elastic tube using shell theory," *Z. Angew. Math. Mech. (ZAMM)*, vol. 101, e201900309, 2021, DOI: 10.1002/zamm.201900309.

[39] X. Wang, S. Pande, and I. C. Christov, "Flow rate–pressure drop relations for new configurations of slender compliant tubes arising in microfluidics experiments," *preprint, arXiv:2205.10973*, 2022, DOI: 10.48550/arXiv.2205.10973.

[40] D. Di Carlo, D. Irimia, R. G. Tompkins, and M. Toner, "Continuous inertial focusing, ordering, and separation of particles in microchannels," *Proc. Natl Acad. Sci. USA*, vol. 104, pp. 18 892–18 897, 2007, DOI: 10.1073/pnas.0704958104.

[41] M. K. S. Verma and V. Kumaran, "A multifold reduction in the transition Reynolds number, and ultra-fast mixing, in a micro-channel due to a dynamical instability induced by a soft wall," *J. Fluid Mech.*, vol. 727, pp. 407–455, 2013, DOI: 10.1017/jfm.2013.264.

[42] J. M. Ottino and S. Wiggins, "Introduction: mixing in microfluidics," *Phil. Trans. R. Soc. A*, vol. 362, pp. 923–935, 2004, DOI: 10.1098/rsta.2003.1355.

[43] R. Karnik, "Microfluidic Mixing," in *Encyclopedia of Microfluidics and Nanofluidics*, D. Li, Ed., Boston, MA: Springer, 2013, pp. 1–13, DOI: 10.1007/978-3-642-27758-0_939-2.

[44] V. Kumaran, G. H. Fredrickson, and P. Pincus, "Flow induced instability of the interface between a fluid and a gel at low Reynolds number," *J. Phys. II France*, vol. 4, no. 6, pp. 893–911, 1994, DOI: 10.1051/jp2:1994173.

[45] V. Kumaran and R. Muralikrishnan, "Spontaneous Growth of Fluctuations in the Viscous Flow of a Fluid past a Soft Interface," *Phys. Rev. Lett.*, vol. 84, pp. 3310–3313, 2000, DOI: 10.1103/PhysRevLett.84.3310.

[46] A. Shrivastava, E. L. Cussler, and S. Kumar, "Mass transfer enhancement due to a soft elastic boundary," *Chem. Eng. Res. Des.*, vol. 63, pp. 4302–4305, 2008, DOI: 10.1016/j.ces.2008.05.030.

[47] P. Krindel and A. Silberberg, "Flow through gel-walled tubes," *J. Colloid Interface Sci.*, vol. 71, pp. 39–50, 1979, DOI: 10.1016/0021-9797(79)90219-4.

[48] K. V. Sharp and R. J. Adrian, "Transition from laminar to turbulent flow in liquid filled microtubes," *Exp. Fluids*, vol. 36, pp. 741–747, 2004, DOI: 10.1007/s00348-003-0753-3.

[49] K. V. Sharp and R. J. Adrian, "Erratum: Transition from laminar to turbulent flow in liquid filled microtubes," *Exp. Fluids*, vol. 38, pp. 132–132, 2005, DOI: 10.1007/s00348-004-0893-0.

[50] M. K. S. Verma and V. Kumaran, "A dynamical instability due to fluid–wall coupling lowers the transition Reynolds number in the flow through a flexible tube," *J. Fluid Mech.*, vol. 705, pp. 322–347, 2012, DOI: 10.1017/jfm.2011.55.

[51] R. Neelamegam and V. Shankar, "Experimental study of the instability of laminar flow in a tube with deformable walls," *Phys. Fluids*, vol. 27, p. 024 102, 2015, DOI: 10.1063/1.4907246.

[52] V. Kumaran and P. Bandaru, "Ultra-fast microfluidic mixing by soft-wall turbulence," *Chem. Eng. Sci.*, vol. 149, pp. 156–168, 2016, DOI: 10.1016/j.ces.2016.04.001.

[53] S. S. Srinivas and V. Kumaran, "After transition in a soft-walled microchannel," *J. Fluid Mech.*, vol. 780, pp. 649–686, 2015, DOI: 10.1017/jfm.2015.476.

[54] S. S. Srinivas and V. Kumaran, "Transitions to different kinds of turbulence in a channel with soft walls," *J. Fluid Mech.*, vol. 822, pp. 267–306, 2017, DOI: 10.1017/jfm.2017.270.

[55] V. Kumaran, "Stability of the viscous flow of a fluid through a flexible tube," *J. Fluid Mech.*, vol. 294, pp. 259–281, 1995, DOI: 10.1017/S0022112095002886.

[56] Gaurav and V. Shankar, "Stability of fluid flow through deformable neo-Hookean tubes," *J. Fluid Mech.*, vol. 627, pp. 291–322, 2009, DOI: 10.1017/S0022112009005928.

[57] M. K. S. Verma and V. Kumaran, "Stability of the flow in a soft tube deformed due to an applied pressure gradient," *Phys. Rev. E*, vol. 91, p. 043 001, 2015, DOI: 10.1103/PhysRevE.91.043001.

[58] V. Gkanis and S. Kumar, "Stability of pressure-driven creeping flows in channels lined with a nonlinear elastic solid," *J. Fluid Mech.*, vol. 524, pp. 357–375, 2005, DOI: 10.1017/S0022112004002472.

[59] R. Patne and V. Shankar, "Stability of flow through deformable channels and tubes: implications of consistent formulation," *J. Fluid Mech.*, vol. 860, pp. 837–885, 2019, DOI: 10.1017/jfm.2018.908.

[60] V. Kumaran, "Stability and the transition to turbulence in the flow through conduits with compliant walls," *J. Fluid Mech.*, vol. 924, P1, 2021, DOI: 10.1017/jfm.2021.602.

[61] D. Dendukuri, S. S. Gu, D. C. Pregibon, T. A. Hatton, and P. S. Doyle, "Stop-flow lithography in a microfluidic device," *Lab Chip*, vol. 7, pp. 818–828, 2007, DOI: 10.1039/b703457a.

[62] P. Panda, K. P. Yuet, D. Dendukuri, T. A. Hatton, and P. S. Doyle, "Temporal response of an initially deflected PDMS channel," *New J. Phys.*, vol. 11, p. 115 001, 2009, DOI: 10.1088/1367-2630/11/11/115001.

[63] U. Mukherjee, J. Chakraborty, and S. Chakraborty, "Relaxation characteristics of a compliant microfluidic channel under electroosmotic flow," *Soft Matter*, vol. 9, pp. 1562–1569, 2013, DOI: 10.1039/c2sm27247d.

[64] J. M. Skotheim and L. Mahadevan, "Soft lubrication," *Physical Review Letters*, vol. 92, p. 245 509, 2004, DOI: 10.1103/PhysRevLett.92.245509.

[65] J. M. Skotheim and L. Mahadevan, "Soft lubrication: The elastohydrodynamics of non-conforming and conforming contacts," *Phys. Fluids*, vol. 17, p. 092 101, 2005, DOI: 10.1063/1.1985467.

[66] A. Martínez-Calvo, A. Sevilla, G. G. Peng, and H. A. Stone, "Start-up flow in shallow deformable microchannels," *J. Fluid Mech.*, vol. 885, A25, 2020, DOI: 10.1017/jfm.2019.994.

[67] J. J. Riley, M. Gad-el-Hak, and R. W. Metcalfe, "Complaint coatings," *Annu. Rev. Fluid Mech.*, vol. 20, pp. 393–420, 1988, DOI: 10.1146/annurev.fl.20.010188.002141.

[68] M. Gad-el-Hak, "Compliant coatings: A decade of progress," *Appl. Mech. Rev.*, vol. 49, S147–S157, 1996, DOI: 10.1115/1.3101966.

[69] M. P. Païdoussis, "Plates in axial flow," in *Fluid-Structure Interactions*, vol. 2, Academic Press, 2003, ch. 10, pp. 1137–1220, DOI: 10.1016/S1874-5652(04)80006-1.

[70] T. J. Pedley, *The Fluid Mechanics of Large Blood Vessels*. Cambridge: Cambridge University Press, 1980, DOI: 10.1017/CBO9780511896996.

[71] J. B. Grotberg and O. E. Jensen, "Biofluid mechanics in flexible tubes," *Annu. Rev. Fluid Mech.*, vol. 36, pp. 121–147, 2004, DOI: 10.1146/annurev.fluid.36.050802.121918.

[72] T. J. Pedley and D. Pihler-Puzović, "Flow and oscillations in collapsible tubes: Physiological applications and low-dimensional models," *Sādhānā: J. Indian Acad. Sci.*, vol. 40, pp. 891–909, 2015, DOI: 10.1007/s12046-015-0363-9.

[73] X. Y. Luo and T. J. Pedley, "A numerical simulation of unsteady flow in a two-dimensional collapsible channel," *J. Fluid Mech.*, vol. 314, pp. 191–225, 1996, DOI: 10.1017/S0022112096000286.

[74] X. Y. Luo and T. J. Pedley, "The effects of wall inertia on flow in a two-dimensional collapsible channel," *Journal of Fluid Mechanics*, vol. 363, pp. 253–280, 1998, DOI: 10.1017/S0022112098001062.

[75] T. Pedley and X. Luo, "Modelling Flow and Oscillations in Collapsible Tubes," *Theor. Comp. Fluid Dyn.*, vol. 10, pp. 277–294, 1998, DOI: 10.1007/s001620050064.

[76] M. Heil and A. L. Hazel, "Fluid-structure interaction in internal physiological flows," *Annu. Rev. Fluid Mech.*, vol. 43, pp. 141–162, 2011, DOI: 10.1146/annurev-fluid-122109-160703.

[77] X. Y. Luo, Z. X. Cai, W. G. Li, and T. J. Pedley, "The cascade structure of linear instability in collapsible channel flows," *J. Fluid Mech.*, vol. 600, pp. 45–76, 2008, DOI: 10.1017/S0022112008000293.

[78] M. Heil and J. Boyle, "Self-excited oscillations in three-dimensional collapsible tubes: simulating their onset and large-amplitude oscillations," *J. Fluid Mech.*, vol. 652, pp. 405–426, 2010, DOI: 10.1017/S0022112010000157.

[79] H. F. Liu, X. Y. Luo, and Z. X. Cai, "Stability and energy budget of pressure-driven collapsible channel flows," *J. Fluid Mech.*, vol. 705, pp. 348–370, 2012, DOI: 10.1017/jfm.2011.254.

[80] D. Wang, X. Luo, and P. Stewart, "Energetics of collapsible channel flow with a nonlinear fluid-beam model," *J. Fluid Mech.*, vol. 926, A2, 2021, DOI: 10.1017/jfm.2021.642.

[81] A. H. Shapiro, "Steady flow in collapsible tubes," *ASME J. Biomech. Eng.*, vol. 99, pp. 126–147, 1977, DOI: 10.1115/1.3426281.

[82] O. E. Jensen and T. J. Pedley, "The existence of steady flow in a collapsed tube," *J. Fluid Mech.*, vol. 206, pp. 339–374, 1989, DOI: 10.1017/S0022112089002326.

[83] O. E. Jensen, "Instabilities of flow in a collapsed tube," *J. Fluid Mech.*, vol. 220, pp. 623–659, 1990, DOI: 10.1017/S0022112090003408.

[84] O. E. Jensen, "Chaotic Oscillations in a Simple Collapsible-Tube Model," *ASME J. Biomech. Eng.*, vol. 114, pp. 55–59, 1992, DOI: 10.1115/1.2895450.

[85] D. Pihler-Puzović and T. J. Pedley, "Flutter in a quasi-one-dimensional model of a collapsible channel," *Proc. R. Soc. A*, vol. 470, p. 20 140 015, 2014, DOI: 10.1098/rspa.2014.0015.

[86] P. S. Stewart, S. L. Waters, and O. E. Jensen, "Local and global instabilities of flow in a flexible-walled channel," *Eur. J. Mech. B/Fluids*, vol. 28, pp. 541–557, 2009, DOI: 10.1016/j.euromechflu.2009.03.002.

[87] P. Stewart, M. Heil, S. L. Waters, and O. E. Jensen, "Sloshing and slamming oscillations in a collapsible channel flow," *J. Fluid Mech.*, vol. 662, pp. 288–319, 2010, DOI: 10.1017/S0022112010003277.

[88] F. Xu, J. Billingham, and O. E. Jensen, "Divergence-driven oscillations in a flexible-channel flow with fixed upstream flux," *J. Fluid Mech.*, vol. 723, pp. 706–733, 2013, DOI: 10.1017/jfm.2013.97.

[89] F. Xu, J. Billingham, and O. E. Jensen, "Resonance-driven oscillations in a flexible-channel flow with fixed upstream flux and a long downstream rigid segment," *J. Fluid Mech.*, vol. 746, pp. 368–404, 2014, DOI: 10.1017/jfm.2014.136.

[90] P. Stewart and A. J. E. Foss, "Self-excited oscillations in a collapsible channel with applications to retinal venous pulsation," *ANZIAM J.*, vol. 61, pp. 320–348, 2019, DOI: 10.1017/S1446181119000117.

[91] O. E. Jensen and M. Heil, "High-frequency self-excited oscillations in a collapsible-channel flow," *J. Fluid Mech.*, vol. 481, pp. 235–268, 2003, DOI: 10.1017/S002211200300394X.

[92] L. N. Trefethen, A. E. Trefethen, S. C. Reddy, and T. A. Driscoll, "Hydrodynamic stability without eigenvalues," *Science*, vol. 261, pp. 578–584, 1993, DOI: 10.1126/science.261.5121.578.

[93] S. C. Reddy and D. S. Henningson, "Energy Growth in Viscous Channel Flows," *J. Fluid Mech.*, vol. 252, pp. 209–238, 1993, DOI: 10.1017/S0022112093003738.

[94] S. C. Reddy, P. J. Schmid, and D. S. Henningson, "Pseudospectra of the Orr-Sommerfeld operator," *SIAM J. Appl. Math.*, vol. 53, pp. 15–47, 1993, DOI: 10.1137/0153002.

[95] J. M. Davis, B. J. Fischer, and S. M. Troian, "A general approach to the linear stability of thin spreading films," in *Interfacial Fluid Dynamics and Transport Processes*, ser. Lecture Notes in Physics, R. Narayanan and D. Schwabe, Eds., vol. 628, Berlin/Heidelberg: Springer, 2003, pp. 79–106, DOI: 10.1007/978-3-540-45095-5_5.

[96] J. M. Davis and S. M. Troian, "On a generalized approach to the linear stability of spatially nonuniform thin film flows," *Phys. Fluids*, vol. 15, pp. 1344–1347, 2003, DOI: 10.1063/1.1564094.

[97] B. F. Farrell and P. J. Ioannou, "Generalized Stability Theory. Part I: Autonomous Operators," *Journal Atmos. Sci.*, vol. 53, pp. 2025–2040, 1996, DOI: 10.1175/1520-0469(1996)053⟨2025:GSTPIA⟩2.0.CO;2.

[98] B. F. Farrell and P. J. Ioannou, "Generalized Stability Theory. Part II: Nonautonomous Operators," *Journal Atmos. Sci.*, vol. 53, pp. 2041–2053, 1996, DOI: 10.1175/1520-0469(1996)053⟨2041:GSTPIN⟩2.0.CO;2.

[99] P. J. Schmid, "Nonmodal stability theory," *Annu. Rev. Fluid Mech.*, vol. 39, pp. 129–162, 2007, DOI: 10.1146/annurev.fluid.38.050304.092139.

[100] V. Theofilis, "Global linear instability," *Annu. Rev. Fluid Mech.*, vol. 43, pp. 319–352, 2011, DOI: 10.1146/annurev-fluid-122109-160705.

[101] X. Wang and I. C. Christov, "Theory of the flow-induced deformation of shallow compliant microchannels with thick walls," *Proc. R. Soc. A*, vol. 475, p. 20 190 513, 2019, DOI: 10.1098/rspa.2019.0513.

[102] T. C. Inamdar, X. Wang, and I. C. Christov, "Unsteady fluid-structure interactions in a soft-walled microchannel: A one-dimensional lubrication model for finite Reynolds number," *Phys. Rev. Fluids*, vol. 5, p. 064 101, 2020, DOI: 10.1103/PhysRevFluids.5.064101.

[103] J. N. Reddy, *Theory and Analysis of Elastic Plates and Shells*, 2nd ed. Boca Raton, FL: CRC Press, an imprint of Taylor & Francis Group, 2007, DOI: 10.1201/9780849384165.

[104] R. L. Panton, *Incompressible Flow*, 4th. Hoboken, NJ: John Wiley & Sons, 2013, DOI: 10.1002/9781118713075.

[105] P. S. Stewart, "Instabilities in flexible channel flow with large external pressure," *J. Fluid Mech.*, vol. 825, pp. 922–960, 2017, DOI: 10.1017/jfm.2017.404.

[106] P. Virtanen, R. Gommers, T. E. Oliphant, *et al.*, "SciPy 1.0: fundamental algorithms for scientific computing in Python," *Nature Methods*, vol. 17, pp. 261–272, 2020, DOI: 10.1038/s41592-019-0686-2.

[107] P. J. Schmid and D. S. Henningson, *Stability and Transition in Shear Flows*, ser. Applied Mathematical Sciences. New York, NY: Springer, 2001, vol. 142, DOI: 10.1007/978-1-4613-0185-1.

[108] J. P. Boyd, *Chebyshev and Fourier Spectral Methods*, 2nd ed. Mineola, NY: Dover Publications, 2000.

[109] W. Huang and D. M. Sloan, "The pseudospectral method for solving differential eigenvalue problems," *J. Comput. Phys.*, vol. 111, pp. 399–409, 1994, DOI: 10.1006/JCPH.1994.1073.

[110] J. Shen, T. Tang, and L.-L. Wang, *Spectral Methods: Algorithms, Analysis and Applications*, ser. Springer Series in Computational Mathematics. Berlin/Heidelberg: Springer-Verlag, 2011, vol. 41, DOI: 10.1007/978-3-540-71041-7.

[111] M. Butler, F. Box, T. Robert, and D. Vella, "Elasto-capillary adhesion: Effect of deformability on adhesion strength and detachment," *Phys. Rev. Fluids*, vol. 4, p. 033 601, 2019, DOI: 10.1103/PhysRevFluids.4.033601.

[112] J. M. Davis and S. M. Troian, "On a generalized approach to the linear stability of spatially nonuniform thin film flows," *Phys. Fluids*, vol. 15, pp. 1344–1347, 2003, DOI: 10.1063/1.1564094.

[113] S. Symon, K. Rosenberg, S. T. M. Dawson, and B. J. McKeon, "On non-normality and classification of amplification mechanisms in stability and resolvent analysis," *Phys. Rev. Fluids*, vol. 3, p. 053 902, 2018, DOI: 10.1103/PhysRevFluids.3.053902.

[114] X. Wang and I. C. Christov, "Reduced models of unidirectional flows in compliant rectangular ducts at finite Reynolds number," *Phys. Fluids*, vol. 33, p. 102 004, 2021, DOI: 10.1063/5.0062252.

[115] F. M. White, *Viscous Fluid Flow*, 3rd ed. New York, NY: McGraw-Hill Higher Education, 2006.

[116] S. B. Elbaz and A. D. Gat, "Dynamics of viscous liquid within a closed elastic cylinder subject to external forces with application to soft robotics," *J. Fluid Mech.*, vol. 758, pp. 221–237, 2014, DOI: 10.1017/jfm.2014.527.

[117] E. Winkler, *Die Lehre von der Elastizität und Festigkeit mit besonderer Rücksicht auf ihre Anwendung in der Technik*. Prag: Verlag von H. Dominicus, 1867, [Online]. Available: https://www.google.com/books/edition/_/25E5AAAAcAAJ.

[118] D. A. Dillard, B. Mukherjee, P. Karnal, R. C. Batra, and J. Frechette, "A review of Winkler's foundation and its profound influence on adhesion and soft matter applications," *Soft Matter*, vol. 14, pp. 3669–3683, 2018, DOI: 10.1039/c7sm02062g.

[119] A. E. H. Love, "The small free vibrations and deformation of a thin elastic shell," *Phil. Trans. R. Soc. Lond. A*, vol. 179, pp. 491–546, 1888, DOI: 10.1098/rsta.1888.0016.

[120] S. Timoshenko and S. Woinowsky-Krieger, *Theory of Plates and Shells*, 2nd. New York: McGraw-Hill, 1959.

[121] E. Reissner, "The effect of transverse shear deformation on the bending of elastic plates," *ASME J. Appl. Mech.*, vol. 12, A68–A77, 1945.

[122] R. D. Mindlin, "Influence of rotatory inertia and shear on flexural motions of isotropic, elastic plates," *ASME J. Appl. Mech.*, vol. 18, pp. 31–38, 1951.

[123] B. Tavakol, G. Froehlicher, H. A. Stone, and D. P. Holmes, "Extended lubrication theory: Improved estimates of flow in channels with variable geometry," *Proc. R. Soc. A*, vol. 473, p. 20 170 234, 2017, DOI: 10.1098/rspa.2017.0234.

[124] S. H. Davis, "The importance of being thin," *J. Eng. Math.*, vol. 105, pp. 3–30, 2017, DOI: 10.1007/s10665-017-9910-1.

[125] O. Reynolds, "On the theory of lubrication and its application to Mr. Beauchamp tower's experiments, including an experimental determination of the viscosity of olive oil," *Phil. Trans. R. Soc. Lond.*, vol. 177, pp. 157–234, 1886, DOI: 10.1098/rstl.1886.0005.

[126] L. G. Leal, *Advanced Transport Phenomena: Fluid Mechanics and Convective Transport Processes*, ser. Cambridge Series in Chemical Engineering. New York, NY: Cambridge University Press, 2007, vol. 7, DOI: 10.1017/CBO9780511800245.

[127] W. M. Lai, D. Rubin, and E. Krempl, *Introduction to Continuum Mechanics*, 3rd ed. Oxford: Pergamon Press, 1993, DOI: 10.1016/C2009-0-07992-6.

[128] R. Hindman, *Magnify*, MATLAB Central File Exchange, https://www.mathworks.com/matlabcentral/fileexchange/5961-magnify, 2016.

[129] N. A. Mortensen, F. Okkels, and H. Bruus, "Reexamination of Hagen-Poiseuille flow: Shape dependence of the hydraulic resistance in microchannels," *Phys. Rev. E*, vol. 71, p. 57 301, 2005, DOI: 10.1103/PhysRevE.71.057301.

[130] J. Happel and H. Brenner, *Low Reynolds number hydrodynamics*, 2nd, ser. Mechanics of fluids and transport processes. Dordrecht: Springer Netherlands, 1983, DOI: 10.1007/978-94-009-8352-6.

[131] S. I. Rubinow and J. B. Keller, "Flow of a viscous fluid through an elastic tube with applications to blood flow," *J. Theor. Biol.*, vol. 34, pp. 299–313, 1972, DOI: 10.1016/0022-5193(72)90041-0.

[132] W. K. Schomburg, *Introduction to Microsystem Design*. Berlin/Heidelberg: Springer-Verlag, 2011, DOI: 10.1007/978-3-642-19489-4.

[133] J. Wells, *R-square: The coefficient of determination, version 1.4.0.0*, MATLAB Central File Exchange, https://www.mathworks.com/matlabcentral/fileexchange/34492-r-square-the-coefficient-of-determination, 2012.

[134] K. Raj M, J. Chakraborty, S. DasGupta, and S. Chakraborty, "Flow-induced deformation in a microchannel with a non-Newtonian fluid," *Biomicrofluidics*, vol. 12, p. 034 116, 2018, DOI: 10.1063/1.5036632.

[135] S. Rubin, A. Tulchinsky, A. D. Gat, and M. Bercovici, "Elastic deformations driven by non-uniform lubrication flows," *J. Fluid Mech.*, vol. 812, pp. 841–865, 2017, DOI: 10.1017/jfm.2016.830.

[136] E. Boyko, R. Eshel, K. Gommed, A. D. Gat, and M. Bercovici, "Elastohydrodynamics of a pre-stretched finite elastic sheet lubricated by a thin viscous film with application to microfluidic soft actuators," *J. Fluid Mech.*, vol. 862, pp. 732–752, 2019, DOI: 10.1017/jfm.2018.967.

[137] A. Raj and A. K. Sen, "Flow-induced deformation of compliant microchannels and its effect on pressure–flow characteristics," *Microfluid. Nanofluid.*, vol. 20, p. 31, 2016, DOI: 10.1007/s10404-016-1702-9.

[138] A. Mehboudi and J. Yeom, "Experimental and theoretical investigation of a low-Reynolds-number flow through deformable shallow microchannels with ultra-low height-to-width aspect ratios," *Microfluid. Nanofluid.*, vol. 23, p. 66, 2019, DOI: 10.1007/s10404-019-2235-9.

[139] S. Timoshenko and J. N. Goodier, *Theory of Elasticity*, 2nd ed., ser. Engineering Societies Monographs. New York: McGraw-Hill, 1951.

[140] N. Challamel and I. Elishakoff, "A brief history of first-order shear-deformable beam and plate models," *Mech. Res. Commun.*, vol. 102, p. 103 389, 2019, DOI: 10.1016/j.mechrescom.2019.06.005.

[141] J. Chakraborty and S. Chakraborty, "Influence of streaming potential on the elastic response of a compliant microfluidic substrate subjected to dynamic loading," *Phys. Fluids*, vol. 22, p. 122 002, 2010, DOI: 10.1063/1.3524530.

[142] P. Karan, J. Chakraborty, and S. Chakraborty, "Influence of non-hydrodynamic forces on the elastic response of an ultra-thin soft coating under fluid-mediated dynamic loading," *Phys. Fluids*, vol. 32, p. 022 002, 2020, DOI: 10.1063/1.5134149.

[143] J. Chakraborty and S. Chakraborty, "Combined influence of streaming potential and substrate compliance on load capacity of a planar slider bearing," *Phys. Fluids*, vol. 23, p. 082 004, 2011, DOI: 10.1063/1.3624615.

[144] X. Yin and S. Kumar, "Lubrication flow between a cavity and a flexible wall," *Phys. Fluids*, vol. 17, p. 063 101, 2005, DOI: 10.1063/1.1914819.

[145] M. Van Dyke, "Slow variations in continuum mechanics," *Adv. Appl. Mech.*, vol. 25, pp. 1–45, 1987, DOI: 10.1016/S0065-2156(08)70276-X.

[146] E. Lauga, A. D. Stroock, and H. A. Stone, "Three-dimensional flows in slowly varying planar geometries," *Phys. Fluids*, vol. 16, pp. 3051–3062, 2004, DOI: 10.1063/1.1760105.

[147] J. Friend and L. Yeo, "Fabrication of microfluidic devices using polydimethylsiloxane," *Biomicrofluidics*, vol. 4, p. 026 502, 2010, DOI: 10.1063/1.3259624.

[148] M. H. Essink, A. Pandey, S. Karpitschka, C. H. Venner, and J. H. Snoeijer, "Regimes of soft lubrication," *J. Fluid Mech.*, vol. 915, A49, 2021, DOI: 10.1017/jfm.2021.96.

[149] T. G. J. Chandler and D. Vella, "Validity of Winkler's mattress model for thin elastomeric layers: beyond Poisson's ratio," *Proc. R. Soc. A*, vol. 476, p. 20 200 551, 2020, DOI: 10.1098/rspa.2020.0551.

[150] S. Zhang, "On the accuracy of Reissner–Mindlin plate model for stress boundary conditions," *ESAIM: M2AN*, vol. 40, pp. 269–294, 2006, DOI: 10.1051/m2an:2006014.

[151] Y. S. Muzychka and J. Edge, "Laminar non-Newtonian fluid flow in noncircular ducts and microchannels," *ASME J. Fluids Eng.*, vol. 130, p. 111 201, 2008, DOI: 10.1115/1.2979005.

[152] Y. Liu, J. Li, and A. J. Smits, "Roughness effects in laminar channel flow," *J. Fluid Mech.*, vol. 876, pp. 1129–1145, 2019, DOI: 10.1017/jfm.2019.603.

[153] K. A. Flack, "Moving beyond Moody," *J. Fluid Mech.*, vol. 842, pp. 1–4, 2018, DOI: 10.1017/jfm.2018.154.

[154] F. L. Moody, "Friction Factors for Pipe Flow," *Trans. ASME*, vol. 66, pp. 671–684, 1944.

[155] K. V. Sharp, R. J. Adrian, J. G. Santiago, and J. I. Molho, "Liquid Flows in Microchannels," in *The MEMS Handbook*, M. Gad-el-Hak, Ed., Boca Raton, FL: CRC Press, Sep. 2001, ch. 6, DOI: 10.1201/9781420050905.ch6.

[156] P. J. Pritchard, *Fox & McDonald's Introduction to Fluid Mechanics*, 8th ed. Hoboken, NJ: John Wiley & Sons, 2011.

[157] C. J. Pipe and G. H. McKinley, "Microfluidic rheometry," *Mech. Res. Commun.*, vol. 36, pp. 110–120, 2009, DOI: 10.1016/j.mechrescom.2008.08.009.

[158] S. Gupta, W. S. Wang, and S. A. Vanapalli, "Microfluidic viscometers for shear rheology of complex fluids and biofluids," *Biomicrofluidics*, vol. 10, p. 043 402, 2016, DOI: 10.1063/1.4955123.

[159] X. Yang, N. T. Weldetsadik, Z. Hayat, *et al.*, "Pressure drop of single phase flow in microchannels and its application in characterizing the apparent rheological property of fluids," *Microfluid. Nanofluid.*, vol. 23, p. 75, 2019, DOI: 10.1007/s10404-019-2241-y.

[160] F. Del Giudice, F. Greco, P. A. Netti, and P. L. Maffettone, "Is microrheometry affected by channel deformation?" *Biomicrofluidics*, vol. 10, p. 043 501, 2016, DOI: 10.1063/1.4945603.

[161] X. Wang and I. C. Christov, "Soft hydraulics in channels with thick walls: The finite-Reynolds-number base state and its stability," in *Proceedings of the 12th International Online Conference for Promoting the Application of Mathematics in Technical and Natural Sciences - AMiTaNS'20*, ser. AIP Conference Proceedings, M. D. Todorov, Ed., vol. 2302, AIP, 2020, p. 020 002, DOI: 10.1063/5.0033517.

[162] D. Stoecklein and D. Di Carlo, "Nonlinear Microfluidics," *Anal. Chem.*, vol. 91, pp. 296–314, 2019, DOI: 10.1021/acs.analchem.8b05042.

[163] E. J. Lim, T. J. Ober, J. F. Edd, *et al.*, "Inertio-elastic focusing of bioparticles in microchannels at high throughput," *Nat. Commun.*, vol. 5, p. 4120, 2014, DOI: 10.1038/ncomms5120.

[164] C. Ruyer-Quil and P. Manneville, "Improved modeling of flows down inclined planes," *Eur. Phys. J. B*, vol. 15, pp. 357–369, 2000, DOI: 10.1007/s100510051137.

[165] N. O. Rojas, M. Argentina, E. Cerda, and E. Tirapegui, "Inertial Lubrication Theory," *Phys. Rev. Lett.*, vol. 104, p. 187 801, 2010, DOI: 10.1103/PhysRevLett.104.187801.

[166] G. G. Peng and J. R. Lister, "Viscous flow under an elastic sheet," *J. Fluid Mech.*, vol. 905, A30, 2020, DOI: 10.1017/jfm.2020.745.

[167] H. B. Keller, *Numerical Solution of Two Point Boundary Value Problems*, ser. CBMS-NSF Regional Conference Series in Applied Mathematics. Philadelphia, PA: SIAM, 1976, vol. 24, DOI: 10.1137/1.9781611970449.

[168] M. H. Holmes, *Introduction to Perturbation Methods*, ser. Texts in Applied Mathematics. New York, NY: Springer Science+Business Media, 2013, vol. 20, DOI: 10.1007/978-1-4614-5477-9.

[169] A. Mehboudi and J. Yeom, "A one-dimensional model for compressible fluid flows through deformable microchannels," *Phys. Fluids*, vol. 30, p. 092 003, 2018, DOI: 10.1063/1.5043202.

[170] H. A. Stone, “Fundamentals of fluid dynamics with an introduction to the importance of interfaces,” in *Soft Interfaces*, ser. Lecture Notes of the Les Houches Summer School, L. Bocquet, D. Quéré, T. A. Witten, and L. F. Cugliandolo, Eds., vol. 98, New York, NY: Oxford University Press, 2017, pp. 3–79, DOI: 10.1093/oso/9780198789352.003.0001.

[171] L. Pekker, “A one-dimensional model of liquid laminar flows with large Reynolds numbers in tapered microchannels,” *Phys. Fluids*, vol. 33, p. 042 003, 2021, DOI: 10.1063/5.0041283.

[172] X. Wang and I. C. Christov, “Reduced modeling and global instability of finite-Reynolds-number flow in compliant rectangular channels,” *preprint, arXiv:2202.11704*, 2022, DOI: 10.48550/arXiv.2202.11704.

[173] K. Pohlhausen, “Zur näherungsweisen Integration der Differentialgleichung der laminaren Grenzschicht,” *Z. Angew. Math. Mech. (ZAMM)*, vol. 1, no. 4, pp. 252–290, 1921, DOI: 10.1002/zamm.19210010402.

[174] P. Howell, G. Kozyreff, and J. Ockendon, *Applied Solid Mechanics*. Cambridge, UK: Cambridge University Press, 2009, DOI: 10.1017/CBO9780511611605.

[175] M. Gad-el-Hak, “Compliant coatings for drag reduction,” *Prog. Aerospace Sci.*, vol. 38, pp. 77–99, 2002, DOI: 10.1016/S0376-0421(01)00020-3.

[176] P. Huerre and P. A. Monkewitz, “Local and Global Instabilities in Spatially Developing Flows,” *Annu. Rev. Fluid Mech.*, vol. 22, pp. 473–537, 1990, DOI: 10.1146/annurev.fl.22.010190.002353.

[177] K. Subbaraj and M. Dokainish, “A survey of direct time-integration methods in computational structural dynamics—II. Implicit methods,” *Comput. Struct.*, vol. 32, pp. 1387–1401, 1989, DOI: 10.1016/0045-7949(89)90315-5.

[178] I. J. Hewitt, N. J. Balmforth, and J. R. De Bruyn, “Elastic-plated gravity currents,” *Eur. J. Appl. Math.*, vol. 26, pp. 1–31, 2015, DOI: 10.1017/S0956792514000291.

[179] Z. X. Cai and X. Y. Luo, “A fluid–beam model for flow in a collapsible channel,” *J. Fluids Struct.*, vol. 17, pp. 125–146, 2003, DOI: 10.1016/S0889-9746(02)00112-3.

[180] A.-R. Kim, S. K. Mitra, and B. Zhao, “Reduced Pressure Drop in Viscoelastic Polydimethylsiloxane Wall Channels,” *Langmuir*, vol. 37, pp. 14 292–14 301, Dec. 2021, DOI: 10.1021/acs.langmuir.1c02087.

[181] P. Karan, S. S. Das, R. Mukherjee, J. Chakraborty, and S. Chakraborty, “Flow and deformation characteristics of a flexible microfluidic channel with axial gradients in wall elasticity,” *Soft Matter*, vol. 16, pp. 5777–5786, 2020, DOI: 10.1039/d0sm00333f.

[182] R. R. Kerswell, C. C. T. Pringle, and A. P. Willis, "An optimization approach for analysing nonlinear stability with transition to turbulence in fluids as an exemplar," *Rep. Prog. Phys.*, vol. 77, p. 085 901, 2014, DOI: 10.1088/0034-4885/77/8/085901.

[183] S. Cherubini, P. De Palma, J. C. Robinet, and A. Bottaro, "Rapid path to transition via nonlinear localized optimal perturbations in a boundary-layer flow," *Phys. Rev. E*, vol. 82, p. 066 302, 2010, DOI: 10.1103/PhysRevE.82.066302.

[184] S. Cherubini, P. De Palma, J. C. Robinet, and A. Bottaro, "The minimal seed of turbulent transition in the boundary layer," *J. Fluid Mech.*, vol. 689, pp. 221–253, 2011, DOI: 10.1017/jfm.2011.412.

[185] R. R. Kerswell, "Nonlinear nonmodal stability theory," *Annu. Rev. Fluid Mech.*, vol. 50, pp. 319–345, 2018, DOI: 10.1146/annurev-fluid-122316-045042.

VITA

Education

Purdue University, West Lafayette **Aug. 2018 – Aug. 2022**

Ph.D. in Mechanical Engineering

Shanghai Jiao Tong University, China **Sept. 2015 – Mar. 2018**

M.S. in Naval Architecture and Ocean Engineering

Tianjin Univeristy, China **Sept. 2011 – Jun. 2015**

B.S. in Ocean and Naval Engineering

Minor in English Literature

Publications resulting from this thesis

- Xiaojia Wang, Ivan C. Christov, "Reduced modeling and global instability of finite-Reynolds-number flow in compliant rectangular channels," *submitted*, 2022, DOI: 10.48550/arXiv.2202.11704.

- Xiaojia Wang, Ivan C. Christov, "Reduced models of unidirectional flows in compliant rectangular ducts at finite Reynolds number," *Physics of Fluids*, 33(10):102004, 2021, DOI: 10.1063/5.0062252.

- Tanmay C. Inamdar, Xiaojia Wang, Ivan C. Christov, "Unsteady fluid-structure interactions in a soft-walled microchannel: A one-dimensional lubrication model for finite Reynolds number," *Physical Review Fluids*, 5(06):064101, 2020, DOI: 10.1103/PhysRevFluids.5.064101.

- Xiaojia Wang, Ivan C. Christov, "Soft hydraulics in channels with thick walls: The finite-Reynolds-number base state and its stability," *AIP Conference Proceedings*, 2302:020002, 2020, DOI: 10.1063/5.0033517.

- Xiaojia Wang, Ivan C. Christov, “Theory of the flow-induced deformation of shallow compliant microchannels with thick walls,” *Proceedings of the Royal Society A*, 475(2231): 20190513, 2019, DOI: 10.1098/rspa.2019.0513.

Conference presentations resulting from this thesis

- Xiaojia Wang, Ivan C. Christov, Dancing microchannels: Reduced models for unsteady fluid–structure interactions at the microscale, poster, The 2021 SES (Virtual) Month: Mechanics Matters, virtual, 2021.

- Xiaojia Wang, Ivan C. Christov, Reduced models for analyzing flow instability in compliant rectangular microchannels, The 74th Annual Meeting of the American Physical Society’s Division of Fluid Dynamics, Phoenix, Arizona, USA, 2021.

- Xiaojia Wang, Ivan C. Christov, Modeling and stability in compliant microchannels, SPARC Workshop on Fluidics involving deformable interfaces, virtual, 2021.

- Xiaojia Wang, Ivan C. Christov, Theory of the bulging effect of soft microchannels with thick walls, The 72nd Annual Meeting of the American Physical Society’s Division of Fluid Dynamics, Seattle, Washington, USA, 2019.

- Xiaojia Wang, Ivan C. Christov, Towards a theory of fluid–structure interaction due to internal flow in deformable microchannels, poster, Mathematical Fluids, Materials and Biology Workshop, Ann Arbor, Michigan, USA, 2019.